Tropospheric ozone in the UK: Modelling its sources and the impact of European anthropogenic emissions

By

Leidy Johana Romero Alvarez

A thesis submitted to the School of Environmental Sciences of the University of East Anglia in partial fulfilment of the requirements for the degree of Doctor of Philosophy

November 2019

Abstract

Ozone (O_3) is a pollutant of concern for policy-makers because of its detrimental effects on human health, agriculture and ecosystems. Near the surface, O_3 has an atmospheric lifetime of hours. However, once it is lifted to the free troposphere, O_3 can live for several weeks and be transported over long distances, jeopardizing the compliance of air quality standards downwind. This thesis aims to further the understanding of the dependence of the UK on domestic and foreign emissions controls to meet local and European ozone air quality standards. Numerical simulations are carried out using WRF-Chem with a novel ozone-tagging method that has been implemented. Meteorology and two different chemical mechanisms, MOZART-4 and CRImech, were evaluated using surface observations acquired during the ICOZA field campaign of 2015.

Results confirm the prominent role of short-range transport of O_3 from continental Europe to the UK as well as from no-controllable O_3 sources such as the hemispheric ozone, which account for 71% of the total modelled O_3 from May to August. The contribution of O_3 from European NOx emissions is principally due to the transport of O_3 rather than NOx reservoir.

It is shown that emission controls would be required in different source regions for compliance of ozone standards such as MDA8 O_3 of 50 and 60 ppbv. For example, emissions controls in France affect mostly the south and southeast of the UK while domestic emissions controls are more relevant for the Midlands and the northern regions. By contrast, attainment of lower exposure thresholds, e.g., AOT40 metric, would primarily require the regulation of the hemispheric ozone levels.

O_3 from Germany, the Benelux, France and ship emissions in the North Sea are responsible for the build-up of O_3 in the southeast UK during the summertime 2015 pollution episode. Furthermore, process analysis diagnostics demonstrates that vertical mixing in the morning can bring O_3 and precursors from the residual layer to the ground which contributes to the build-up of O_3 during pollution episodes.

Access Condition and Agreement

Each deposit in UEA Digital Repository is protected by copyright and other intellectual property rights, and duplication or sale of all or part of any of the Data Collections is not permitted, except that material may be duplicated by you for your research use or for educational purposes in electronic or print form. You must obtain permission from the copyright holder, usually the author, for any other use. Exceptions only apply where a deposit may be explicitly provided under a stated licence, such as a Creative Commons licence or Open Government licence.

Electronic or print copies may not be offered, whether for sale or otherwise to anyone, unless explicitly stated under a Creative Commons or Open Government license. Unauthorised reproduction, editing or reformatting for resale purposes is explicitly prohibited (except where approved by the copyright holder themselves) and UEA reserves the right to take immediate ‘take down’ action on behalf of the copyright and/or rights holder if this Access condition of the UEA Digital Repository is breached. Any material in this database has been supplied on the understanding that it is copyright material and that no quotation from the material may be published without proper acknowledgement.

Acronyms

AOT40 - Accumulated O_3 over the Threshold value of 40 ppbv

CRImech - Common Representative Intermediates mechanism

DEFRA - Department for Environment, Food and Rural Affairs

ECMWF - European-Centre for medium-Range Forecast

EU - European Union

HTAP - Task Force on Hemispheric Transport of Air Pollution

IBL - Internal Boundary Layer

KPP - The Kinetic Pre-Processor

MBL - Marine Boundary Layer

MDA8 - Maximum Daily 8 Hour Average

MOZART-4 - Model for Ozone and Related chemical Tracers version 4

NAEI - National Emissions Inventory

NBL - Nocturnal Boundary Layer

PBL - Planetary Boundary Layer

ppbv - Parts per billion (by volume)

UK - United Kingdom

UTC - Coordinated Universal Time

WHO - World Health Organisation

WMO - World Meteorological Organisation

WRF-Chem - Weather Research and Forecasting model coupled with Chemistry

To the silenced and traded dreams in the 90s and early 2000s in Medellin-Colombia and to the ***warriors that made it through****!*

Acknowledgments

First and foremost, I would like to thank Professor Roland von Glasow for believing in my abilities when giving me the opportunity to start a PhD program. His sudden departure has deprived us of an exceptional academic and friend.

I would like to acknowledge the ICOZA Team for providing the observational data, Professor Jan Kaiser (UEA) for helping cover the expenses of the high-performance computing usage, and Leo Earl and Jimmy Cross (high-performance computing UEA) for their support in the compilation of WRF-Chem.

I would like to thank Dr Douglas Lowe (University of Manchester) for showing me how to implement the anthropogenic emissions into WRF-Chem and for helping me complete my first model setup. Also, I would like to thank Dr Scott Archer-Nichols (currently at Cambridge University) for his assistance on the speciation of the VOCs anthropogenic emissions and for his valuable insights. Chapter three and five would not have been possible without their valuable contributions.

Part of this project was done in collaboration with the Institute for Advanced Sustainability Studies in Germany (IASS). I would like to acknowledge Professor Tim Butler, who is the mind behind the ozone-tagging method. I also would like to thank Dr Aurelia Lupascu for showing me ways of implementing the ozone-tagging mechanism into WRF-Chem and for her useful advices on potential applications. Chapter three, four and six, would not have been possible without her precious collaboration.

Last but not least, I would like to thank my supervisory team: Professor Claire Reeves, Professor Stephen Dorling and Dr Alba Badia for providing me with their valuable guidance and assistance throughout these four years. In particular, I would like to thank them for their moral support and encouragement during the last stage of the project.

Table of Contents

List of Figures

List of Tables

Chapter 1

INTRODUCTION

Ozone (O_3) is a multifaceted secondary trace gas that impacts the Earth's atmosphere in many ways. In the stratosphere, it shields the earth's surface from damaging UV radiation. Conversely, in the troposphere, it behaves as an important short-lived greenhouse gas (Myhre et al., 2013). Near the earth's surface, O_3 is regarded as a hazardous oxidant with detrimental effects on human health, crops, and ecosystems (e.g., Fuhrer, 2009; World Health Organization, 2016). Still, it plays a vital role as the primary source of OH radicals in the troposphere, which drives the removal of many trace gases, including the most abundant species such as carbon monoxide (CO) and methane (CH_4) (Monks, 2005).

The mechanisms leading to O_3 formation in the troposphere are well understood. Photolysis of nitrogen dioxide (NO_2) and the subsequent reaction of the product $O(^3P)$ (ground state atomic oxygen) with a molecule of oxygen (O_2) is the only known mechanism for chemical O_3 production in the troposphere (Monks et al., 2005). Production of O_3 is highly non-linear and depends on the abundance of its precursors nitrogen oxides (NOx) and volatile organic compounds (VOCs) (Atkinson, 2000). Net production is achieved when NOx is available at moderate levels in a narrow window (Atkinson, 2000; Monks, 2005). Very low concentrations of NOx lead to overall O_3 destruction while high NOx concentration reduces O_3 production rate, unless VOCs concentrations rise to balance the competing reactions (Monks, 2005). These dynamics characterise the so-called NOx-limited and NOx-saturated regimes. Furthermore, O_3 concentrations not only depend on the availability of its precursors but also on its deposition and meteorological variables such as temperature, winds (direction and speed), cloud cover formation and precipitation (e.g. Logan, 1985; Coyle et al., 2002). For instance, high O_3 concentration episodes in the UK have been associated with abnormally hot years, such as the 2003 European heatwave (Lee et al., 2006). It is also well established that the concentration of O_3 at a given location is determined by a combination of hemispheric, regional and local-scale factors (Jenkin, 2008). Examples of this are photochemical reactions on a local and regional scale, and transport of O_3 and precursors from other continents and from the stratosphere (e.g., Monks, 2000; HTAP, 2007).

In the UK, tighter European emissions controls in the last 30 years have led to a substantial decrease in the concentration of ozone's primary precursors and successfully reduced the intensity and severity of the high O_3 concentration episodes (AQEG, 2009). Even so, exposure to surface O_3 continues to cause considerable damage to human health in Europe with an estimated 17,000 premature deaths in 2015 (EEA, 2017). Moreover, evidence suggests that the annual mean O_3 concentrations in the UK have been increasing in both rural and urban areas (Jenkin et al., 2008; AQEG, 2009; Munir et al., 2013). It is believed that reductions in NOx emissions, mainly by road traffic, have led to reductions in the ozone scavenging in urban areas so that ozone concentrations have generally increased (AQEG, 2009). The increase in rural areas, on the other hand, is largely driven by rising hemispheric ozone levels, up to 0.3 ppbv/year (~5ppb over 25 years) (Jenkin, 2008; Derwent et al., 2013). Accordingly, increasing emissions of precursors in Asia and North America are known to influence O_3 concentrations entering Europe (HTAP, 2010). Therefore, efficient emissions control policies aimed at reducing O_3 concentration at a given region rely on the assessment of both O_3 transport from outside the region and in-situ O_3 production. Such quantitative estimations can be made by applying source-receptor methods (S-R) within Chemical Transport Models (CTMs) (Li, 2002; Wild et al., 2004; Auvray & Bey, 2005; Sudo & Akimoto, 2007; Derwent et al., 2008; Emmons et al., 2012; Derwent., 2015; Butler et al., 2018).

S-R studies often compare simulations that include all anthropogenic emissions with those obtained after changing emissions from the region of interest (the so-called perturbation approach). As O_3 chemistry is non-linear, this approach can lead to unrealistic attribution estimates, e.g. Emmons et al. (2012) underestimated the O_3 contribution by up to a factor of 4 when perturbing NO emissions by 20%. So-called tagged-ozone methods, which use additional diagnostics to follow the reaction of different emissions to the formation of O_3, are better suited to investigate the contribution of different precursors to the total amount of O_3 (e.g., Emmons et al., 2012; Butler et al., 2018).

This thesis investigates the sources of tropospheric O_3 in the UK using a novel S-R method for tagged-ozone that is implemented into the Regional Weather Forecast and Research Model couple with chemistry (WRF-Chem). The study aims to expand the current understanding of the dependence of the UK on domestic and foreign emissions controls to meet the local and European O_3 air quality standards.

The modelling system is described in Chapter 2. Chapter 3 presents the results from the meteorological and chemical evaluation of the model system, including a comparison between the two chemical mechanisms used in the present study: MOZART and CRImech. Results are presented in Chapters 4, 5 and 6. The impacts of European and domestic emissions on the different UK regions are discussed in Chapter 4. The contributions of the factors controlling surface O_3 concentrations (chemical production and loss, advection, vertical mixing and dry deposition) during a high O_3 concentration episode in the East Anglia region are analysed in Chapter 5. The application of the O_3 tagging method to a case study in Weybourne Norfolk characterised by easterly winds and high O_3 concentrations is presented in Chapter 6. Finally, the conclusions are summarised in Chapter 7.

The present, introductory Chapter gives an overview of the relevant background information on which this investigation is based. Sections 1.1 and 1.2 briefly describe the processes governing O_3 abundance in the troposphere and Section 1.3 gives an introduction to chemical transport models.

1.1 Structure of the atmosphere

The 'Planetary Boundary Layer' (PBL) is the layer closest to the earth's surface where the majority of the air pollutants are emitted. Its behaviour is directly influenced by interactions with the earth's surface through transport of water vapour, heat, momentum and other atmospheric constituents by molecular processes and turbulence. Turbulence in the PBL is associated with wind shear and buoyancy, which is caused by differential solar heating of the earth's surface that creates thermals, or convection, and compensates subsidence. The frictional stress in the horizontal wind exerted by obstacles such as vegetation and topography creates vertical gradients in the horizontal wind flow (vertical shear) and introduces chaotic wind patterns. By contrast, when the shear is small and there is no buoyancy, the flow of the air is laminar, i.e. non-turbulent (Warner, 2011).

The thickness of the PBL varies: it tends to be thicker during the daytime and in the warmer months and shallower during night-time and in cold months. This is because the Earth surface is a much more efficient absorber and emitter of radiation than the atmosphere. During daylight hours, the earth surface heats up faster and transfers that heat to the atmosphere by conduction in the laminar sublayer, which is the no-turbulent interface between the ground level and the surface layer of a few centimetres in depth, and by convection above the laminar-sublayer, heating the uppermost parts of the PBL. Intense radiation during hot days induces turbulent convection and strong winds forcing the PBL to expand. The opposite occurs during the night-time of cold days, as the land surface and the bottom layers of the troposphere cool down faster than the upper layers creating a temperature inversion. In addition, buoyancy-driven convective turbulence is switched off during the night, so any turbulent-energy in the layer must originate from the vertical shear in the horizontal wind. Unless the horizontal wind is particularly strong, the resulting boundary layer is thus much shallower and stable. Fig. 1.1 shows a schematic of the daytime (convective) and nocturnal (stable) structure of the PBL and the processes regulating O_3

concentrations within the PBL at a rural location in the UK (Warner, 2011). Four major divisions of the PBL can be observed during daylight hours:

- The **surface layer** is within the bottom 50-100 metres of the mixed layer.
- The **mixed layer** is the turbulent interface between the laminar sublayer and the free troposphere. Above the surface layer, convective thermals mix atmospheric constituents such as moisture and air pollutants more efficiently.
- The **entrainment zone** is often an inversion layer that acts as a stable interface between the mixed layer and the free troposphere. Turbulence and well-mixed atmospheric constituents penetrate the PBL through the entrainment zone mostly during the daylight hours.
- Above the PBL lies the free troposphere where the wind speeds are more uniform and higher due to the decrease in friction. In this layer, chemical constituents, such as O_3, are transported faster and more efficiently than in the surface layer (Wild et al., 2004)

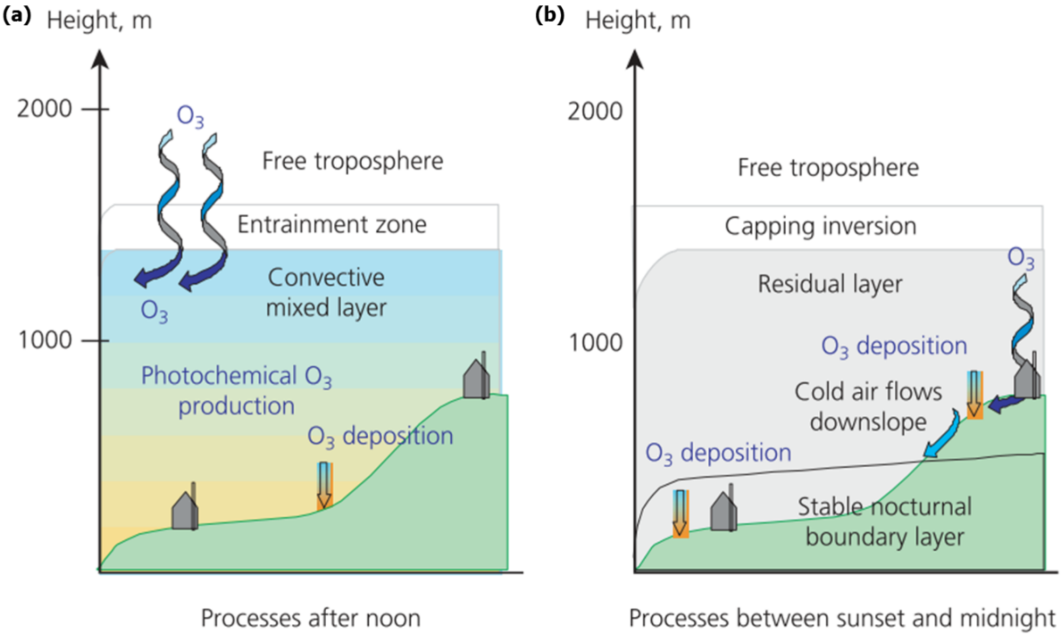

Figure 1.1. Schematic of the Planetary Boundary Layer structure during daylight hours (a) and at night (b) at a rural location in the UK, and the processes regulating O_3 concentrations within the PBL. The figure is taken from the Royal Society, (2008).

During daylight hours, Fig. 1.1a, the thickness of the convective mixed layer increases as it erodes up into the troposphere, allowing O_3 and other chemical species from the day before to penetrate the mixed layer. Under these conditions, O_3 concentrations tend to rise because downward input and photochemical production operate simultaneously exceeding the rate of depletion of O_3 by dry deposition. The thickness of the PBL typically reaches ~1 km in the afternoon depending on the location. After sunset, Fig. 1.1b, and as the evening progresses, the land surface cools down via radiational cooling, and the buoyant-energy derived from the thermals ceases. A shallow stable nocturnal boundary layer (NBL) forms which reduces the entrainment of O_3 from the free troposphere. The nocturnal boundary layer can be 0-200m high and characterised by strong static stability and calm winds at the surface. Depletion of O_3 by dry deposition exacerbates O_3 loss at lower ground sites because mixing from above and photochemical production cannot invert the decline in the concentrations.

Above the NBL, a 'residual layer' decoupled from the stable NBL might develop. Residual atmospheric constituents such as O_3 from the daytime mixed layer can remain in such residual layer. Apart from the meteorology, local topography can determine the degree to which the NBL detaches from the rest of the troposphere (Coyle et al., 2004). Hill-tops sites, for instance, remain more turbulent as cold air circulates down-slope and the surface air is replaced by ozone-rich air from above, as illustrated in Fig. 1b. The diurnal evolution of O_3 in coastal regions resembles that seen on hill-tops: sea-lake breezes maintain mixing as O_3 rich air is advected over the land (Coyle et al., 2004).

1.2 Ozone in the troposphere

Tropospheric O_3 is a multifaceted trace gas that acts as a pollutant, greenhouse gas, and precursor of hydroxyl radicals (OH). Short-term exposure to O_3 is associated with respiratory morbidity and mortality (e.g., Stieb et al., 2009) while long-term exposure has been associated with premature respiratory mortality (e.g., Turner et al., 2016). It is a secondary pollutant, meaning that is not emitted directly but produced chemically in the atmosphere.

O_3 precursors originate mainly from anthropogenic sources, in particular, fossil fuel combustion, agriculture, biomass burning, and oil and gas production, and from biogenic sources, which include emissions from vegetation, soil and the ocean. In urban and suburban sites, O_3 is primarily formed by the sunlight initiating chemical reactions of NOx and NMVOCs. In remote regions, it is instead produced mostly after the oxidation of carbon monoxide (CO) and methane (CH_4) (Royal Society, 2008). Once produced at the surface, O_3 can be lifted into the free troposphere where it has a longer lifetime, spanning from days to weeks (Stevenson et al., 2006), and can be transported efficiently across regions an even continents (HTAP, 2007). O_3 is mainly loss, on a global scale, by chemical destruction which accounts roughly for 4100 Tg y^{-1} and dry deposition to the Earth's surface accounting for approximately 1000 Tg y^{-1}, see Fig. 1.2. The primary sources and sinks of tropospheric O_3 are also illustrated in Fig 1.2, along with estimates of global budgets.

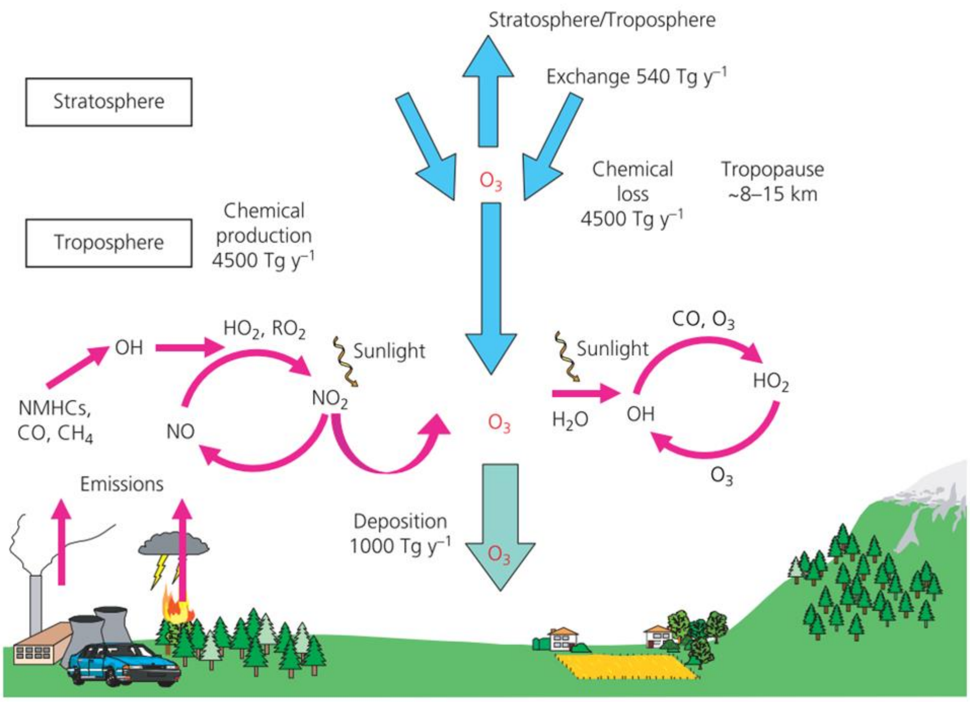

Figure 1.2. Illustration of the tropospheric O_3 budget, and some of the main processes governing O_3 abundance. Annual global fluxes of O_3 were calculated using a Global Chemistry Transport Model. The figure is taken from the Royal Society, (2008).

Production of O_3 varies diurnally, seasonally and inter-annually. In polluted continental sites, surface O_3 exhibits a distinct diurnal pattern with a maximum in the early afternoon due to photochemical production and entrainment as discuss above, and a minimum between the evening and early morning that is caused by dry deposition and NO_x titration (Monks, 2005). Nevertheless, sporadic nocturnal peaks have been observed during the winter months in different parts of Europe and more recently in urban sites in the UK (Kulkarni et al., 2015). These peaks have been in part attributed to a thicker night-time PBL. In particular, Bohnenstengel et al. (2015) have shown that anthropogenic heat fluxes in urban environments may offset the balance between a stable and unstable urban PBL at night in winter, meaning that the nocturnal urban PBL could remain convectively forced and therefore deeper and well mixed even after sunset (Hunt et al., 2012). Weekly patterns are less predictable partly because O_3 has a hemispheric background level upon which local and regional factors may either produce or destroy O_3 (AQEG, 2009). Nevertheless, evidence suggests that O_3 episodes in the UK are more prevalent at the end of the week, with greater exposure occurring on Fridays (Jenkin et al., 2002).

Seasonal O_3 often reaches a springtime maximum over remote northern mid-latitudes that is controlled by both photochemical production within the troposphere and the downward transport of O_3 from the stratosphere (Monks, 2000), see Fig. 1.3. Moreover, a broad spring-summer maximum controlled primarily by regional photochemical production within the lower troposphere (Monks, 2000) is often observed on mid-latitude populated continental areas. In the summertime, meteorological variations across the region and air mass trajectories generally promote higher levels of O_3 in the Mediterranean than in the northern EU countries (Lelieveld et al., 2002; EEA, 2015)

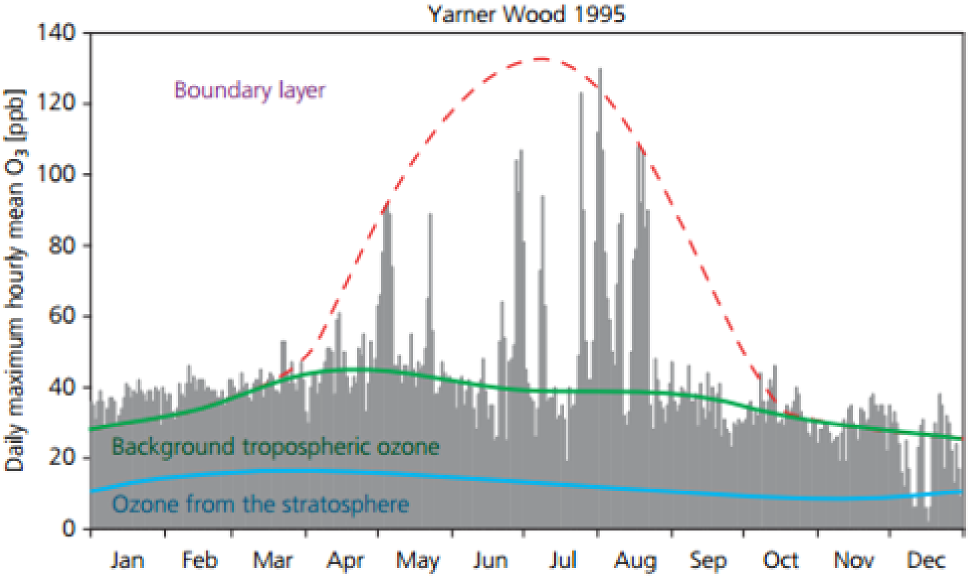

Figure 1.3. O_3 concentration measured at the near surface in rural southern UK in 1995 showing daily variability in surface O_3 (grey peaks) within the PBL. Superimposed is the annual cycle of O_3 showing a spring and early summer peak concentrations (red line). The seasonal cycle of the hemispheric background O_3 concentrations is depicted in green (which represents the remaining concentration of O_3 once the emissions of anthropogenic O_3 precursors are switched off), while that from the stratosphere is exhibited in blue. The figure was taken from the Royal Society, (2008).

Because of its trans-boundary nature, O_3 health-related standards in the European directive are treated as a target value (vs. mandatory limit values in the case of other pollutants). The mandatory aspects of O_3 are then included within the National Emission Ceilings Directive for individual member states for NOx and VOCs, which are designed to achieve reductions in O_3 levels (Monks et al., 2015). The current health-related standard is based on studies of human exposure and is expressed as 8-hour averages and sets a limit for the maximum daily 8h average concentration (MDA8 O_3) of 120μg m^{-3} (~60 ppbv). By contrast, the World Health Organisation (WHO) and the UK Air Quality Strategy suggests a limit for MDA8 O_3 of 100 μg m^{-3} (~50 ppbv) (Royal society, 2008). There are also standards in place to protect against damage to vegetation. The EU Directive on Ambient Air and the UK Air Quality Strategy sets an AOT40 target value (which corresponds to the seasonal accumulated exposure to O_3 above 40 ppbv (80 μgm^{-3}) during daylight hours of 9000 ppb h^{-1} over three months (May–July) averaged value over 5 years (Royal Society, 2008).

1.2.1 High ozone episodes during heat waves

Clear skies, high temperatures, light winds, and low humidity associated with summertime anticyclonic conditions tend to trigger photochemical O_3 episodes at mid-latitude sites. Very high pollution episodes in the UK (with O_3 mixing ratios over 90 ppbv) are frequently linked to temperatures over 28–30 °C (Lee et al., 2006). Moreover, evidence suggests that the highest O_3 levels in the UK tend to occur in days when back trajectories bring highly polluted air masses to the UK after looping over mainland Europe (Jenkin et al., 2002), see Fig. 1.4. These trajectories are similar to those observed during anticyclonic conditions.

More recently, Ordóñez el al. (2017) assessed the impact of high latitude blocking anticyclones on surface O_3 in Europe. The data showed that during summertime over 30% of the days with blocks within Europe (between 0–30°E and 50-70°N) coincided with exceedances of the 90th percentile of the O_3 distribution in those regions. Furthermore, an uncommon synoptic situation, in which a blocking high set ups over the eastern Atlantic (15–0°W) preventing other weather systems from moving through while the UK is under the influence of an anticyclone, was found to be very efficient at rising O_3 levels in the UK and the north-west of France, with an increase in the occurrence of MDA8 O_3 mixing ratios of about 35–55 ppbv.

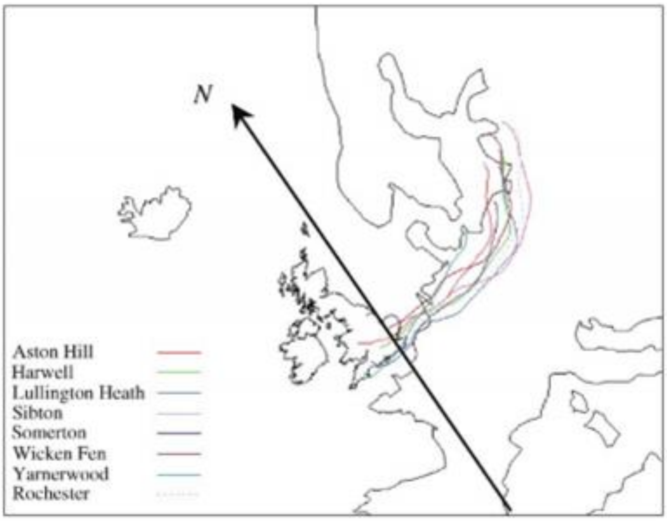

Figure 1.4. Back trajectories arriving at eight southern UK rural sites at 16:00 hours on 31st July 1999. The figure is taken from Jenkin et al. (2002).

During high-pressure weather (anticyclonic conditions) air tends to subside toward the earth's surface, limiting cloud formation and the mixing up of pollutants. As the latter stagnate, the severity of the high O_3 concentration episodes tends to escalate daily during the residence time of the synoptic system (Ordonez et al., 2017). The same conditions enhance downward shortwave radiation flux as well as daily maximum temperatures (Ordonez et al., 2017), boosting photolysis reactions and emissions of some VOCs species, in particular of biogenic origin. Soil drying can also promote positive feedbacks causing an additional temperature increase (Solberg et al., 2008; Vieno et al., 2010). Furthermore, high temperatures induce stomatal closing, which limits O_3 uptake by plants and therefore enhance O_3 build-up (e.g., Grünhage et al., 2012).

The great pollution event of 2003 provides an illustrative example. A blocking high located above northern France caused temperatures anomalies in excess of 6-7 °C in the UK, resulting in the European MDA8 O_3 of 120 µgm–3 being repeatedly exceeded in Southeast England (Lee et al., 2006). Since then, several studies have investigated the contributing factors leading to high O_3 episodes in Europe and the UK (e.g., Vautard et al., 2005; Lee et al., 2006; Solberg et al., 2008; Vieno et al. 2010; Francis et al., 2011; Strong et al., 2013; Safieddine et al., 2014). Lee et al. (2006) observed that local emissions of isoprene and monoterpenes increased dramatically in the UK during the heat wave, suggesting that O_3 could have been generated in-situ. Similarly, the numerical simulations by Vieno et al. (2010) and Solberg et al. (2008) identified the increase of local isoprene emissions and the suppression of dry deposition as the primary causes of the high O_3 concentrations in the southeast UK. Predictions in Francis et al. (2011), on the other hand, has shown that the convergence of westerly and easterly winds and the downward entrainment of ozone-rich air from residual layers are important mechanisms responsible for the accumulation of surface O_3 in the UK.

1.2.2 Overview of chemical production and destruction of ozone

Urban emissions are dominated by carbon monoxide (CO), NOx (NO + NO_2) and VOCs, which include methane and non-methane compounds. These species react in the atmosphere to create secondary pollutants such as O_3, oxygenated VOCs, secondary organic aerosol, and reservoir species such as peroxyacetyl nitrates (PAN), among others (Atkinson, 2000). Solar short wave radiations can dissociate specific trace gases "photolysable species" into high reactive atoms and radicals, such as hydroxyl radical (OH), which is a key oxidant that drives daytime chemistry in the tropospheric (Monks et al., 2009). An extremely short lifetime (about 1 second) makes the concentration of OH highly dependable on the concentration of its sources and sinks (Atkinson, 2000). Nevertheless, OH is ubiquitous throughout the troposphere due to the widespread nature of its primary precursors.

Photolysis of O_3 (at wavelengths < 320 nm) yields an excited $O(^1D)$ oxygen atom, which reacts with water vapour to form OH (Atkinson, 2000), see reactions R. 1.1 – 1.4:

$$O_3 + hv \rightarrow O_2 + O(^1D) \quad (R.\ 1.1)$$

$$O(^1D) + M \rightarrow O + M \quad (R.\ 1.2)$$

$$O(^1D) + H_2O \rightarrow 2OH \quad (R.\ 1.3)$$

$$O(^3P) + O_2 + M \rightarrow O_3 + M \quad (R.\ 1.4)$$

At typical atmospheric conditions, only a small fraction of all $O(^1D)$ atoms react with H_2O to form OH, as the majority of $O(^1D)$ atoms are converted to ground state $O(^3P)$ by collision with N_2 and O_2 (Atkinson, 2000), and go on to regenerate O_3.

OH reacts mainly with atmospheric species such as VOCs and CO to initiate the reaction cycles that produce and remove tropospheric O_3 (Monks et al., 2005). The photolysis of NO_2 (at wavelengths < 420 nm), and the subsequent reaction of the product $O(^3P)$ with a molecule of oxygen, are the only known mechanism for chemical O_3 production in the troposphere (Monks et al., 2005), as in reactions R. 1.5 – 1.7:

$$NO_2 + hv \rightarrow NO + O \quad \text{(R. 1.5)}$$
$$O + O_2 + M \rightarrow O_3 + M \quad \text{(R. 1.6)}$$
$$NO + O_3 \rightarrow NO_2 + O_2 \quad \text{(R. 1.7)}$$

The production takes place via a fast catalytic cycle catalysed by NO_x. Therefore, reactions R.1.5 - 1.6 do not consume any NO_x molecules, and consequently, several O_3 molecules can be produced by one NO_x molecule before NO_x is removed from the atmosphere by other processes, such as the reaction of NO_2 with OH and deposition. As long as no other reactions take place, reactions R. 1.5 - 1.7 do not destroy or produce O_3 molecules, suggesting a steady-state for O_3.

The amount of O_3 present in the troposphere cannot be explained only by this photochemical cycle. In clean environments (i.e. very low NO_x) typical of remote areas, the primary fate of OH is the reaction with the longer-lived carbon monoxide CO and methane CH_4 to produce peroxy radicals HO_2 and CH_3O_2, as in reactions R. 1.8 – 1.11:

$$CO + OH \rightarrow CO_2 + H \quad \text{(R. 1.8)}$$
$$H + O_2 + M \rightarrow HO_2 + M \quad \text{(R. 1.9)}$$
$$CH_4 + OH \rightarrow CH_3 + H_2O \quad \text{(R. 1.10)}$$
$$CH_3 + O_2 + M \rightarrow CH_3O_2 + M \quad \text{(R. 1.11)}$$

At very low NO_x concentrations in the troposphere, practically no O_3 production occurs through the NO_x-cycle. The fate of the peroxy radicals is their mutual reaction to form methyl hydroperoxide (CH_3OOH) and hydrogen peroxide (H_2O_2), see R. 1.12 and R. 1.13, respectively.

$$HO_2 + HO_2 \rightarrow H_2O_2 + O_2 \quad \text{(R. 1.12)}$$
$$CH_3O_2 + HO_2 \rightarrow CH_3OOH + O_2 \quad \text{(R. 1.13)}$$

These two species often dissolve in water droplets and rain as their sinks.

Being initiated by photolysis of O_3, the reactions constitute a loss channel for O_3, as shown in reaction R. 1.1 (Monks 2005).

O_3 can be further lost by direct reaction with HO_2 radicals, leading to the regeneration of OH, which can eventually contribute to catalytic destruction of O_3 (Monks 2005). Conversely, in a more polluted environment (low NOx) typical of rural areas of industrialised countries, OH initiated reactions cause the production of O_3 due to the oxidation of NO to NO_2 (Reaction R. 1.14 and 1.15) (Atkinson, 2000). O_3 formation in this regime is referred to as NO_x sensitive since the increase of NO_x increases the amount of free-radical promoting O_3 forming cycles (e.g., reactions R. 1.14 and R. 1.15) before radical termination reactions (R. 1.12 and R. 1.13) (Sillman, 2002).

$$CH_3O_2 + NO \rightarrow CH_3O + NO_2 \quad \text{(R. 1.14)}$$
$$HO_2 + NO \rightarrow OH + O_2 \quad \text{(R. 1. 15)}$$

The picture changes when looking at very polluted urban sites. Increases in NO_x concentrations inhibit the formation of O_3 due to the reaction of OH with NO_2 to form nitric acid (HNO_3) and reaction of NO with O_3 (NOx titration), see Reaction R. 1.16 and 1. 7.

$$OH + NO_2 + M \rightarrow HNO_3 + M \quad \text{(R. 1.16)}$$
$$NO + O_3 \rightarrow NO_2 + O_2 \quad \text{(R. 1.7)}$$

Reaction R. 1.16 represents an important OH sink in urban polluted areas. However, elevated input of NMVOCs allows the formation of analogous O_3 formation cycles leading to a general increase in the O_3 formation rates (Monks, 2005). This condition is referred to as VOC-sensitive or NO_x-saturated, as O_3 is produced and increases with increasing NMVOCs (Sillman, 1999; Monks, 2005).

Due to their short lifetime, most reactive NMVOCs are chemically decomposed before they reach the free troposphere. Their decomposition generally occurs through reaction with OH, HO_2, NO_3 and O_3, which leads to the formation of free radicals, as for CO and CH_4 in reactions R. 1.8 to R. 1.11 (Atkinston, 2000). Oxidation of NMVOCs by OH in the presence of NOx can also cause the formation of organic nitrate compounds, such as peroxyacetyl nitrate (PAN), that can act as a temporary reservoir of NOx and even as radical sinks. The formation of PAN is driven by the reversible reaction of the peroxy acetyl radical (PA) with NO_2, see Reactions R. 1.17 and 1.18, where the thermolysis of PAN induces the reformation of the PA radical and NO_2 (Brasseur et al., 1999), see R.1.18.

$$CH_3C(O) + O_2 + M \rightarrow CH_3C(O)O_2 + M \quad \text{(R. 1.17)}$$
$$CH_3C(O)O_2 + NO_2 + M \leftrightarrow CH_3C(O)O_2NO_2 + M \quad \text{(R. 1.18)}$$

Dominant sources of acetyl radicals ($CH_3C(O)O_2$ in the troposphere include NMVOC species. These can be either directly emitted or produced after the oxidation of >C2 species in the atmosphere (Brasseur et al., 1999), such as in the oxidation of acetaldehyde (CH_3CHO), which accounts for 44 % of the global source of PAN, and the photolysis of acetone ($CH_3C(O)CH_3$) and methylglyoxal (CH_3COCHO), which accounts for 7% and 30 % of the global source of PAN from carbonyl precursors. Isoprene and other terpene oxidation products on the other hand accounts for about 19% of the global sources of PAN (Fischer et al., 2015), see reactions R.1.19 – R.1.21.

$$CH_3CHO + OH + O_2 \rightarrow CH_3C(O)O_2 + H_2O \quad \text{(R. 1.19)}$$
$$CH_3C(O)CH_3 + hv + O_2 \rightarrow CH_3C(O)O_2 + CH_3 \quad \text{(R. 1.20)}$$
$$CH_3COCHO + hv + O_2 \rightarrow CH_3C(O)O_2 + HCO \quad \text{(R. 1.21)}$$

In polluted environments, PAN formation represents a sink for both NOx and hydrogen oxide radicals (HOx), limiting the formation of O_3 within the PBL. However, due to its large life time in cold temperatures, PAN enables the long-range transport of NOx in the free troposphere as well as peroxy acetyl radicals (precursors to the formation of other peroxy radicals). In particular, Lee et al., 2006 identified the thermolysis of PAN as the largest source of (organic peroxy radicals) ROx production, with 67% of radical production in the afternoon (12:00–18:00) attributed to it at a rural site in England during the August 2003 heatwave. The main sink of PAN is its thermal degradation (R.1.18) and the reaction with the OH radical. Its overall lifetime is largely controlled by the ratio of $\frac{NO}{NO_2}$ (Lee et al., 2006), either in the released PA radical reacts with NO_2 to return PAN (R.1.18), or with NO leading to irreversible loss (R.1.22).

$$CH_3C(O)O_2 + NO \rightarrow CH_3 + CO_2 + NO_2 \quad \text{(R. 1.22)}$$

Besides the destruction of O_3 by reactions with NO and by photolysis of O_3 there are additional chemical sinks for O_3, such as the reaction with halogenated species (Saiz-Lopez et al., 2007) and reactions with some NMVOCs. This is discussed in greater detail in Atkinson, (2000) and Monks et al. (2005). Fig. 1.5 summarises the main mechanisms of O_3 formation under three different regimes (very low, intermediate and high NOx). This complex interaction of different reactions highlights the non-linear behaviour of O_3 production (Atkinson, 2000; Sillman, 1999).

A schematic of the rate of O_3 production as a function of VOC and NOx (ozone isopleths plot) is shown in Fig. 1.6. Two regimes with different O_3- NOx - VOC sensitivity are identified. The first one is the NOx -sensitive regime (under the red line with relatively low NOx and high VOCs), where O_3 increases with increasing NOx and changes little in response to increasing VOC. The other regime is the NOx -saturated regime, where O_3 decreases with increasing NOx and increases with increasing VOC. The relation between O_3 and its two main precursors represents a significant challenge for environmental policy. Reductions in NO_x are effective only when NO_x-sensitive chemistry predominates and may otherwise increase O_3 in NO_x-saturated environments regions (Sillman, 1999).

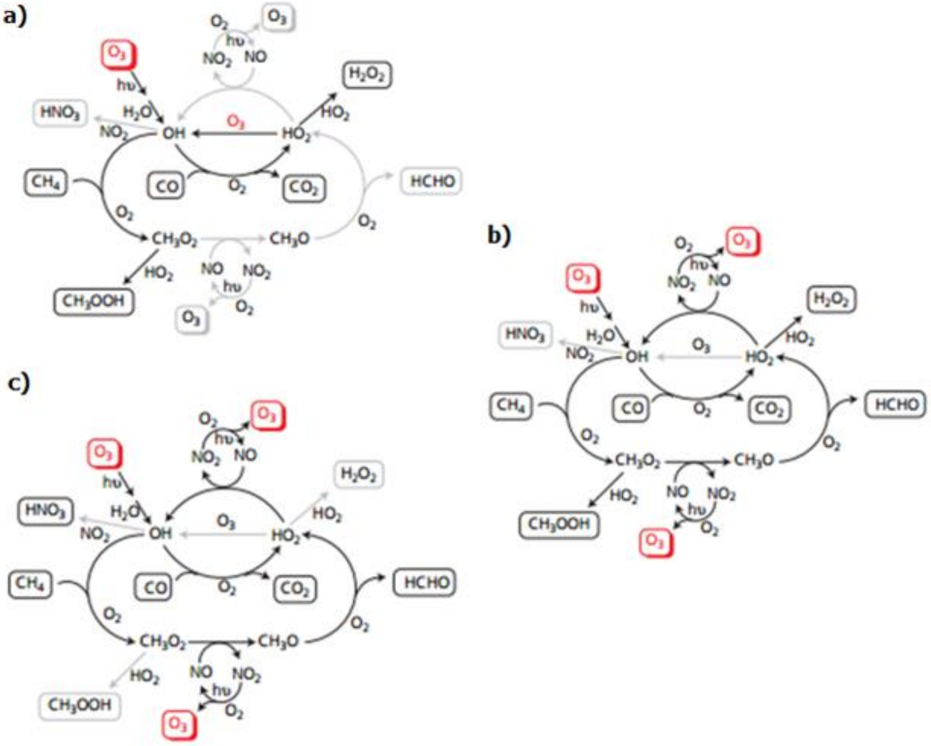

Figure 1.5. Schematic of O_3 production and loss as a function of NOx availability during the oxidation of CO and CH_4. Three chemical regimes are illustrated a) very low NOx; b) low NOx and c) high NOx. Dominant processes are shown in black. The figure is taken from the Royal Society, (2008).

Non-linearities in the O_3 chemistry affect the production of O_3 downwind of large cities, as shown in Fig. 1.6. The dashed arrows indicate the evolution of an air mass as it moves downwind from the emission sources with initial VOC/NO_x ratio of 6 and chemical speciation typical of urban centres in the US. During the evolution of the air masses, the VOC/NOx ratio increases due to the shorter lifetime of NO_x compared with most of the VOCs. The O_3 production might shift from NO_x-saturated to NO_x-limited. The reduction of the NO_x mixing ratio might also increase the O_3 production within the air mass. Furthermore, abundant biogenic sources of VOCs can further enhance the O_3 production outside the cities (e.g. Ehlers et al., 2016).

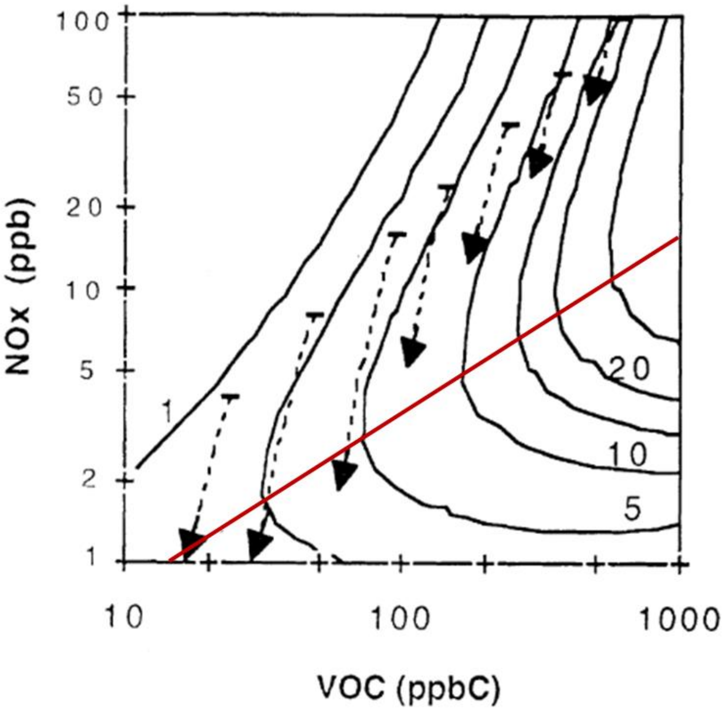

Figure 1.6. Isopleths plot showing the net rate of O_3 production in ppb h-1 (solid black lines) as a function of VOC (ppbC) and NOx (ppbv). The underlying calculations were performed for mean summer daytime meteorology and clear skies under urban US conditions (Sillman, 1999). The arrows indicate the evolution of the NOx and VOC mixing ratios in air parcels due to chemical ageing over 8-hours period (during daytime). The red line (the ridge) separates the NOx -sensitive (below the ridge line) and NOx-saturated regimes. In practice, the ridge is a broad transitional region rather than a sharp dividing line. The figure is taken from Sillman, (1999).

1.2.3 Long range transport

In general, chemical species such as O_3 and its precursors (including reservoir species such as PAN) have a longer lifetime in the free troposphere than in the surface level because of the absence of dry deposition and the reduction in the rate of chemical transformations associated with low temperatures (Wild et al., 2004). The increase in the lifetime of O_3 and its precursors, coupled with fast wind speeds allows their transport over long distances. Hence, boundary layer ventilation, which is the mechanism that lifts pollutants from the surface into the middle and upper troposphere, can be considered as a key process that expands the range of influence of the pollutants (HTAP, 2007). Once detached from the earth's surface, air masses tend to follow transport paths that rest along surfaces of constant potential temperature. The processes that determine boundary layer ventilation and the overall patterns of transport are well understood (HTAP, 2007). Mid-latitude cyclones associated with frontal systems are important mechanisms that lift and export pollutants from the east coasts of Asia to North America and from North America to Europe. For instance, North American and Asian O_3 account for 10.9% and 7.7% of the annual O_3 budget over Europe respectively (Auvray & Bey, 2005).

Deep convection during summertime is considered a key mechanism for PBL ventilation in continental USA and Asia (Lelieveld & Crutzen, 1994). However, deep convection is less likely than shallow convection over Europe (Dacre et al., 2007) so that a considerable proportion of pollution transport in Europe is believed to happen within the boundary layer (Wild et al., 2004). Nonetheless, pollutants can also be transported efficiently over long distances without being lifted to the free troposphere. This often involves the formation of a residual layer, decoupled from the stable nocturnal boundary layer, that experiences high wind speeds mainly when nocturnal low-level jet winds are present (Angevine et al., 1996). Sea breeze circulations and coastal outflow, which refers to the decoupling of pollution from the surface through the formation of an internal boundary layer, are also effective processes that export pollution (Dacre et al., 2007). Because dry deposition and vertical mixing are limited under such conditions, trace gases can be transported over long distances, even though transport speeds are lower than in the upper troposphere.

The impact of long-distance transport depends on the ability of the pollutants to reach the surface. Transport of pollutants from North America, for instance, has a significant impact over the North Atlantic and the Mediterranean due to anticyclonic descent of polluted air through the Azores' High (Auvray & Bey, 2005; HTAP, 2007). Moreover, O_3 concentrations reaching 50 ppbv in the remote site of Mace Head in the western edge of Ireland suggests that O_3 entering the UK with the prevailing westerly winds already contains a large fraction of the 60 ppbv European air quality standard (Derwent et al., 2013).

1.2.4 Dry deposition of ozone

Dry deposition to land and water surfaces constitutes an important loss mechanism for O_3 on a global scale accounting for approximately 1000 Tg y^{-1} of the global average O_3 budget, see Fig. 1.2. Ozone is a very reactive chemical species but not a very soluble one. Dry deposition to land surfaces is much more efficient compared to the water surface, and depends largely on the type of land (Monks et al., 2015). The process can be described as follows. First, turbulence transports the chemical species downward to the interface between the surface layer and the laminar sublayer. Diffusive transport from the laminar sublayer to the Earth's surface then takes place. Ultimately, different receptors, including plant's stomata, ground surfaces and water surfaces, take up the trace gases. The dry deposition mass flux is usually calculated as E. 1.1 (Wesely & Hicks, 2000):

$$F = -vd \cdot C \quad \text{(E. 1.1)}$$

Where F is the dry deposition mass flux, vd is the dry deposition velocity, and C is the concentration of a given species in molecules. The minus sign indicates the downward flux. In the Wesely scheme, which is the parameterization used in this study, vd consist of three main phases represented by three primary resistances namely: the aerodynamic resistance (ra) which represents the resistance between the surface and a specific height; the resistance of the laminar sublayer adjacent to the surface (rb); and the bulk surface resistance (rc) which is estimated as the sum of seven resistances that depends on five seasonal categories and the type of land use. The vd is then expressed as the inverse of three resistances as in E. 1.2:

$$vd = \frac{1}{r} = \frac{1}{r_a + r_b + r_c} \quad \text{(E. 1.2)}$$

The aerodynamic resistance (ra) depends largely on the atmospheric stability and so the diurnal cycle, which in WRF-Chem is estimated by the PBL scheme. The resistance of the laminar sublayer (rb), on the other hand, depends mostly on the turbulent fluxes, and molecular conduction and diffusion at the lowest levels of the surface, which is obtained from the coupling between WRF and Noah Land Surface Model (LSM) (Chen & Dudhia, 2001). Likewise, the bulk surface resistance (rc), which comprises non-stomatal uptake (e.g., by leaf surfaces, soil and water) and the stomata uptake, is subjected to meteorological factors provided by the coupling between WRF and the LSM. A comprehensive description of the parameterisation of the resistances is found in Wesely (1989).

The coupling between WRF and the LSM contributes to resolving the land surface energy and water balance in the model, which ultimately influence important atmospheric processes such as temperature, winds, and boundary layer structure (Chen & Dudhia, 2000). The coupling also permits a concurrent response to short-term weather events such as heatwaves.

In nature, the opening and closing of stomata depend on meteorological factors such as water vapour, temperature and solar radiation (e.g., Grünhage et al., 2012). High temperatures lead to dryer soils which in turns lead to stressed vegetation affecting the uptake of O_3 by plants. The surface water budget in WRF-Chem, estimated by the LSM, depends largely on precipitation, runoff and evaporation, see E. 1.3.

$$\partial S = P - R - E \quad \text{(E 1.3)}$$

Where ∂S refers to the change in soil moisture content, P-R represents infiltration and E represents the evaporation from the soil, plant canopy, canopy-intercepted rainfall and sublimation from snowpack which depends largely on soil moisture and vegetation cover and type (Chen, 2007). Likewise, the resistance to potential evaporation of water from the plant canopy is affected by the amount of solar insolation, air temperature, air humidity and soil moisture, as these factors encourage stress in vegetation reducing their transpiration. Thus the stomatal resistance to O_3 uptake in WRF-Chem is largely dependent on the availability of water vapour in the atmosphere. However, the Wesely (1989) dry deposition scheme used in WRF-Chem only considers changes in temperature and solar radiation, and not in soil moisture or near-surface humidity to estimate the uptake of O_3 by plants and the Earth's surfaces (Hodnebrog et al., 2011).

Vautard et al. (2005) showed that doubling the bulk deposition resistance (*rc*) in the Wesely scheme for two land-use types increased model performance in terms of O_3 when modelling the summer 2003 heatwave.

1.3 Chemical transport models

Chemical transport models (CTM) are widely employed to support studies where field measurements are either limited or impossible to obtain. Unlike direct observations, CTMs give the opportunity to examine all aspects of the simulations and untangle the relevant processes contributing to the problem on hand. A complete review of CTMs can be found in Baklanov et al. (2014).

The meteorology in the CTMs has often been computed separately from the chemistry using so-called off-line methods. Although the approach is flexible and computationally efficient, the time resolution typical of hours limits the determination of some processes that require a finer time scale (e.g., wind speed and direction, cloud formation, and rainfall) (Im et al., 2014; Zhang, Sartelet, Zhu, et al., 2013). WRF-Chem belongs to a new generation of "online" coupled regional models where both meteorology and chemistry are resolved at the same horizontal and vertical grids and time intervals with no need of interpolation in time or space. The model also offers various physics and chemistry options, as well as different run choices such as nesting configurations, nudging options, which can be combined to create many different model configurations. These are reviewed in detail in the following chapter.

Chapter 2

THE MODELLING SYSTEM

This chapter describes the modelling system. Section 2.1 gives an overview of WRF-Chem. The input data are presented in section 2.2. Introduction of the ozone- tagging mechanism is given in section 2.3. Finally, section 2.4 describes the default model setup used in the investigations.

2.1 Overview of the WRF-Chem system

This study employs the Weather Research and Forecasting Chemistry Model (WRF-Chem) version 3.7.1. The software has been developed collaboratively by the National Centre for Atmospheric Research (NCAR), the National Oceanic and Atmospheric Administration (NOAA), the National Centres for Environmental Prediction (NCEP), and other research institutes. WRF-Chem is maintained and supported as a freely available community model. The model contains two dynamical solvers: the Non-hydrostatic Mesoscale Model (NMM) solver which is not currently compatible with the chemistry extension (Janjic, 2003) and the Advanced Research WRF solver (ARW) (Skamarock et al., 2005) which is used in this research. WRF (ARW) core is a three dimensional Eulerian weather prediction model designed for atmospheric research and operational forecast. The model equations are solved numerically for fully compressible and non-hydrostatic conditions using Runge-Kutta 3rd order time integration schemes

(Skamarock et al., 2008). The model uses terrain-following hydrostatic pressure coordinates and Arakawa-C grid staggering. WRF-Chem is a chemical module for air quality prediction built to work with the Advanced Research WRF (ARW) core; it is coupled online so that the same time steps, grid cells and transport scheme of WRF are used. The WRF-Chem system can be described as a modular system where information is passed between different modules, as shown in Fig. 2.1. The three main components are: WRF Pre-processing system (WPS), the WRF ARW solver, and the Chemical module Chem. A detailed description of these components can be found in Grell et al. 2005.

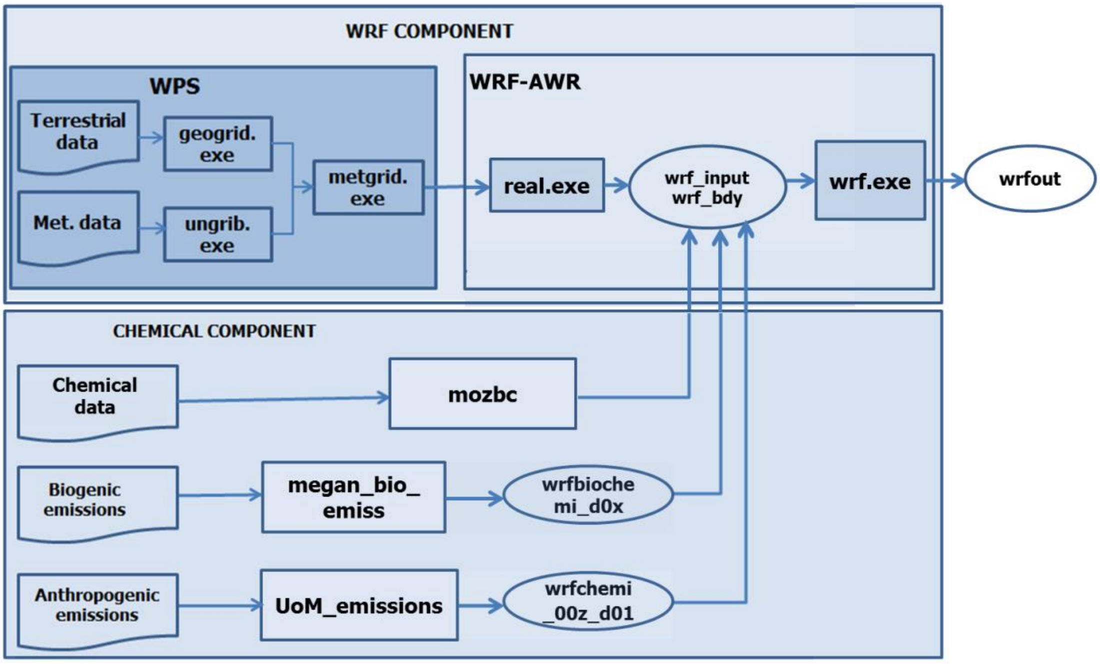

Figure 2.1. Schematic of the main components and flow of information of the WRF-Chem system.

WRF-Chem uses parameterizations for those physical processes that happen on length scales that are smaller than the grid cell size. Parameterizations are basically approximations that simplify each process and are based on independent models embedded into WRF-Chem. Several options of physical parameterizations schemes can be set by the user through the namelist file *namelist.input*. Care must be taken when selecting a scheme, since the choice can have a major impact on the model output (Misenis & Zhang, 2010).

The schemes used here to parameterize the atmospheric processes are those used successfully to evaluate the meteorology, and O_3 and nitrogen oxides (NO_x) concentrations in a European domain in (Mar et al., 2016). The Lin et al. (1983) scheme handles the microphysical processes required to simulate internal cloud processes such as cloud formation. Radiation processes, which describe the surface energy balance that drives the evolution of the boundary layer, are simulated by the RRTMG (Iacono et al., 2008) for longwave and Goddard shortwave scheme (Chou & Suarez, 1994) for shortwave radiation. The Noah Land Surface Model (LSM) (Chen & Dudhia, 2001) is used to characterise the heat and moisture fluxes throughout soil levels. These fluxes provide a lower boundary condition for the vertical transport calculated in the Planetary Boundary Layer PBL schemes, which are used to resolve vertical sub-grid-scale fluxes caused by eddy transport. Here, the Yonsei University scheme (YSU) PBL scheme in Hong et al. (2006) is used. In a European domain, this scheme was shown to give summer temperatures much closer to observations than the Mellor–Yamada–Janjic (MJY, Mellor and Yamada (1982)) and the Asymmetric Convective Model2 (ACM2, Pleim 2007, 2007b) schemes (Garcia et al., 2013). Lowe et al. (2015) also concluded that YSU gives summer temperatures that are closer to observations, even when scheme tends to produce warmer, drier and more mixed PBL.

The Grell 3-D scheme (Grell & Dévényi, 2002) handles the cumulus convention, which is needed for the simulations with grid-spacing > 10 km. Advection and diffusion are instead calculated by the WRF-ARW solver. Table 2.1 summarises the options that have been selected to parameterize the atmospheric processes.

Table 2.1. Parameterizations options used in the study.

Process	Option
Cloud microphysics	Lin et al. scheme (Lin et al. 1983)
Long wave radiation	RTTM (Iacono et al. 2008)
Short wave radiation	Goddar (Chou & Suarez 1994)
Surface layer	Monin-Obukhov scheme (Beljaars 1995)
Land surface physics	Noah LSM (Chen et al. 2016)
Cumulus parameterization	Grell 3-D scheme (Grell and Dévényi, 2002)
Planetary boundary layer scheme PBL	Yonsei University scheme YSU (Hong et al. 2006)

2.2 Input data, initial and boundary conditions

2.2.1 The WRF Pre-processing System (WPS)

The WRF Pre-processing System (WPS) is a collection of 3 programs (*geogrid*, *ungrib* and *metgrid*) the combined role of which is to produce non-chemical initial and boundary conditions for WRF. ***Geogrid*** defines the size and location of the model domain and the map scale factor, and interpolates static geographical data (e.g., terrain height, monthly vegetation fraction, and land use) at every grid point (Wang et al., 2014). Here, a States Geological Survey (USGS) dataset with a 30s and 10s resolution was downloaded from the WRF download webpage http://www2.mmm.ucar.edu/. Latitude, longitude and map projection are also provided by the user in a shared namelist file 'namelist.wps'. ***Ungrib*** simply extracts meteorological fields in GRIB format and writes them in an intermediate format that can be read by the ***metgrid*** utility.

Being a regional model, WRF requires meteorological information from external sources (e.g., long term climatic outputs from Global Circulation Models or reanalysis data, among others) to produce the initial boundary conditions. Here, this information was obtained from the ERA-Interim reanalysis dataset, which has a spatial grid resolution of 0.75° × 0.75° and 6 hours temporal resolution. ***Metgrid*** interpolates the meteorological fields, from ***ungrib***, horizontally into the selected model domain. Ultimately, the geographical static data and meteorological data are combined into ***'met_em'*** files. The utility **real** reads the ***met_em*** files and creates the non-chemical initial and boundary condition files (*wrf_input* and *wrf_bdy*, respectively).

2.2.2 Chemical components

2.2.2.1 Chemical boundary conditions

Similar to the meteorology, it is necessary to set the chemical initial and boundary conditions to adequately model atmospheric chemistry. Here, these conditions were taken from global simulations produced by the Chemistry Transport Model for O_3 and Related Chemical Tracers (MOZART-4 GEOS-5, Emmons et al. (2010) and inputted into the model every 3 hours. The MOZART-4 product has a horizontal resolution of 1.9° × 2.5° and 56 pressure levels. The utility ***mozbc*** is used to read the dataset from the global model and define the initial and boundary conditions of gas species.

2.2.2.2 Gas-phase chemical mechanism

In the present study, simulations were conducted only for gas-phase chemistry. Two chemical mechanisms were used: the Model for Ozone and Related chemical Tracers, version 4 (MOZART-4) and a reduced version of the Common Representative Intermediates CRIv2-R5 (CRImech) mechanism (Archer-Nicholls et al., 2014).

Note that omission of heterogeneous chemistry can lead to overestimation of NOx and O_3 due to the absence of aerosol nitrate formation through the reaction of OH + NO_2 as well as N_2O_5 hydrolysis (Badia & Jorba, 2014; Archer-Nicholls et al., 2014; Stone et al., 2014). Nitric acid (HNO_3) is formed during day time by the reaction between OH and NO_2 (R. 2.1 to R. 2.4), and at night by the hydrolysis of dinitrogen pentoxide (N_2O_5) on aerosols, see R. 2.5 and R. 2.6. The formation of HNO_3 is considered one of the dominant transformations of NOx in the troposphere (Brasseur et al., 1999). Because HNO_3 is a highly soluble species, it can be incorporated into aerosol particles or cloud droplets and loss through dry and wet deposition (Brasseur et al., 1999). Thermal decomposition of N_2O_5 gives back NO_3 and NO_2. However, loss of N_2O_5 is largely associated with reactions on aerosol surfaces (Brown & Stutz, 2012).

$$OH + NO_2 + M \rightarrow HNO_3 + M \quad \text{(R. 2.1)}$$

$$HNO_3 + hv \rightarrow OH + NO_2 \quad \text{(R. 2.2)}$$

$$HNO_3 + OH \rightarrow H_2O + NO_3 \quad \text{(R. 2.3)}$$

$$HNO_3 + \frac{H_2O_{(liquid)}}{aerosol} \rightarrow removal\ gas\ phase \quad \text{(R. 2.4)}$$

$$NO_2 + O_3 \rightarrow NO_3 + O_2 \quad \text{(R. 2.5)}$$

$$NO_3 + NO_2 \leftrightarrow N_2O_5 + M \quad \text{(R. 2.6)}$$

The fundamental differences between chemical mechanisms lie mostly in the way the organic compounds are treated. The version of MOZART-4 chemical mechanism used in this study contains 85 gas-phase species and 157 gas-phase reactions and requires emissions input from 16 NMVOC categories; a complete description of this chemistry mechanism is given in Emmons et al. (2010). The degradation of primary species such as ethane, propane, ethene, propene, methanol and isoprene are explicitly represented in the scheme. Other NMVOCs are lumped together based on a molecule approach that involves grouping organics, molecule by molecule, into surrogate species according to reactive functional groups, e.g. alkanes and alkenes with four or more carbon atoms and aromatic compounds are lumped into BIGALK, BIGENE and TOLUENE (Emmons et al., 2010). By contrast, CRImech contains 220 species and 609 reactions for the degradation of 26 emitted NMVOCs species (Archer-Nicholls et al., 2014). This results in the most explicit representation of atmospheric VOC degradation than currently available in WRF-Chem (Archer-Nicholls et al., 2014). As in MOZART, the degradation of ethane, propane, ethene, propene, methanol and isoprene are explicitly represented in the scheme. Other NMVOCs are lumped into surrogate species that shares similar chemical properties. The NMVOC lumping in CRImech is based on the principle of the ozone-forming potential of each VOC species: the total yield of O_3 potentially formed as a by-product during the complete OH-initiated and NOx-catalysed oxidation of a given VOC to CO_2 and H_2O is comparable with the number of reactive C–C and C–H bonds that eventually brake during the complete oxidation (Watson et al., 2008). A series of generic intermediate species are then defined which are used to represent large sets of VOCs species, which are explicitly represented in the Master Chemical Mechanism (Watson et al., 2008).

2.2.2.3 Anthropogenic emissions

Anthropogenic emissions of CO, NO_x, SO_2 and total NMVOCs for the European domain, including shipping lines, were taken from the latest version of the TNO-MACC-III European inventory (Kuenen et al, 2014) for the year 2011 (hereafter the TNO-MACC inventory). The emissions are provided as yearly totals (kg yr^{-1}) by source sector following the SNAP (selected nomenclature for sources of air pollution) convention at a 0.125° × 0.0625° longitude–latitude resolution. The different SNAP sectors are listed in Table 2.2. Road transport emissions are further disaggregated into fuel type.

TNO-MACC was built from emissions reported by member countries to the European Monitoring and Evaluation Program (EMEP). Emissions were further refined to fill gaps and correct errors and obvious inconsistencies (Kuenen et al., 2014). The anthropogenic emissions of CO, NO_x, SO_2 and total NMVOCs for the UK domain were taken from the latest UK national emissions inventory (NAEI) for the year 2014, http://naei.beis.gov.uk/, which has a spatial resolution of 1 km. Emissions are split into eleven categories depending on the chemical species: domestic, energy production, industrial combustion, industrial processes, nature, off-shore, road transport, other transport, waste and total area.

Table 2.2. Selected Nomenclature for reporting of Air Pollutants (SNAP) sectors.

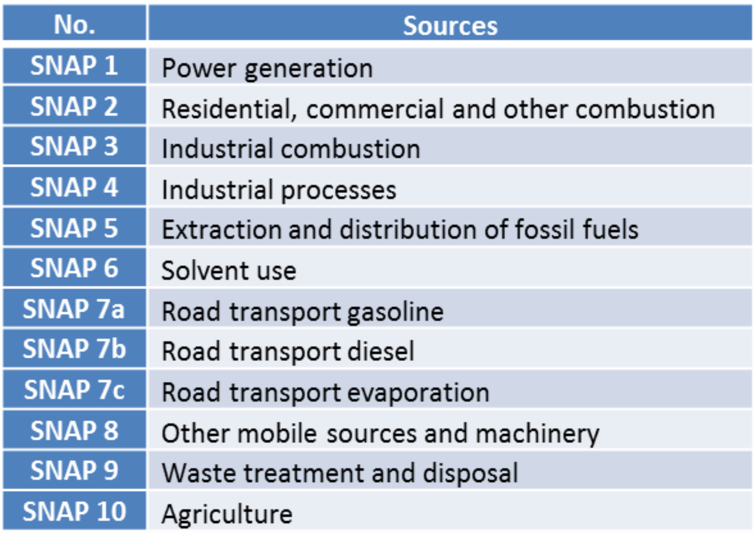

No.	Sources
SNAP 1	Power generation
SNAP 2	Residential, commercial and other combustion
SNAP 3	Industrial combustion
SNAP 4	Industrial processes
SNAP 5	Extraction and distribution of fossil fuels
SNAP 6	Solvent use
SNAP 7a	Road transport gasoline
SNAP 7b	Road transport diesel
SNAP 7c	Road transport evaporation
SNAP 8	Other mobile sources and machinery
SNAP 9	Waste treatment and disposal
SNAP 10	Agriculture

A FORTRAN program, developed by Hodnebrog et al. (2012) with adaptations by Dr. Thom Pugh, Dr. Steve Utembe and Dr. Douglas Lowe of the University of Manchester, was used to pre-process both the NAEI and the TNO-MACC inventories and generate the inter-media binary emission data (*wrfchemi_00z_d01* and *wrfchemi_00z_d02*) for the WRF-Chem model. The code is referred hereafter as the UoM_emissions_pre-processor.

Since the UoM_emissions_pre-processor is designed to work with emissions from an old version of TNO-MACC inventory, an additional Python program was here created to read the raw emissions data from TNO-MAC-III and produce individual, compatible netCDF files. Some modifications to the UoM_emissions_pre-processor were also made to account for the changes between inventory versions, e.g. the spatial coverage of the TNO-MAC inventory. In particular, an additional module was created to produce emissions compatible with MOZART chemical mechanism in WRF-Chem. The modified UoM_emissions_pre-processor was then used to map the TNO-MACC and NAEI emissions to MOZART and CRImech speciation, and horizontally interpolate the emissions inventory into projected model grids.

Speciation methodology: Anthropogenic emissions for WRF-Chem must be specified in a format compatible with the selected chemical mechanism. As the MOZART gas phase scheme carries fewer chemical species than CRImech, the 26 emitted CRI NMVOCs were lumped into 14 MOZART species according to the mappings of MOZART-4 NMVOCs to CRIv2-R5 mechanisms described in Archer-Nichols et al. (2014) and Emmons et al. (2010), see Table 2.3. The VOCs emission fractions were taken from Archer-Nicholls et al. (2014); these are based on the 50 most significant NMVOC species in terms of mass emissions in the UK (Dore et al. 2007). NO_x was emitted as 95% NO and 5% NO2 following Mar et al. (2016) methodology.

Table 2.3. Approximate mappings of MOZART-4 VOCs to CRImech mechanisms used in WRF-Chem runs. Based on Table 7 of Emmons et al. (2010), and Tables 4 and 7 of Archer-Nichols et al. (2014). The table list the emitted VOC species as a fraction of total VOC emissions.

Name of VOC	MOZART	CRImech	VOC fraction
Ethane	C_2H_6	C_2H_6	2.47%
Propane	C_3H_8	C_3H_8	4.29%
Butane	BIGALK	$1.25\times NC_4H_{10}$	39.90%
Ethene	C_2H_4	C_2H_4	3.15%
Propene	C_3H_6	C_3H_6	1.48%
Trans-2-butene	BIGENE	TBUT2ENE	3.37%
Ethyne	C_2H_6	C_2H_6	1.20%
Formaldyhyde	CH_2O	HCHO	1.33%
Ethanal	CH_3CHO	CH_3CHO	0.13%
Propanal	CH_3CHO	C_2H_5CHO	0.21%
Acetone	CH_3COCH_3	KET	1.15%
Methyl ethyl ketone	MEK	MEK	1.66%
Methanol	CH_3OH	CH_3OH	1.16%
Ethanol	C_2H_5OH	C_2H_5OH	13.40%
Acetic acid	CH_3COOH	CH_3CO_2H	0.14%
Benzene	TOLUENE	BENZENE	2.02%
Toluene	TOLUENE	TOL	5.82%
o-Xylene	TOLUENE	OXYL	8.54%
1,2,3-Trimethylbenzene	TOLUENE	TM123B	0.36%
1,2,4-Trimethylbenzene	TOLUENE	TM124B	1.18%
Mesitylene	TOLUENE	TM135B	0.41%
2-Ethyltoluene	TOLUENE	OETHTOL	0.32%
3-Ethyltoluene	TOLUENE	METHTOL	0.51%
4-Ethyltoluene	TOLUENE	PETHTOL	0.45%
1,3-Dimethyl-5-ethylbenzene	TOLUENE	DIME35EB	0.93%

Temporal disaggregation: Emissions are temporarily disaggregated to take into account monthly, day of the week and hour of the day changes in the emissions. This is done by sectors according to the SNAP nomenclature based on Tables 8.1, 8.2, and 8.4 of Kuenen et al. (2011). Longitudinal (local time) dependent diurnal variations were also applied. Ultimately, emissions were distributed vertically to the lowest five model levels for each source sector based on (Bieser et al., 2010).

2.2.2.4 Biogenic emissions

Biogenic emissions were calculated online using the Model of Emissions of Gases and Aerosols from Nature (MEGAN) version V2.04 (Guenther et al., 2012) which is embedded into the WRF-Chem source code. The model calculates emissions of isoprene and other emitted biogenic trace gases and aerosols from terrestrial ecosystems into the above canopy atmosphere at a specific location and time using model-derived weather and land use data at 1km × 1km resolution (Guenther et al., 2012). To do this, the utility ***megan_bio_emiss*** must be executed. The utility generates the *wrfbiocemi_d0* emissions files needed by the wrf.exe executable.

2.3 The ozone tagging

The contribution of domestic and European anthropogenic emissions to tropospheric O_3 in the UK was studied using a source attribution technique known as "ozone tagging" in which O_3 molecules are labelled with the identity of their source regions. This is achieved by the tagging of nitrogen oxides emissions (NO and NO_2) at selected source regions. The tagged NOx is tracked through all of the odd nitrogen species (e.g., PAN, HNO_3, organic nitrates), to account for the recycling of $NO_{x,}$ and followed to the formation of ozone as in Emmons et al. (2012). This enables the direct attribution of O_3 concentrations in receptor regions to specific sources (Butler et al., 2018), as illustrated in Fig. 2.2.

Ozone formation requires both NO and peroxy radicals from VOCs, so source attribution would generally require the tagging of both NO or VOCs (Emmons et al., 2012). Here, however, tagging of NOx emission only is a suitable choice, as the northern hemispheric surface ozone is mostly dominated by anthropogenic emissions of NOx year-round (Butler et al., 2018), and the spatial resolution adopted in the study (27 km) is representative of a regional background. Moreover, all tropospheric contributions to ozone are here tagged (e.g., all industrial sectors). When doing so, tracing nitrogen compounds should give comparable results to tracing VOCs and peroxy radicals (Emmons et al., 2012).

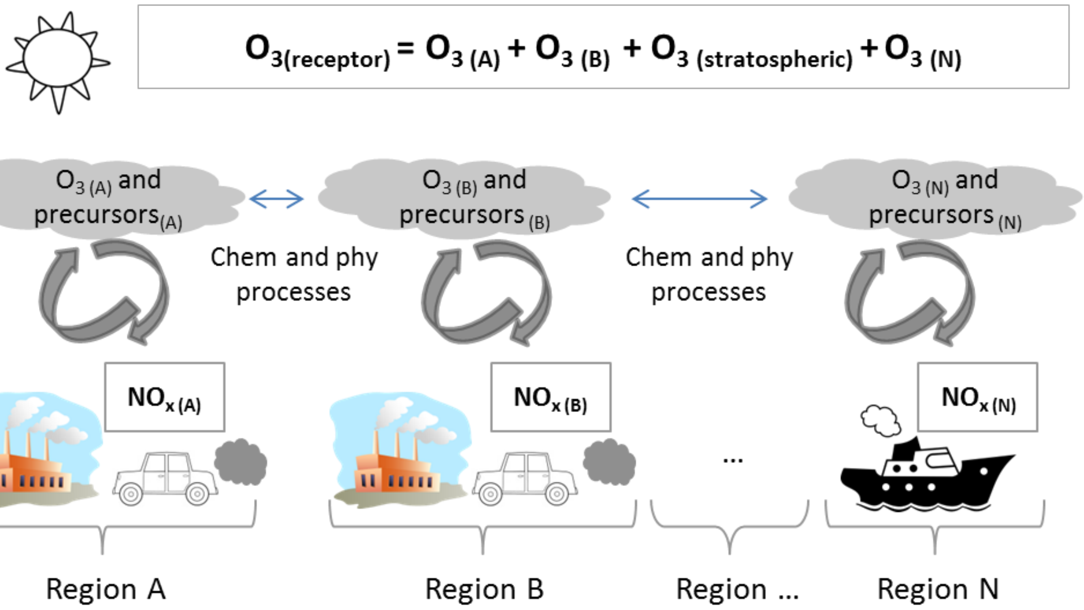

Figure 2.2. Illustration of the O_3 tagging technique. Each bracket depicts the emissions of NO_x labelled with the identity of their source region (A, B, and N). The arrows represent chemical and physical processing (e.g. O_3 formation), and the clouds shaped boxes indicate the transport of labelled O_3 and precursors. Note that ideally the total O_3 at a specific receptor area (e.g. $O_{3\ (receptor)}$) is equivalent to the sum of O_3 from the different source regions.

Different tagging approaches exist (Grewe, 2004; Emmons et al., 2012; Derwent et al., 2015; Butler et al., 2018). The technique used here is an expanded version of on the method proposed in Emmons et al. (2012) and further developed in Butler et al., (2016). The technique was implemented into the WRF-Chem model with the collaboration of the Institute for Advanced Sustainability

Studies (IASS) in Potsdam Germany. The method is complementary to the source-receptor approach (Emmons et al., 2012), in that tagging provides quantification regarding the contribution of different sources (regions, SNAP sectors, etc.) to the total amount of O_3 in a simulation. Source-receptor methods, on the other hand, gives information regarding the response of O_3 to changes in emissions (HTAP, 2010).

To track the source of O_3 within WRF-Chem simulations, the chemical system in the model needs to be expanded with additional tracers to account for the emission regions of interest. Therefore, several changes were made to the model code to implement the tagging approach. First, a new chemical mechanism based on the MOZART-4 gas-phase, chem–opt=113, was created using the KKP protocol. The new chemical mechanism contains the original chemistry reactions in the MOZART mechanism plus a duplicated set of reactions that includes twenty-four tagged species. Table 2.4 lists the tagged species representing the UK source region and their corresponding species atomic composition. An example of photolysis reactions of tagged species is instead given in Table 2.5.

Table 2.4. Example of tagged species for the UK source region based on Table 2 of Emmons et al. (2010).

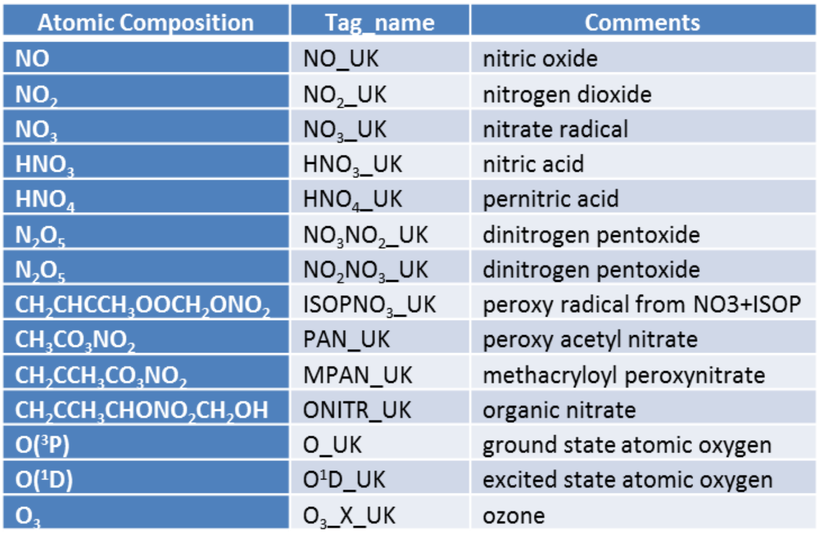

Atomic Composition	Tag_name	Comments
NO	NO_UK	nitric oxide
NO_2	NO_2_UK	nitrogen dioxide
NO_3	NO_3_UK	nitrate radical
HNO_3	HNO_3_UK	nitric acid
HNO_4	HNO_4_UK	pernitric acid
N_2O_5	NO_3NO_2_UK	dinitrogen pentoxide
N_2O_5	NO_2NO_3_UK	dinitrogen pentoxide
$CH_2CHCCH_3OOCH_2ONO_2$	$ISOPNO_3$_UK	peroxy radical from NO3+ISOP
$CH_3CO_3NO_2$	PAN_UK	peroxy acetyl nitrate
$CH_2CCH_3CO_3NO_2$	MPAN_UK	methacryloyl peroxynitrate
$CH_2CCH_3CHONO_2CH_2OH$	ONITR_UK	organic nitrate
$O(^3P)$	O_UK	ground state atomic oxygen
$O(^1D)$	O^1D_UK	excited state atomic oxygen
O_3	O_3_X_UK	ozone

The size of the modified chemical mechanism scales linearly with the number of added tag identities. The chemical families NO_y (which includes NOx and all NO_x reservoir species) and the O_x family are tagged separately to allow an arbitrary number of tags in a single model run, and avoid the replacement of tagged O_3 identities by the O_3–NO_x null chemical cycle. The following species from the base chemical mechanism belong to the NO_y family: NO, NO_2, NO_3, N_2O_5, HNO_3, HNO_4, $ISOPNO_3$, ONIT, ONITR, PAN, and MPAN. The following species from the base chemical mechanism belong to the O_x family: O_3, $O(^1D)$, O, NO_2, NO_3, N_2O_5, HNO_3, HO_2NO_2, $ISOPNO_3$, ONIT, ONITR, PAN, and MPAN.

As in Butler et al. 2018, the reaction of NO with any peroxy radical (HO_2) and all organic peroxy radicals (RO_2) and subsequent production of NO_2 is regarded as a process that effectively generates O_3, reaction R. 2.7.

$$NO + HO_2 \rightarrow NO_2 + OH \quad \text{(R. 2.7)}$$

Table 2.5. Example of the photolysis reactions for the UK source region. Table was created to allow direct comparison with Table 2 in Emmons et al. (2010).

Original reaction	Tagged reactions
$O_3 + hv \rightarrow O1D + O_2$	$O_3\_X\_UK + hv = O1D\_X\_UK$
$O_3 + hv \rightarrow O + O_2$	$O_3\_X\_UK + hv = O\_X\_UK$
$NO_2 + hv \rightarrow NO + O$	$NO_2\_UK + hv = NO\_UK$
$N_2O_5 + hv \rightarrow NO_2 + NO_3$	$NO_3NO_2\_UK + hv = NO_2\_UK$
$N_2O_5 + hv \rightarrow NO_2 + NO_3$	$NO_2NO_3\_UK + hv = NO_3\_UK$
$HNO_3 + hv \rightarrow NO_2 + OH$	$HNO_3\_UK + hv = NO_2\_UK$
$NO_3 + hv \rightarrow 0.89{*}NO_2 + 0.11{*}NO + 0.89{*}O_3$	$NO_3\_UK + hv = 0.89\ NO_2\_UK + 0.11\ NO\_UK$
$HO_2NO_2 + hv \rightarrow 0.33{*}OH + 0.33{*}NO_3 + 0.66{*}NO_2 + 0.66{*}HO_2$	$HNO_4\_UK + hv = 0.66\ NO_2\_UK + 0.33\ NO_3\_UK$
$PAN + hv \rightarrow 0.6{*}CH_3CO_3 + 0.06{*}NO_2 + 0.4{*}CH_3O_2 + 0.4{*}NO_3$	$PAN\_UK + hv = 0.6\ NO_2\_UK + 0.4\ NO_3\_UK$
$MPAN + hv \rightarrow MCO_3 + NO_2$	$MPAN\_UK + hv = NO_2\_UK$
$ONITR + hv \rightarrow HO_2 + CO + NO_2 + CH_2O$	$ONITR\_UK + hv = NO_2\_UK$

Some decisions and trade-off in the design of the source attribution method can lead to unphysical results (Butler et al., 2018). For instance, in the tagging mechanism the reaction between NO and O_3 producing NO_2 and the subsequent rapid reformation of O_3 from NO_2 photolysis (see reactions R. 2.8, 2.9 and 2.10) can lead to over-representation of NO_x identities from nearby sources due to overwriting of tagged O_3 identities (Butler et al., 2018).

$$NO + O_3 \rightarrow NO_2 + O_2 \quad \text{(R. 2.8)}$$
$$NO_2 + hv \rightarrow NO + O_3 \quad \text{(R. 2.9)}$$
$$O + O_2 \rightarrow O_3 \quad \text{(R. 2.10)}$$

It follows that the reaction R. 2.8 can be interpreted as chemical loss of O_3 and the subsequent reformation of O_3 (R. 2.10) as new O_3 production due to nearby emitted NO_x, overwriting the identity of tagged O_3 from remote sources with the identity of tagged NOx emissions from more nearby sources (Butler et al., 2018). Since NO_2 belongs to both the NOy and Ox chemical families, in the tagging system used in this investigation, two different tagged versions of NO_2 are produced representing the distinct roles of NO_2 in each of these chemical families. Thus reaction (R. 2.7) from the base chemical mechanism is represented in the tagging system as follows:

$$NO_{tag} + HO_2 \rightarrow NO_{2\_tag} + NO_{2\_x\_tag} + HO_2 \quad \text{(R. 2.11)}$$

Where *_tag* refers to the NOy-tagged family and *x_tag* identifies the source belonging to the Ox-tagged family. The over-writing issue is then addressed by preserving the tagged identity of emitted NO_x precursors in reaction R. 2.12 and the tagged identity of O_x is preserved in reaction R. 2.13.

$$NO_{tag} + O_3 \rightarrow NO_{2\_tag} + O_3 \quad \text{(R. 2.12)}$$
$$NO + O_{3\_x\_tag} \rightarrow NO_{2\_x\_tag} + NO \quad \text{(R. 2.13)}$$
$$NO_{2\_x\_tag} + hv \rightarrow O_{x\_tag} \quad \text{(R. 2.14)}$$
$$O_{\_x\_tag} + O_2 \rightarrow O_{3\_x\_tag} + O_2 \quad \text{(R. 2.15)}$$
$$NO_{2\_tag} + hv \rightarrow NO_{tag} \quad \text{(R. 2.16)}$$

The NO_2_x_tag goes on and photolysis to produce tagged O_3, e.g., reactions R. 2.14 and 2.15. The fate of the NO_2_tag from the NO_y-family is different (see reaction R. 2.16), as NO remains available for further subsequent conversion of NO to NO_2. Table 2.6 provides an example of the gas phase reactions included in the tag mechanism.

The full mechanism is computed in a single simulation using the mixing ratios and the loss rates of the base chemistry. Each tagged species undergoes the same chemical and physical processes of its corresponding species in the basic chemical mechanism. However, the concentrations of untagged species are not affected by the tagged species because any non-tagged one acting as a reactant in a tagged reaction is also included as a product. In other words, untagged reactants appear in stoichiometrically identical amounts in the reactants and products of each tagged reaction, e.g., reaction R. 2.17 and R. 2.18. Likewise, any non-tagged products are not included in the tagged reaction (Butler et al., 2018).

$$NO + HO_2 \rightarrow NO_2 + HO \quad \text{(R. 2.17)}$$

Reaction (R. 2.17) from the base chemical mechanism is represented in the tagging system as follows:

$$NO_{tag} + HO_2 \rightarrow NO_{2\_tag} + HO_2 \quad \text{(R. 2.18)}$$

Table 2.6. Example gas-phase reactions of for the UK source region.

Original reaction	Tagged reactions
O + O2 + M → O3 + M	O_X_UK + O2 + M= O3_X_UK
O + O3 → 2*O2	O_X_UK + O3 = O3
	O + O3_X_UK = O
O1D + N2 → O + N2	O1D_X_UK + N2 = O_X_UK + N2
O1D + O2 → O + O2	O1D_X_UK + O2 = O_X_UK + O2
O1D + H2O → 2*OH	O1D_X_UK + H2O = H2O
H2 + O1D → HO2 + OH	O1D_X_UK + H2= H2
O + OH → HO2 + O2	O_X_UK + OH = OH
HO2 + O → OH + O2	O_X_UK + HO2 = HO2
OH + O3 → HO2 + O2	OH + O3_X_UK = OH
HO2 + O3 → OH + 2*O2	HO2 + O3_X_UK = HO2
N2O + O1D → N2 + O2	N2O + O1D_X_UK = N2O
N2O + O1D → 2*NO	O3_X_UK + NO = NO2_X_UK
NO + HO2 → NO2 + OH	NO_UK + HO2 = NO2_UK + NO2_X_UK + HO2
NO + O3 → NO2 + O2	O3 + NO_UK = NO2_UK + O3
NO2 + O → NO + O2	O + NO2_UK = NO_UK + O
	O + NO2_X_UK = O
	O_X_UK + NO2 = NO2
NO2 + O3 → NO3 + O2	O3 + NO2_UK = NO3_UK + O3
	O3 + NO2_X_UK = NO3_X_UK
	O3_X_UK + NO2 = NO2
NO3 + HO2 → OH + NO2	NO3_UK + HO2 = HO2 + NO2_UK
	NO3_X_UK + HO2 = HO2 + NO2_X_UK
NO2 + NO3 + M → N2O5 + M	NO3_UK + NO2 = NO2NO3_UK + NO2
	NO3_X_UK + NO2 = NO2NO3_X_UK + NO2
NO2 + NO3 + M → N2O5 + M	NO3 + NO2_UK = NO3NO2_UK + NO3
	NO3 + NO2_X_UK = NO3NO2_X_UK + NO3
N2O5 + M → NO2 + NO3 + M	NO3NO2_UK = NO2_UK
	NO3NO2_X_UK = NO2_X_UK
N2O5 + M → NO2 + NO3 + M	NO2NO3_UK = NO3_UK
	NO2NO3_X_UK = NO3_X_UK
NO2 + OH + M → HNO3 + M	OH + NO2_UK = HNO3_UK + OH
	OH + NO2_X_UK = HNO3_X_UK + OH
HNO3 + OH → NO3 + H2O	OH + HNO3_UK = NO3_UK + OH
	OH + HNO3_X_UK = NO3_X_UK + OH
NO3 + NO → 2*NO2	NO3_UK + NO = NO2_UK + NO3
	NO3_X_UK + NO = 2.0 NO2_X_UK + NO
	NO3 + NO_UK = NO2_UK + NO3
NO2 + HO2 + M → HO2NO2 + M	HO2 + NO2_UK = HNO4_UK + HO2
	HO2 + NO2_X_UK = HNO4_X_UK + HO2
HO2NO2 + OH→ H2O + NO2 + O2	OH + HNO4_UK = NO2_UK + OH
	OH + HNO4_X_UK = NO2_X_UK + OH
HO2NO2 + OH→ H2O + NO2 + O2	HNO4_UK = NO2_UK
	HNO4_X_UK = NO2_X_UK
HO2NO2 + M → HO2 + NO2 + M	HNO4_UK + M= NO2_UK + M
CH4 + O1D → 0.75*CH3O2 + 0.75*OH + 0.25*CH2O + 0.4*HO2 + 0.05*H2	CH4 + O1D_X_UK
CH3O2 + NO → CH2O + NO2 + HO2	CH3O2 + NO_UK = CH3O2 + NO2_UK + NO2_X_UK
CH2O + NO3 → CO + HO2 + HNO3	CH2O + NO3_UK = CH2O + HNO3_UK
	CH2O + NO3_X_UK = CH2O + HNO3_X_UK
C2H4 + O3 → CH2O + 0.12*HO2 + 0.5*CO + 0.12*OH + 0.25*CH3COOH	C2H4 + O3_X_UK = C2H4
EO2 + NO → EO + NO2	EO2 + NO_UK = EO2 + NO2_UK + NO2_X_UK
C2H5O2 + NO → CH3CHO + HO2 + NO2	C2H5O2 + NO_UK = C2H5O2 + NO2_UK + NO2_X_UK
CH3CHO + NO3 → CH3CO3 + HNO3	CH3CHO + NO3_UK = CH3CHO + HNO3_UK
	CH3CHO + NO3_X_UK = CH3CHO + HNO3_X_UK
CH3CO3 + NO → CH3O2 + NO2	CH3CO3 + NO_UK = CH3CO3 + NO2_UK + NO2_X_UK
CH3CO3 + NO2 + M → PAN + M	CH3CO3 + NO2_UK + M = PAN_UK + CH3CO3 + M
	CH3CO3 + NO2_X_UK + M = CH3CO3 + PAN_X_UK + M
PAN + OH → CH2O + NO3	PAN_UK + OH = NO3_UK +OH
	PAN_X_UK + OH = OH + NO3_X_UK
PAN + M → CH3CO3 + NO2 + M	PAN_UK + M = NO2_UK + M
	PAN_X_UK = NO2_X_UK

Table 2.6 continued.

Original reaction continue	Tagged reactions continue
C3H6 + O3 → 0.54*CH2O + 0.19*HO2 + 0.33*OH + 0.5*CH3CHO + 0.56*CO+ 0.31*CH3O2 + 0.25*CH3COOH + 0.08*CH4	C3H6 + O3_X_UK = C3H6
C3H6 + NO3 → ONIT	C3H6 + NO3_UK = ONIT_UK + C3H6
	C3H6 + NO3_X_UK = C3H6 + ONIT_X_UK
PO2 + NO → CH3CHO + CH2O + HO2 + NO2	PO2 + NO_UK = PO2 + NO2_UK + NO2_X_UK
C3H7O2 + NO → 0.82*CH3COCH3 + NO2 + 0.27*CH3CHO + HO2	C3H7O2 + NO_UK = C3H7O2 + NO2_UK + NO2_X_UK
RO2 + NO → CH3CO3 + CH2O + NO2	RO2 + NO_UK = RO2 + NO2_UK + NO2_X_UK
ONIT + OH → NO2 + CH3COCHO	ONIT_UK + OH = NO2_UK + OH
CH3COCHO + NO3 → HNO3 + CO + CH3CO3	CH3COCHO + NO3_UK = HNO3_UK + CH3COCHO
	CH3COCHO + NO3_X_UK = CH3COCHO + HNO3_X_UK
ENEO2 + NO → CH3CHO + 0.5*CH2O + 0.5*CH3COCH3 + HO2 + NO2	ENEO2 + NO_UK = ENEO2 + NO2_UK + NO2_X_UK
MEKO2 + NO → CH3CO3 + CH3CHO + NO2	MEKO2 + NO_UK = MEKO2 + NO2_UK + NO2_X_UK
MPAN + OH + M → .5*HYAC + 0.5*NO3 + 0.5*CH2O + 0.5*HO2 + M	MPAN_UK + OH = .5 NO3_UK + OH
	MPAN_X_UK + OH = OH + .5 NO3_X_UK
ALKO2 + NO → 0.4*CH3CHO + 0.1*CH2O + 0.25*CH3COCH3 + 0.9*HO2 +0 .75*MEK + 0.9*NO2 + 0.1*ONIT	ALKO2 + NO_UK = ALKO2 + .9 NO2_UK + .9 NO2_X_UK + .1 ONIT_UK + .1 ONIT_X_UK
ISOP + O3 → 0.4*MACR + 0.2*MVK + 0.07*C3H6 + 0.27*OH + 0.06*HO2+ 0.6*CH2O + 0.3*CO + 0.1*O3 + 0.2*MCO3 + 0.2*CH3COOH	ISOP + O3_X_UK = ISOP +.1 O3_X_UK
ISOPO2 + NO → 0.08*ONITR + 0.92*NO2 + HO2 + 0.55*CH2O + 0.23*MACR+ .32*MVK + .37*HYDRALD	ISOPO2 + NO_UK = ISOPO2 + .08 ONITR_UK + .08 ONITR_X_UK + .92 NO2_UK + .92 NO2_X_UK
ISOPO2 + NO3 → HO2 + NO2 + 0.6*CH2O + 0.25*MACR + 0.35*MVK+ 0.4*HYDRALD	ISOPO2 + NO3_UK = ISOPO2 + NO2_UK
	ISOPO2 + NO3_X_UK = ISOPO2 + NO2_X_UK
ISOP + NO3 → ISOPNO3	ISOP + NO3_UK = ISOP + ISOPNO3_UK
	ISOP + NO3_X_UK = ISOPNO3_X_UK + ISOP
ISOPNO3 + NO → 1.206*NO2 + 0.072*CH2O + 0.167*MACR+ 0.039*MVK + 0.794*ONITR + 0.794*HO2	ISOPNO3_UK + NO = .206 NO2_UK + NO +.794 ONITR_UK
	ISOPNO3_X_UK + NO = .206 NO2_X_UK + .794 ONITR_X_UK + NO
ISOPNO3 + NO → 1.206*NO2 + 0.072*CH2O + 0.167*MACR+ 0.039*MVK + 0.794*ONITR + 0.794*HO2	ISOPNO3 + NO_UK = NO2_UK + NO2_X_UK + ISOPNO3
ISOPNO3 + NO3 → 1.000*XNO2 + ISOPNO3+ 0.039*MVK + 0.794*ONITR + 0.039*MVK + 0.794*ONITR + 0.794*HO2	ISOPNO3_UK + NO3 = .206 NO2_UK + .794 ONITR_UK + NO3
	ISOPNO3_X_UK + NO3 = .206 NO2_X_UK + .794 ONITR_X_UK + NO3
	ISOPNO3 + NO3_X_UK = 1.0 NO2_X_UK + ISOPNO3
	ISOPNO3 + NO3_UK = NO2_UK + ISOPNO3
ISOPNO3 + HO2 → 0.206*NO2 + 0.008*CH2O + 0.167*MACR + 0.039*MVK + 0.794*ONITR + 0.794*HO2	ISOPNO3_UK + HO2 = .206 NO2_UK + .794 ONITR_UK + HO2
	ISOPNO3_X_UK + HO2 = .206 NO2_X_UK + .794 ONITR_X_UK + HO2
MVK + O3→ 0.8*CH2O + 0.95*CH3COCHO + 0.08*OH+ 0.2*O3 + 0.06*HO2 + 0.05*CO + 0.04*CH3CHO	MVK + O3_X_UK = MVK + .2 O3_X_UK
MACR + O3 → 0.8*CH3COCHO + 0.275*HO2 + 0.2*CO+ 0.2*O3 + 0.7*CH2O + 0.215*OH	MACR + O3_X_UK = MACR + .2 O3_X_UK
MACRO2 + NO → NO2 + 0.47*HO2 + 0.25*CH2O + 0.25*CH3COCHO+ 0.53*CH3CO3 + 0.53*GLYALD + 0.22*HYAC+ 0.22*CO	MACRO2 + NO3_X_UK = MACRO2 + NO2_X_UK
MACRO2 + NO → 0.8*ONITR	MACRO2 + NO_UK = MACRO2 + NO2_UK + NO2_X_UK
MACRO2 + NO → 0.8*ONITR	MACRO2 + NO_UK = MACRO2 + .8 ONITR_UK + .8 ONITR_X_UK
MACRO2 + NO3 → NO2 + 0.53*GLYALD + 0.22*HYAC + 0.53*CH3CO3	MACRO2 + NO3_UK = MACRO2 + NO2_UK
MCO3 + NO → NO2 + CH2O + CH3CO3	MCO3 + NO_UK = MCO3 + NO2_UK + NO2_X_UK
MCO3 + NO3 → NO2 + CH2O + CH3CO3	MCO3 + NO3_UK = MCO3 + NO2_UK
	MCO3 + NO3_X_UK = MCO3 + NO2_X_UK
MCO3 + NO2 + M → MPAN + M	MCO3 + NO2_UK + M = MCO3 + MPAN_UK + M
	MCO3 + NO2_X_UK {+M} = MCO3 + MPAN_X_UK {+M}
MPAN + M→ MCO3 + NO2 + M	MPAN + M = NO2_UK + M
	MPAN_X_UK + M}= = NO2_X_UK + M
ONITR + OH→ HYDRALD + 0.4*NO2 + HO2	ONITR_UK + OH = OH + .4 NO2_UK
	ONIT_X_UK + OH = NO2_X_UK + OH
	ONITR_X_UK + OH= .4 NO2_X_UK + OH
ONITR + NO3 → HYDRALD + NO2 + HO2	ONITR + NO3_UK = .5 NO2_UK + ONITR
	ONITR + NO3_X_UK = .5 NO2_X_UK + ONITR
	ONITR_UK + NO3 = .5 NO2_UK + NO3
	ONITR_X_UK + NO3 = .5 NO2_X_UK + NO3
XO2 + NO→ NO2 + 1.5*HO2 + CO + 0.25*CH3COCHO + 0.25*HYAC + 0.25*GLYALD	XO2 + NO_UK = NO2_UK + NO2_X_UK + XO2
XO2 + NO3→ NO2 + 1.5*HO2 + CO + 0.25*CH3COCHO + 0.25*HYAC + 0.25*GLYALD	XO2 + NO3_UK = NO2_UK + XO2
	XO2 + NO3_X_UK = XO2 + NO2_X_UK
XOH + NO2 → 0.7*NO2 + 0.7*BIGALD + 0.7*HO2	XOH + NO2_X_UK = .7 NO2_X_UK + XOH
	XOH + NO2_UK = .7 NO2_UK + XOH
TOLO2 + NO→ 0.45*GLYOXAL + 0.45*CH3COCHO + 0.9*BIGALD + 0.9*NO2 + 0.9*HO2	TOLO2 + NO_UK = TOLO2 + .9 NO2_UK + .9 NO2_X_UK
C10H16 + O3→ 0.7*OH + MVK + MACR + HO2	C10H16 + O3_X_UK = C10H16
C10H16 + NO3 → TERPO2 + NO2	C10H16 + NO3_UK = C10H16 + NO2_UK
	C10H16 + NO3_X_UK = C10H16 + NO2_X_UK
TERPO2 + NO → 0.1*CH3COCH3 + HO2 + MVK + MACR + NO2	TERPO2 + NO_UK = TERPO2 + NO2_UK + NO2_X_UK
DMS + NO3→ SO2 + HNO3	DMS + NO3_UK = DMS + HNO3_UK
	DMS + NO3_X_UK = DMS + HNO3_X_UK

Several edits were made to include the new chemical species and the new mechanism into WRF-Chem. The following routines were edited:

- ***module_plumerise.F*** and ***module_add_emiss_burn.F***: added tags from NO_x biomass burning emissions;
- ***module_emissions_anthropogenics.F***: added tags for NOx from anthropogenic emissions;
- ***module_bioemi_megan.F*** and ***module_data_mgn2mech.F***: added tags for NOx from biogenic emissions;
- ***module_lightning_nox_driver.F*** : added tags for lightning-generated NO_x emissions;
- ***module_dep_simple.F*** and ***module_mozcart_wetscav.F***: added tag species to account for dry and wet deposition of tagged tracer. All tagged species yield the same dry deposition velocities and wet removal rates of their corresponding *non-tagged counterpart;*
- ***module_ftuv_driver.F***: added lines to consider the photolytic reaction of the new package MOZART_TAG;
- ***emissions_driver.F***;
- ***chem_driver.F;***
- ***chemics_init.F***;
- ***module_input_chem_data.F;***
- **The Registry**: to account for the new package associated with the new *chem–opt=113* chemistry option;
- Scripts handling initial and boundary conditions (***mozbc_inp***) to account for the impact of initial and boundary conditions emissions on O_3 concentration.

2.4 Model setup

In this section, the default setup used in the investigations is described. These options are tuned directly in the *namelist.inp* rather than in the model source code or in external utilities. The focus of the investigation is the UK and most of continental Europe. The modelled area is centred at 3° E, 53° N, and covers nearly the entire European region. The horizontal resolution is of 27 km, with 35 vertical levels starting from the surface up to 10hPA. The model domain has 151 and 128 grid points in the west–east and south–north directions, respectively, and a time-step of 150 seconds. A nested domain (9 km horizontal resolution) was placed to cover the UK and parts of Western Europe as shown in Fig. 2.3. The nested domain has 169 and 157 grid points in the west–east and south–north directions, respectively. The time step chosen was 45 seconds. A 1-way nesting was employed using the ***ndown*** utility, in which the parent provides lateral boundary conditions on every time step (once per hour) but no information is passed back to the parent from the nest, this decision was made to reduce computational expenses. The parent domain carries the same dimensions considered in the AQMEII inter-comparison project (http://aqmeii.jrc.ec.europa.eu/) in which the meteorology and chemistry have been validated for the year 2006, whereas nested domain has similar dimensions as (Steele et al., 2014).

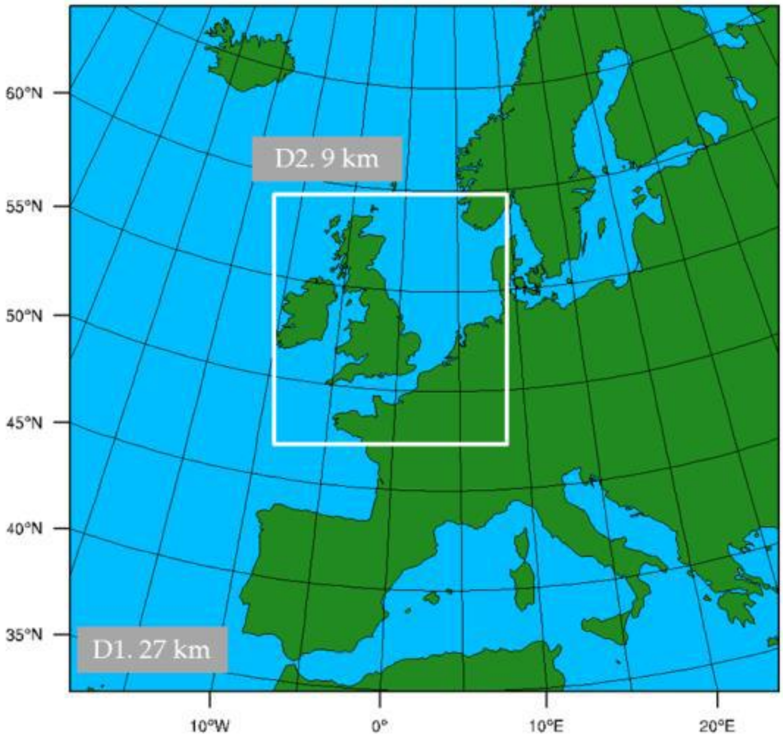

Figure 2.3. Area modelled in this study, including a higher resolution nested domain. D1 refers to the parent domain which has a 27 km spatial resolution, while D2 denotes the nested domain which has a 9 km horizontal resolution.

Model simulations were conducted for the period between April 24 and August 31, 2015. The first week of output was treated as model spin up and hence discarded. It was observed that after six days of simulations the contribution of O_3 from the initial conditions was reduced to less than 0.2 ppbv in the whole UK and between 0.1 and 1 ppbv in continental Europe, see Fig. 2.4. Model simulations were limited to gas-phase chemistry.

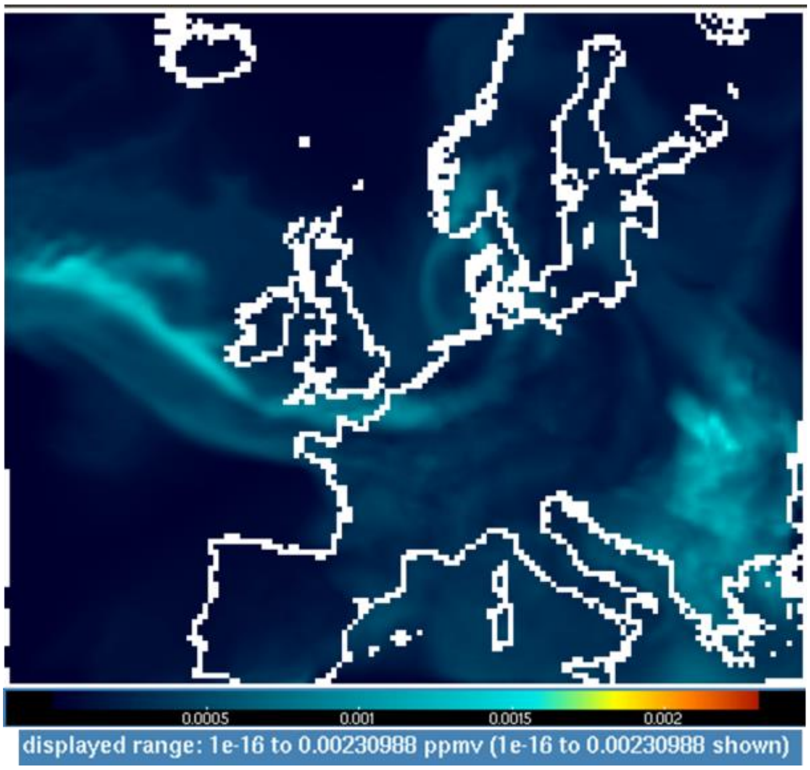

Figure 2.4. Initial O_3 concentrations of at the first model layer (~50 m height) after 6 days of spin-up.

The meteorology was not nudged but re-started every three days as in the methodology adopted in the AQMEII inter-comparison project (Rao et al., 2011), see Fig. 2.5. This decision was made after a test analysis had shown that nudging of winds above the PBL and temperature at all layers, as done in Mar et al. (2016), leads to a representation of hourly NO_2 and O_3 mixing ratios at Weybourne Observatory that is inconsistent with observations. This was due to nudging predicting a shallower boundary layer nearby Weybourne (over the Norfolk sea coast) than that obtained using the re-starting method, as in the example given in Fig. 2.6.

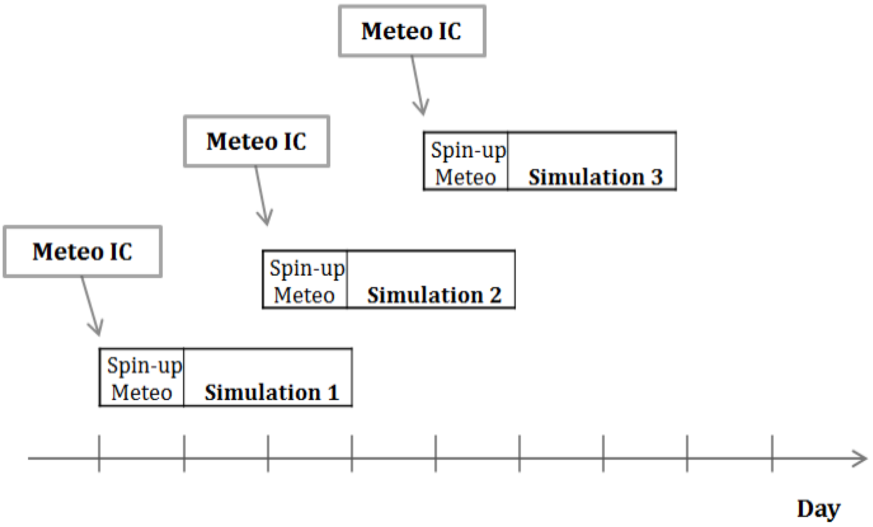

Figure 2.5. Schematic of the running option approach used in the simulation. Meteo IC refers to the initial conditions for meteorology.

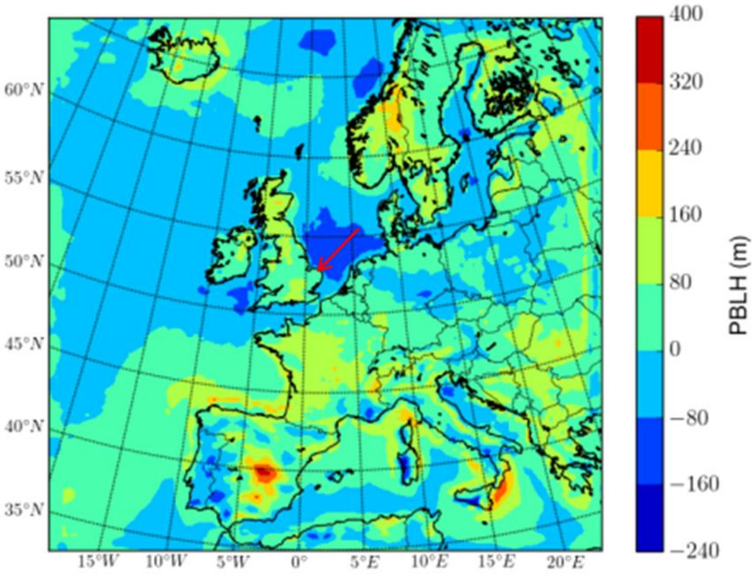

Figure 2.6. Difference between planetary boundary layer height (PBLH) with and without nudging, in metres. The value is obtained from the PBLH mean calculate from June 29 to July 31. Red arrow points the location of WAO.

The effect of the different boundary layer heights can be seen in the time series of hourly NO_2 and O_3 mixing ratios in Fig. 2.7a and b, respectively. Consistent with the PBL height, NO_2 tends to be higher at night in the nudging run while more O_3 is lost due to dry deposition. Despite that, the nudging simulation shows better agreement with O_3 observations for the whole campaign (~4% improvement in the Index of Agreement IOA which quantifies the degree to which the model predictions are error free). Yet, the reinit_met case performs better during the high O_3 concentrations episodes. Both cases had very similar correlations coefficients, however, the mean biased in the reinit_met run is ~3 ppbv lower.

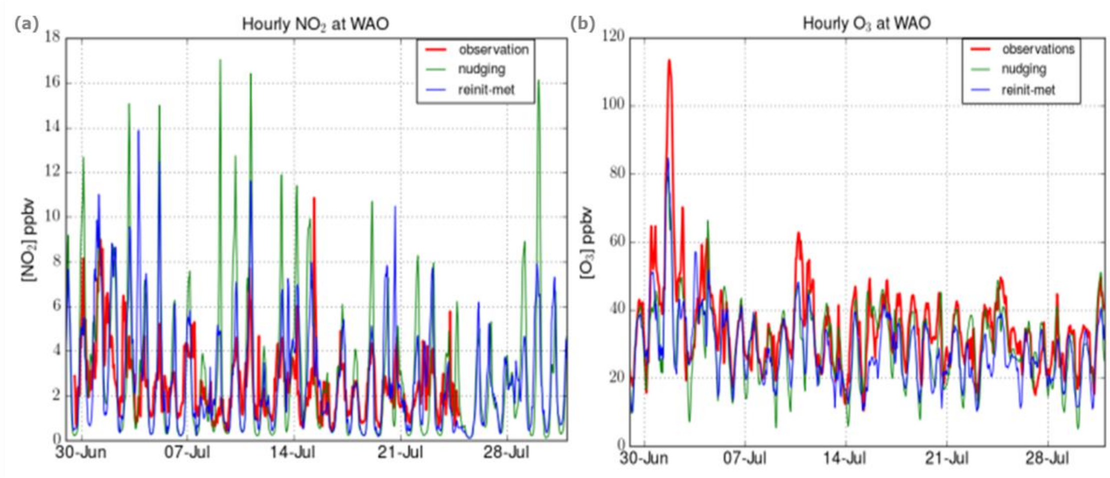

Figure 2.7. Comparison of hourly observed (red) and modelled NO_2 (a) and O_3 (a) at WAO, from the nudging and reinitialized meteorology every three days (reinit_met) runs (green and blue, respectively).

Bug fixes: A line in the chemical module was changed to correct the double counting of NO_2 emissions in the file "module_emissions_anthropogenics.F” for the CRImech mechanism following a personal notification from Dr Douglas Lowe.

Chapter 3

MODEL EVALUATION

3.1 Rationale

Regional chemical transport models are widely employed in air quality studies to assess the effectiveness of emissions control strategies, support the formulation of emissions control policies and complement atmospheric field campaign data when measurements are limited or challenging to obtain (e.g. Lei et al., 2006; Francis et al., 2011; Archer-Nicholls et al., 2014). However, even though models are intended to offer a reasonable representation of the atmospheric processes and parameters, uncertainties in the predictions are inevitable. These uncertainties are inherited from errors or biases in the input fields, such as the lateral and initial conditions and emissions inventories, that can further propagate into the regional model (Zhang et al., 2013, 2013a;; Brunner et al., 2015; Li et al., 2016). Other aspects, such as the choice of physical parameterizations, chemical mechanisms, and running options, are also known to influence model performance (e.g., Garcia et al., 2013; Zhang et al., 2013a-b; Derwent et al., 2014; Knote et al., 2014; Mar et al., 2016). Brunner et al. (2015), in particular, reported large variability in the prediction of meteorological parameters (e.g. winds at the near surface and in the vertical profile, surface incoming shortwave radiation, PBL height, water vapour and precipitation) between model ensembles due to differences in the model inputs and physical configurations. Inconsistencies in these meteorological variables are known to further affect the air quality predictions in a manner inconsistent with observations (e.g., Im et al., 2014). The versatility of the WRF-Chem system provides the advantage to tailor the model input and settings according to the problem on hand. However, there is no consensus on which set of schemes performs better for a given application. Prior evaluation of the model system with a focus on the meteorology and tropospheric chemistry is therefore essential.

The study of Mar et al. (2016) offers a valuable reference of a model configuration suitable for a European domain. It also highlights the dependence of modelled surface O_3 over Europe on the choice of gas-phase chemical mechanism, with MOZART-4 leading to lower absolute biases than RADM2 when compared to ground-based chemical observations. Archer-Nicholls et al. (2014), on the other hand, describe model setup options suitable for a UK domain, although the evaluation of the metrological variables was not carried out.

This chapter builds on the above studies as it compares results obtained using the CRImech and MOZART-4 chemical mechanisms with observations for a European domain. Near-surface concentrations of O_3, NO_x, NOy, CO and VOCs (primary and secondary species) taken from the Integrated Chemistry of Ozone in the Atmosphere (ICOZA) field campaign, summertime 2015, are used to evaluate the model performance. The ultimate goal of the chapter is to identify the most suitable model setup for subsequent investigations. The specific objectives are:

1. Assess the ability of the model to reproduce the meteorological and atmospheric-chemical conditions observed during summertime 2015.
2. Assess the ability of the model to represents high O_3 events (when concentrations exceed 60 ppbv), health-related metrics such as MDA8 O_3 and vegetation metrics such as AOT40.
3. Identify which model configuration better reproduces the observations.
4. Understand whether poor model performance affect specific geographical locations.

3.2 Methods

3.2.1 Model Setup

The model domain was located over Europe as shown in Fig. 3.1, and given a horizontal resolution of 27 km and 35 vertical levels. The first 12 levels divided the first 3 km with the lowest level at ~50 m, and the remaining 23 levels between the 3 and ~20 km (10hPa). The model input data set included anthropogenic emissions from the TNO-MACC inventory for the year 2011 (resolution 0.125° longitude × 0.0652° latitude) and the latest UK NAEI for the year 2014 (resolution of 1 km), see section ***2.2.2.3***. The model configuration shared the same physical parameterizations and running options described in sections 2.1 and 2.5. Simulations were conducted for the period between 24th April and 1st September 2015. The first week of output was treated as spin-up.

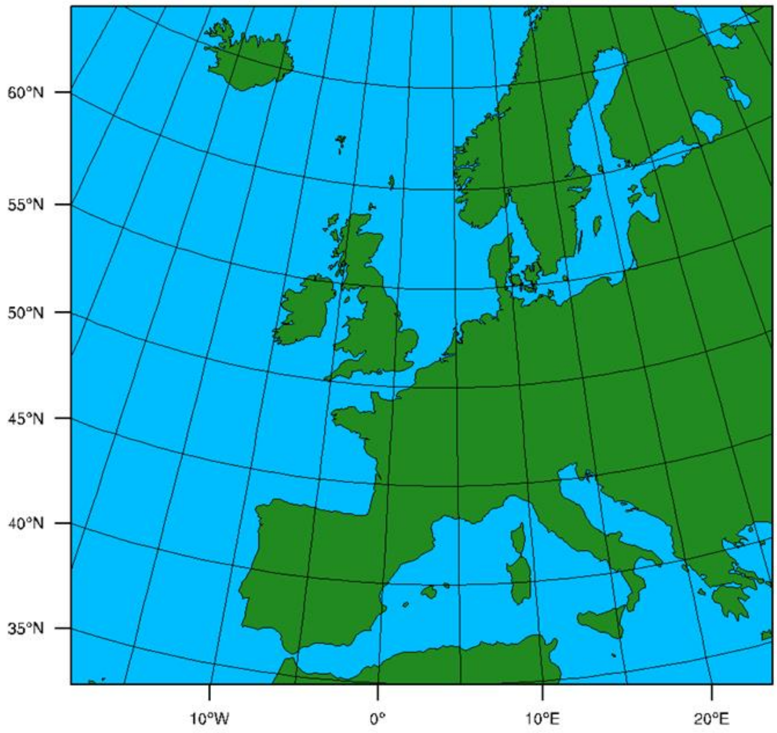

Figure 3.1. Schematic of the WRF-Chem domain.

3.2.2 Description of the observational dataset

The data sources and variables selected for the model evaluation are listed below. Table 3.1 summarises the dataset used in the evaluation of meteorology and Fig. 3.2 shows their location in the map. Table 3.2 and Fig. 3.3 both describe the dataset used in the evaluation of the chemistry.

3.2.2.1 Meteorological datasets

The meteorological datasets include observations of air temperature at 1.25 meters (m) above the ground (T) and wind speed and direction at 10 m above the ground (WS and WD, respectively) from the land surface observational data from the UK Met Office Integrated Data Archive System (MIDAS: UK hourly weather observation data) (Met Office, 2012). Additional modelled temperature at 2m (T2) and wind (direction and speed) from the Defra air quality modelling program were employed in places where observations were not accessible in order to build a general picture of the model performance over the UK. The data product used here were taken from the WRF 3.1.1 model run with a nested 10 km horizontal resolution centred in the UK (Defra, 2015).

Table 3.1. List of observational data used in the validation of meteorology. The abbreviated name (Abbr.) is used in the map showing the location of the sites and in the tables summarising statistics.

Station	Area	Abbr.	Database	Parameters
Bainbridge	North Yorkshire	bai	MIDAS	T
Westleton	Suffolk	wes	MIDAS	T
Aldeburgh	Suffolk	ald	MIDAS	T
Boxworth: Samson Field	Cambridgeshire	box	MIDAS	T
Wellingborough	Northamptonshire	wel	MIDAS	T
Edgbaston	West Midlands	edg	MIDAS	T
Brawdy	Dyfed	bra	MIDAS	T
Alnwick	Northumberland	aln	MIDAS	T
Raby castle	Durham	rab	MIDAS	T, WS, WD
Scaling	Cleveland	sca	MIDAS	T
Beverley: Lairgate	Humberside	bev	MIDAS	T
Osmotherly Filters	North Yorkshire	osm	MIDAS	T
Wilford Hill	Nottinghamshire	wil	MIDAS	T, WS, WD
Sibsey	Lincolnshire	sis	MIDAS	T, WS, WD
Dagenham: Central Park Nursery	Greater London	dag	MIDAS	T, WS, WD
Cirencester: Somerford Road	Gloucestershire	cir	MIDAS	T, WS, WD
Holsome	Devon	hol	MIDAS	T, WS, WD
Taunton Rectory	Somerset	tau	MIDAS	T, WS, WD
Charing P Sta	Kent	cha	MIDAS	T, WS, WD
Pembrey Sands	Dyfed	pen	MIDAS	T
Rhoose	South Glamorgan	rho	MIDAS	T
Cardiff: Bute Park	South Glamorgan	car	MIDAS	T
Badworthy	Devon	bad	MIDAS	T2, WS, WD
Mace Head	Galway	mac	DEFRA-Modelling	T2, WS, WD
Lough Navar	Fermanagh	lnv	DEFRA-Modelling	T2, WS, WD
Bush Estate	Midlothian	bsh	DEFRA-Modelling	T2, WS, WD
Aston Hill	Flintshire	ahl	DEFRA-Modelling	T2, WS, WD
Strathvaich	Ross & Cromarty	str	DEFRA-Modelling	T2, WS, WD
Weybourne	Norfolk	wao	ICOZA	T2, WS, WD

3.2.2.2 The ICOZA field campaign

The Integrated Chemistry of Ozone in the Atmosphere (ICOZA) field campaign took place at Weybourne Atmospheric Observatory (WAO) (52.95 N, 1.12 E) on the North Norfolk Coast, UK, during the summer of 2015 (29th June to 1st August), see Fig. 3.2. In this chapter, observations of CO, O_3, NO_x, NO_y and VOCs (primary emitted and those produced after the oxidation of hydrocarbons) described in detail in Crilley et al. (2015) are used to assess the model performance. Meteorological fields such 2m temperature and wind speed and direction are also compared with model output. Note that costal effects, e.g. sea breezes, may greatly impact modelled output (Steele et al., 2014).

Figure 3.2. Spatial distribution of the sites used in the evaluation of the meteorology. Green circles represents data from the UK Met Office Integrated Data Archive System (MIDAS: UK hourly weather observation data), while yellow circles refers to datasets from modelling output from DEFRA.

3.2.2.3 Additional chemical surface datasets

Hourly surface O_3 measurements were also taken from the European Monitoring and Evaluation Programme (EMEP) (http://www.nilu.no/projects/ccc/) from April to August 2015 at sites in the UK, Ireland, France, The Netherlands, Switzerland, Denmark, Austria and Germany. The EMEP dataset contains hourly data from the Convention on Long-Range Transboundary Air Pollution at regional background sites mostly at farmland and rural areas (Tørseth et al., 2002). The choice of analysing only rural EMEP stations is indicated by the need to provide a comparison with spatial scales consistent with the model resolution. Kuik et al. (2016) have shown that a resolution of 15 km is too coarse to resolve the differences between urban and rural atmospheric chemical composition. The resolution of the domain considered here is even coarser. The EMEP dataset was therefore selected as it provides surface measurements at sites that are intended to be representative of regional background pollution. In addition, surface measurements of NO_X (NO and NO_2) were also taken for the same stations when available. Table 3.2 lists the observational data used in the evaluation of the chemistry and Fig. 3.3 shows the spatial distribution of the dataset.

Table 3.2. List of observational data used in the validation of the chemistry. The abbreviated name (Abbr.) is used in the map showing the location of the sites and in the tables summarising statistics. The MASL indicates the altitude above sea level of the sites.

Site	Abbr.	MASL	Country	Parameters
Weybourne	wao	16	UK	O_3, NO, NO_2, CO, C_2H_6, C_3H_8, C_7H_8, C_4H_{10}, C_2H_4, C_3H_6, C_5H_8, MEK, CH_3OH, CH_3COCH_3
Bush-state	bsh	180	UK	O_3, NO, NO_2
Auchencorth Moss	ams	260	UK	O_3
Lullington Heath	lul	120	UK	O_3
Mace Head	mac	15	Ireland	O_3
Sibton	sib	46	UK	O_3
Wicken Fen	wkf	5	UK	O_3, NO, NO_2
Lerwick	ler	85	UK	O_3
Charlton Mackrell	cha	54	UK	O_3, NO, NO_2
St Osyth	st.o	8	UK	O_3, NO, NO_2
Harwell	har	137	UK	O_3, NO, NO_2
Narberth	nar	160	UK	O_3, NO, NO_2
Aston-hill	ahl	370	UK	O_3, NO, NO_2
Lough Navar	lnv	126	UK	O_3
Yarner Wood	ywd	119	UK	O_3, NO, NO_2
Strathvaich	str	270	UK	O_3
Eskdalemuir	esk	243	UK	O_3
High Muffles	hig	267	UK	O_3, NO, NO_2
de Zilk	zil	4	Netherlands	O_3
Cabauw	cab	4	Netherlands	O_3
Eibergen	eib	20	Netherlands	O_3
Vredepeel	vre	28	Netherlands	O_3
Kollumerwaard	kol	1	Netherlands	O_3
Westerland	wes	12	Germany	O_3, NO, NO_2
Neuglobsow	neg	62	Germany	O_3, NO, NO_2
Schmücke	sch	937	Germany	O_3
Waldhof	wal	74	Germany	O_3, NO, NO_2
Schauinsland	scha	1205	Germany	O_3, NO, NO_2
Zingst	zin	1	Germany	O_3, NO_2
Donon	don	775	France	O_3
Revin	rev	390	France	O_3
Coulonche	cou	309	France	O_3
La Tardière	tar	133	France	O_3
Morvan	mor	620	France	O_3
Montfranc	mfr	810	France	O_3
Pic du Midi	pdm	2877	France	O_3
Payerne	pay	489	Switzerland	O_3, NO, NO_2
Rigi	rig	1031	Switzerland	O_3, NO, NO_2
Ulborg	ulb	10	Denmark	O_3
Keldsnor	kel	10	Denmark	O_3
Chaumont	chau	1137	Switzerland	O_3
Tänikon	tan	539	Switzerland	O_3
Jungfraujoch	jun	3578	Switzerland	O_3
Heidenreichstein	hei	570	Austria	O_3
Haunsberg	hau	730	Austria	O_3
Masenberg	mase	1170	Austria	O_3
Gerlitzen	ger	1895	Austria	O_3
Sonnblick	son	3106	Austria	O_3
Sulzberg	sul	1020	Austria	O_3
Pillersdorf	pil	315	Austria	O_3
Illmitz	ill	117	Austria	O_3
Vorhegg	vor	1020	Austria	O_3

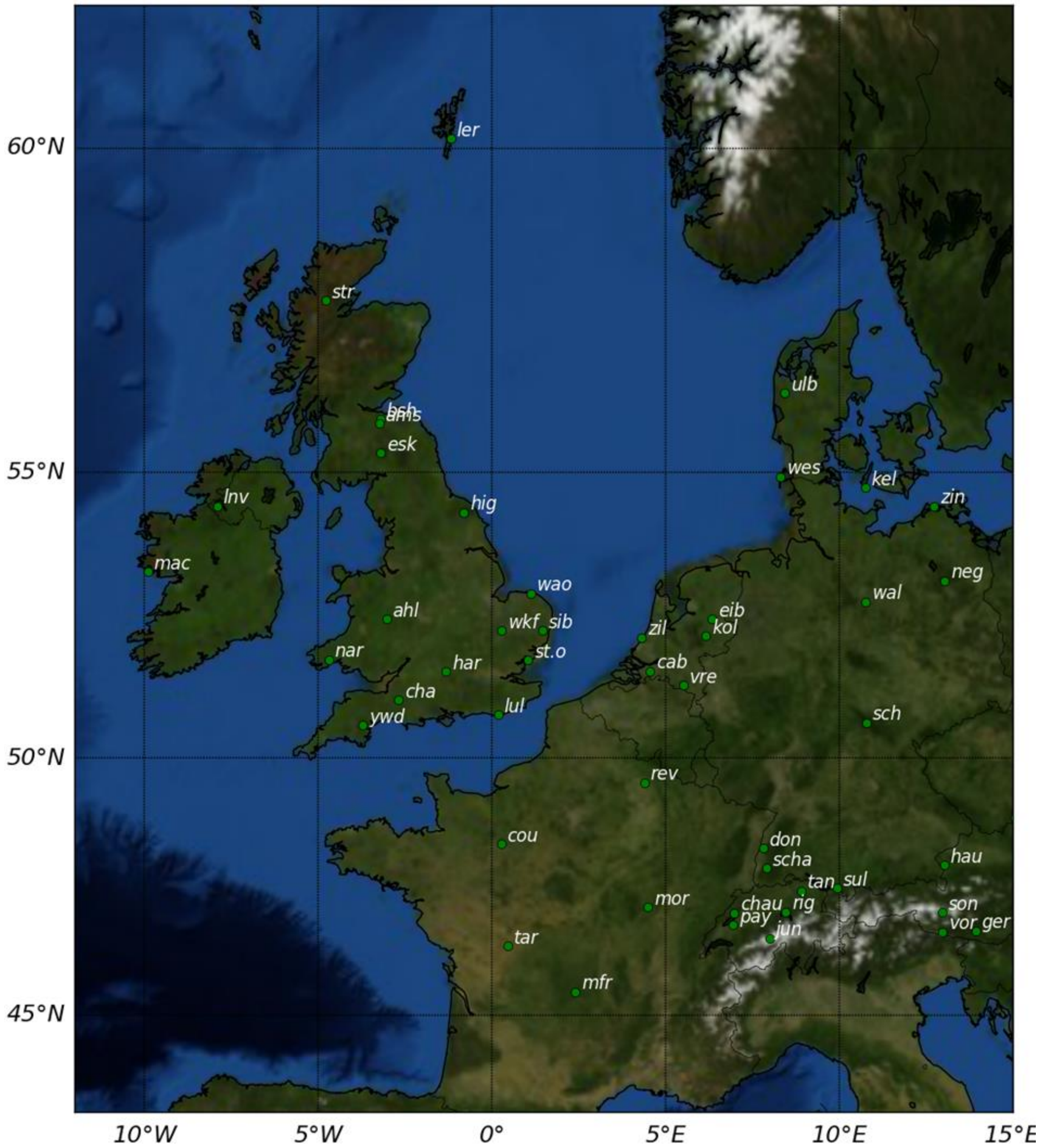

Figure 3.3. Spatial distribution of the sites used in the evaluation of the chemistry.

3.2.3 Model evaluation methodology

The grid point closest to the latitude and longitude of each station was selected for comparison of modelled variables with in-situ observations. Hourly values of 2m temperature and 10m wind speed and direction (WS10 and WD10) were compared at specific sites and the performance of statistics calculated also at individual sites. In addition, conditional quantile plots of temperature and wind speed produced using the '*conditionalQuantile*' function in the R-Openair package (Carslaw & Ropkins, 2012) were calculated. For this purpose, observations at each site were split into evenly spaced bins and the median, 25/75th and 10/90th percentiles calculated for each bin.

The methodology for the operational evaluation for both meteorology and chemical fields followed the general guidance for evaluation of air quality model's performance produced by DEFRA (Derwent et al., 2010). Statistics includes the Fraction of predictions within a factor or two (FAC2), Mean Bias (MB), Mean Gross Error (MGE), the Normalized Mean Bias (NMB), Normalised mean gross error (NMGE), Root mean squared error (RMSE), and Person correlation coefficient (r). The statistical analysis was also performed using R-Openair. No metrics were calculated for wind direction.

Terms:
M = predicted concentration
O = observed concentration
$\overline{M}, \overline{O}$ = predicted and observed mean
σ = standard deviation
n = number of samples

I. Mean Observations ($\overline{O}$): the time-averaged mean observed value

$$\overline{O} = \frac{1}{n}\sum_1^n O_i = \frac{O_1 + O_{\dots} + O_n}{n} \quad \text{(E. 3.1)}$$

II. Mean Model ($\overline{M}$): the time-averaged mean predicted value

$$\overline{M} = \frac{1}{n}\sum_1^n M_i = \frac{M_1 + M_{\dots} + M_n}{n} \quad \text{(E. 3.2)}$$

III. Fraction of predictions within a factor or two (FAC2): count of the fraction of points within ½ and 2 times the observations

$$0.5 \geq \frac{M_i}{O_i} \leq 2 \quad \text{(E. 3.3)}$$

IV. Mean Bias (MB): averaged modelled and observation residuals. The metric is used to determine whether the model under-predict or over-predict the observation.

$$MB = \frac{1}{n}\sum_{i=1}^{n}(M_i - O_i) \quad \text{(E. 3.4)}$$

V. Mean Gross Error (MGE): quantifies the departure between modelled and observed concentrations.

$$MGE = \frac{1}{n}\sum_{i=1}^{n}|\ M_i - O_i\ | \quad \text{(E. 3.5)}$$

VI. Normalized Mean Bias (NMB)(dimensionless): normalisation of the MB with respect to the average observed value

$$NMB = \frac{\sum_{i=1}^{n}(M_i - O_i)}{\sum_{i=1}^{n}(O_i)} \quad \text{(E.3.6)}$$

VII. Normalised mean gross error (NMGE)(dimensionless): normalisation of the MGE with respect to the average observed value

$$NMGE = \frac{\sum_{i=1}^{n}|\ M_i - O_i\ |}{\sum_{i=1}^{n}(O_i)} \quad \text{(E. 3.7)}$$

VIII. Root mean squared error (RMSE): a measure of how close modelled values are to predicted values

$$RMSE = \left(\frac{\sum_{i=1}^{n}(M_i - O_i)^2}{n}\right)^{\frac{1}{2}} \quad \text{(E. 3.8)}$$

IX. Person correlation coefficient (r) (dimensionless): a measure of the degree to which both modelled and observed values are linearly related. A correlation coefficient closed to 0 means that there is no linear relationship between the variables. Values bigger than 0.70 indicate a strong positive linear relationship while values between 0.70 and 0.50 moderate positive linear relationship.

$$r = \frac{1}{(n-1)} \sum_{i=1}^{n} \left(\left(\frac{Oi-\bar{O}}{\sigma_O} \right) \left(\frac{Mi-\bar{M}}{\sigma_M} \right) \right) \quad \text{(E. 3.9)}$$

Two additional metrics were considered for O_3: the maximum daily 8 hour (h) mean (MDA8 O_3) concentrations, which is a health-related metric commonly used to assess the impacts of O_3 exposure on the population (e.g. Mar et al., 2016; Reidmiller et al., 2009; Stock et al., 2013), and the accumulated amount of O_3 over the threshold value of 40 ppbv (AOT40), which is commonly used to assess the effects of O_3 on crops and vegetation (e.g., Mar et al., 2016). The health metric was estimated by computing 8 h moving mean of O_3, for both modelled and observations at each site, and by selecting the hours when the MDA8 of 50 and 60 ppbv is exceeded, in accordance with the current European and National air quality standards (Royal Society, 2008). The AOT40 is defined as the accumulated excess of hourly O_3 concentrations above 40 ppbv measured during daylight hours (between 08:00 and 20:00) Central European Time (CET) over a typical three month growing season May-July (EU Ambient Air Quality Directive (2008/50/EC)). Here, the AOT40 metric was calculated by extracting the hours when O_3 mixing ratios exceeded the hourly 40 ppbv threshold between 08:00 and 20:00 CET.

3.2.4 Parameterization of gas phase chemistry

Two different parameterizations of the chemical processes were compared: the setup included the CRImech chemical scheme (Watson et al., 2008; Archer-Nicholls et al., 2014) and the Model for Ozone and Related chemical Tracers (MOZART) gas-phase mechanism (Emmons et al., 2010). The evaluation of the two model scenarios was conducted for the period between 29th June and 31st July

2015. The summer 2015 was chosen as this corresponds to the time period of the Integrated Chemistry of Ozone in the Atmosphere (ICOZA) field campaign carried out at Weybourne Atmospheric Observatory (WAO), Norfolk. The meteorology was not nudged but re-started every three days following the methodology used in the AQMEII inter-comparison project. This decision was justified by the sensitivity analysis discussed in Chapter 2 having shown that nudging of winds and temperature following Mar et al. (2016) leads to a representation of hourly NO_2 and O_3 mixing ratios that is inconsistent with observations. Moreover, simulations were run without aerosol-radiative feedbacks to ensure that the differences in the prediction of the chemical fields for the two models (MOZART and CRImech) were due predominately to differences in the treatment of the chemistry rather than aerosol-radiative feedbacks.

3.3 Model evaluation results

3.3.1 Evaluation of the meteorology

Modelled meteorological fields were compared with in-situ measurements of air temperature at 1.25 m above the ground and wind speed and direction at 10m above the ground from the Met Office MIDAS archive. These meteorological variables are known to impact the representation of gas phase chemistry (Im et al., 2014). As stated in session 3.2.2.1, additional modelled temperature and wind (direction and speed) from the Defra's air quality modelling program were used in places where observations were not accessible. Table 3.3 lists the statistic performance of modelled temperature and wind speed across the assessed sites between May and September 2015.

Table 3.3. Summary statistics for modelled temperature and wind speed performance, from May to August 2015, at 26 sites across the UK. (Par.) refer to parameter. The units of MB, MGE and RMSE are the same as the observations.

Site	Par.	FAC2	MB	MGE	NMB	NMGE	RMSE	r
Bainbridge	T	1.0	0.6	1.8	0.1	0.2	2.4	0.8
Westleton	T	0.9	2.4	3.2	0.2	0.3	3.8	0.6
Boxworth	T	0.9	3.7	4.1	0.3	0.4	4.9	0.7
Wellingborough	T	0.9	2.6	3.3	0.2	0.3	4.1	0.8
Edgbaston	T	0.9	1.6	2.7	0.1	0.2	3.5	0.7
Brawdy	T	0.9	2.3	3.4	0.2	0.3	4.2	0.5
Alnwick	T	1.0	-0.5	1.6	0.0	0.1	2.1	0.9
Raby castle	T	0.9	2.1	2.8	0.2	0.3	3.4	0.8
Scaling resr 1	T	1.0	-0.5	2.1	0.0	0.2	2.7	0.7
Beverley: Lairgate	T	1.0	0.7	1.8	0.1	0.1	2.3	0.9
Osmotherly Filters	T	1.0	-0.8	1.9	-0.1	0.1	2.4	0.9
Wilford Hill resr	T	1.0	-1.6	2.5	-0.1	0.2	3.2	0.8
	WS	0.7	-1.6	3.0	-0.3	0.5	4.0	0.5
Sibsey	T	1.0	0.8	2.5	0.1	0.2	3.1	0.8
	WS	0.7	-3.3	4.1	-0.4	0.5	5.2	0.3
Dagenham: Central Park Nursery	T	1.0	0.7	1.9	0.0	0.1	2.5	0.8
	WS	0.8	-2.3	2.7	-0.4	0.4	3.4	0.7
Cirencester: Somerford Road	T	1.0	-0.9	1.8	-0.1	0.1	2.4	0.9
	WS	0.8	-0.9	2.2	-0.2	0.4	2.9	0.7
Holsome	T	0.9	-2.3	4.1	-0.1	0.3	6.0	0.6
Taunton Rectory	T	1.0	-0.4	2.1	0.0	0.2	2.6	0.7
	WS	0.5	-5.3	5.6	-0.5	0.6	7.0	0.4
Badworthy	T	1.0	-1.5	1.9	-0.1	0.1	2.5	0.9
Pembrey Sands	T	0.9	2.3	3.2	0.2	0.3	4.0	0.6
Rhoose	T	0.9	0.4	2.9	0.0	0.3	3.6	0.5
Cardiff: Bute Park	T	1.0	1.4	2.6	0.1	0.2	3.2	0.7
Macehead	T	1.0	-0.8	1.6	-0.1	0.1	2.1	0.7
	WS	0.9	-1.5	2.0	-0.2	0.3	2.5	0.8
Lough Navar	T	1.0	-0.3	1.7	0.0	0.2	2.2	0.8
	WS	0.9	0.2	1.1	0.0	0.2	1.4	0.8
Bush Estate	T	1.0	-1.2	2.5	-0.1	0.2	3.2	0.7
	WS	0.9	0.9	1.8	0.2	0.4	2.3	0.7
Aston Hill	T	1.0	0.7	1.6	0.1	0.1	2.1	0.9
	WS	0.9	-0.1	0.9	0.0	0.2	1.2	0.8
Strathvaich	T	1.0	1.0	1.5	0.1	0.2	1.9	0.9
	WS	0.9	0.4	1.0	0.1	0.2	1.3	0.8

3.3.1.1 Ambient temperature

In general, the model represents well the observed near-surface air temperature variability over the UK, with correlation values raging between 0.9 and 0.5, see Table 3.3. The poorest correlation is obtained in sites near the coast, e.g. Rhoose (0.51), Brawdy (0.54) and Holsom (0.59), where the model struggles to capture the diurnal variation in the air temperature (Fig. 3.4c-d). The histograms in the conditional quantile plots, Fig. 3.5, further show that the model captures observations for a wide range of values. Nevertheless, in some sites the model does not reproduce the highest and lowest observed temperatures. This is shown in the histogram in the conditional quantile plot, e.g. Brawdy in Fig. 3.5, as well as in the extent of the red median line spreading only to less than half of the observations 'blue line'.

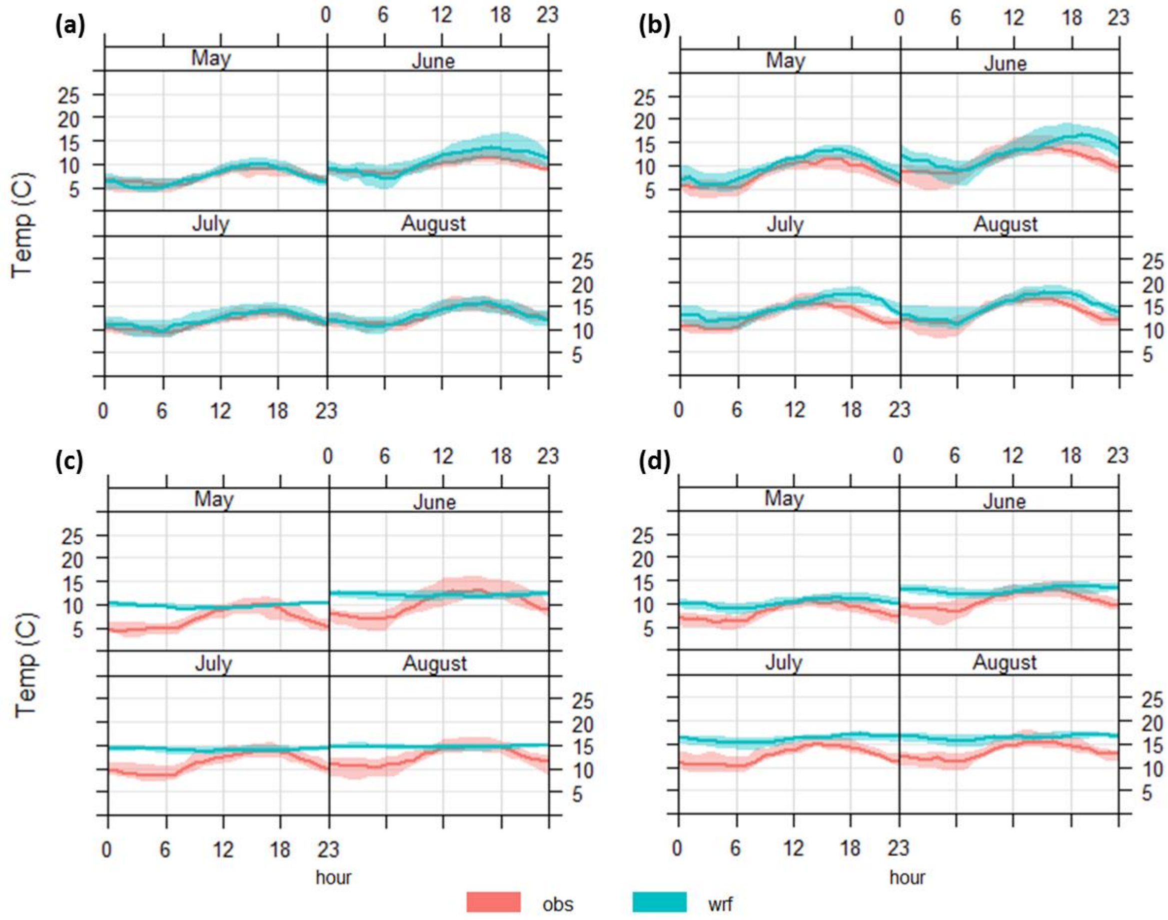

Figure 3.4. Comparison of the mean diurnal variation in temperature from May to August 2015 on land sites Bainbridge and Wellingborough (a and b, respectively) and near the coast sites Brawdy and Westleton (c and d, respectively).

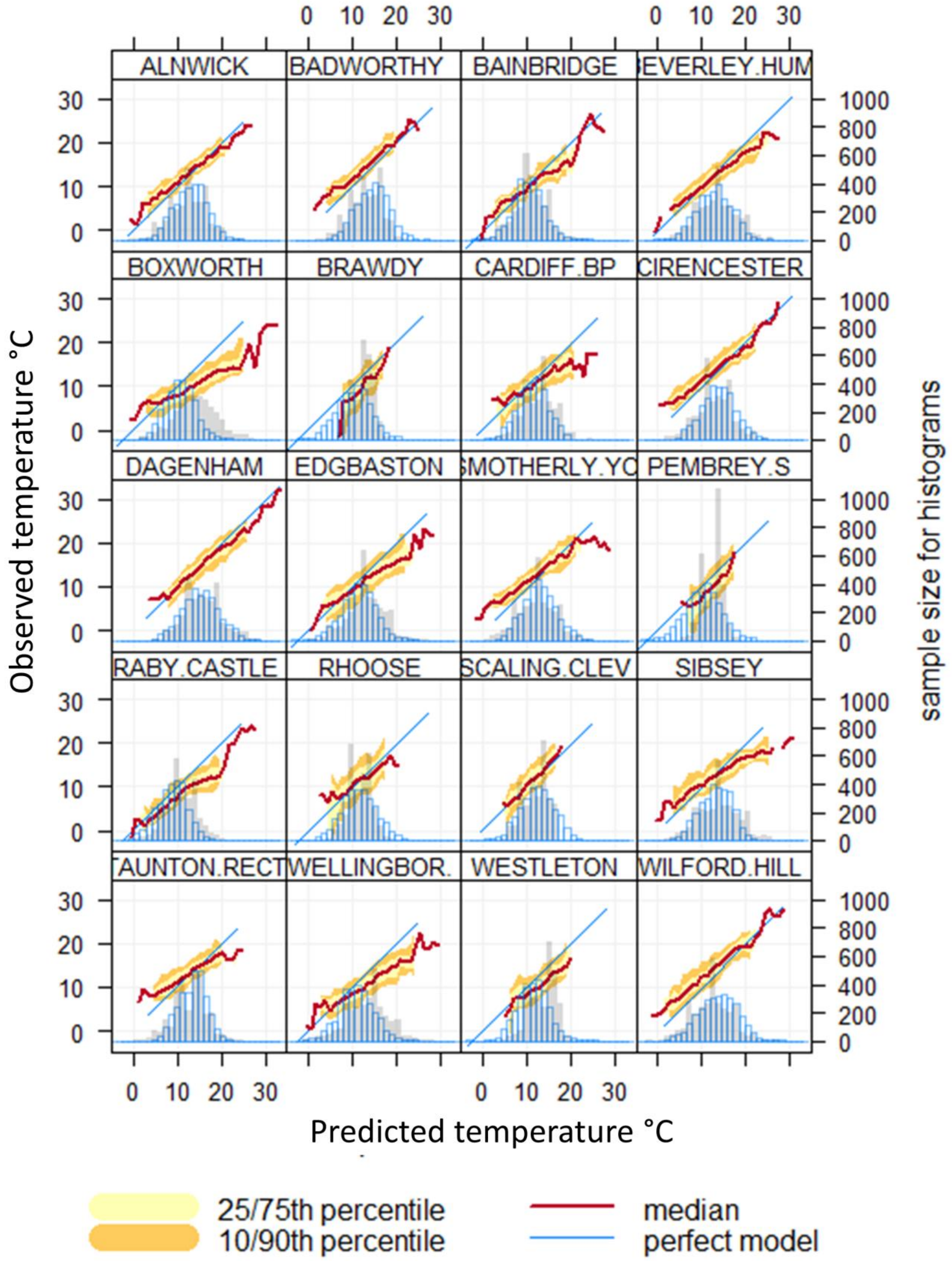

Figure 3.5. Conditional quantile plots of hourly temperature performance, from May to August 2015, at 21 Met-office sites in the UK. The blue diagonal line shows the results for a perfect model (1:1) while the red line and the yellow shading denotes the median and the modelled quantile intervals (25/75th and 10/90th), respectively. Grey bars show the distribution of model results while the blue bars the distribution of observations.

Table 3.3 further shows that the model is biased positively in most of the assessed sites. This is also discernible by looking at the position of the median red line with respect to the blue line in Fig. 3.5, e.g. the Boxworth site. The largest warm bias (MB = 3.7°C) is obtained at Boxworth Cambridgeshire, and is driven by overestimation of daytime temperatures in all months, as shown in Fig. 3.6a. By contrast, the biggest cold biases (MB = -2.3 °C) are obtained at Holsome Devon mainly because he model fails to predict warmer temperatures in July, Fig. 3.6b. The values of MB in the temperature over the UK are consistent with that reported by Mar et al. (2016) in the June-July-August 2006 evaluation of WRF-Chem over Europe, where cold bias mostly concentrates over Northern Ireland and the North and southwest UK.

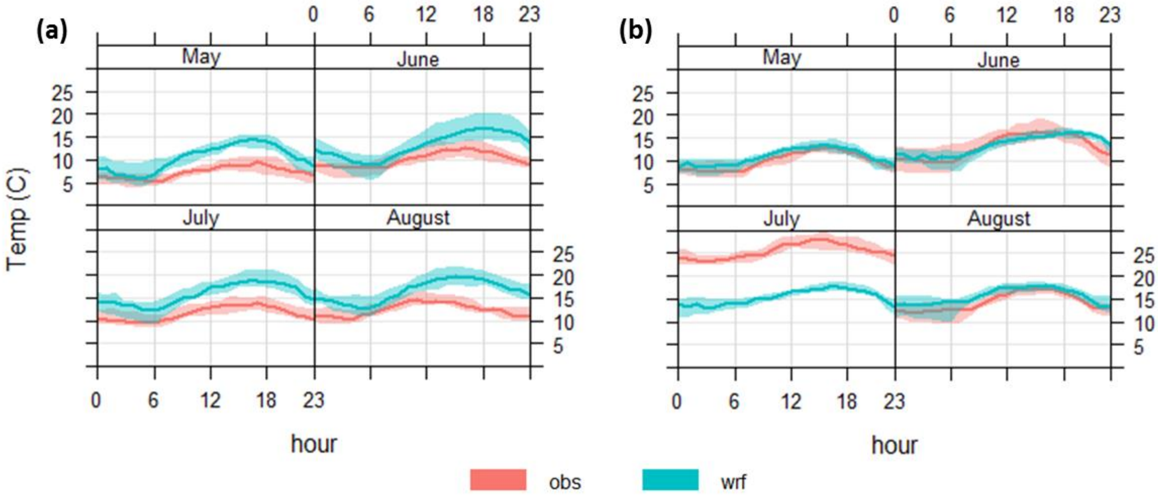

Figure 3.6. Comparison of mean diurnal variation in modelled and observed ambient temperature, from May to August 2015, at (a) Boxworth Cambridgeshire and (b) Holsome Devon.

The simulation gives a NMB between +0.3 and -0.1 for the period between May and August, though the NMB is smaller than +0.3 at the majority of the sites. The obtained MB ranges between +3.7 and -2.3 °C, and the MGE between 1.5 and 4.1.

Meteorological model evaluation benchmarks, such as those in Tesche et al. (2002) and Derwent et al. (2010) consider the use of an air quality model to be acceptable for policy applications if the NMB values for ambient temperature is within ±0.2, the MGE is ≤2 K, MB is within ±0.5 K, and the FAC2 is within ½ and

2 times the observations. Overall, based on the FAC2 and NMB results, it can be concluded that the model exhibits a relatively good performance for temperature.

3.3.1.2 Wind speed

Wind speed exhibited a fair statistical performance, see Table 3.3. The correlation coefficients obtained at individual sites ranged between 0.3 and 0.8, with the lowest values showing no geographical preference. The histograms in the conditional quantile plots, Fig. 3.7, further highlight the poor correlation performance of wind speed. In all sites, the model struggles to capture its distribution. In particular, the model tends to predict moderate wind speed more frequently and fails to reproduce the highest observed wind speed values. Furthermore, the model is biased negatively in the majority of the sites with both the lowest biases (MB = -5.3 ms^{-1}) and the highest biases (MB = +0.9 ms^{-1}) obtained for the southwest. The MB values are closer to the those reported by Zhang et al. (2013) in the model validation of WRF/Chem-MADRID and WRF/Polyphemus over Europe where wind speed is under-predicted at many sites in the UK (with MBs of –4 to –0.8ms^{-1}). It is worth noting that positive biases were restricted to the sites where the simulated wind was compared with output from WRF from the Defra's air quality modelling program (e.g. Mace Head, Lough Navar, Bush Estate, Aston Hill and Strathvaich).

The simulation gives a NMB between +0.2 and -0.5 for the period between May and August. The obtained MB ranged between +0.9 and -5.3 ms^{-1}, the RMSE is between 1.2 and 7.0, and FAC2 between 0.5 and 0.9. Meteorological model evaluation benchmarks, e.g. Tesche et al. (2002) and Derwent et al. (2010), consider the use of an air quality model acceptable for policy applications if the NMB values for WS is between ±0.2, the RMSE is about $\leq 2ms^{-1}$, MB is within ±0.5 ms^{-1}, and the FAC2 is within ½ and 2 times the observations. Overall, based on the FAC2 and NMB results, it can be concluded that the model performs fairly well for wind speed.

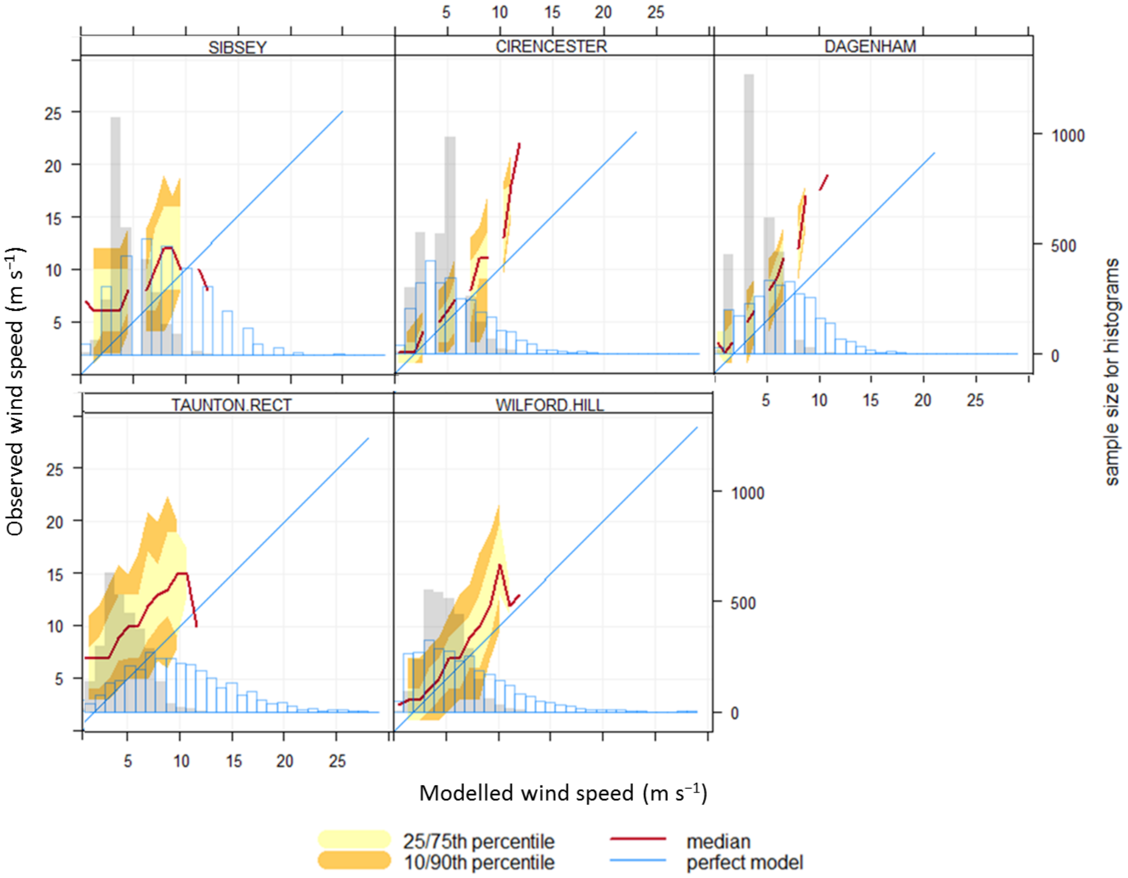

Figure 3.7. Conditional quantile plot of wind speed performance, from May to August 2015, at five Met-office sites in the UK. The blue diagonal line shows the results for a perfect model (1:1) while the red line and the yellow shading denotes the median and the modelled quantile intervals (25/75th and 10/90th), respectively. Grey bars show the distribution of model results while the blue bars the distribution of observations.

3.3.1.3 Wind direction

Fig. 3.8 shows five wind roses displaying the difference between modelled and observed wind direction. The plot is mostly aimed at presenting wind direction biases, however it also show the wind speed bias but only if there is a wind direction bias too. The comparison of modelled and observed wind direction shows that all sites are predominately positive bias (bias shown in polar coordinates) ranging between 3 and 23.7° North. The model does a better job simulating winds from south, southwest and southeast. The spread in the wind direction tends to be narrower across land sites, such as Cirencester, Dagenham and Wilford Hill, when compared to those sites that are closer to the coast, e.g., Sibsey. Fig. 3.8 also shows that the bias in the wind speed depends on wind direction. Positive biases in wind speed tends to predominate during southerly, easterly and westerly winds at most of the stations, while negative biases in wind speed are mostly associated with northerly winds. Tesche et al. (2002) recommend benchmark with regard to MB for wind direction of ≤±10° for an air quality model to be considered acceptable. This highlights the relatively poor performance of the model with respect to wind direction.

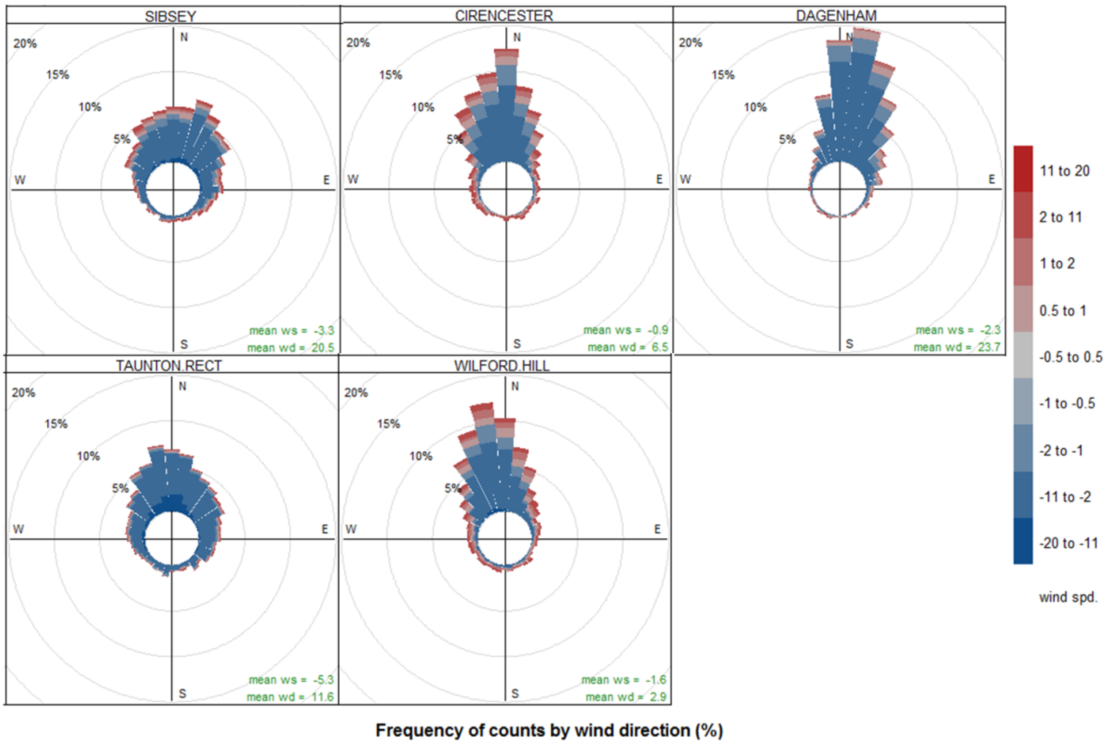

Figure 3.8. Bias between modelled and observed wind direction and speed, from May to August 2015, at five Met-office sites in the UK. Colours denote whether wind speed tend to be positively or negatively biased with respect to observations. Mean wind speed and direction bias are included as numerical values.

3.3.2 Evaluation of the chemistry, MOZART chemical mechanism

3.3.2.1 Nitrogen oxides

Modelled NO and NO_2 were compared with observations at sixteen EMEP sites across Europe (see Fig. 3.3 for information regarding the geographical location of the sites), with nine of the sites located in the UK. Table 3.4 summarizes the statistics of modelled and observed hourly NO and NO_2.

Table 3.4. Statistics of hourly NO and NO_2 calculated for May to September. MB, MGE and RMSE are given in ppbv.

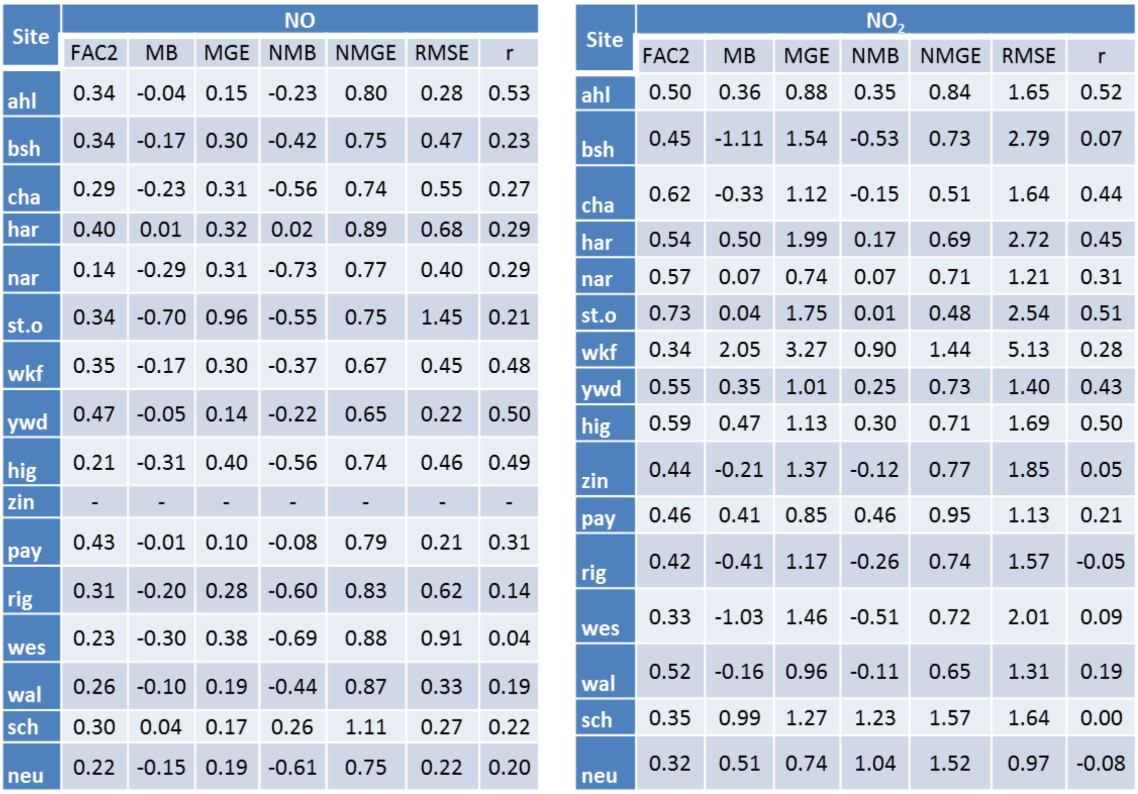

Site	NO						
	FAC2	MB	MGE	NMB	NMGE	RMSE	r
ahl	0.34	-0.04	0.15	-0.23	0.80	0.28	0.53
bsh	0.34	-0.17	0.30	-0.42	0.75	0.47	0.23
cha	0.29	-0.23	0.31	-0.56	0.74	0.55	0.27
har	0.40	0.01	0.32	0.02	0.89	0.68	0.29
nar	0.14	-0.29	0.31	-0.73	0.77	0.40	0.29
st.o	0.34	-0.70	0.96	-0.55	0.75	1.45	0.21
wkf	0.35	-0.17	0.30	-0.37	0.67	0.45	0.48
ywd	0.47	-0.05	0.14	-0.22	0.65	0.22	0.50
hig	0.21	-0.31	0.40	-0.56	0.74	0.46	0.49
zin	-	-	-	-	-	-	-
pay	0.43	-0.01	0.10	-0.08	0.79	0.21	0.31
rig	0.31	-0.20	0.28	-0.60	0.83	0.62	0.14
wes	0.23	-0.30	0.38	-0.69	0.88	0.91	0.04
wal	0.26	-0.10	0.19	-0.44	0.87	0.33	0.19
sch	0.30	0.04	0.17	0.26	1.11	0.27	0.22
neu	0.22	-0.15	0.19	-0.61	0.75	0.22	0.20

Site	NO_2						
	FAC2	MB	MGE	NMB	NMGE	RMSE	r
ahl	0.50	0.36	0.88	0.35	0.84	1.65	0.52
bsh	0.45	-1.11	1.54	-0.53	0.73	2.79	0.07
cha	0.62	-0.33	1.12	-0.15	0.51	1.64	0.44
har	0.54	0.50	1.99	0.17	0.69	2.72	0.45
nar	0.57	0.07	0.74	0.07	0.71	1.21	0.31
st.o	0.73	0.04	1.75	0.01	0.48	2.54	0.51
wkf	0.34	2.05	3.27	0.90	1.44	5.13	0.28
ywd	0.55	0.35	1.01	0.25	0.73	1.40	0.43
hig	0.59	0.47	1.13	0.30	0.71	1.69	0.50
zin	0.44	-0.21	1.37	-0.12	0.77	1.85	0.05
pay	0.46	0.41	0.85	0.46	0.95	1.13	0.21
rig	0.42	-0.41	1.17	-0.26	0.74	1.57	-0.05
wes	0.33	-1.03	1.46	-0.51	0.72	2.01	0.09
wal	0.52	-0.16	0.96	-0.11	0.65	1.31	0.19
sch	0.35	0.99	1.27	1.23	1.57	1.64	0.00
neu	0.32	0.51	0.74	1.04	1.52	0.97	-0.08

The predicted temporal correlation coefficient for NO and NO_2 is fairly low in the majority of the analysed sites, with values ranging between 0.1 and 0.5. These values are much smaller than those obtained for O_3 (up to 0.9), which is an interesting feature exhibited also in other regional studies in Europe using WRF-Chem with MOZART as a chemical mechanism. Fig. 3.9 shows simulated and observed hourly concentrations of NO and NO_2 at some selected sites in the UK.

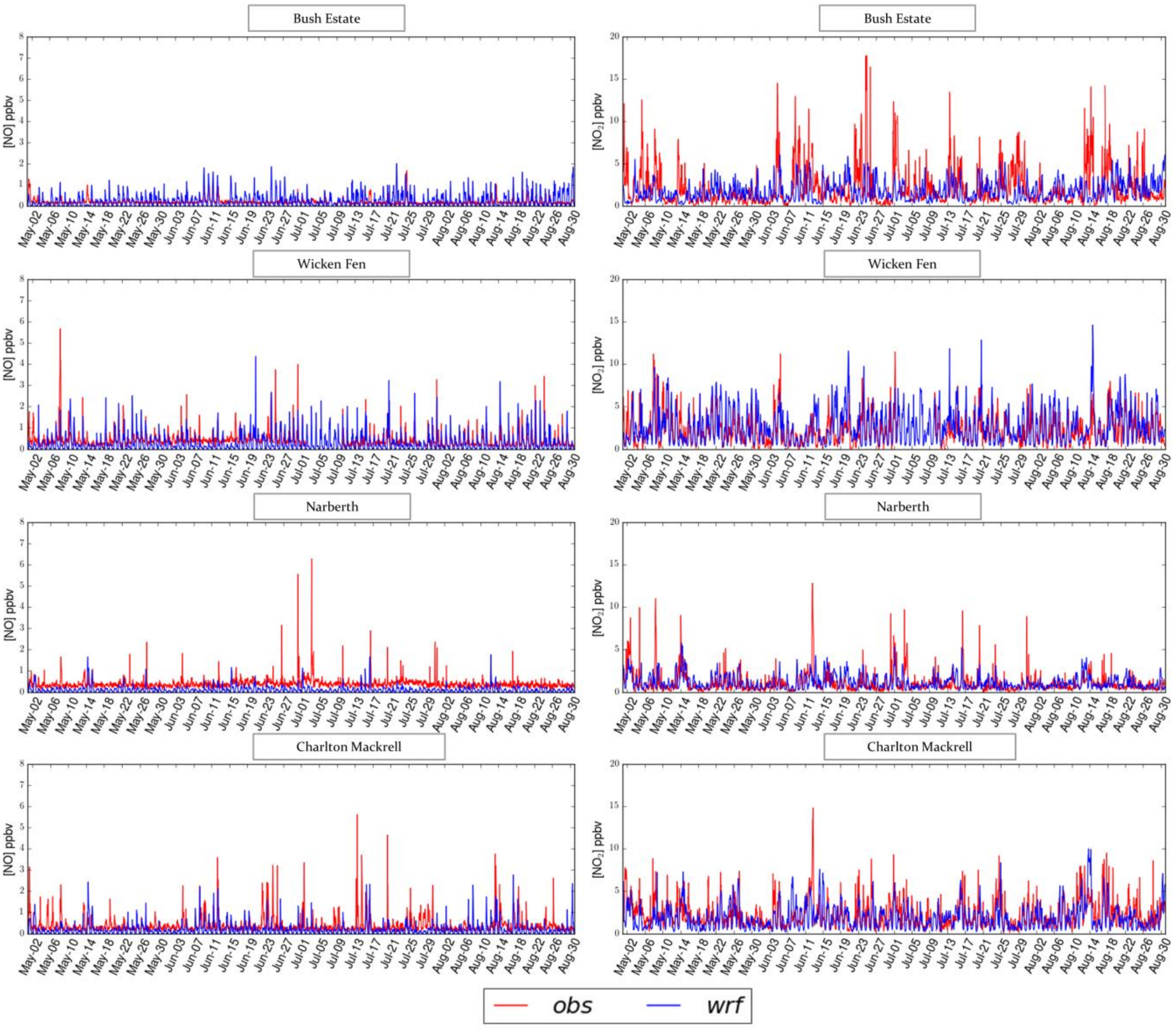

Figure 3.9. Modelled and observed hourly concentrations of NO and NO_2 from May to August 2015 at selected sites over the UK.

Considering both Table 3.4 and Fig. 3.9, it can be seen that the model simulation tends to underestimate NO concentrations in most of the analysed sites with MB of up to -3 ppbv. In particular, observed night-time concentrations for NO typically remain above zero, whereas modelled concentrations at night reach zero most of the times. By contrast, NO_2 concentrations are generally overestimated with MB of up to 8 ppbv, and no specific patterns are distinguished in the distribution of the bias. This is consistent with the negative NO biases and positive NO_2 biases obtained across Europe and reported in Mar et al. (2016), negative NO biases were attributed, among other reasons, to deficiencies of the model to represent NO_x chemical cycles and to errors in reported low NO observations due to artefacts introduced when recording NO concentrations approaching the minimum detection limit. Further comparison of the diurnal cycles for NO at selected stations in the UK, Fig. 3.10, shows that the model underestimates nocturnal NO concentrations and has difficulties capturing the timing of the NO peaks. NO_2 diurnal cycles, on the other hand, are well captured.

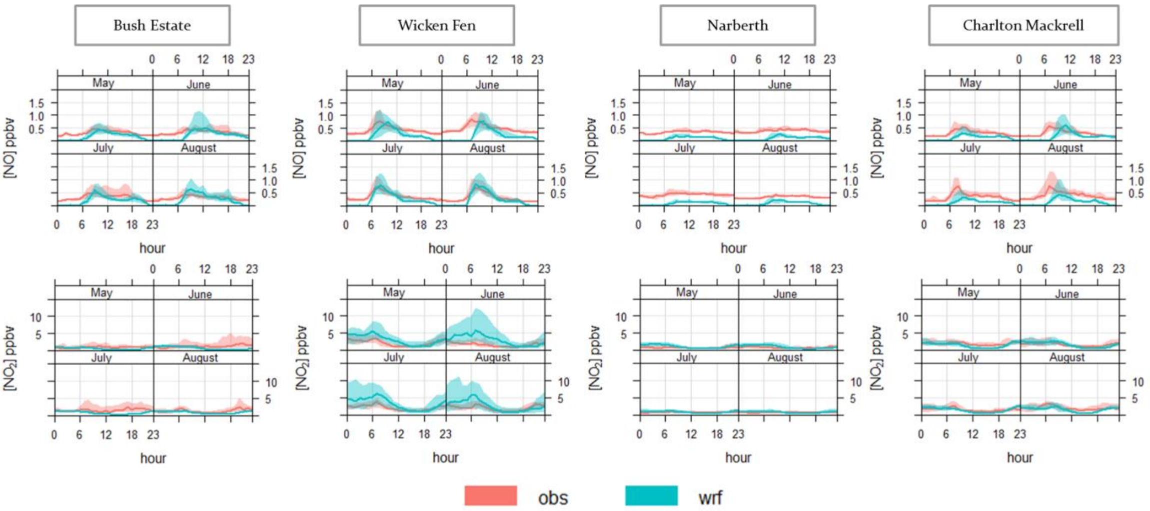

Figure 3.10. Mean diurnal variation in modelled and observed NO and NO_2 mixing ratios at selected sites in UK. The shaded areas represent the variability between the different days, showing the 25th and 75th percentiles.

Derwent et al. (2010) recommend benchmarks based on FAC2 and NMB statistics states. Air quality models are considered acceptable for policy applications if NMB values lie within ±0.2 and more than half of the model predictions lie within 0.5 and 2 times the observations. The predicted values of NMB for NO range between -0.7 and +0.2, while the NMB for NO_2 ranges between -0.5 and +1.2. In contrast, the average FAC2 is 0.3 for NO 0.5 for NO_2, suggesting that the model displays a more acceptable level of performance in terms of FAC2 for the NO_2 concentrations.

3.3.2.2 Ozone

Fig. 3.11 shows simulated and observed hourly concentrations of O_3 at twelve selected sites in the UK and the Republic of Ireland. A summary of the statistics by site is shown in Table 3.5. In general, the temporal variation in hourly O_3 concentrations at most sites are well represented by the model, except for large under-predictions during 1–3 July and 22-24 August, particularly at stations located in the east of UK, e.g. Weybourne, High Muffles, Sibton and Wicken Fen. Note that the observed maximum hourly O_3 at the four sites are much higher than those in the western and northern UK, e.g., Bush State, Strathvaich, Charlton Mackrell and Narberth. This may indicate inflow of O_3 and precursors (NO_x and VOCs) from nearby large metropolitan areas within the UK (e.g., London) or to longer-range transport from continental Europe.

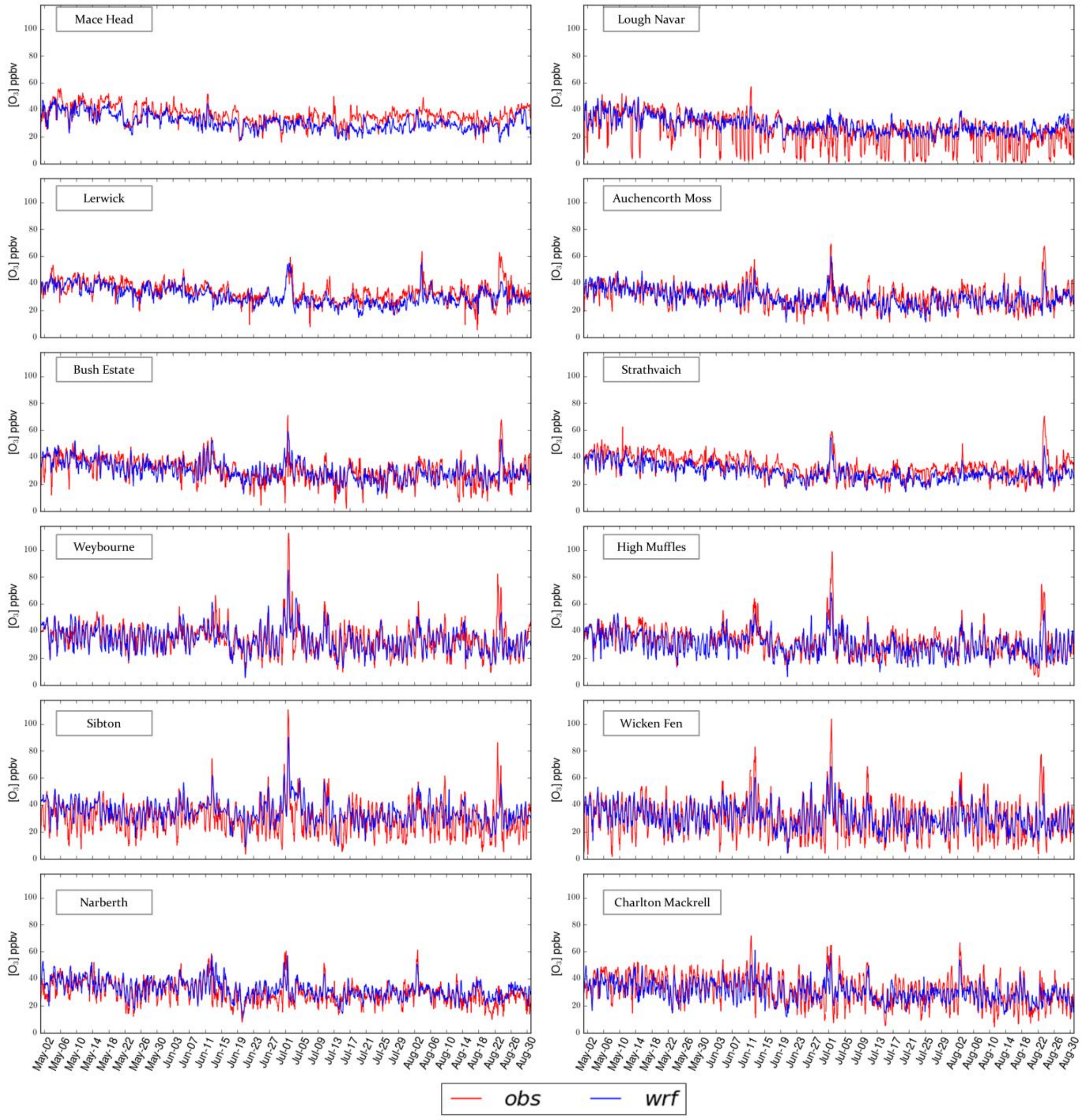

Figure 3.11. Modelled and observed hourly concentrations of O_3 from May to August 2015 at selected sites over the UK.

Ordóñez et al. (2017) reported that exceedances of the 90th percentile of the O_3 distribution in the southeast of UK and northern Europe (between 0–30º E above 50º N) during summertime correlate with days with long-lived high pressure systems stablished over northern Europe. This is due to the associated weather being efficient at increasing O_3 concentrations, e.g. decrease in cloud cover and consequent increase in the downward shortwave radiation influx and daily maximum temperatures. UK is also exposed to air masses from continental Europe under such weather (Jenkin et al., 2002; Jenkin, 2003; Pope et al., 2016). Moreover, the position of the blocking anticyclone with respect to the UK is thought to impede the arrival of westerly winds inhibiting the transport of cleaner air from the Atlantic (Ordóñez et al., 2017). This indicates a very important role of long-range transport during high O_3 episodes in southeast of UK. The observed hourly O_3 concentrations shown in Fig. 3.11 reached up to 100 ppbv on the 1st July at Weybourne, Wicken Fen and Sibton, which is well above the hourly O_3 standard of 60 ppbv for European countries.

Table 3.5. Statistics of hourly O_3 calculated for May to September. MB, MGE and RMSE are given in ppbv.

Site	FAC2	MB	MGE	NMB	NMGE	RMSE	r
ahl	0.99	-2.58	4.99	-0.08	0.15	6.58	0.66
bsh	0.95	0.30	6.39	0.01	0.21	8.56	0.42
cha	0.96	-1.64	6.36	-0.05	0.20	8.04	0.66
har	0.97	-1.08	5.66	-0.04	0.19	7.42	0.70
ler	1.00	-3.02	4.59	-0.09	0.14	5.90	0.72
lnv	0.85	3.78	6.60	0.15	0.26	9.19	0.65
lul	0.95	2.90	6.69	0.09	0.22	8.85	0.63
mac	1.00	-4.68	5.70	-0.13	0.16	6.92	0.66
nar	0.99	2.51	4.78	0.08	0.16	6.37	0.68
sib	0.95	3.51	6.68	0.12	0.22	8.91	0.71
st.o	0.93	3.87	6.66	0.13	0.23	9.14	0.65
sta	1.00	-4.02	5.36	-0.12	0.16	6.59	0.75
wao	0.99	-1.00	5.21	-0.03	0.15	7.29	0.73
wkf	0.93	0.40	6.88	0.01	0.23	9.31	0.70
ywd	0.97	-1.11	6.20	-0.03	0.19	7.77	0.66
ams	0.99	-0.70	4.42	-0.02	0.15	5.93	0.67
hi	0.99	-1.21	5.02	-0.04	0.16	6.78	0.75
zin	0.99	0.24	5.88	0.01	0.16	7.75	0.58
pay	0.91	-0.66	10.43	-0.02	0.26	13.08	0.59
rig	0.97	-9.28	11.38	-0.18	0.23	14.21	0.61

Site	FAC2	MB	MGE	NMB	NMGE	RMSE	r
wes	0.99	-1.03	5.45	-0.03	0.14	7.38	0.59
wal	0.90	0.09	9.02	0.00	0.26	11.82	0.64
scha	0.92	-15.33	16.05	-0.29	0.30	19.60	0.62
neu	0.87	0.64	9.26	0.02	0.27	12.11	0.59
sch	0.95	-10.12	11.62	-0.21	0.24	15.22	0.67
ulb	0.98	-3.06	5.99	-0.08	0.16	8.24	0.48
kel	0.99	2.78	5.76	0.08	0.17	7.61	0.61
cha	0.96	-12.51	13.36	-0.25	0.26	16.31	0.57
tan	0.92	-0.62	10.61	-0.02	0.27	13.21	0.61
jun	1.00	2.98	6.91	0.07	0.16	8.58	0.45
hei	0.89	-1.67	11.07	-0.04	0.27	14.16	0.60
hau	0.96	-8.25	11.44	-0.18	0.24	14.34	0.57
mas	0.97	-9.11	11.62	-0.18	0.23	14.25	0.49
ger	0.96	-12.71	13.51	-0.23	0.24	16.07	0.49
son	0.95	-14.94	15.04	-0.26	0.26	17.50	0.41
sul	0.95	-12.76	14.09	-0.24	0.27	17.20	0.55
pil	0.96	-5.05	9.30	-0.12	0.22	11.93	0.68
ill	0.97	-4.04	10.15	-0.10	0.24	12.81	0.63
vor	0.93	5.21	9.45	0.13	0.24	11.93	0.55

The mean concentration of observed O_3 is also well captured by the model, see Fig. 3.12a, with low mean concentrations over the UK (~ 25- 30 ppbv) and higher values over the mountainous region of the Alps (values greater than 45 ppbv). Values of r above 0.5 are obtained in most sites particularly over the UK, see Fig. 3.12b, while low values (r values about 0.4) are concentrated on high altitude sites in the mountainous regions of the Alps, see Fig. 3.12b, which might indicate difficulties in the representation of O_3 concentrations at different vertical levels. The results in term of correlation values are consistent with hourly r values of summer O_3 (June, July and August) > 0.40 reported on the WRF-Chem model evaluation over a European domain on Mar et al. (2016) using MOZART as a chemical mechanism.

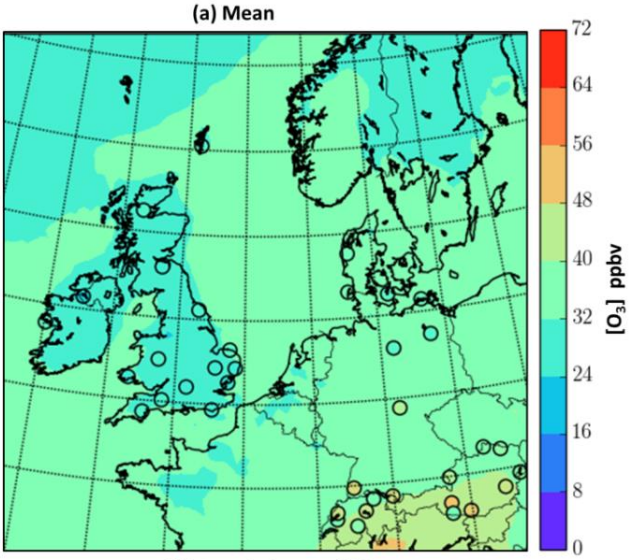
(a) Mean

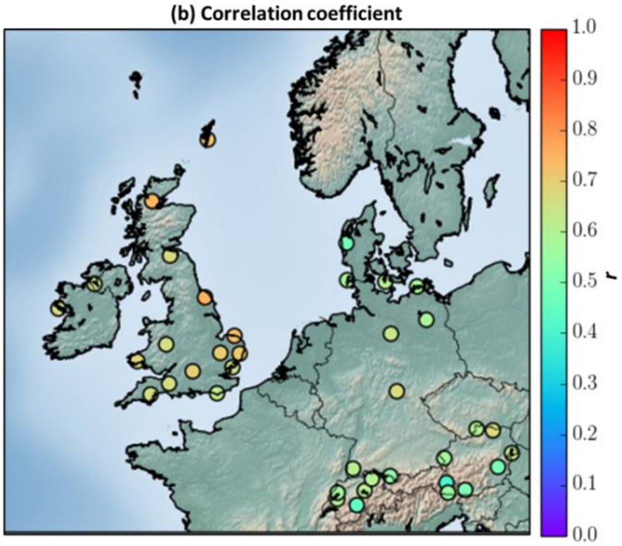
(b) Correlation coefficient

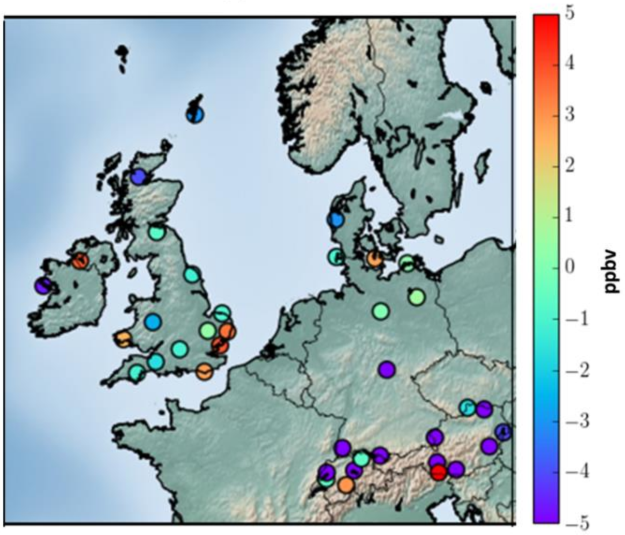
(c) MB

Figure 3.12. Modelled (coloured fields) and observed (coloured circles) mean O_3 concentrations in ppbv (a) from May to August, temporal correlation coefficient r (b) calculated from hourly measurements at each site and mean bias MB (b).

Nonetheless, the model tends to underestimate concentrations in most of the sites, with model negative biases of up to -15 ppbv and positive MB of up to and + 5 ppbv. Negative bias are mostly restricted to sites in the North, and West of the UK and the throughout the Alps, see Fig 3.12c. Mace Head, for instance, exhibits a negative MB of -4.6 ppbv. Due to its geographical location on the western fringe of the UK, this site is strongly influenced by the model boundary conditions. Hence, the underestimations are most likely caused by biases in the representation of background O_3 in the model used for boundary conditions (MOZART-4). Fig. 3.13 further shows that underestimations of O_3 in Mace Head are greatest during July and August. In contrast, underestimations of O_3 in sites such as Charlton Mackrell, Strathvaich, Weybourne, Auchencorth Moss and High Muffles, arise from the model having difficulties in capturing the diurnal changes in O_3, and in particular day time concentrations during the summer months (see Fig. 3.13).

On the other hand, positive biases are mostly observed in the east and southeast UK and north of Germany, with a few exceptions, see Fig 3.12c. Overestimated O_3 concentrations at Lough Navar, Bush Estate, Narberth, Sibton and Wicken Fen, for instance, are due to the model struggling to reproduce the diurnal changes in O_3, giving high O_3 concentrations during night-time, see Fig. 3.13. This is consistent with insufficient titration of O_3 at night due to the underestimated NO discussed in the previous section.

An additional source of model bias may be also caused by the limitation of comparing grid cell averages with point observations and by the choice of the grid cell representing each site, e.g. Lough Navar. While rural sites in the UK generally exhibit a mid-afternoon peak in O_3 concentrations and night-time minimum, coastal sites experienced much smaller diurnal changes in the O_3 concentrations, in particular reduced night-time depletion of O_3, due to the interaction with the marine environment (Coyle et al., 2002). The thickness of marine PBL is nearly constant through the day because of the little changes in temperature between day and night happens over the ocean. In addition, dry deposition of O_3 is lower over water surfaces than on land (Monks et al. 2015). Lough Navar is located at near the edge of a semi-mature forest about 6 km from Lough Ern the second-biggest lake system in Northern Ireland. Since sea/lake breezes can maintain mixing and advection of O_3-rich air to the land (Blaylock et al., 2016), it is likely that the obtained diurnal concentration of modelled O_3 at Lough Navar is highly influenced by the nearby lake.

The domain average obtained FAC2 is 0.9 while the domain NMB ranges between – 0.3 and +0.2. Based on the Derwent et al. (2010) recommend benchmark, it can be concluded that the model does a good job simulating the concentrations of O_3 in the European domain.

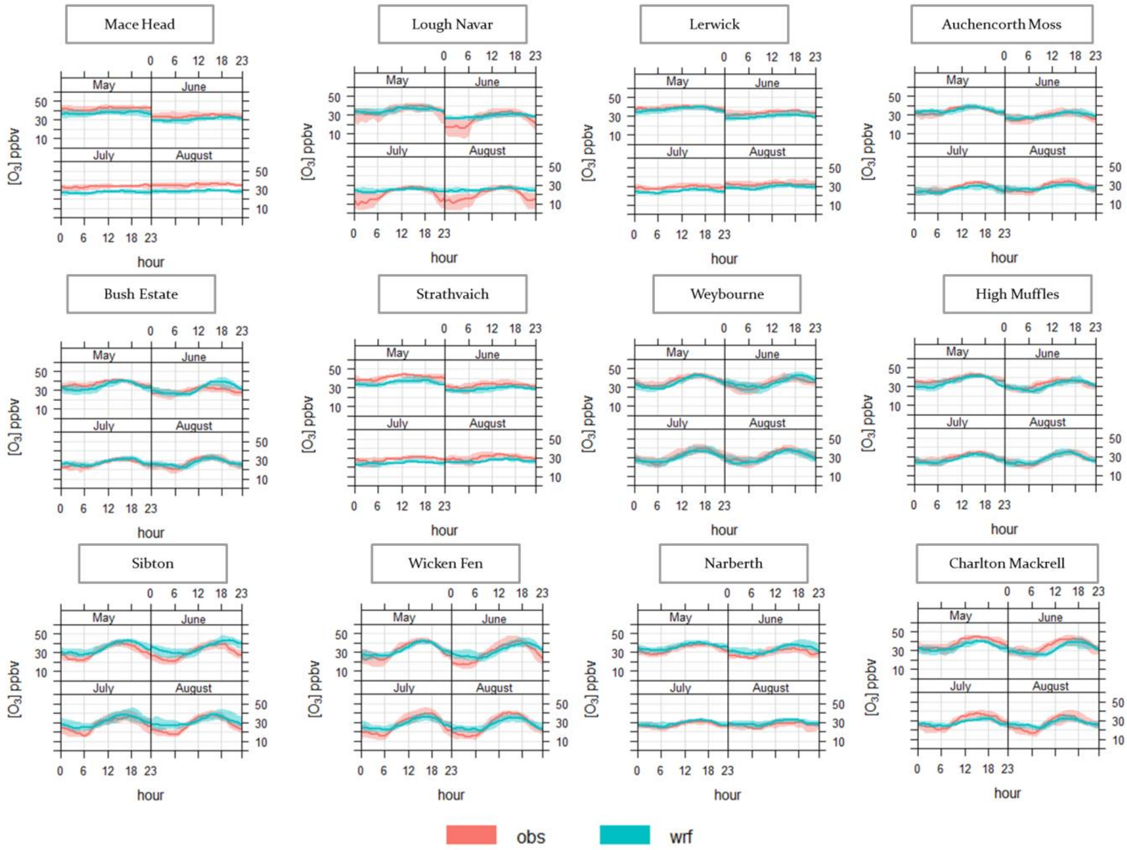

Figure 3.13. Diurnal variation in modelled and observed O_3 mixing ratios at selected sites in UK and the Republic of Ireland. The shaded areas represent the variability between the different days, showing the 25th and 75th percentiles.

3.3.2.3 Evaluation of high ozone metrics

In this section, the capability of the model to predict O_3 metrics of policy relevance such as the number of days with a MDA8 O_3 above 100 and 120 µg m^{-3} (~50 and 60 ppbv) and the AOT40 (accumulated O_3 over a threshold of 80 µg m^{-3}, ~40 ppbv) is assessed. The first two metrics are a health-related standard and tend to be influenced by summertime regional photochemical episodes, while the AOT40 relates to the protection of vegetation and has a threshold closer to the tropospheric O_3 level (Monks et al., 2015). The MDA8 days were calculated by extracting the days in which the maximum hourly running mean exceeded 50 and 60 ppbv. Similarly, the AOT40 was calculated by extracting daylight hourly values (between 8:00 to 20:00 CET) with O_3 concentrations above 80 µg m^{-3} (~40 ppbv) during the growing season considered from May to July, 80 µg m^{-3} was then subtracted from each hourly value and the resultant value was summed. Fig. 3.14 shows the number of days with the MDA8 O_3 above 50 ppbv at 15 EMEP monitoring sites from May to August over the UK and the Republic of Ireland.

The UK's Air quality strategy states that the MDA8 O_3 should not exceed the threshold value of 50 ppbv more than ten times a year. Fig. 3.14 shows that most of the observed concentrations at the stations had less than ten days above 50 ppbv apart from those located in the East Anglia region, southwest and southeast England. The largest MDA8 O_3 is seen at Wicken Fen, Yarner Wood, Weybourne, Sibton and Lullington Heath with 17, 15, 14, 12 and 12 days with MDA8 O_3 values above 50 ppbv respectively. Fig. 3.14 further shows that the model does a fair job capturing the spatial distribution of the MDA8 O_3 above 50 ppbv with the largest number of days of concentrated in the East Anglia region and Southeast England. Nonetheless, the model tends to underestimate the number of days with MDA8 O_3 above 50 ppbv, in particular over the East Anglia region, which is in line with earlier studies stressing the poor performance of many air quality models in simulating peak O_3 concentrations in the UK (e.g. Francis et al., 2011; Archer-Nicholls et al., 2014).

(a) MDA8 obs

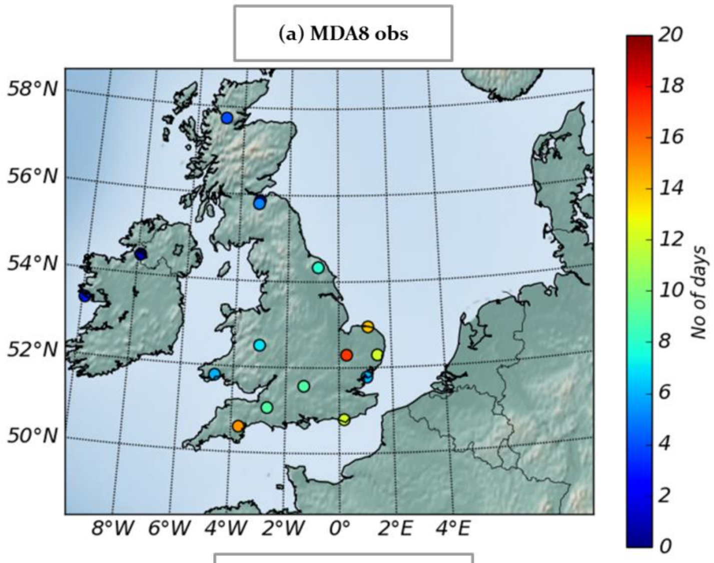

(b) MDA8 model

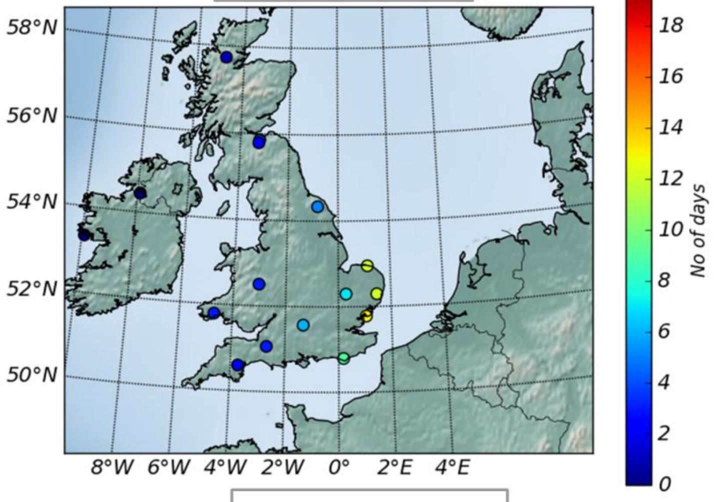

(c) MDA8 obs-model

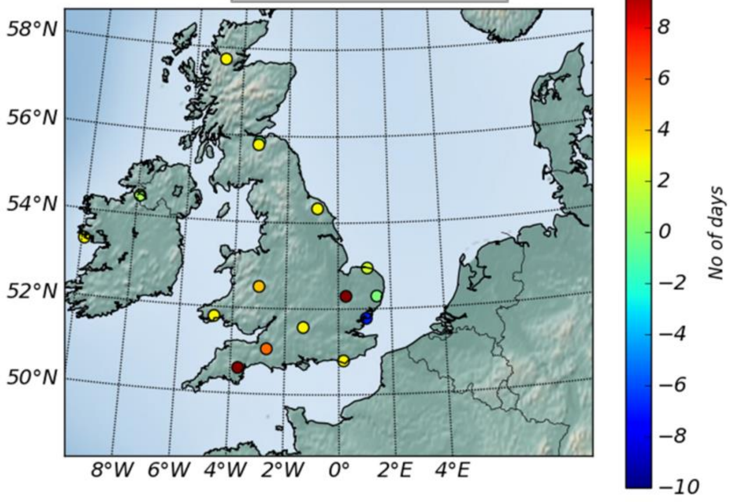

Figure 3.14. Spatial distribution of (a) observed and (b) modelled number of days with a daily MDA8 O_3 above 50 ppbv at EMEP monitoring sites calculated from May to September. The difference between observed and modelled MDA8 (observations – model) is also shown in (c). Please note the different scale used on (c).

The spatial distribution of the number of days with MDA8 O_3 above 60 ppbv is shown in Fig. 3.15. The European Union's Air Quality Directive long term objective states that the MDA8 O_3 should not exceed the threshold value of 60 ppbv within a calendar year. The observed values in Fig. 3.15 show that most of the sites have less than five days above 60 ppbv, except for some sites in the East of UK (East Anglia and the East Midlands). Similar to the MDA8 O_3 above 50 ppbv metric, the model tends to underestimate the number of days with MDA8 O_3 above 60 ppbv in particular in the East Anglia Region. This is consistent with what has been reported for coarse simulations over a European domain for summertime using MOZART chemistry within WRF-Chem (Mar et al., 2016). Some overestimations of the metric, never higher than 5 days, are observed in the northeast UK, see Fig. 3.15b.

The metric for vegetation exposure AOT40 is shown in Fig. 3.16. The UK's Air Quality Directive states a target value of 9000 ppb h (~18000 μg m^{-3} hours) averaged over five years. The highest observed values are seen in the east of England (with up to 6000 μg m^{-3} hours observed at Weybourne and Wicken Fen) and the southwest. The model captures most of the spatial distribution of the AOT40, with the largest values obtained for East Anglia. However, it tends to underestimate observations in the southeast (up to - 3000 μg m^{-3} hours), and overestimate them mostly in the southeast and Suffolk coast (e.g. St. Osyth up to 3000 μg m^{-3} hours).

(a) MDA8 obs

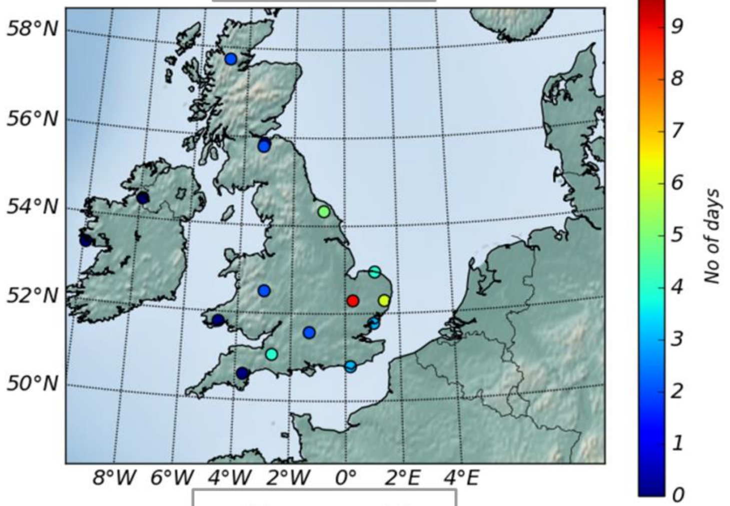

(b) MDA8 model

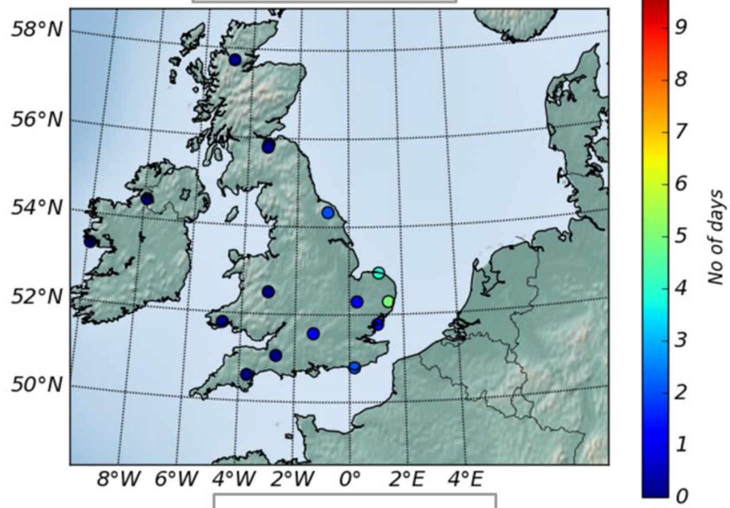

(c) MDA8 obs-model

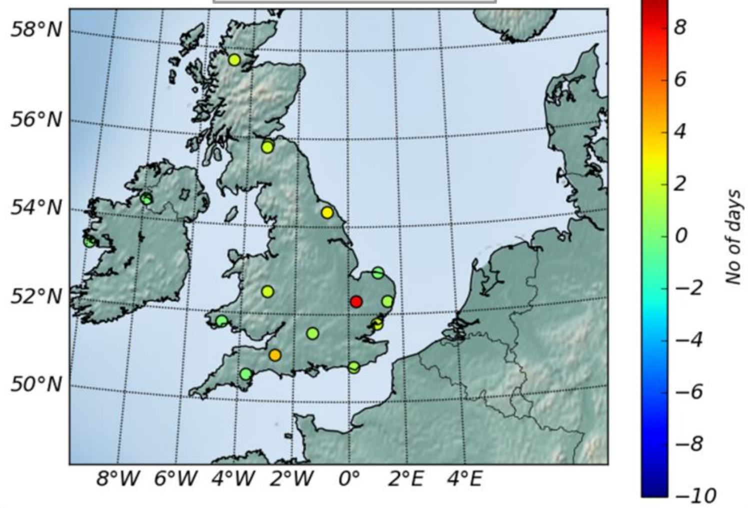

Figure 3.15. Spatial distribution of (a) observed and (b) modelled number of days with a daily MDA8 O_3 above 60 ppbv at EMEP monitoring sites calculated from May to September. The difference between observed and modelled MDA8 (observations – model) is also shown in (c).

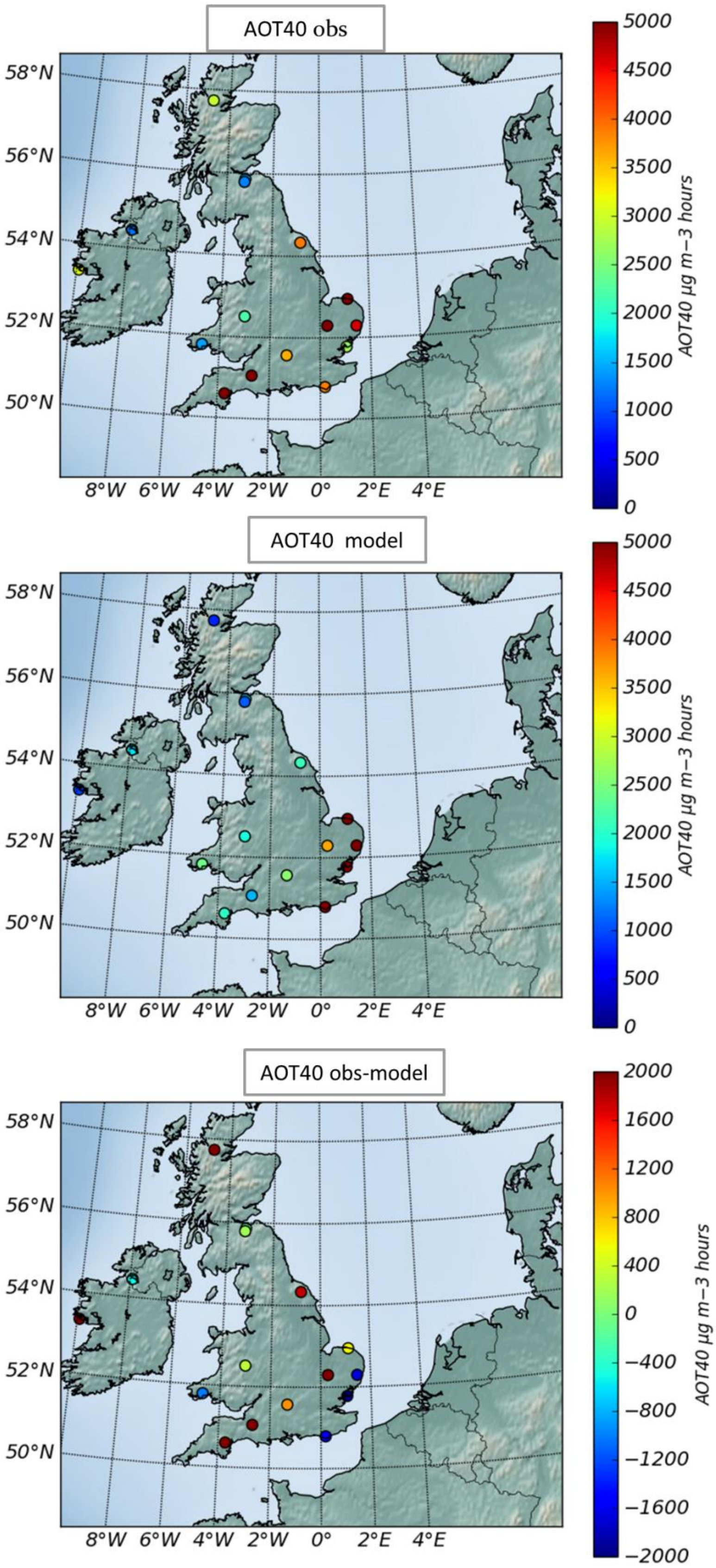

Figure 3.16. Spatial distribution of (a) observed and (b) modelled AOT40 calculated from May to September. The difference between observed and modelled AOT40 (observations – model) is also shown in (c). Please note the different scale used on (c).

3.4 Sensitivity to chemical mechanism: MOZART vs. CRImech

In this section, measurements from the ICOZA field campaign and EMEP sites are used to explore the sensitivity of O_3 and selected species to the choice of chemical mechanism: MOZART and CRImech. The comparison is performed for the period between 29th June and 31st July 2015. First, the differences in the representation of hourly NO, NO_2 and O_3 mixing ratios between the two mechanisms and the ability of the models to represent the MDA8 O_3 metric are discussed. Predicted NOy and VOC species are then compared with a range of observations described in Crilley et al. (2018).

3.4.1 Differences in mean NO and NO_2 concentrations

Table 3.6 and 3.7 summarize the statistics of hourly NO and NO_2 at several EMEP stations across Europe.

Modelled NO show a very similar behaviour when either MOZART or CRImech chemical mechanism are used. However, less than half of the predicted values at the majority of the assessed sites lie within a factor of 2 of the observations, with an average FAC2 of 0.4 for MOZART and 0.1 for CRImech. In addition, both mechanisms tend to underestimate NO concentrations in the majority of the sites, with concentrations slightly lower for CRImech than for MOZART with MB values ranging between -0.88 and +0.54, and -0.09 and 1.32 respectively. MOZART gives higher correlation coefficients across the domain ranging from approximately 0.1 to 0.6, with a few exceptions. Remarkably, in the UK, the largest difference in the NO concentration between the two models is observed for June 29-1 July, 10-11 July and 16-17, which are days of high O_3 concentrations, Fig. 3.17. In both cases, low errors (RMSE > 0.3 ppbv) with mainly positive mean bias (MB up to 0.3 ppbv) are obtained in high altitude sites such as Schauinsland, Neuglobsow and Waldhof in Germany, indicating that the model does a fair job representing the vertical distribution of NO. Conversely, the highest errors (RMSE > 1 ppbv) with mostly negative mean bias (MB up to -1 ppvb) are concentrated in areas exposed to greater anthropogenic NO_x emissions such as Harwell, UK; St. Osyth, UK; and Westerland, Germany. As stated in Mar et al. (2016), underestimation in the NO concentrations may be caused by uncertainties in the emission inventories.

Table 3.6. Summary of statistics of hourly NO for MOZART and CRImech from June 29th to July 31st. MB, MGE and RMSE are given in ppbv.

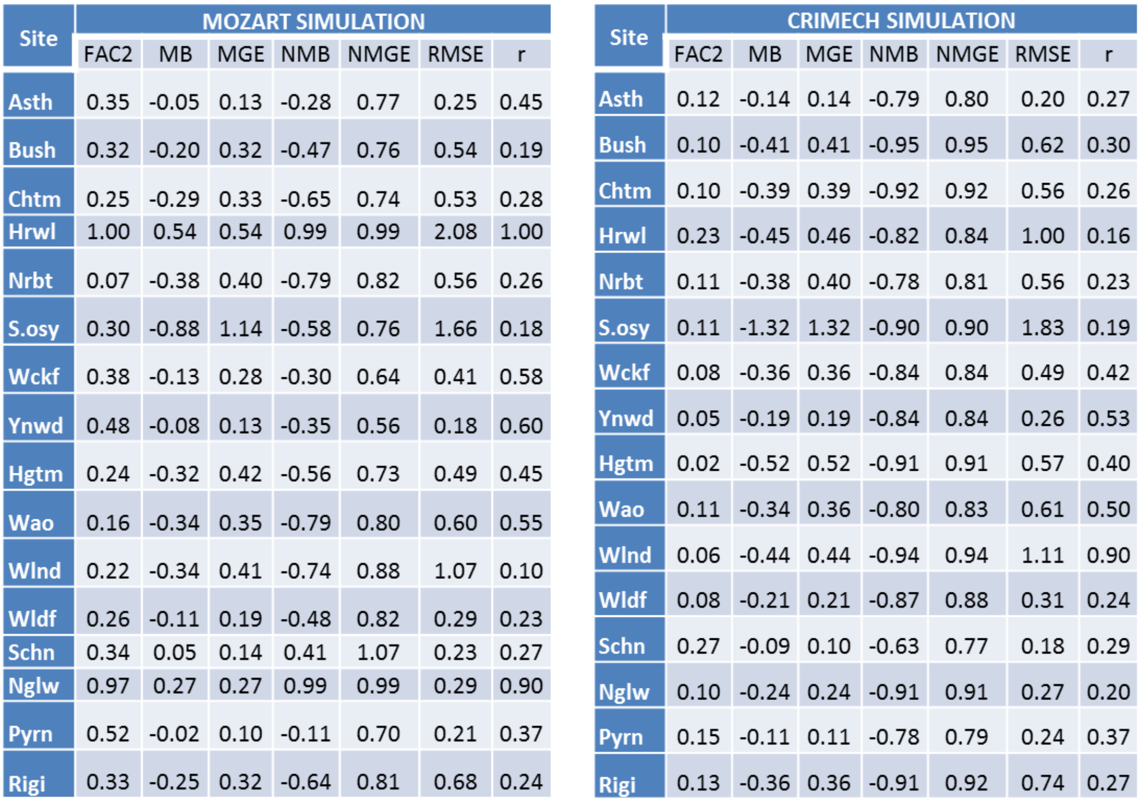

Site	MOZART SIMULATION						
	FAC2	MB	MGE	NMB	NMGE	RMSE	r
Asth	0.35	-0.05	0.13	-0.28	0.77	0.25	0.45
Bush	0.32	-0.20	0.32	-0.47	0.76	0.54	0.19
Chtm	0.25	-0.29	0.33	-0.65	0.74	0.53	0.28
Hrwl	1.00	0.54	0.54	0.99	0.99	2.08	1.00
Nrbt	0.07	-0.38	0.40	-0.79	0.82	0.56	0.26
S.osy	0.30	-0.88	1.14	-0.58	0.76	1.66	0.18
Wckf	0.38	-0.13	0.28	-0.30	0.64	0.41	0.58
Ynwd	0.48	-0.08	0.13	-0.35	0.56	0.18	0.60
Hgtm	0.24	-0.32	0.42	-0.56	0.73	0.49	0.45
Wao	0.16	-0.34	0.35	-0.79	0.80	0.60	0.55
Wlnd	0.22	-0.34	0.41	-0.74	0.88	1.07	0.10
Wldf	0.26	-0.11	0.19	-0.48	0.82	0.29	0.23
Schn	0.34	0.05	0.14	0.41	1.07	0.23	0.27
Nglw	0.97	0.27	0.27	0.99	0.99	0.29	0.90
Pyrn	0.52	-0.02	0.10	-0.11	0.70	0.21	0.37
Rigi	0.33	-0.25	0.32	-0.64	0.81	0.68	0.24

Site	CRIMECH SIMULATION						
	FAC2	MB	MGE	NMB	NMGE	RMSE	r
Asth	0.12	-0.14	0.14	-0.79	0.80	0.20	0.27
Bush	0.10	-0.41	0.41	-0.95	0.95	0.62	0.30
Chtm	0.10	-0.39	0.39	-0.92	0.92	0.56	0.26
Hrwl	0.23	-0.45	0.46	-0.82	0.84	1.00	0.16
Nrbt	0.11	-0.38	0.40	-0.78	0.81	0.56	0.23
S.osy	0.11	-1.32	1.32	-0.90	0.90	1.83	0.19
Wckf	0.08	-0.36	0.36	-0.84	0.84	0.49	0.42
Ynwd	0.05	-0.19	0.19	-0.84	0.84	0.26	0.53
Hgtm	0.02	-0.52	0.52	-0.91	0.91	0.57	0.40
Wao	0.11	-0.34	0.36	-0.80	0.83	0.61	0.50
Wlnd	0.06	-0.44	0.44	-0.94	0.94	1.11	0.90
Wldf	0.08	-0.21	0.21	-0.87	0.88	0.31	0.24
Schn	0.27	-0.09	0.10	-0.63	0.77	0.18	0.29
Nglw	0.10	-0.24	0.24	-0.91	0.91	0.27	0.20
Pyrn	0.15	-0.11	0.11	-0.78	0.79	0.24	0.37
Rigi	0.13	-0.36	0.36	-0.91	0.92	0.74	0.27

Table 3.7. Summary of statistics of hourly NO_2 for MOZART and CRImech from June 29th to July 31st. MB, MGE and RMSE are given in ppbv.

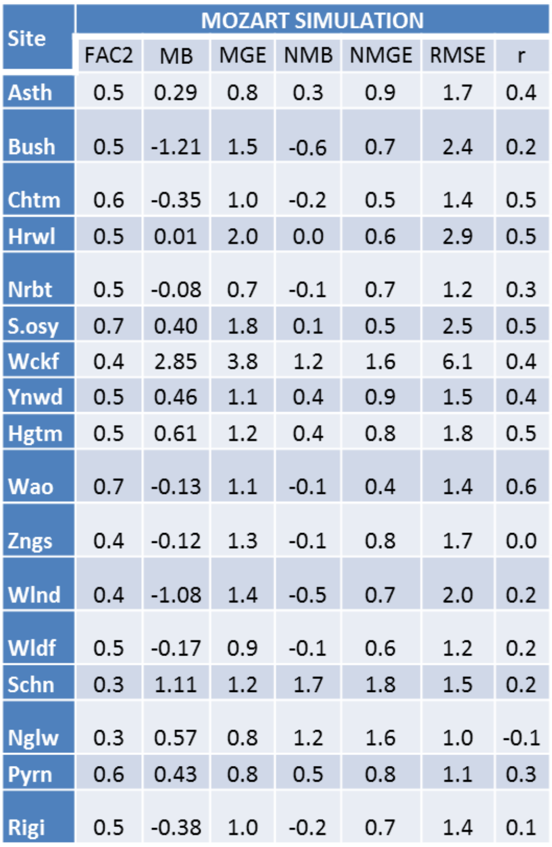

Site	MOZART SIMULATION						
	FAC2	MB	MGE	NMB	NMGE	RMSE	r
Asth	0.5	0.29	0.8	0.3	0.9	1.7	0.4
Bush	0.5	-1.21	1.5	-0.6	0.7	2.4	0.2
Chtm	0.6	-0.35	1.0	-0.2	0.5	1.4	0.5
Hrwl	0.5	0.01	2.0	0.0	0.6	2.9	0.5
Nrbt	0.5	-0.08	0.7	-0.1	0.7	1.2	0.3
S.osy	0.7	0.40	1.8	0.1	0.5	2.5	0.5
Wckf	0.4	2.85	3.8	1.2	1.6	6.1	0.4
Ynwd	0.5	0.46	1.1	0.4	0.9	1.5	0.4
Hgtm	0.5	0.61	1.2	0.4	0.8	1.8	0.5
Wao	0.7	-0.13	1.1	-0.1	0.4	1.4	0.6
Zngs	0.4	-0.12	1.3	-0.1	0.8	1.7	0.0
Wlnd	0.4	-1.08	1.4	-0.5	0.7	2.0	0.2
Wldf	0.5	-0.17	0.9	-0.1	0.6	1.2	0.2
Schn	0.3	1.11	1.2	1.7	1.8	1.5	0.2
Nglw	0.3	0.57	0.8	1.2	1.6	1.0	-0.1
Pyrn	0.6	0.43	0.8	0.5	0.8	1.1	0.3
Rigi	0.5	-0.38	1.0	-0.2	0.7	1.4	0.1

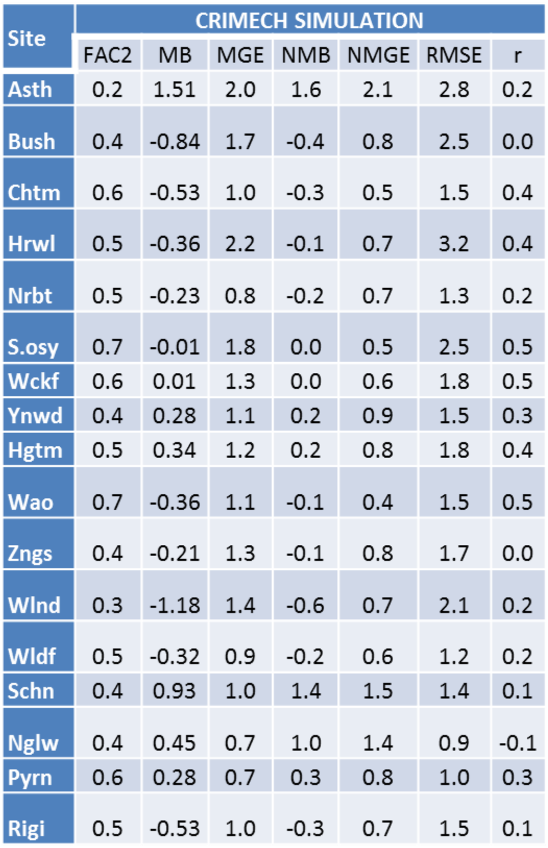

Site	CRIMECH SIMULATION						
	FAC2	MB	MGE	NMB	NMGE	RMSE	r
Asth	0.2	1.51	2.0	1.6	2.1	2.8	0.2
Bush	0.4	-0.84	1.7	-0.4	0.8	2.5	0.0
Chtm	0.6	-0.53	1.0	-0.3	0.5	1.5	0.4
Hrwl	0.5	-0.36	2.2	-0.1	0.7	3.2	0.4
Nrbt	0.5	-0.23	0.8	-0.2	0.7	1.3	0.2
S.osy	0.7	-0.01	1.8	0.0	0.5	2.5	0.5
Wckf	0.6	0.01	1.3	0.0	0.6	1.8	0.5
Ynwd	0.4	0.28	1.1	0.2	0.9	1.5	0.3
Hgtm	0.5	0.34	1.2	0.2	0.8	1.8	0.4
Wao	0.7	-0.36	1.1	-0.1	0.4	1.5	0.5
Zngs	0.4	-0.21	1.3	-0.1	0.8	1.7	0.0
Wlnd	0.3	-1.18	1.4	-0.6	0.7	2.1	0.2
Wldf	0.5	-0.32	0.9	-0.2	0.6	1.2	0.2
Schn	0.4	0.93	1.0	1.4	1.5	1.4	0.1
Nglw	0.4	0.45	0.7	1.0	1.4	0.9	-0.1
Pyrn	0.6	0.28	0.7	0.3	0.8	1.0	0.3
Rigi	0.5	-0.53	1.0	-0.3	0.7	1.5	0.1

NO_2 shows much better agreement with the observations in both cases, with more than half of the predicted values at most sites lying within a factor of two of the observations, FAC2 ~ 0.5. However, similar to NO, both mechanisms tend to poorly represent the hourly changes in NO_2 concentrations with CRImech showing slightly lower correlation coefficient values than MOZART at most of the assessed sites (average temporal correlation coefficients for CRImech 0.2 and for MOZART 0.3). There is no particular pattern distinguishable in the distribution of the mean bias, as both mechanisms tend to equally underestimate or overestimate NO_2 concentrations at the assessed sites, with CRImech showing a slightly better performance than MOZART in terms of mean bias and errors (MB ranging between -1.2 and 1.5 ppbv for CRImech, and -1.2 and 2.9 ppvb for MOZART). As for NO, the discrepancies between the two are more marked during days of high O_3 concentrations (e.g. between the 29th June and 2nd July) over some sites in the UK. For the rest of the month, the hourly concentrations of NO_2 are very well correlated in both cases.

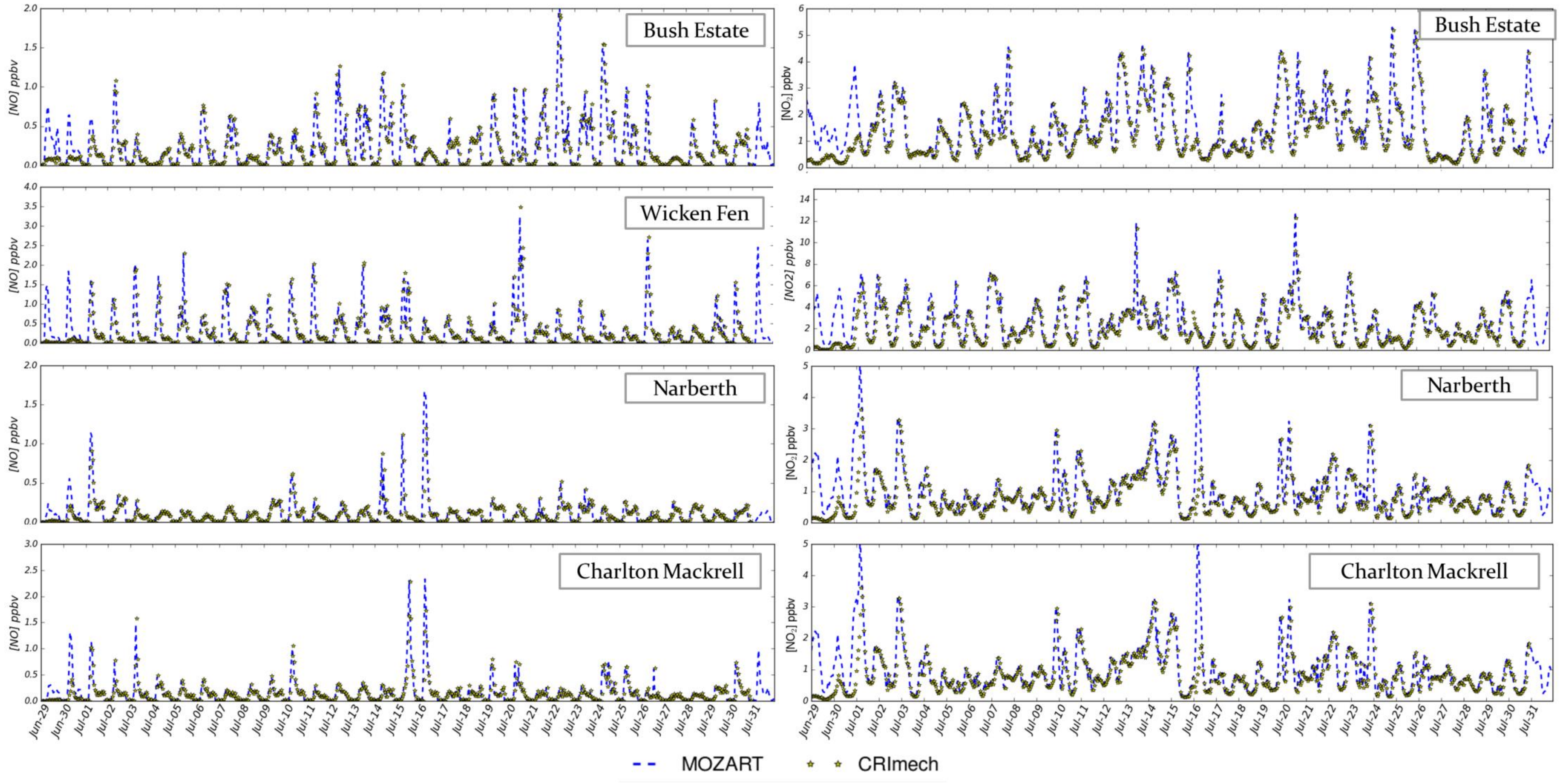

Figure 3.17. Modelled hourly concentrations of NO and NO_2 at selected sites over the UK from 29th June to 31st July 2015 for MOZART and CRImech.

3.4.2 Differences in O_3 concentrations

The statistics obtained for O_3 using MOZART and CRImech chemical mechanisms are shown in Table 3.8.

Table 3.8. Summary of statistics of hourly O_3 for MOZART and CRImech from June 29th to July 31st. MB, MGE and RMSE are given in ppbv.

Site	MOZART SIMULATION						
	FAC2	MB	MGE	NMB	NMGE	RMSE	r
Ahl	0.98	-2.42	4.89	-0.08	0.16	6.42	0.65
Bsh	0.96	2.29	5.19	0.09	0.20	7.21	0.51
Cht	0.95	-2.82	7.07	-0.02	0.21	7.77	0.69
Har	0.93	7.88	12.63	0.14	0.23	16.93	0.78
Nar	0.97	1.89	4.74	-0.02	0.20	7.47	0.76
st.o	0.93	-1.63	2.04	0.14	0.23	8.48	0.78
Wkf	0.91	-1.49	7.56	0.02	0.25	9.55	0.78
Ywd	0.93	0.96	5.65	0.10	0.21	7.71	0.64
Hig	1.00	-4.35	6.78	-0.06	0.17	7.29	0.79
Wao	0.99	-2.00	5.84	-0.06	0.17	8.58	0.78
Ams	0.99	-1.22	4.61	-0.04	0.17	6.09	0.66
Lul	0.93	2.86	6.63	0.10	0.22	9.04	0.73
mac	1.00	-5.06	6.23	-0.16	0.19	7.49	0.21
Sib	0.95	3.08	6.50	0.10	0.22	8.66	0.82
Ler	0.94	-2.35	7.50	-0.08	0.25	9.52	0.33
Lnv	0.81	4.68	6.94	0.23	0.34	9.31	0.37
Stra	1.00	-4.86	5.96	-0.12	0.18	6.11	0.59
Esk	0.94	0.21	4.66	0.08	0.21	7.23	0.66
Zng	0.99	-0.84	5.19	-0.02	0.14	6.75	0.79
Wes	0.99	-0.67	5.74	-0.02	0.15	7.63	0.70
Wal	0.92	0.21	9.12	0.01	0.26	11.99	0.71
Scha	0.91	-20.67	20.81	-0.34	0.35	24.24	0.75
Neu	0.88	2.15	8.74	0.07	0.27	11.31	0.65
Scha	0.97	-11.26	12.56	-0.23	0.25	16.21	0.77
zil	0.89	1.91	8.55	0.06	0.26	12.24	0.64
ca	0.91	0.64	7.90	0.02	0.26	10.69	0.77
Eib	0.81	4.94	9.97	0.17	0.34	12.37	0.83
vre	0.87	1.81	9.31	0.06	0.29	12.42	0.81
Kol	0.95	0.33	7.23	0.01	0.23	9.23	0.77
Don	0.99	-4.27	8.77	-0.10	0.20	11.67	0.73
Rev	0.97	-4.55	8.63	-0.12	0.23	12.07	0.78
Col	0.99	-4.17	7.02	-0.12	0.20	9.56	0.74
Tar	0.98	-1.05	6.77	-0.03	0.21	8.53	0.69
Mor	0.95	-7.75	12.06	-0.18	0.27	14.64	0.70
Pay	0.96	-5.23	11.04	-0.11	0.24	13.37	0.70
Rig	1.00	-14.21	14.64	-0.25	0.26	17.10	0.79
Ulb	0.99	-3.19	6.47	-0.09	0.18	8.34	0.52
Kel	1.00	3.37	5.85	0.10	0.17	7.61	0.72
Cha	0.97	-16.71	16.92	-0.30	0.30	19.36	0.72
Tän	0.97	-4.33	11.68	-0.10	0.26	14.03	0.67
Jun	1.00	1.74	7.60	0.04	0.17	9.33	0.20
Hei	0.91	-5.83	12.44	-0.13	0.28	15.58	0.56
Hau	0.97	-13.74	14.59	-0.26	0.27	16.73	0.64
Mas	0.98	-11.35	13.12	-0.22	0.25	15.43	0.54
Ger	0.95	-15.03	15.82	-0.26	0.27	18.46	0.48
Son	0.94	-17.24	17.32	-0.29	0.29	19.83	0.39
Sul	0.94	-17.79	18.21	-0.30	0.31	20.98	0.59
Pil	0.97	-7.55	10.19	-0.17	0.22	13.08	0.65
ill	0.97	-5.83	11.16	-0.13	0.25	13.74	0.65
Vor	0.97	3.89	9.52	0.10	0.23	11.82	0.58
Mfr	0.99	-10.04	10.88	-0.22	0.24	12.73	0.74
Pdm	0.99	-6.44	11.42	-0.13	0.23	14.19	0.19

Site	CRIMECH SIMULATION						
	FAC2	MB	MGE	NMB	NMGE	RMSE	r
Ahl	0.98	-4.12	5.71	-0.14	0.19	7.27	0.63
Bsh	0.98	-1.10	4.70	-0.04	0.18	6.17	0.64
Cht	0.93	-2.82	7.07	-0.10	0.24	8.94	0.61
Har	0.98	-2.17	6.06	-0.07	0.21	7.58	0.77
Nar	1.00	0.15	4.62	0.01	0.16	5.96	0.60
st.o	0.98	-1.63	2.04	-0.05	0.06	3.82	0.90
Wkf	0.91	-1.49	7.56	-0.05	0.26	9.74	0.76
Ywd	0.93	0.96	5.65	0.04	0.21	7.53	0.62
Hig	0.97	-4.35	6.78	-0.14	0.22	8.91	0.73
Wao	1.00	-3.31	6.26	-0.10	0.18	8.56	0.81
Ams	0.99	-1.22	4.68	-0.04	0.17	6.16	0.65
Lul	0.92	1.24	6.42	0.04	0.21	8.73	0.73
mac	1.00	-6.45	7.21	-0.20	0.22	8.52	0.17
Sib	0.96	1.81	6.17	0.06	0.21	8.06	0.83
Ler	1.00	-5.15	5.86	-0.17	0.20	6.97	0.69
Lnv	0.83	3.30	6.58	0.16	0.32	8.72	0.35
Stra	1.00	-4.86	5.96	-0.17	0.21	7.05	0.56
Esk	0.95	0.21	4.66	0.01	0.18	5.94	0.76
Zng	0.99	-2.30	5.79	-0.06	0.16	7.26	0.78
Wes	0.99	-2.06	6.29	-0.05	0.16	8.04	0.70
Wal	0.93	-1.32	9.30	-0.04	0.27	12.13	0.70
Scha	0.85	-22.86	22.92	-0.38	0.38	26.13	0.76
Neu	0.89	0.42	8.96	0.01	0.28	11.14	0.65
Scha	0.95	-13.05	13.97	-0.26	0.28	17.53	0.77
zil	0.89	1.11	8.38	0.03	0.25	11.91	0.66
ca	0.93	-0.35	6.93	-0.01	0.23	9.45	0.82
Eib	0.84	3.85	8.98	0.13	0.31	11.40	0.85
vre	0.90	0.87	8.40	0.03	0.26	11.53	0.84
Kol	0.95	0.33	7.23	0.01	0.23	9.23	0.77
Don	0.99	-6.06	8.98	-0.14	0.21	11.93	0.76
Rev	0.96	-5.74	8.99	-0.15	0.23	12.39	0.79
Col	0.99	-5.65	7.67	-0.16	0.22	10.17	0.75
Tar	0.98	-2.74	6.99	-0.08	0.21	8.91	0.69
Mor	0.96	-9.71	13.25	-0.22	0.30	15.58	0.71
Pay	0.96	-7.55	12.05	-0.17	0.26	14.47	0.70
Rig	0.99	-16.98	17.18	-0.30	0.30	19.51	0.80
Ulb	0.99	-4.67	7.34	-0.13	0.20	9.16	0.50
Kel	0.99	1.86	5.59	0.05	0.16	7.24	0.72
Cha	0.94	-18.97	19.04	-0.34	0.34	21.24	0.73
Tän	0.97	-6.69	12.47	-0.15	0.28	15.14	0.65
Jun	1.00	-1.46	7.33	-0.03	0.17	9.10	0.19
Hei	0.91	-7.66	13.67	-0.17	0.30	16.84	0.51
Hau	0.94	-15.76	16.38	-0.30	0.31	18.56	0.62
Mas	0.96	-13.92	15.17	-0.26	0.29	17.46	0.53
Ger	0.92	-17.61	17.97	-0.30	0.31	20.52	0.50
Son	0.90	-19.98	19.98	-0.34	0.34	22.26	0.39
Sul	0.88	-20.22	20.42	-0.35	0.35	23.00	0.60
Pil	0.96	-9.40	11.55	-0.21	0.25	14.37	0.63
ill	0.95	-7.82	12.21	-0.17	0.27	14.88	0.63
Vor	0.98	1.33	8.88	0.03	0.22	11.18	0.58
Mfr	0.98	-12.32	12.72	-0.27	0.28	14.47	0.77
Pdm	0.97	-8.61	12.65	-0.17	0.25	15.54	0.17

Modelled O_3 for both scenarios are in good agreement with measurements, as more than half of the predicted values at most sites lie within a factor of two of the observations. The average FAC2 for both model scenarios is ~0.9 and the domain average correlation coefficient (*r*) is ~0.7, with CRImech exhibiting slightly higher correlation values than MOZART. Although model performance varies from site to site, correlation coefficients are highest (*r* > 0.7) in the east and southeast UK and Western Europe while lower (<0.7 and >0.3) at sites in the West of UK (including Northern Ireland) and the mountainous regions of the Alps, see Fig. 3.18.

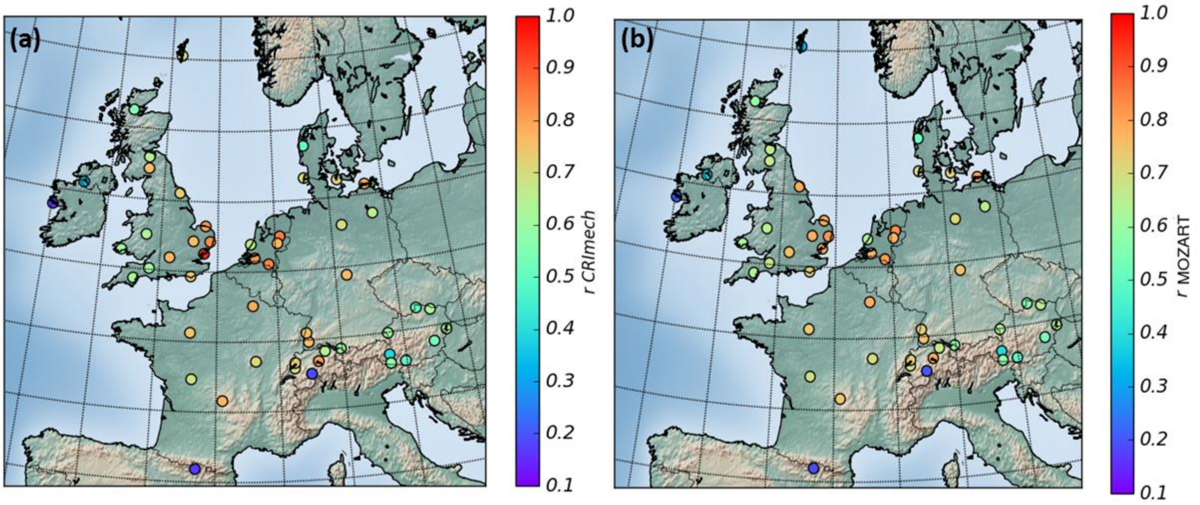

Figure 3.18. Spatial distribution of the correlation coefficients (r) calculated for both model scenarios: CRImech (a) and MOZART (b). Coefficients are calculated from hourly measurements at EMEP sites from 29th June to 31st July, the values are shown at the location of the stations.

Fig. 3.19 compares the spatial distributions of modelled average O_3 mixing ratios against observations for both scenarios. High O_3 mixing ratios are obtained over the Mediterranean region (mean O_3 above 45 ppbv), while concentrations below 30 ppbv are obtained in the Scandinavia, Ireland and most of the UK. In both scenarios, the simulated mean concentrations show a good agreement with the observations. Nonetheless, CRImech exhibits slightly lower mean concentrations for most of the UK, Western France and Ireland when compared with the mean O_3 concentrations in MOZART.

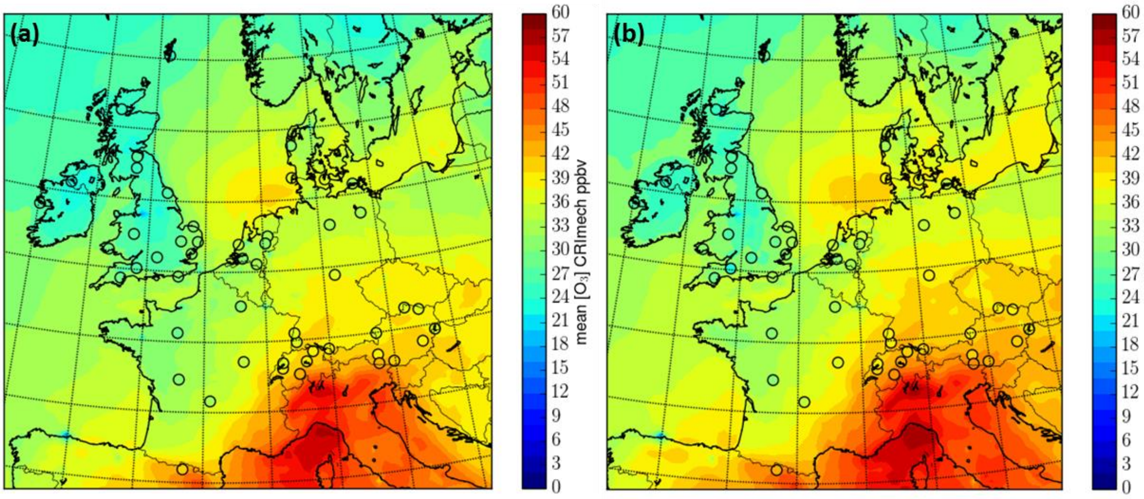

Figure 3.19. Spatial distribution of modelled (coloured fields) and observed (coloured circles) average O_3 concentrations in ppbv for both scenarios CRImech (a) and MOZART (b) at EMEP sites from 29th June to 31st July.

Modelled hourly O_3 mixing ratios are lower than the measurements throughout the domain with CRImech giving slightly larger negative bias (MB of up to -23 ppbv compare with -21 ppbv), see Fig. 3.20. For both scenarios, positive biases are generally obtained in the east and southeast UK, the Netherlands and north of Germany (with MB between 0 and 5 ppbv), while negative biases are concentrated mostly in France and mountainous regions of the Alps. This suggests that both mechanisms underestimate O_3 mixing ratios at different vertical levels since most of these sites are at different altitudes.

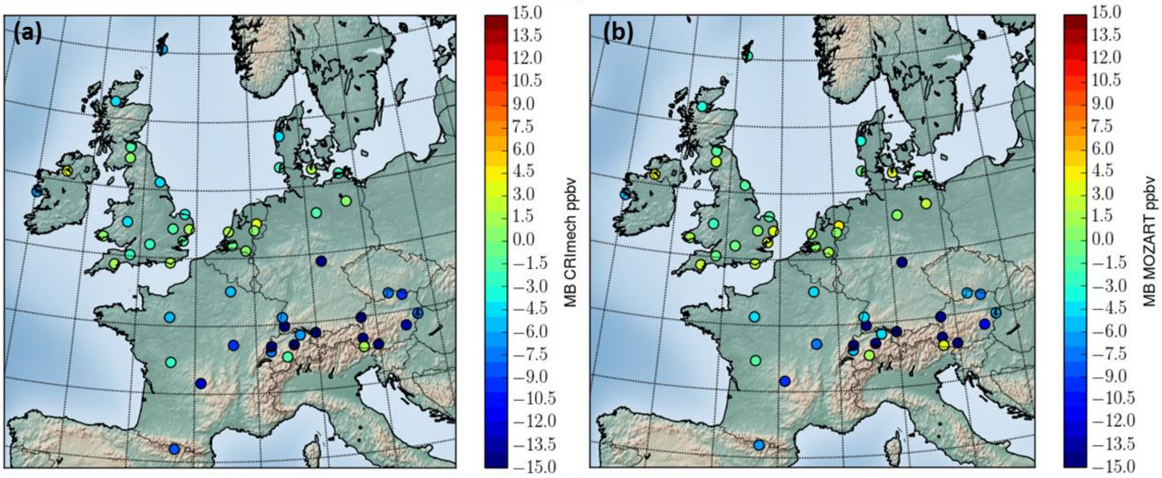

Figure 3.20. Spatial distribution of Mean Bias (MB) calculated for two scenarios: CRImech (a) and MOZART (b) at EMEP sites from 29th June to 31st July. The values are shown at the location of the stations.

Fig. 3.21 provides a comparison of modelled hourly O_3 mixing ratios at 12 selected sites across Europe. Predictions are very well correlated in both model scenarios with many similarities between the two mechanisms. Marked differences in the O_3 mixing ratios are nevertheless observed in some stations in the UK and Western Europe (e.g., Weybourne, UK; Bush, UK; Wicken Fen, UK; De Silk, NE; Cabauw, NE; and Westerland, DE) during the 29-30 June see Fig. 3.21. This is in part due to the underestimation of NO_x mixing ratios in the CRImech scenario and the subsequent reduction of O_3 chemical production and O_3 build-up, see blue arrow, Fig. 3.22. Moreover, it was found that the differences between the two chemical mechanisms during June 29 and 30 were caused by the use of different spin-up methods. Nonetheless the impact of the spin-up is expected to be negligible after three to four days into the simulation, as illustrated in Session 2.4, Fig. 2.4. Accordingly, predictions obtained for June 29 and 30 are not considered in the discussion that follows. Deviations between the chemical mechanisms are also seen in different days at high altitude sites such as Jungfraujoch, CH and; Schauinsland, DE; and Donon, FRA, with MOZART giving the best agreement with observations. It is plausible to rule out the possibility of chemical mechanisms being responsible for the differences found in the O_3 concentrations, particularly the recycling/treatment of reactive nitrogen species.

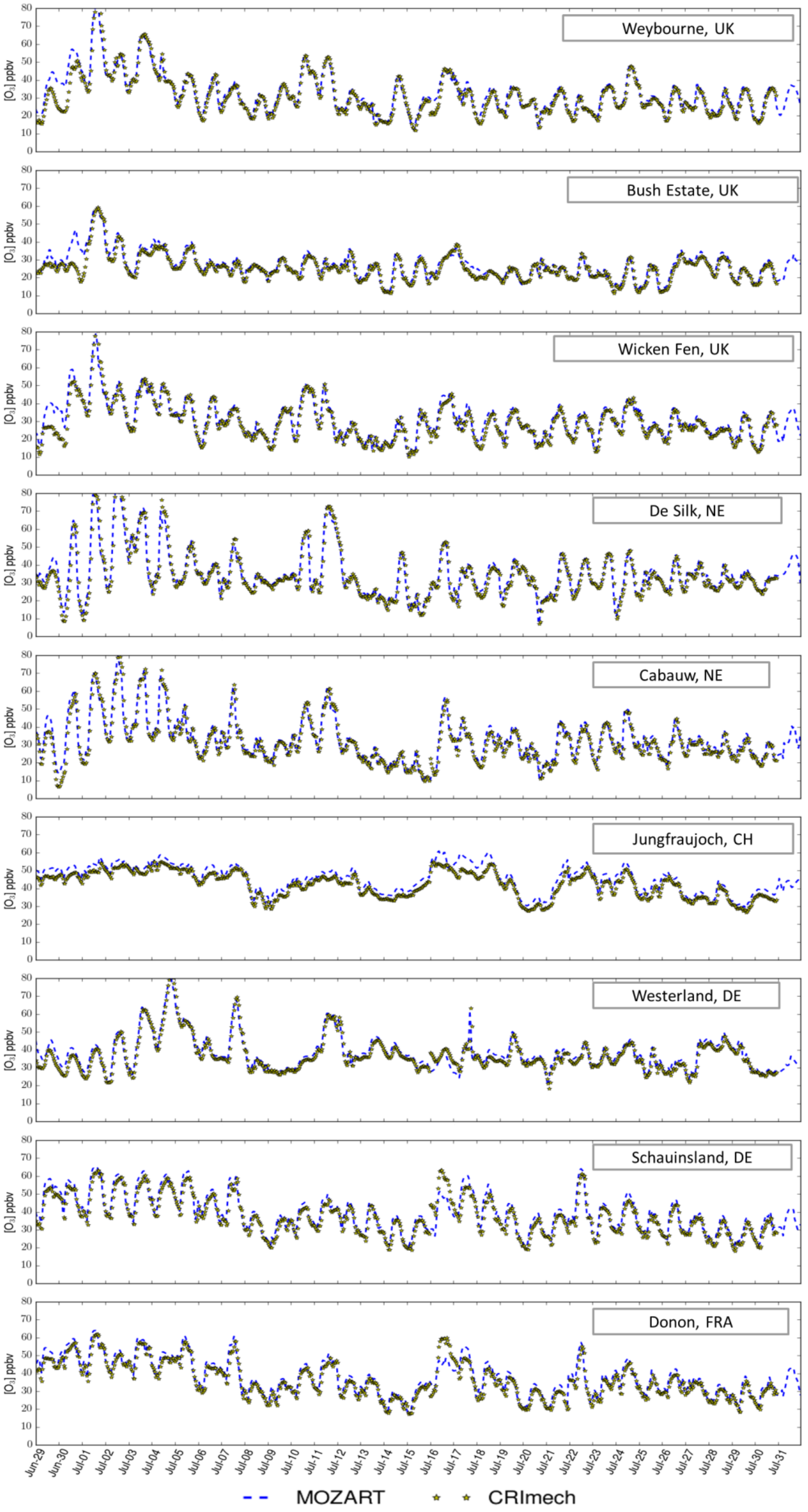

Figure 3.21. Modelled hourly concentrations of O_3 at selected sites over the UK and Western Europe from 29th June to 31st July 2015.

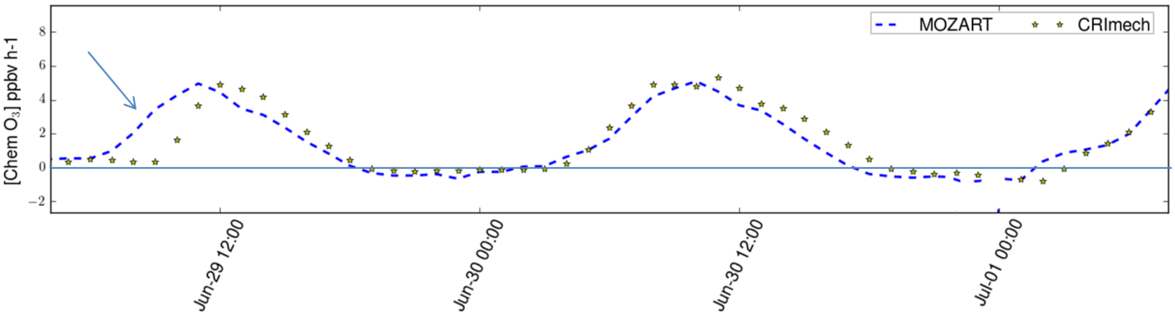

Figure 3.22. Differences in O_3 chemical production between the two scenarios (MOZART and CRImech) at Weybourne from the 29th June till July 1st. The blue arrow points earlier and higher O_3 production in the MOZART scenario.

3.4.3 Evaluation of high ozone concentrations metrics

The MDA8 metric was obtained by calculating the eight hourly running mean of O_3 concentrations at each station and then extracting the maximum value. Fig. 3.23 shows the spatial distribution in observed and modelled MAD8 O_3 during the high O_3 episode. Very high MDA8 O_3 values (> 90 ppbv) are observed in the east and southeast UK, the Netherlands and at some sites over Germany, while high concentrations (between 70-90 ppvb) are seen in France, Denmark and the mountainous regions of the Alps. Concentrations lower than 70 ppbv are generally observed on the west of UK and even lower values (< 50 ppbv) in Ireland and Scotland.

Both chemical mechanisms give similar MDA8 O_3 concentrations over most continental Europe and the UK. However, CRImech better captures MDA8 concentrations on the Netherlands and east and southeast UK (with MDA8 values up to 80 ppbv), indicating that it better predicts health metrics over the UK in this situation. By contrast, MOZART gives better agreements at high altitude sites in France and in the mountainous regions of the Alps.

(a) Observed MDA8 O_3

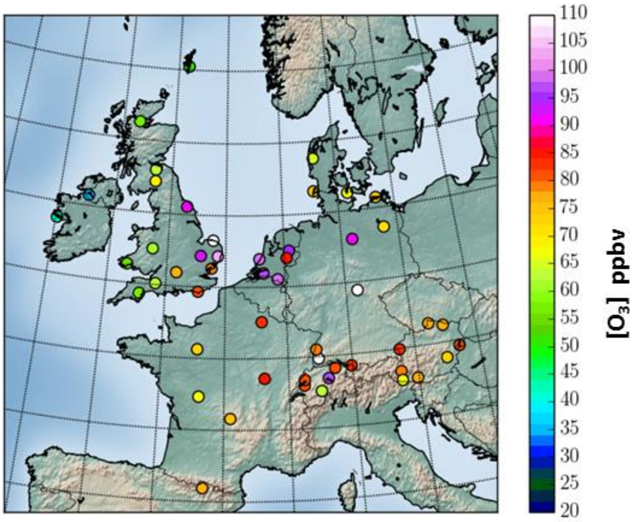

(b) MDA8 O_3 CRImech

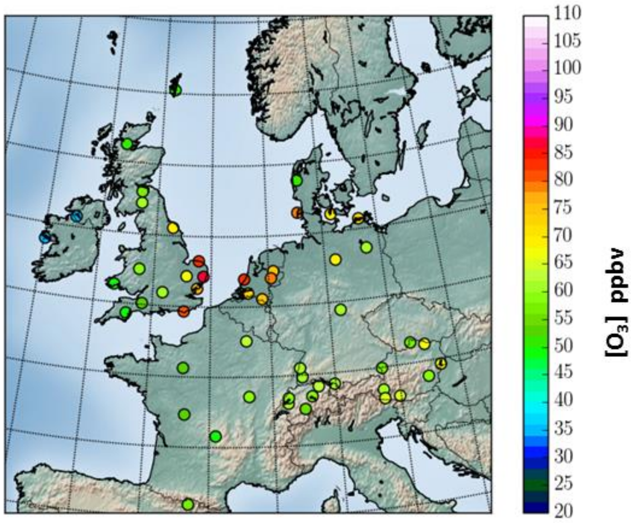

(c) MDA8 O_3 MOZART

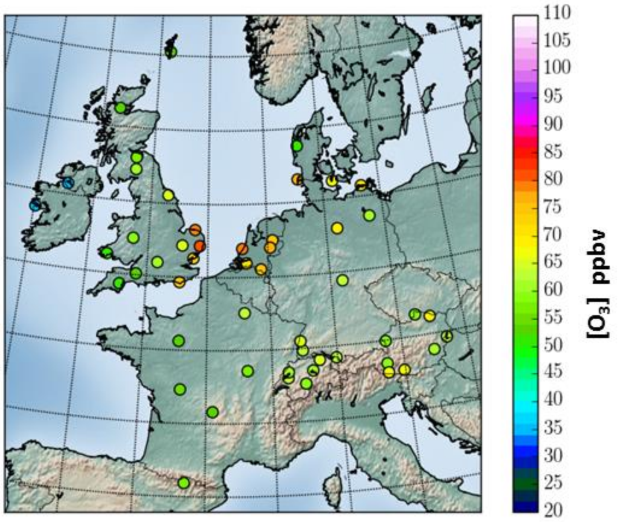

Figure 3.23. Spatial distribution of the maximum daily O_3 concentration observed (a) and calculated for two scenarios: CRImech (b) and MOZART (c) at EMEP sites from 29th June to 31st July. The values are shown at the location of the stations.

3.4.4 Evaluation against ICOZA field campaign dataset

Near-surface concentrations of O_3, NOx, NOy, CO and VOCs (primary and secondary species) taken from the ICOZA field campaign were also used to evaluate the two chemical mechanisms. The summary of their performance is shown in Table 3.9.

Table 3.9. Summary of statistics of hourly O_3, NOx, CO, toluene, alkanes, t-2-butene, alkenes, isoprene, NOy, methanol, acetone and MEK for MOZART and CRImech from June 29th to July 31st at WAO. MB, MGE and RMSE are given in ppbv.

Species	MOZART SIMULATION						
	FAC2	MB	MGE	NMB	NMGE	RMSE	r
O_3	0.99	-2.00	5.84	-0.06	0.17	8.58	0.78
NO	0.16	-0.34	0.35	-0.79	0.80	0.60	0.55
NO_2	0.73	-0.13	1.06	-0.05	0.42	1.45	0.59
CO	1.00	13.01	17.63	0.12	0.16	20.85	0.68
Toluene	0.46	0.04	0.05	0.90	1.11	0.07	0.51
Ethane	0.96	-0.15	0.20	-0.15	0.20	0.31	0.05
Propane	0.67	-0.13	0.16	-0.38	0.49	0.29	0.34
T_2_Butene	0.10	0.07	0.07	16.19	16.22	0.10	0.14
Ethene	0.45	0.11	0.15	0.76	1.01	0.20	0.45
Propene	0.38	-0.08	0.09	-0.55	0.65	0.12	-0.02
Isoprene	0.16	-0.11	0.11	-0.75	0.77	0.14	0.43
NOy	0.57	-2.07	2.21	-0.40	0.43	2.67	0.66
Methanol	0.49	-1.36	1.52	-0.48	0.54	2.03	0.49
Acetone	0.14	-0.67	0.68	-0.65	0.66	0.78	0.78
MEK	0.60	0.10	0.12	0.90	1.02	0.18	0.70

Species	CRIMECH SIMULATION						
	FAC2	MB	MGE	NMB	NMGE	RMSE	r
O_3	1.00	-3.31	6.26	-0.10	0.18	8.56	0.81
NO	0.11	-0.34	0.36	-0.80	0.83	0.61	0.50
NO_2	0.68	-0.36	1.08	-0.14	0.43	1.52	0.54
CO	1.00	16.38	19.92	0.15	0.18	22.65	0.71
Toluene	0.50	0.02	0.03	0.35	0.78	0.05	0.44
Ethane	0.95	-0.16	0.21	-0.16	0.20	0.31	0.07
Propane	0.50	-0.19	0.20	-0.55	0.58	0.32	0.35
T_2_Butene	0.22	0.02	0.02	4.13	4.18	0.03	0.14
Ethene	0.46	0.11	0.15	0.77	1.00	0.20	0.46
Propene	0.39	-0.08	0.09	-0.55	0.64	0.12	-0.07
Isoprene	0.15	-0.11	0.11	-0.75	0.76	0.14	0.48
NOy	0.89	-0.37	1.48	-0.07	0.29	1.95	0.66
Methanol	0.49	-1.28	1.54	-0.45	0.55	2.04	0.43
Acetone	0.85	-0.34	0.38	-0.33	0.37	0.53	0.77
MEK	0.45	-0.06	0.07	-0.52	0.62	0.11	0.04

Fig. 3.24 shows that both mechanisms capture the day-to-day variation in the O_3 concentration, with CRImech exhibiting slightly larger *r* coefficient than the MOZART scenario. The two chemical mechanisms give very close concentrations for most of the campaign, closer than the fit between prediction and measurements. In both cases, O_3 concentrations are underestimated through the campaign with similar errors values (RMSE = 8.6 ppbv). In particular, predictions fail to capture the peak maximum O_3 concentrations on 1st July when O_3 exceeded 90 ppbv, with CRImech giving a slightly better agreement with observations.

It was found that underestimation during the pollution episode is in part due to difficulty in simulating wind fields at the site. Fig. 3.25 shows that although predictions of wind direction agree reasonably well with observations through the campaign, values of ~50° on 1st July are underestimated. Modelled winds are predominately southeast (SE) while the observed winds are mostly from the south. In southeast UK, wind direction plays a decisive role during high O_3 episodes. High O_3 episodes are associated with the transport of O_3 and precursors from continental Europe under anticyclonic weather (AQEG, 2009). Thus, biases in the wind direction predictions can be a major factor explaining the underestimation of concentrations above 90 ppbv when using both mechanisms.

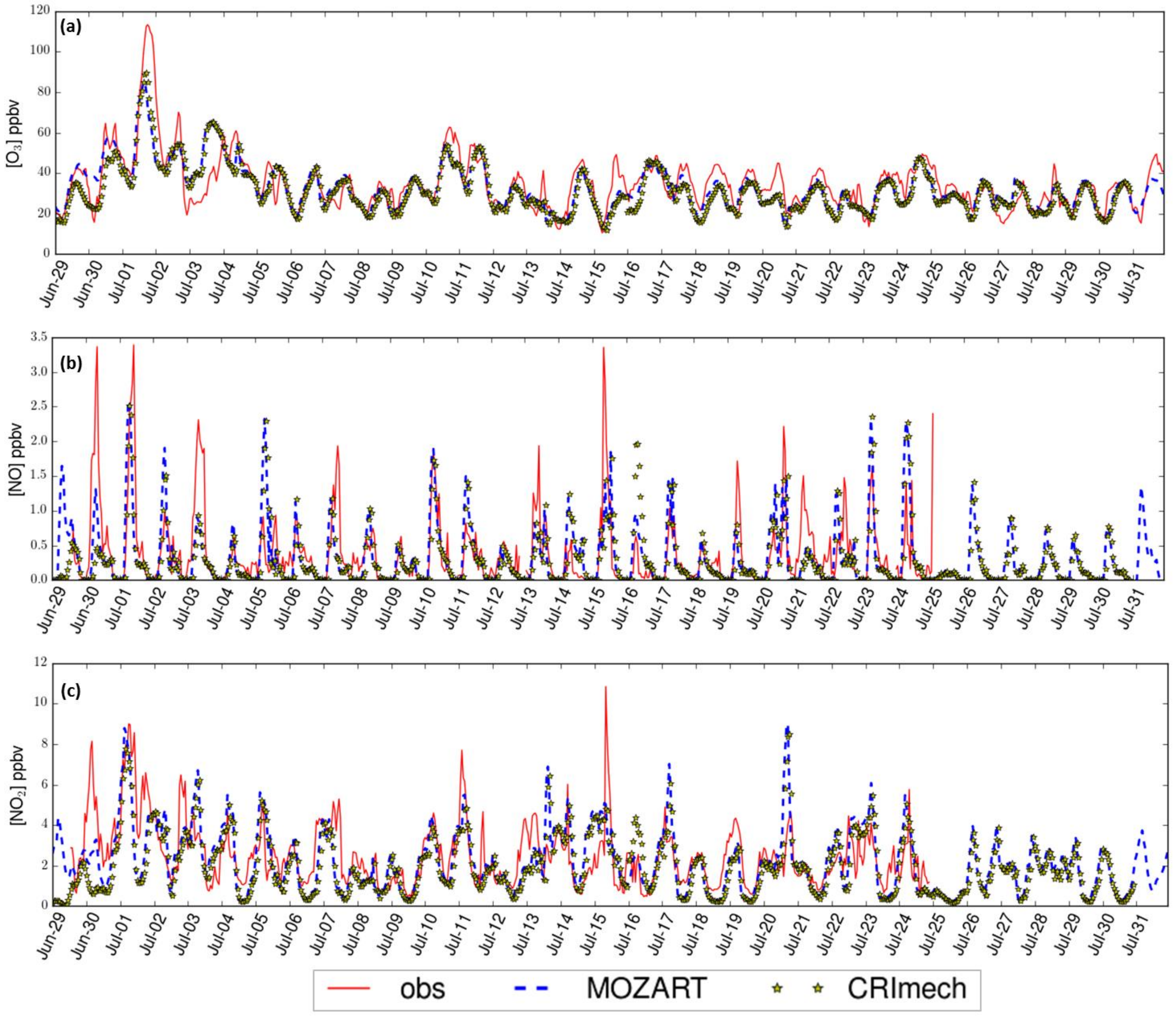

Figure 3.24. Comparison between model runs using CRImech (yellow stars) and MOZART (blue dashed line) and observed (red line) hourly concentrations of O_3 (a), NO (b) and NO_2 (c) at Weybourne from 29th June to 31st July.

NO concentrations are poorly represented with up to 16% of the predicted values lying within 0.5 and 2 times the observations (average FAC2 = 0.16). In addition, both mechanisms make it difficult to capture the hourly changes in the concentrations, giving *r* close to 0.5. NO concentrations between the two models scenarios are very similar for most of the campaign, and so are the statistics, with both mechanisms showing a tendency to underestimate NO concentrations (MB = -0.34 ppbv in both models). NO_2 concentrations are also underestimated by both mechanisms (MB of up to -0.36 ppbv) with MOZART giving slightly better performance than CRImech.

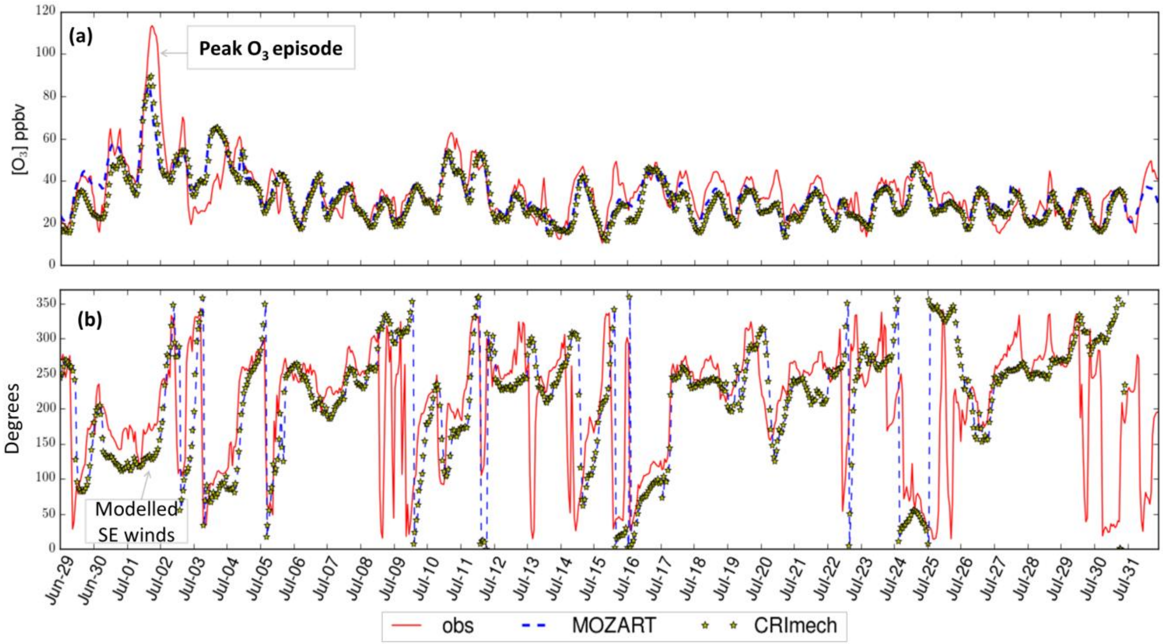

Figure 3.25. Comparison between models runs using CRImech (yellow stars) and MOZART (blue dashed line) and observed (red line) hourly concentrations of O_3 (a) and wind direction (b) at Weybourne from 29th June to 31st July.

Regarding primary organics, both mechanisms tend to overestimate CO concentrations, as shown in the plot in Fig. 3.26a. This is particularly evident for CO background concentrations (e.g. Fig. 3.26a between 5-8 July when the site is under westerly winds). Nevertheless, hourly variations in CO concentrations are well captured in both cases, with CRImech giving slightly higher positive bias and errors (MB = 13 and 16 ppbv and RMSE 21 and 23 ppbv, respectively). Concentrations of other long-live hydrocarbons such as alkenes (ethane C_2H_6 and propane C_3H_8, Fig. 3.26b and Fig. 3.26c, respectively) are poorly described in both scenarios, with correlation coefficients ranging between 0.1 and 0.3. This is particularly evident when assessing days with fluctuating easterly winds (e.g., 1st July and 11th -12th July). As both MOZART and CRImech have an explicit treatment of ethane and propane, deviation between predictions is likely due to disagreements in the reaction rates, particularly for propane.

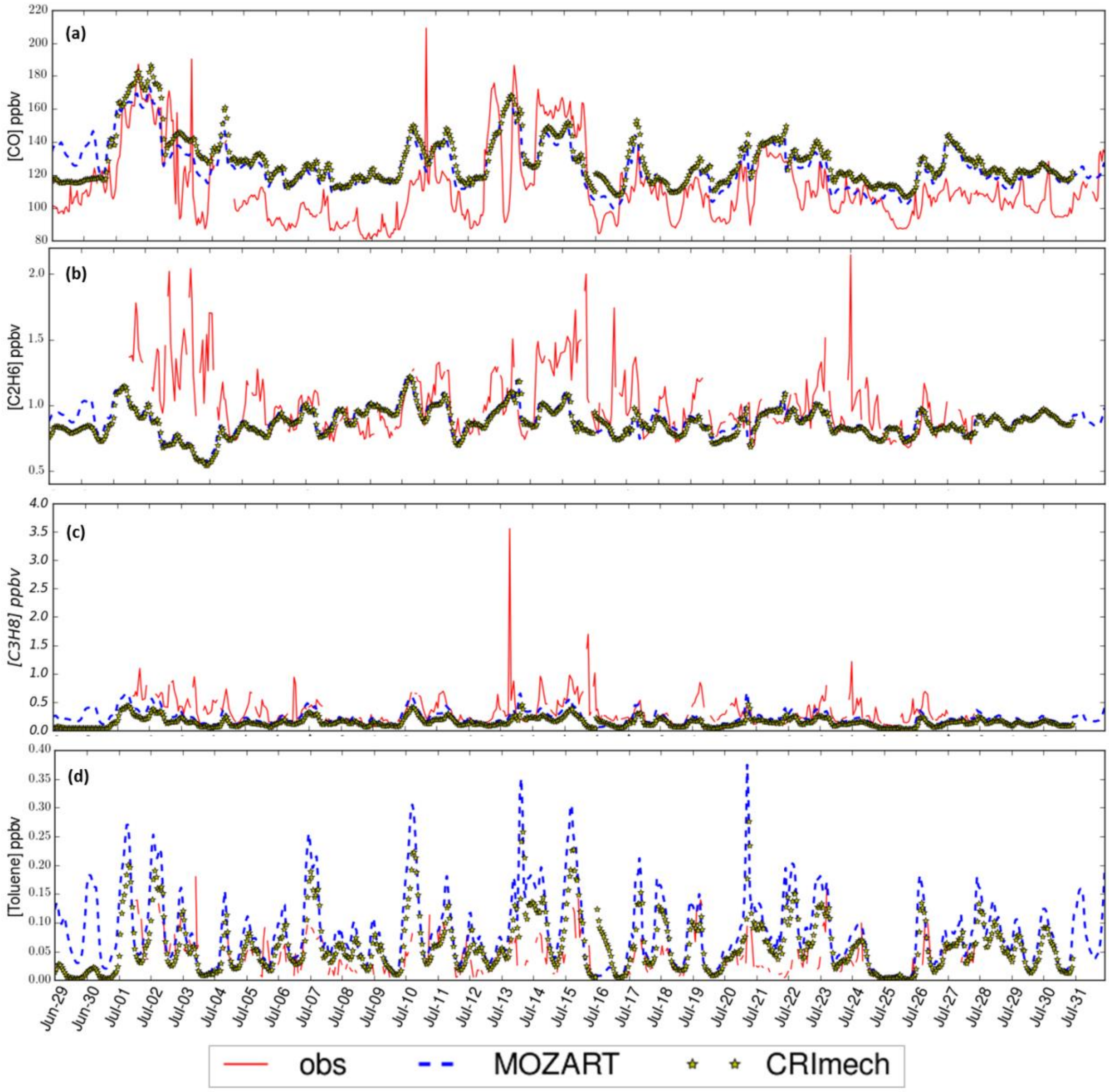

Figure 3.26. Comparison between models runs using CRImech (yellow stars) and MOZART (blue dashed line) and observed (red line) hourly concentrations of CO (a), ethane (b), propane (c) and toluene (d) at Weybourne from 29th June to 31st July.

Toluene (C_7H_8) concentrations, on the other hand, are overestimated by both mechanisms, see Fig. 3.26d. While MOZART captures the hourly changes in the observed concentrations (exhibiting slightly higher r coefficient than CRImech, 0.5 compared to 0.4), it tends to overestimate the observed concentration slightly more than CRImech, leading to larger errors (RSME = 0.1 and 0.04 ppbv, respectively).

Therefore, CRImech gives much better agreement for the observed toluene concentrations. Such differences can be partially attributed to the VOC emission pre-processing. In WRF-Chem, MOZART carries a reduced number of VOC species compared to CRImech. Thus, for MOZART, the emitted CRImech VOCs species need to be lumped to the available VOCs species in the MOZART mechanism, as discussed in Chapter 3. Since Benzene is not included as an emission input in the version of MOZART used in this study, its emissions have been lumped to toluene following the approximate VOCs mappings of MOZART-4 to CRIv2-R5 presented in Table 7 in Archer-Nicholls et al. (2014). Meaning that the fraction of Toluene in MOZART is slightly higher than in CRImech (7.82% of total VOCs compared to 5.82% in CRImech). This could in part explain the larger concentrations of toluene in the MOZART simulation when compared to CRImech.

Fig. 3.27 shows time series of modelled and observed short-live hydrocarbons trans-2-butene (C_4H_8), alkenes (ethene (C_2H_4) and propene (C_3H_6)) and isoprene (C_5H_8). The models largely underestimate trans-2-butene concentrations, see Fig. 3.27a. These can differ up to three times, with MOZART giving higher mixing ratios particularly during night despite using same emissions fractions in both model scenarios. After examining the reactions in the chemical mechanism, the only loss mechanism of trans-2-Butene in MOZART (BIGENE) is via reaction with OH, while in CRImech trans-2-butene is also lost by reaction with NO_3 and O_3. This may explain the abundance of trans-2-butene at night in the MOZART mechanism.

The mechanisms poorly represent the hourly variation in the concentration of alkenes (ethene C_2H_4 and propene C_3H_6, Fig. 3.27b and c). In particular, ethene is largely overestimated while propene is underestimated, with both model scenarios showing similar errors (RMSE = 0.20 and 0.12 ppbv for Ethane and Propene respectively). Concentrations of isoprene (C_5H_8, Fig. 3.27d), a biogenic tracer and highly reactive specie with a daytime lifetime of 1-2 hours are also underestimated. As C_5H_8 concentrations are largely dependent of a variety of factors such as ambient temperature, land use and radiation, further sensitivity studies are needed to rule out the cause of model underestimations. Notably, despite using identical biogenic emissions in both model scenarios, some discrepancies between the isoprene concentrations between the two models are observed. In particular, peak concentrations during the periods of 10-11 July and 20-21 July. This is consistent with what has been reported in the inter-comparison of the different chemical mechanisms within the context the Air Quality Modelling Evaluation International Initiative Phase 2 which included the MOZART chemical mechanism (Knote et al., 2014). Knote et al. (2014) suggested that the discrepancies in modelled isoprene between the mechanisms could be partially explained by differences in predicted concentrations of OH/NO_3 radicals amongst the mechanisms.

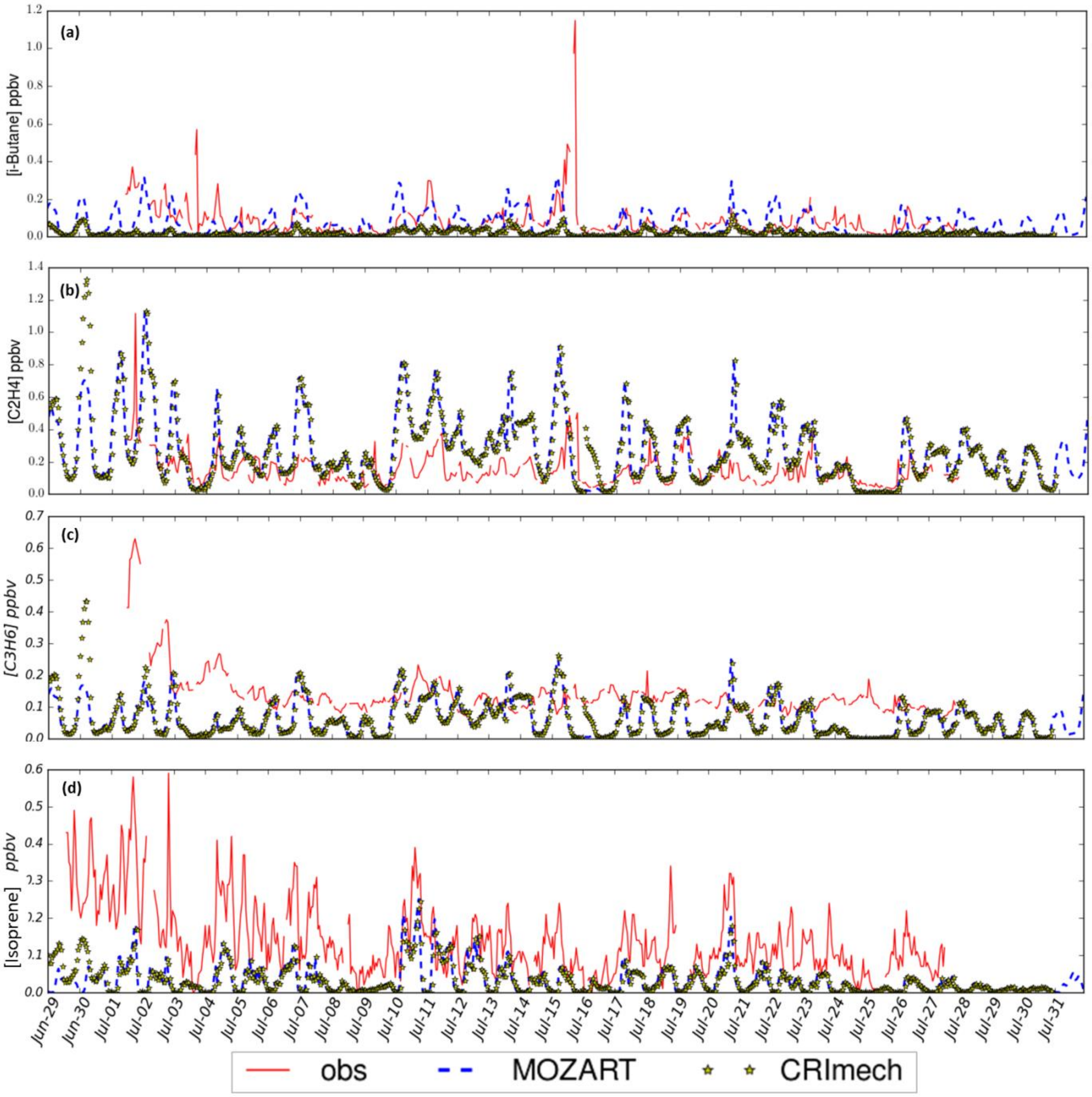

Figure 3.27. Comparison between simulations using CRImech (yellow stars) and MOZART (blue dashed line) and observed (red line) hourly concentrations of trans-2-butene (a), ethene (b), propene (c) and isoprene (d) at Weybourne from 29th June to 31st July.

Based on these comparisons, it seems that emissions of most of the assessed primary VOC species are generally underestimated by both mechanisms. Future studies should consider the implementation of more recent emissions inventories for EU.

Both mechanisms give better predictions of secondary organic species than primary species (Fig. 3.28) with the correlation coefficient *r* ranging between 0.5 and 0.8. However, with the exception of methanol (CH_3OH Fig. 3.28c), most species exhibit large differences in the concentrations between the two model scenarios. As expected, NOy is found to be better represented in CRImech in terms of FACT2 (0.9 against 0.6 in the MOZART scenario), and mean bias and errors due to a more explicit representation of the recycling of NOx in the CRImech mechanism with respect to MOZART. Similarly, acetone (CH_3COCH_3), an oxidation product of higher hydrocarbons with a lifetime with respect to OH of about 50 days is found to be better represented by CRImech in terms of FAC2, mean bias and error in part due to a more explicit oxidation of hydrocarbons in the CRImech mechanism. Finally, it was shown that methanol (CH_3OH), both an oxidation product of primary hydrocarbons and primary emitted specie with a life time of about 2 weeks, is largely overestimated by the two model scenarios, up to five times. Yet, it exhibits a very similar hourly evolution in the concentrations between the two mechanisms.

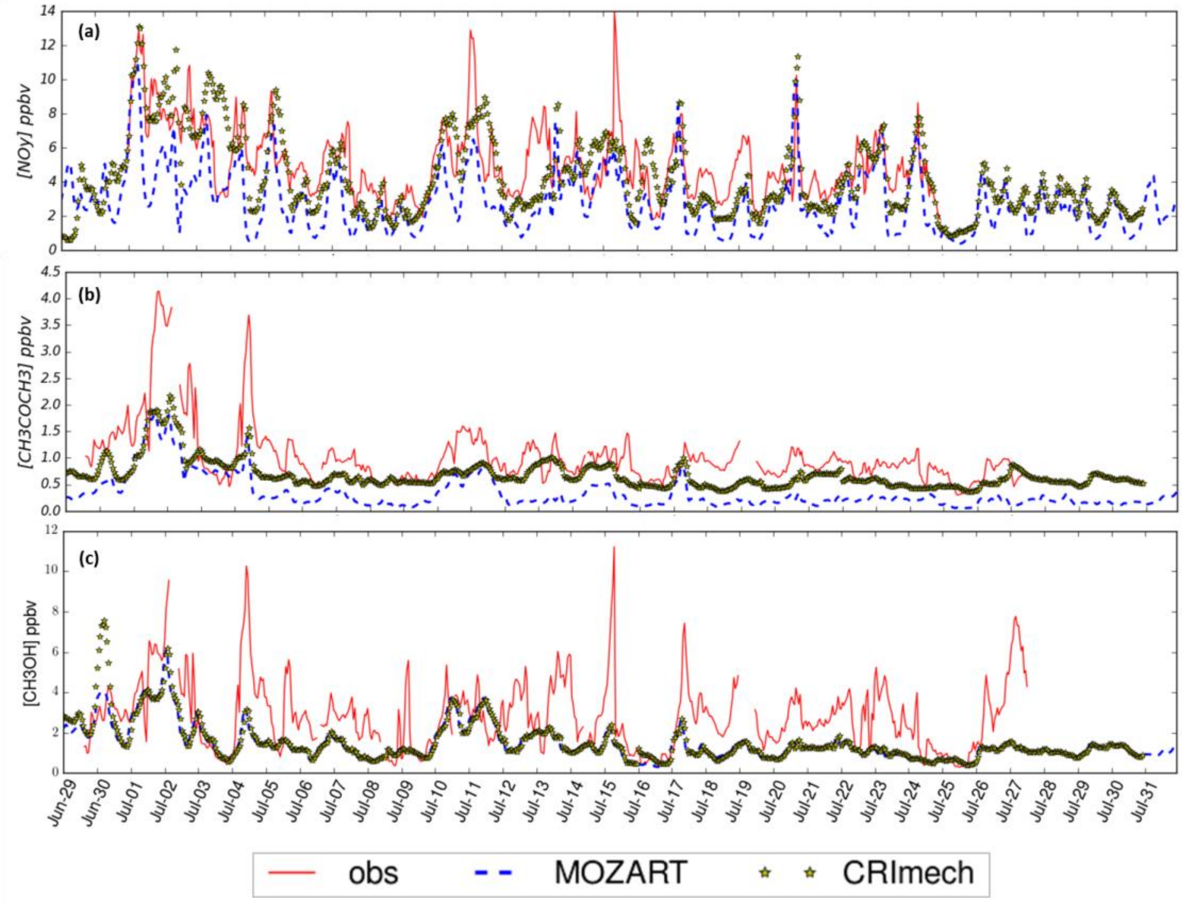

Figure 3.28. Comparison between model runs using CRImech (yellow stars) and MOZART (blue dashed line) and observed (red line) hourly concentrations of NOy (a), Acetone (b) and, Methanol (c) at Weybourne from 29th June to 31st July.

3.5 Summary and Conclusions

In this chapter, a four months evaluation of meteorological and chemical fields on a European domain with an emphasis on the UK is provided.

The results show that the WRF-Chem setup gives a very good representation of temperature and wind speed, with biases consistent with previous studies. However, wind direction is mostly positive bias ranging between 3 and 24°. NOx concentrations are well predicted with NO_2 showing a better performance than NO. NO mixing ratios tend to be underestimated while NO_2 concentrations are generally overestimated, particularly during nigh-time.

Overall, the model does a good job simulating the concentrations of O_3 in the European domain. In particular, the model captures the spatial distribution in surface O_3 domain-wide. Nonetheless, it tends to underestimate concentrations in most of the assessed sites, which is consistent with results from previous modelling studies using the MOZART-4 chemical mechanism over Europe. The most important findings of particular importance for this study are:

- ✓ Underestimation of the hemispheric concentrations of O_3 entering the western fringe of the UK, which is attributed to lower O_3 concentration in the model used to provide the boundary conditions.
- ✓ When considering metrics of relevance for human health, such as MDA8 O_3, it was found that the model well captures the spatial distribution of the MDA8 O_3 above 50 and 60 ppbv across the UK with the largest number of days of concentrated on the East Anglia region and Southeast England. Nonetheless, the model tends to underestimate the number of days with MDA8 O_3 above 50 and 60 ppbv, in particular over the East Anglia region, which is consistent with the results from previous modelling studies using MOZART-4 as a chemical mechanism.
- ✓ Evaluation of the metric for vegetation exposure AOT40 shows that the model captures most of the spatial distribution of the AOT40 in the UK, with the largest obtained values concentrated on East Anglia. However, it tends to underestimate the values in the southeast (up to - 3000 $\mu g\ m^{-3}\ h$).
- ✓ Comparison of two different chemical mechanisms: MOZART-4 and CRImech (for which the first model evaluation for a European domain is also provided) shows that predictions of most chemical species between both model scenarios are very well correlated so that concentrations obtained using both chemical mechanisms are much closer than the fit between prediction and measurements.
- ✓ Overall, the two mechanisms show relatively similar behaviour for NOx, with both MOZART and CRImech simulations resulting in underestimations of NO, with less than half of the predicted values at the majority of the assessed sites lying within 1/2 and a factor of 2 of the observations. NO_2, on the other hand, is both under- and over-estimated across the domain with CRImech showing a

slightly better performance than MOZART in terms of mean bias and errors.

- ✓ Some differences were found in O_3 concentrations predicted using both mechanisms. Whereas MOZART gives better agreements at high altitude sites, CRImech gives better predictions of the MDA8 O_3, in particular over the Netherlands, east and the southeast UK. It is then concluded that using CRImech mechanism is a better choice when studying peak O_3 episodes in the southeast UK.

Chapter 4

AN EVALUATION OF THE SOURCES OF OZONE IN THE UK

4.1 Rationale

Tropospheric ozone (O_3) is a pollutant of concern for policy-makers because of its detrimental effect on human health, agriculture and ecosystems (Fuhrer, 2009; WHO, 2016). Near the surface, O_3 has an atmospheric lifetime typically of hours. In the free troposphere, however, the lifetime could be up to several weeks (Stevenson et al., 2006). O_3 can therefore be transported from its point of production downwind over long distances crossing countries and even continents ((Wild et al., 2004; HTAP, 2007).

Several studies have investigated the contribution of intercontinental transport to O_3 in Europe, in particular from North America and Asia, using different modelling techniques (e.g. Wild et al., 2004; Derwent et al, 2004, 2008, 2015; Auvray & Bey, 2005; HTAP, 2007). However, these studies do not provide a quantitative estimate of the contribution of the different source regions to the total amount of O_3 over the UK at a national scale, but rather an estimate at individual locations across Europe (e.g. Derwent, 2004) or for the European region as a whole. In the study presented in this chapter, WRF-Chem is used to quantify how much of the UK (hereafter domestic) and European (i.e. non-UK European) NO_x emissions contribute to UK surface O_3 concentrations. The study period spans from May to August 2015 covering the ICOZA field campaign, which provides the dataset against which the model output is compared. Model experiments are set up to answer the following research questions:

I. How important is the contribution from European NO_x emissions to surface O_3 in the UK?

II. How do the contributions of European and domestic UK anthropogenic emissions of NO_x to surface O_3 compare in different regions across the UK?

III. What are the impacts of European and domestic UK NO_x emissions on ozone-policy relevant standards, and how does this relationship vary among the UK regions?

IV. How important is the contribution of O_3 from outside Europe (i.e. from the lateral model boundaries) to surface O_3 in the UK and what are its impacts on ozone-policy relevant standards?

The reader is referred to Chapter 2 for details on the WRF-Chem settings. For convenience, the tagging approach presented in section 2.3 is summarised below in Section 4.2. In section 4.3, results for the monthly mean contributions of domestic, European and the lateral boundaries (LB) to surface O_3 in the UK are presented and discussed. The regional differences in the estimated monthly contributions for domestic, lateral boundary, European super-region are discussed in section 4.4. The impacts of the lateral boundaries, European sub-regions and domestic source regions on policy relevant standards are discussed in section 4.5. Conclusions are finally given in section 4.6.

4.2 Methods

4.2.1 Principles of ozone tagging

The contribution of domestic and European anthropogenic emissions to tropospheric O_3 in the UK is studied using a tagged-ozone method in which O_3 molecules are labelled with the identity of their source (sectors and/or source regions). This enables the direct attribution of O_3 concentrations in receptor regions to specific sources (Butler et al., 2018). The technique used here is based on the method described in Emmons et al. (2012) and Butler et al. (2018). As O_3 is not directly emitted into the atmosphere but instead produced via the chemical reactions of its precursors, quantifying the O_3 contribution not only requires tagging O_3 but also tracking the relevant precursors. Here, NO_x emissions are tagged at different geographical locations across Europe and then followed to the production of O_3 so that the total O_3 mixing ratio in a receptor region (e.g. South East England) can be attributed to the different source regions, as illustrated in session 2.3 Fig. 2.2.

Following Emmons et al. (2012), a duplicated set of reactions involving all species containing nitrogen and O_3 was added to the original chemical mechanism file. Essentially, the NO_x in the analogous reactions carried a label with the identity of their source region. The tagged NO_x is traced through all of the odd nitrogen species (e.g., PAN, HNO_3, organic nitrates) to account for the recycling of NO_x. As in Butler et al. 2018, the reaction of NO with any peroxy radical (HO_2) and all organic peroxy radicals (RO_2) and subsequent production of NO_2 is regarded as a process that effectively generates tropospheric O_3, see reaction R. 4.1 and 4.2.

Reaction base mechanism:

$$NO + HO_2 \rightarrow NO_2 + HO_2 \quad \text{(R. 4.1)}$$

Reaction of tag tagged species:

$$NO_{tag} + HO_2 \rightarrow NO_2 + HO_2 \quad \text{(R. 4.2)}$$

All tracers' reactions are run concurrently with the base mechanism. Each tagged species undergoes the same chemical and physical processes of its corresponding species in the based chemical mechanism. Ideally the sum of O_3 for all tags at a given grid cell should equal the concentration O_3 in the base mechanism at the same grid cell. However, since only NO_x emissions are tagged, discrepancies may originate from O_3 being formed through the oxidation of hydrocarbons by peroxy radicals without NO_x catalysis which is not accounted for in a NOx tagging scheme (Emmons et al., 2010, 2012), see reaction R. 4.3 and R. 4.4.

$$MCO_3 + HO_2 \rightarrow .25O_3 + .25CH_3COOH + .75CH_3COOOH \quad \text{(R. 4.3)}$$

$$CH_3CO_3 + HO_2 \rightarrow .75CH_3COOOH + .25CH_3COOH + .25O_3 \quad \text{(R. 4.4)}$$

Fig. 4.1 shows that the largest difference between the sum of the individual tagged sources and the total O_3 in the base mechanism at the East Anglia region happens under south-easterly winds on the 1st July.

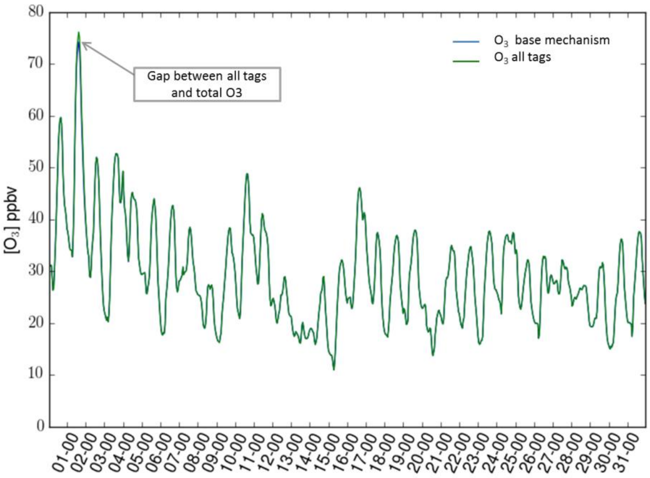

Figure 4.1. Comparison between total O_3 and tagged O_3 from all anthropogenic sources at the East Anglia region on July 2015.

4.2.2 Source regions settings

The contribution from Europe (excluding the UK) is derived by assigning Europe as a super region (EU super-region). Fig. 4.2a shows the model domain divided into two source regions: 1) the UK, including England, Wales, Northern Ireland and Scotland; and 2) EU super-region including the contribution from the remaining areas within the model domain as well as shipping routes. The chemical lateral boundaries are defined as an independent source region (LB) and provided by MOZART-4.

The EU super-region is further divided into eight source regions. Each O_3 molecule originating from the respective source region was tracked as an independent variable. These regions were chosen as shown in Fig. 4.2b: 1) France (FRA); 2) Belgium (BEL); 3) The Netherlands (NET); 4) Luxemburg (LUX); 5) Germany (GER); 6) The North Sea and English Channel (NOS); 7) the rest of Central Europe (Rest_CEU), containing Austria, Switzerland, the Czech Republic, Hungary, Poland, Slovakia, Slovenia and Romania; and 8) Rest of EU (Rest_EU), containing the remaining areas in the model domain including the Iberian peninsula, Southern Europe, South-eastern Europe, Eastern Europe, Northern Europe, Ireland, and shipping emissions from the Atlantic, Baltic Sea and the Mediterranean. Please note that in section 4.4 the contributions from the Netherlands, Luxemburg and Belgium have been lumped into the Benelux region due to small values obtained in each country. Such setting of source regions enables untangling the derived contributions from western and central Europe and from the busiest shipping route in Europe.

It is also important to note that the LB tracer includes O_3 contributions of stratospheric origin. Moreover, all O_3 that enters the model domain through the lateral boundaries will be tagged as LB. Moreover, any tagged O_3 molecule formed within the model domain that exits the domain will no longer be attributed to its original source but instead to the LB. Note that the LB tracer is tagged as a single source, it is impossible to attribute the contributions from this source to any specific geographical location (e.g. North America). Therefore, a detailed investigation of long-range transport from sources outside the EU domain is beyond the scope of the present study.

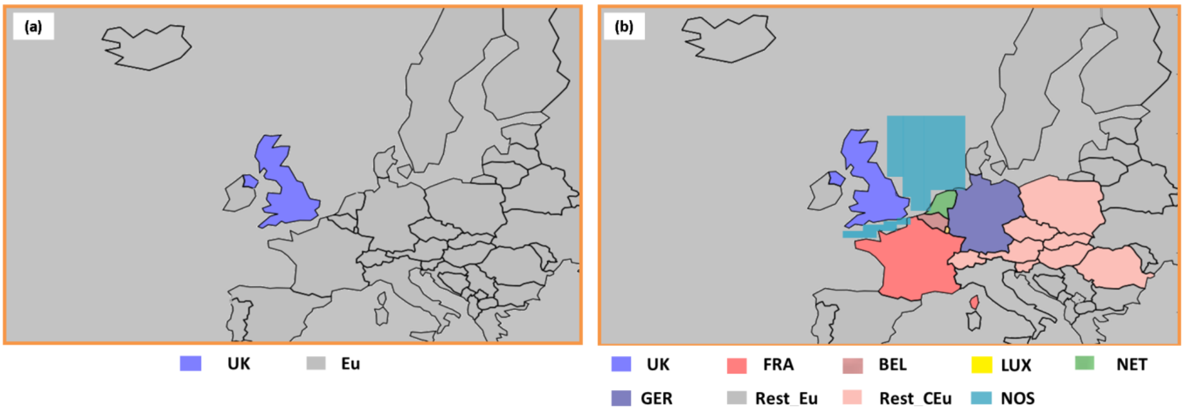

Figure 4.2. Source regions settings: (a) EU super-region which includes ship emissions from the Atlantic, Baltic Sea, Mediterranean, North Sea and English Channel; (b) division of the EU super-region into 8 sub-regions. Note that Rest_EU tagged also includes ship emissions from the Atlantic, Mediterranean and Baltic Sea whilst emissions from shipping routes in the North Sea and the English Channel are tagged as NOS. The orange line surrounding the domain indicates LB tag.

4.2.3 UK receptor regions

The UK domain was divided into its 12 administrative regions, as shown in Fig. 4.3: East Anglia, South-East, London area, South-West, Wales, West Midlands, East Midlands, Yorkshire and Humberside, North-East, North-West, Northern Ireland and Scotland. The separations of the receptor areas were based on the UK administrative boundaries which have been used in previous air quality studies such as Heal et al. (2013). Shape-files were then used to extract the model output for each region using the Salem library for Python.

Figure 4.3. Map of the UK showing the receptor regions.

The UK is well known for the variability of its weather. Generally, places in the east and south tend to be drier, warmer, sunnier and less windy than those in the west and north (Jenkin, 2008). Thus dividing the UK into several regions allows separating meteorological features, such as temperature, sunshine, precipitation and wind as well as emissions within each region that are known to have an impact in the spatial distribution and temporal variation of air pollutants (Coyle et al., 2002; Jenkin, 2008).

4.2.4 Policy relevant standards

Current European and National air quality standards to mitigate the effects of O_3 on human health are expressed as 8-hour (h) averages. O_3 exceedance occurs when the maximum 8-h mean O_3 concentration (MDA8) exceeds 60 ppbv (EU, 2008), and when the 8-h mean exceeds 50 ppbv (DEFRA, 2008). Thus, the first two metric used in this chapter consider the hours when the MDA8 exceeds either 50 or 60 ppbv, in accordance with the UK's (DEFRA, 2008) and the European Union's (EU, 2008) O_3 air quality objectives, respectively. The MDA8 is a health-related metric commonly used to assess the impacts of O_3 exposure on the population (e.g. Reidmiller et al. 2009; Stock et al. 2013; Mar et al. 2016) and is strongly influenced by photochemical episodes (AQEG, 2009). Here, the contributions to the health metrics are estimated by computing 8-h moving mean of O_3 for each receptor region and selecting the hours when the MDA8 of 50 and 60 ppbv is exceeded between May to August.

The third type of metric is the accumulated amount of O_3 over the threshold value of 40 ppbv (AOT40) commonly used to assess the effects of O_3 on crops and vegetation (EU, 2008). The AOT40 is based on exposure over 40 ppbv using only the 1-h values measured during daylight hours (between 08:00 and 20:00) Central European Time (CET) over a typical three month growing season May-July (EU Ambient Air Quality Directive (2008/50/EC)). Here the O_3 contributions to the AOT40 index are calculated by looking at the hours when O_3 mixing ratios exceeded the hourly 40 ppbv threshold between 08:00 and 20:00 from May-July only over the relevant arable areas in the UK, the south east England (East Anglia and the South East).

4.3 Source contributions to UK surface ozone: results and discussion

Consistent with previous work (e.g. Karamchandani, et al., 2017; Butler et al., 2018), the hemispheric O_3 level, represented here by the lateral boundary source region, dominated the monthly O_3 concentrations in the UK during the entire study period. The relative contribution from the LB averaged over May to August is 71%, while the contribution from the Eu super-region accounts for nearly 16 % of the simulated O_3. Emissions from the UK (including England, Scotland, Wales and Northern Ireland, hereafter referred to as domestic emissions) on the other hand accounted for 13 % of the simulated O_3.

4.3.1 Spatial variations in the contributions

Surface O_3 in the UK is known to exhibit a significant spatial variability that is driven by global (hemispheric), regional and local-scale processes (Jenkin, 2008). The contribution of each process varies with the location. For instance, remote sites are largely controlled by hemispheric background O_3 (AQEG, 2009). Photochemical pollution episodes, on the other hand, are more severe in the south and east of the UK and O_3 titration by NO_x are higher in urban areas (Jenkin, 2008). The spatial distribution of the monthly O_3 concentrations and the absolute contribution of the source regions (UK, Eu super-region and LB) to surface O_3 in the UK are shown in Fig. 4.4.

4.3.1.1 Monthly O_3 mixing ratios

The spatial distribution of the monthly O_3 concentrations and the absolute contribution of the source regions (UK, Eu super-region and LB) to surface O_3 in the UK are shown in Fig. 4.4. There is a marked latitudinal gradient in the monthly O_3 mixing ratios, fist column in Fig. 4.4, in particular during summertime. Over the ocean areas, O_3 concentrations tend to be higher at the lower latitudes and in the proximity of continental EU and the UK (e.g. the North Sea), see Figs. 4.4e, 4.4i and 4.4m. Likewise, mean O_3 mixing ratios as low as 22 ppbv (Fig. 4.4i) are observed in most of the UK and Scandinavia while mixing ratios as high as 32 ppbv (Fig. 4.4e) are calculated for southern locations in the UK and Western Europe. This is consistent with previous estimates such as those in Butler et al. (2018).

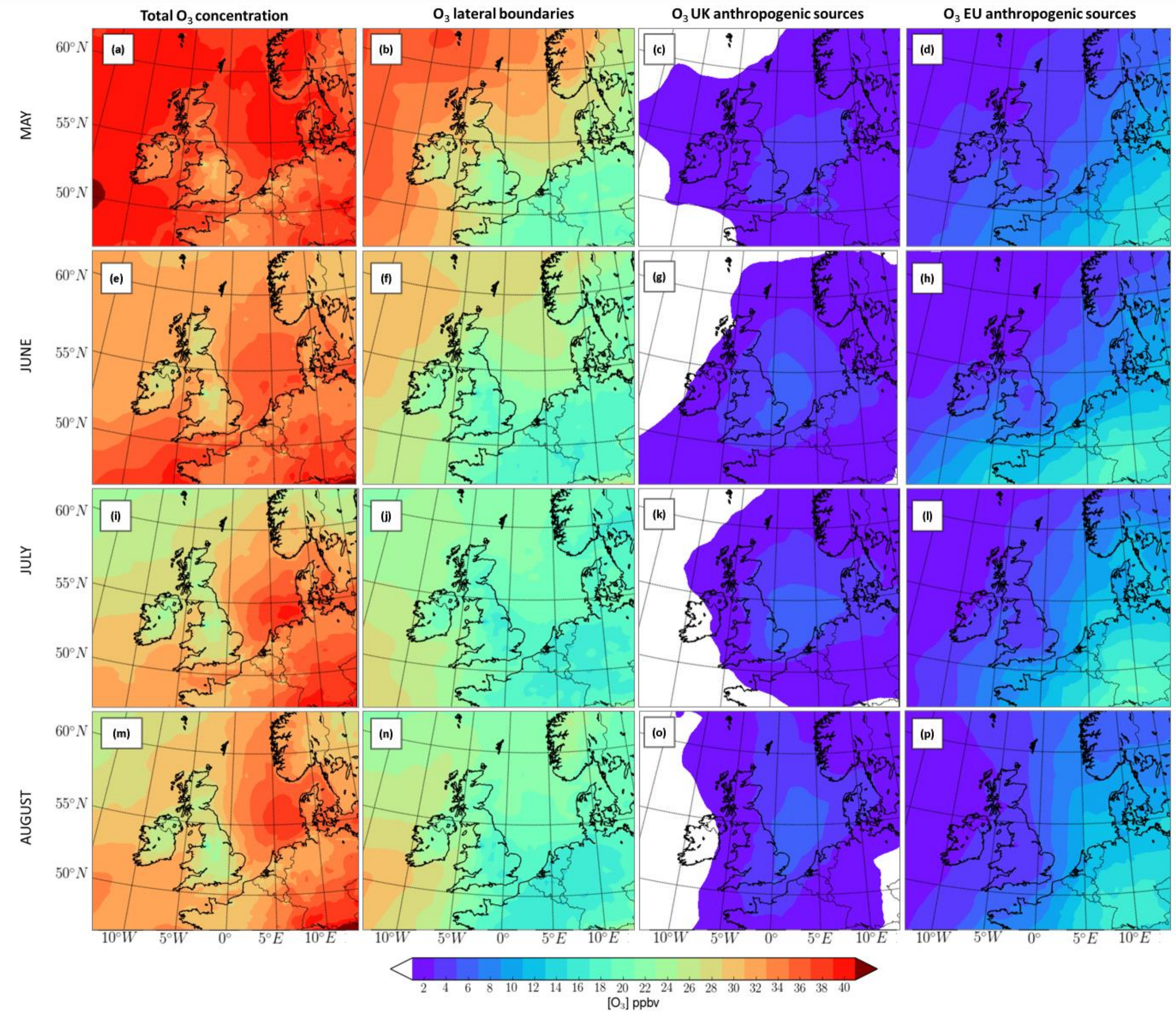

Figure 4.4. Spatial distribution of the monthly mean surface O_3 from May to August 2015. The first column depicts the mean O_3 concentration in May, June, July and August; the absolute monthly contribution from the lateral boundaries are shown in the second column; the third column shows the contribution from domestic emissions; and the contribution from the Eu super-region, which includes emissions from main shipping routes over the European seas and the Atlantic, are presented in the fourth column.

Part of the latitudinal gradient in surface O_3 over land can be attributed to the changing O_3 mixing ratios arriving from the Atlantic Ocean. Moreover, high mixing ratios in the south-east UK during summertime are generally associated to photochemical production of O_3 (Monks et al., 2015), in particular from anthropogenic NO_x and biogenic non-methane VOCs (NMVOCs) emissions (Atkinson, 2000; Butler et al., 2018) as well as transport from of O_3 rich air masses from continental Europe during anticyclonic conditions (Lee et al., 2006; Jenkin et al., 2002; Francis et al., 2011).

Low mean O_3 mixing ratios (as low as 20 ppbv) are also observable in the vicinity of the main urban centres e.g. in the Midlands and the London area (First column Fig. 4.4). This is because strong titration by excessive domestic NO_x emissions takes place over the main urban centres, whereas high O_3 production rates are expected in the outskirts following the progressive reduction in NO_x concentration with respect to that from the VOCs (Jenkin, 2008).

A suitable way to identify the areas influenced by fresh NO_x emissions is comparing the mixing ratios of O_3 with that from O_x (= O_3 + NO_2) (Kley et al., 1994). Fresh emitted NO reacts with O_3 to form NO_2 on a time scale of about 2 minutes. As about 90% of the emissions of oxides of nitrogen occur as NO, an amount of O_3 equivalent to the flux of emitted NO will be converted to NO_2 (Kley et al., 1994). That is to say that, on a time scale of few minutes, practically all local NO_2 has been produced at the expense of O_3 (Kley et al., 1994).

O_x is considered a conservative quantity as it is, to a large extent, free from the titration effect of $NO + O_3 \rightarrow NO_2$. The effect of titration for July is evident in Fig. 4.5. When O_x is considered, the concentrations tend to increase over main urban centres such as London, Birmingham, Nottingham, Sheffield, and Manchester, and to a lesser extent over Edinburgh and Glasgow. The NO_x titration effect is also observed within the main urban centres in continental Europe and along the shipping lanes over the North Sea and the English Channel due to the high NO_x content of ship emissions compare with that from VOCs (Aulinger et al., 2016).

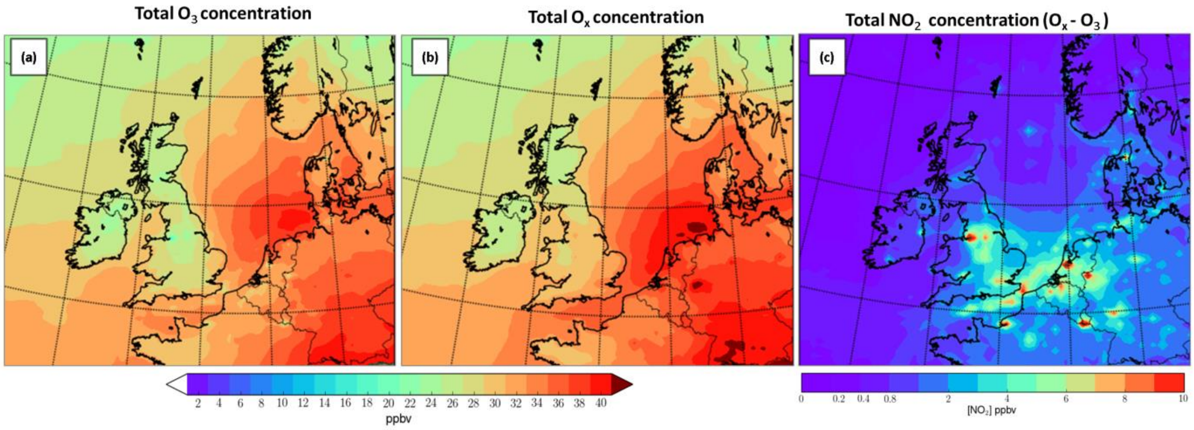

Figure 4.5. Spatial distribution for July 2015 of total surface O_3 (a), total O_x (b), and total NO_2 (c). Please note the different scale on figure c.

4.3.1.2 Contributions from the lateral boundary

The second column in Fig. 4.4 can be compared with the features observed in the simulated mean surface O_3 (section 4.3.1.1). The absolute contribution from the LB decreases southward and eastwards. Over the Atlantic, part of this might be attributed to a greater chemical sink O_3 due to the increase in photolysis of O_3 and subsequent production of OH radicals from water vapour (Johnson et al., 1999). Over the UK, depletion of surface O_3 by dry deposition, and chemical loss processes, such as the reaction of O_3 with NO, possibly explain the observed spatial gradient. Increase in the removal of O_3 through dry deposition can also occur under easterly and south-easterly winds when air masses have travelled over the continental Europe prior to arrival to the UK (AQEG, 2009). This may partly explain why the locations towards the south and east of the UK experienced the lowest % contribution from the LB tracer as those regions are closest to the continental sources.

Low O_3 mixing ratios are also obtained in the Midlands and the Southeast owing to the effect of local O_3 scavenging by reaction with NO discussed in section 4.3.1.1, see Fig. 4.5. When O_x is considered, the mixing ratios over most of the Atlantic remain similar to the concentrations of O_3. Except at the coast of France where NO_x emissions from the main shipping routes lead to titration of O_3. This confirms that O_3 is lost over the Atlantic Ocean by an alternative mechanism to the reaction with NO.

Such mechanism includes the photolysis of O_3, as discussed earlier and dry deposition over the ocean surface which is not as fast as it is on land surface, but it can still be important. Consistent with Fig. 4.5, the LB O_x over the Atlantic are equivalent to the O_3 mixing ratios (Fig. 4.6) and only the contributions vary along the main shipping routes over the English Channel, the Southern North Sea and most of the east of the UK and Midlands.

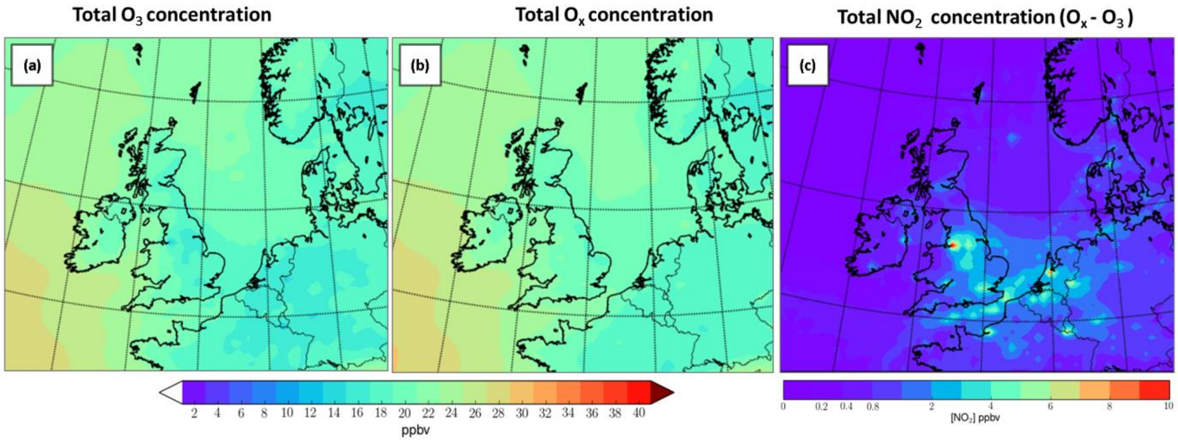

Figure 4.6. Spatial distributions for July 2015 of surface LB O_3 (a), LB O_x (b) and NO_2_LB inheriting tag from O_3_LB (c). Please note the different scale on figure c.

4.3.1.3 Contributions from the domestic source region

Whereas the absolute contribution from the LB over the UK tends to decline with distance towards the south-east, the absolute contribution of domestic anthropogenic NO_x emissions to the mean surface O_3 over the UK (Fig. 4.4 third column) decreases from the south-east to the north and west. Over most of the north and the west, the domestic contributions are rather low, ranging from 1–3 ppb. By contrast, maximum domestic contributions can reach up to 7 ppb in the east and the Midlands during the summer months, as there are here favourable weather conditions for photochemical production and availability of precursors.

4.3.1.4 Contributions from the Eu super-region

The contribution from European NO_x emissions to the mean surface O_3 over the UK (Fig. 4.4 fourth column) is comparable to that observed from the domestic contribution which tends to be higher along much of the eastern, southern and south-west borders, reaching up to 10 ppb in East Anglia during July. This is likely to reflect the effective transport of continental O_3 by south-easterly winds during O_3 pollution events. The European contributions then decreased towards the northern and western areas, with a minimum (1–3 ppb) over Scotland and Ireland.

4.3.2 Monthly variations

In May, the monthly surface O_3 concentrations (Fig. 4.4) are higher than during the summer months, in particular over Ireland, most of the Atlantic Ocean, north of UK, Scandinavia, and part of the North Sea. This is consistent with the Northern Hemisphere mid-latitude spring maximum (Monks, 2000), which is a larger scale phenomenon characteristic of remote locations and so far attributed to both transport of O_3 from the stratosphere to the troposphere (Monks, 2000) and transport of O_3 produced from anthropogenically emitted precursors (NO_x and VOCs) (Monks, 2000; Butler et al., 2018). By contrast, the south east of the UK and part of the North Sea and continental Europe exhibit sustained high O_3 mixing ratios throughout the entire analysed period (May to August) reflecting a spring–summer maximum frequently attributed to photochemical O_3 production (Monks, 2000).

The decrease in the monthly average O_3 mixing ratios towards the summer months over the Atlantic Ocean and most of the British Isles coincided with a progressive reduction in the contribution from LB O_3 over the same areas (second column). Over remote marine areas, it is likely that the decrease in total O_3 is due to an increase in the photochemical activity during the summer months (June-August), as discussed in the previous section. By contrast, O_3 concentrations over land are likely to be altered by the changing background contribution from over the ocean, and by processes occurring at the regional and local scale (Jenkin, 2008). Such processes include O_3 scavenging near emission sources, changes in meteorology (wind direction influencing transport, temperature and radiation influencing photochemical production of O_3), and planetary boundary layer stability (influencing vertical mixing and deposition) (AQEG, 2009). Fig. 4.7 shows that LB O_3 is chemically lost near emissions sources and over an extended area on the southern part of the Atlantic Ocean from May to August.

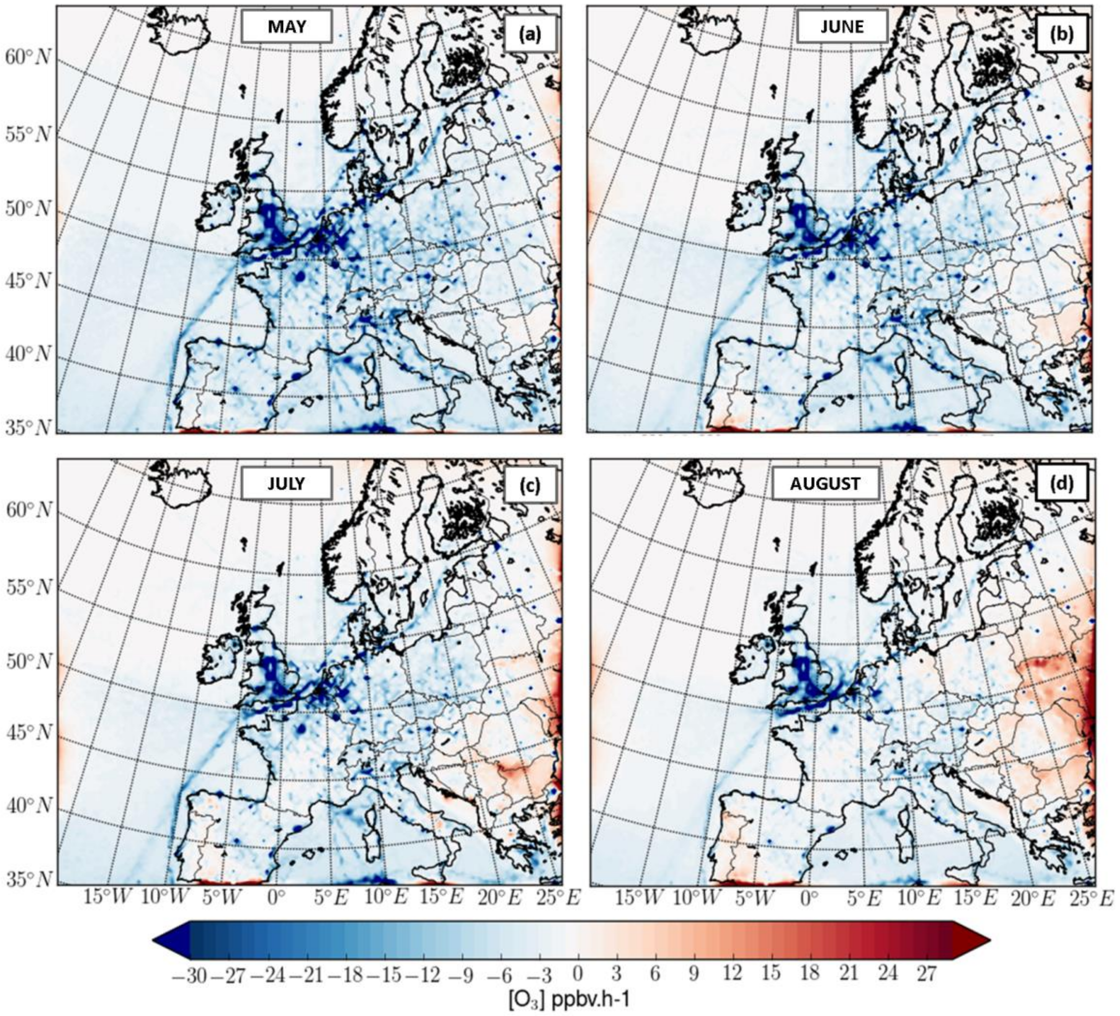

Figure 4.7. Net midday (11:00–14:00 UTC) near surface lateral boundary O_3 production rate in ppbh^{-1} on (a) May, (b) June, (c) July and (d) August 2015. Note that the production is due to NOy that has entered the model domain via the LB.

The monthly relative contributions (%) of each source region calculated from the sum of the absolute contributions of each receptor region are shown in Fig. 4.8. Displayed are the means (red squares), median, 25th and 75th percentile, the maximum and minimum. Whereas the mean hemispheric O_3 background contribution peaks in May, Fig. 4.8a, the contributions from domestic and Eu super-region O_3 are at their largest during the summer months, Fig. 4.8b.

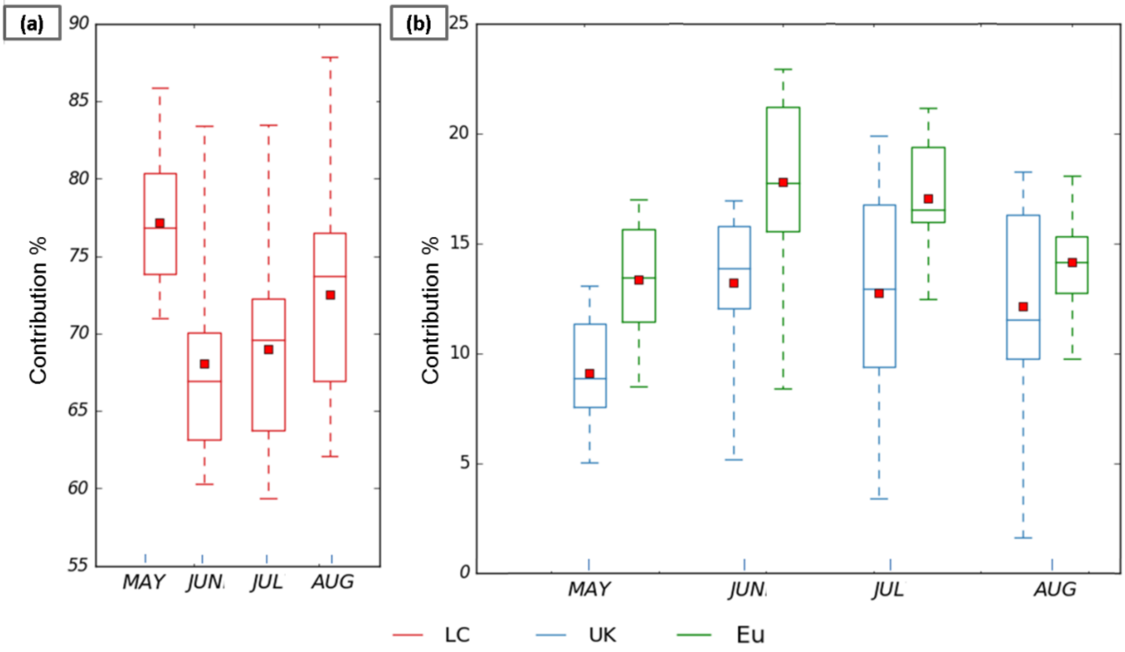

Figure 4.8. Relative contributions (%) to surface O_3 in UK, calculated from May to August 2015, from the lateral boundaries (a), domestic and Eu super_region (b). The lower and upper end of the boxes indicate the 25th and 75th percentiles, the bar the medians, the square the means and the whiskers the minima and maxima, calculated from the monthly values at the 12 receptor regions shown in fig. 4.3. Note the differences in the scales in the *y* axes.

4.3.2.1 *Contributions from the lateral boundary*

Generally, the LB contributed the largest proportion from May to August, exhibiting a maximum in May (mean 76%), a minimum in June (mean 66%), and an increase in August (mean 72%). Note that the monthly maxima (top whiskers on Fig 4.8a) vary very little form May to August. These maxima correspond to Scotland (May and June) and Northern Ireland (July and August); regions that are well-known for exhibiting a pronounced impact from hemispheric O_3 background due to their geographical positions and low regional NO_X emissions (AQEG, 2009). The differences between the minimum and the maximum values are very large in the summer months (June to August) compared with May, indicating that the monthly relative contributions can vary considerably between receptor regions during those months. The minima (lower whiskers) correspond to East Anglia (May, July and August) and the South East (June).

The median divides the contributions into the regions that exhibit the highest contribution (the west and north) and those that receive a lesser contribution (the east and south). The drop in the LB % contribution in the summer months reflects the seasonal cycling in the northern hemispheric background O_3 (e.g. Monks, 2000; AQEG, 2009).

4.3.2.2 Contributions from the domestic source region

The domestic contributions tend to increase in June and decrease again in August, Fig. 4.8b. This monthly variation in the O_3 contributions is mainly caused by larger photochemical activity taking place during the summer months (e.g. Derwent et al., 2010); Monks et al., 2015). In this condition, O_3 is formed by reactions involving the oxidation of VOCs in the presence of NO_x and under the influence of solar radiation (Monks et al., 2015). In addition, the spatial gradient in the contributions (gap between the 25th and the 75th) tends to be smaller in May and June (less than 5%) compared with the July and August (over 10%). In the hottest months, the spread in the domestic contribution reflects the spatial distribution in the photochemical O_3 formation (Fig. 4.9). Overall, the 75th percentile contains the receptor regions located in the east, south east and the east Midlands. These areas tend to be drier, warmer, and sunnier than those regions further west and north (lower percentiles), features that are conducive to photochemical O_3 formation (e.g., Jenkin, 2008; Coyle et al., 2002). Furthermore, these regions hold some of the largest cities in UK (e.g. London, Birmingham, Nottingham, Manchester and Leeds) which can lead to net O_3 formation downwind of the emission sources where the NO_x titration effect is reduced. In fact, Fig. 4.9 shows that, overall, the south and east of the UK exhibit the highest midday (11:00–14:00) O_3 chemical production from UK anthropogenic sources, especially during June and July. By contrast, lower O_3 chemical production is observed in the west and the north beyond Yorkshire and Humberside (the same regions that fall under the 25th percentile in Fig. 4.8b).

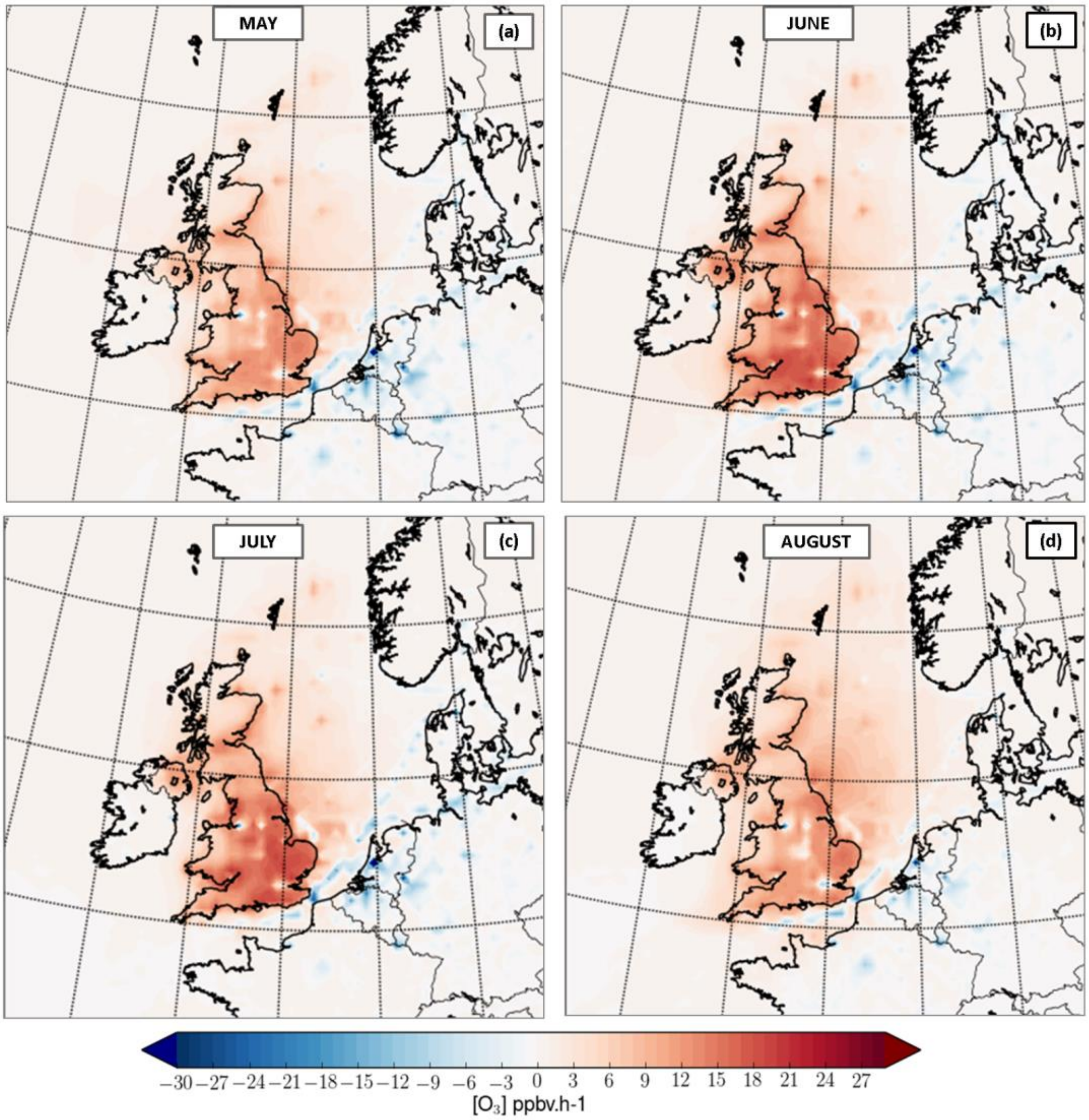

Figure 4.9. Net midday (11:00–14:00 UTC) surface chemical production rate in ppbh^{-1} for O_3 from UK anthropogenic NO_x emissions in May (a), June (b), July (c) and August (d) 2015.

Note that it is not possible to disentangle the source of O_3 on the east of Scotland and the Norfolk coasts over the North Sea. This is due to an error in the emissions file arising after the merging of the emissions inventories TNO-MAC and NAEI. The error comes from missing point sources from oil and gas operations in the North Sea in the TNO-MAC inventory that filtered out in the merged file. Thus, any O_3 production near these point sources is either originating from either UK NOx or NOx coming from oil and gas operations. Nevertheless, the presence of these discrete O_3 production points reveals that oil and gas operations in the North Sea are a significant source of pollutants.

4.3.2.3 Contributions from Europe super-region

The biggest contributions from European emissions to surface O_3 in the UK are observed in the locations closer to the continent (East Anglia, South-East England and Yorkshire), Fig. 4.9. The lowest contributions are observed over Scotland (May and June) and Ireland (July and August). Fig. 4.10 further shows that surface O_3 from anthropogenic sources from the Eu super-region is mainly produced outside the UK. This indicates that the contribution from EU emissions to UK surface O_3 is predominantly due to transport of O_3 rather than its NOy precursors. Fig. 4.10 also shows that O_3 from EU sources is chemically lost nearby the largest cities in UK (e.g. London area, Birmingham, Nottingham, Manchester and Leeds) and also in the English Channel and North Sea. Another notable feature of Fig. 4.10 is that chemical production peaked in June and July and was generally concentrated over central Europe and the Baltic Sea. By contrast, chemical loss happened within the main urban centres, nearby point sources and along the shipping routes around Western Europe, the North Sea and English Channel, e.g., sites previously identified to be influenced by NO_x titration.

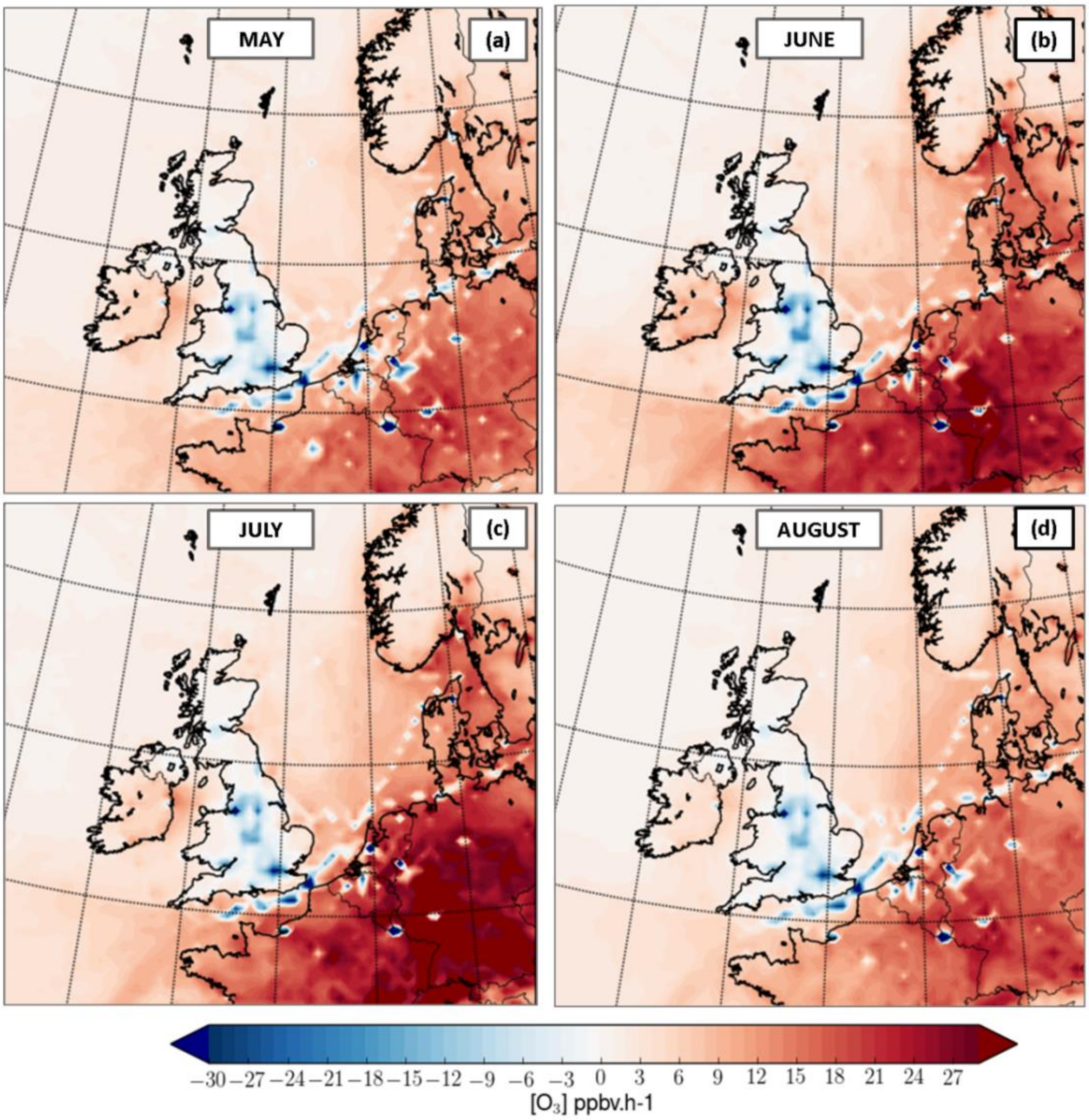

Figure 4.10. Net midday (11:00–14:00 UTC) surface chemical production rate in ppbh^{-1} for O_3 from European anthropogenic NO_x emissions in May (a), June (b), July (c) and August (d) 2015.

So far, the discussion regarding the impact of Eu super-region NO_x emissions on UK surface O_3 has included emissions from shipping routes in the North Sea and the English Channel. Fig. 4.11 shows that when those sources are excluded the contributions from the Eu super-region decrease in all months. This suggests that ship emissions along these routes could exert a negative impact on the air quality over the UK. O_3 production over the UK driven by NOx emissions from ship traffic over the English Channel has been previously identified (Huszar et al., 2010).

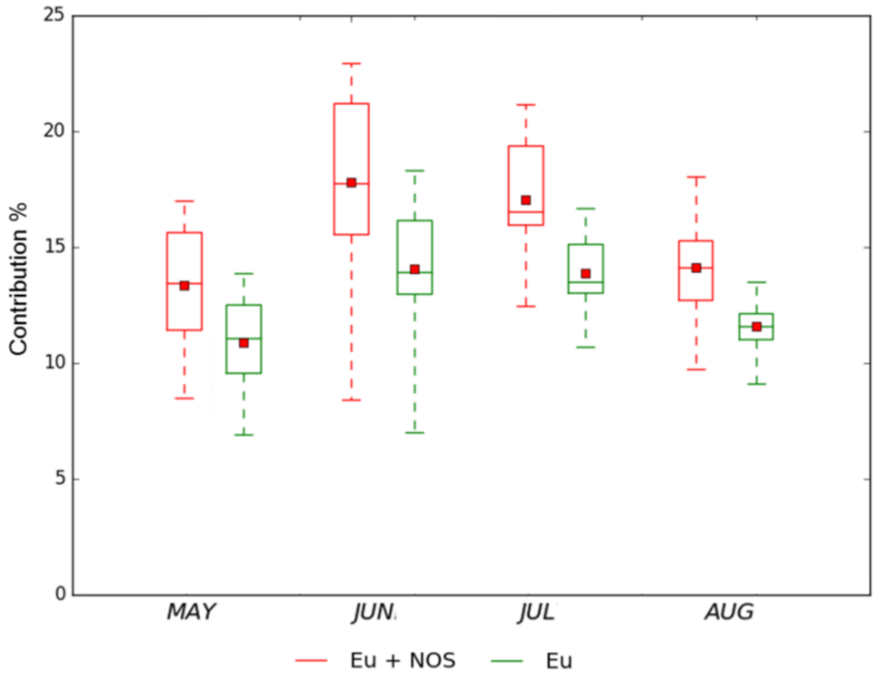

Figure 4.11. Eu super-region contributions to surface O_3 in the UK from May to August 2015: including ship emissions from North Sea and English Channel (red) and excluding ship emissions (green).

4.3.3 Summary

In this section the contribution of domestic and European NO_x emissions and lateral boundary O_3 to surface O_3 in the UK was quantitatively assessed using a tagged-ozone method (Research question I and IV). It has been shown that, between May and August 2015, 71% of the modelled UK surface O_3 comes from the lateral boundaries. About 16 % is instead produced from anthropogenic NO_x emissions in the EU super-region (which contains lumped NO_x emissions from Europe (excluding UK), and from ship emissions in the Atlantic, North Sea, Baltic Sea and the Mediterranean). Domestic UK emissions (England, Scotland, Wales and Northern Ireland) contribute for 13%. The findings are in good agreement with previous source contribution studies in Europe (e.g. Karamchandani et al., 2017; Butler et al., 2018).

The relative contribution from LB O_3 is larger on May than in the summer months, this is attributed to air coming from the clean marine sector depleting O_3 during the warmer months. Moreover, the absolute contribution exhibits a marked dependence on latitude and longitude; high mixing ratios are predicted in the north and west of UK while low values are obtained in the south-east. It has been also demonstrated that overall LB O_3 is chemically lost near emissions sources in the Midlands, London area and the shipping lanes in the North Sea, English Channel and Atlantic Ocean. LB O_3 is also depleted over an extended sector in the Atlantic below latitude 50° which is attributed to the photolysis of O_3 and subsequent production of OH rather than to reaction with NO.

The relative contributions from the Eu super-region source tend to increase towards June and decrease again in August. The absolute contribution to UK surface O_3 is comparable to that observed from the domestic contribution, which tends to be higher along much of the eastern, southern and south-west borders possibly reflecting the effective transport of continental O_3 by south-easterly winds during O_3 pollution events. The contributions then decreased towards the northern areas.

It has been shown that O_3 from anthropogenic sources from within the Eu super-region is mostly transported to the UK rather than produced in-situ. Similarly, the domestic relative contribution to UK surface O_3 tend to increase towards June and decrease again in August. There is also a marked spatial gradient, with high mixing ratios obtained in the south-east and lower values in the north and west. This monthly and spatial variation is primarily caused by larger photochemical activity taking place during the summer months in the south and downwind emissions sources. It was also demonstrated that ship emissions in the North Sea have a negative impact on the air quality of the UK, in particular over the East Anglia region, the South-east and Yorkshire.

4.4 Regional differences

Table 4.1 summarises the absolute monthly mean contributions to surface O_3 at twelve UK regions from the lateral boundaries, domestic, North Sea and English Channel and four Eu sub-regions. The differences in the simulated contributions across the UK regions are further presented in Figs. 4.12 to 4.15. The figures contain 12 nested pie charts, each one associated with a specific region in the UK, which give the absolute and relative contributions to O_3 mixing ratios in the UK from all anthropogenic NO_X sources including ship emissions. The outer circle of the charts shows the contributions from four source regions: Domestic, Eu super-region, North Sea and English Channel, and the lateral boundaries. The inner circle breaks up the contributions from the Eu super-region into 4 sub-regions (The Benelux, France, Germany and the rest of EU). It is worth noting that the contributions from the Rest_EU source need to be carefully interpreted since these include emissions from the Iberian Peninsula, Southern EU, South-eastern EU, Eastern EU, Northern EU, and ship emissions from the Atlantic, Baltic Sea and the Mediterranean. As in the previous sections, the results are discussed by grouping contributions with common features.

4.4.1 Contributions from lateral boundary ozone

In every receptor area, the LB is the principal contributor to the simulated monthly mean O_3 from May to August. The contributions peak in May (mean absolute contribution 25 ppbv) and the share is larger at the regions located in the north and west of the UK (e.g. Scotland (30 ppbv), Northern Ireland (28 ppbv), North-East (27 ppbv), the North-West and Wales (26 ppbv)), while the contributions in the South-East, East Anglia and East Midlands can be up to 8 ppbv smaller than in those regions in the north and west. A particular pattern is observed during summer July and August. Although the relative contributions in the north-western regions are still larger than in the south-western counterparts, the absolute contributions are slightly higher in the South-West (72%, ~21 ppbv) and Wales (76%, ~21 ppbv) compared with Scotland (76%, ~20 ppbv) and Ireland (79%, ~20 ppbv).

Table 4.1. Absolute monthly contributions (in ppbv) to surface O_3 in the UK regions from May to August 2015. The reported values correspond to the contributions from anthropogenic sources only, thus the differences between the sum of the contributions and the total simulated O_3 correspond to the O_3 form from naturally emitted NO_x and biomass burning.

Receptor		East Anglia	Southeast	Southwest	Wales	East Midlands	West Midlands	Yorkshire	Northwest	Northeast	Scotland	Ireland	London	Mean
Lateral Boundaries	May	22.8	22.8	25.3	26.3	22.9	23.9	25.1	26.3	27.9	30.1	28.1	22.4	25.3
	June	19.6	19.1	20.5	21.5	19.1	19.5	20.3	20.3	21.2	24.5	23.0	18.7	20.7
	July	17.4	18.4	20.7	21.3	17.0	18.6	17.2	18.3	18.3	19.8	19.8	16.9	18.7
	August	17.7	17.9	20.8	22.1	17.6	18.6	18.3	19.7	20.2	21.5	21.3	16.2	19.5
Domestic	May	4.2	3.6	2.5	2.6	3.6	3.0	3.2	2.6	2.6	1.9	2.3	3.9	3.0
	June	5.4	4.9	3.9	3.7	4.9	4.4	4.3	3.9	4.0	2.3	2.2	5.3	4.0
	July	5.8	4.0	2.2	2.2	4.9	3.3	4.4	3.2	3.6	2.6	1.9	4.8	3.6
	August	5.2	4.4	3.0	2.3	4.3	3.1	3.9	2.6	2.9	2.4	1.1	4.6	3.3
Benelux	May	0.7	0.8	0.7	0.7	0.6	0.6	0.6	0.6	0.6	0.5	0.6	0.8	0.6
	June	1.0	0.6	0.4	0.4	0.5	0.4	0.4	0.3	0.2	0.0	0.0	0.7	0.4
	July	0.6	0.2	0.0	0.1	0.4	0.2	0.5	0.2	0.4	0.2	0.0	0.3	0.3
	August	0.5	0.3	0.1	0.1	0.2	0.1	0.2	0.1	0.2	0.1	0.0	0.3	0.2
France	May	0.6	0.7	0.6	0.4	0.4	0.4	0.3	0.3	0.2	0.2	0.3	0.7	0.4
	June	0.7	1.1	1.0	0.5	0.4	0.4	0.2	0.2	0.1	0.1	0.1	1.0	0.5
	July	1.1	1.5	1.0	0.7	0.7	0.7	0.5	0.6	0.5	0.5	0.5	1.4	0.8
	August	0.8	0.9	0.5	0.4	0.5	0.5	0.3	0.3	0.2	0.2	0.2	0.9	0.5
Germany	May	0.2	0.2	0.2	0.2	0.2	0.2	0.2	0.2	0.2	0.2	0.2	0.2	0.2
	June	0.8	0.7	0.7	0.9	0.7	0.8	0.7	0.6	0.5	0.1	0.0	0.7	0.6
	July	0.3	0.0	0.0	0.0	0.1	0.0	0.2	0.0	0.2	0.1	0.0	0.0	0.1
	August	0.4	0.2	0.1	0.1	0.2	0.1	0.3	0.2	0.3	0.2	0.0	0.2	0.2
North Sea and Channel	May	1.1	1.3	0.9	0.6	0.8	0.7	0.8	0.7	0.8	0.6	0.5	1.1	0.8
	June	1.8	2.0	1.5	1.0	1.3	1.0	1.2	0.7	0.8	0.4	0.3	1.7	1.1
	July	1.3	1.4	1.0	0.5	0.9	0.6	1.0	0.7	0.9	0.8	0.4	1.2	0.9
	August	1.3	1.1	0.7	0.5	0.8	0.5	0.7	0.5	0.6	0.4	0.2	1.0	0.7
Rest of Europe	May	2.4	2.7	3.3	3.1	2.1	2.5	2.0	2.2	2.0	1.6	1.9	2.4	2.4
	June	2.5	2.8	3.8	3.6	2.3	2.7	2.6	2.9	2.6	1.9	2.6	2.6	2.8
	July	2.4	2.9	3.8	3.4	2.3	2.7	2.4	2.7	2.4	2.0	2.3	2.5	2.6
	August	2.1	2.2	2.6	2.5	2.1	2.2	2.3	2.3	2.5	2.3	2.2	1.9	2.3
Sum of the Contributions/ Total simulated ozone	May	32.1	32.1	33.6	34.0	30.6	31.5	32.4	32.9	34.3	35.0	33.8	31.5	32.1
	Total O_3	32.8	33.1	34.6	35.0	31.5	32.5	33.3	33.8	35.2	35.8	35.0	32.5	32.8
	June	31.7	31.3	31.9	31.6	29.2	29.1	29.6	29.0	29.4	29.2	28.3	30.7	31.7
	Total O_3	32.0	31.7	32.2	31.9	29.5	29.4	29.9	29.2	29.7	29.4	29.5	31.0	32.0
	July	28.9	28.5	28.7	28.2	26.4	26.1	26.1	25.8	26.3	26.0	25.0	24.9	28.9
	Total O_3	29.3	28.9	29.3	28.5	26.8	26.4	26.5	26.1	26.6	26.3	25.6	25.3	29.3
	August	28.0	27.0	27.8	28.0	25.8	25.1	26.0	25.6	26.9	27.2	25.2	25.1	28.0
	Total O_3	28.4	27.4	28.1	28.2	26.1	25.4	26.3	25.9	27.3	27.6	25.7	25.5	28.4

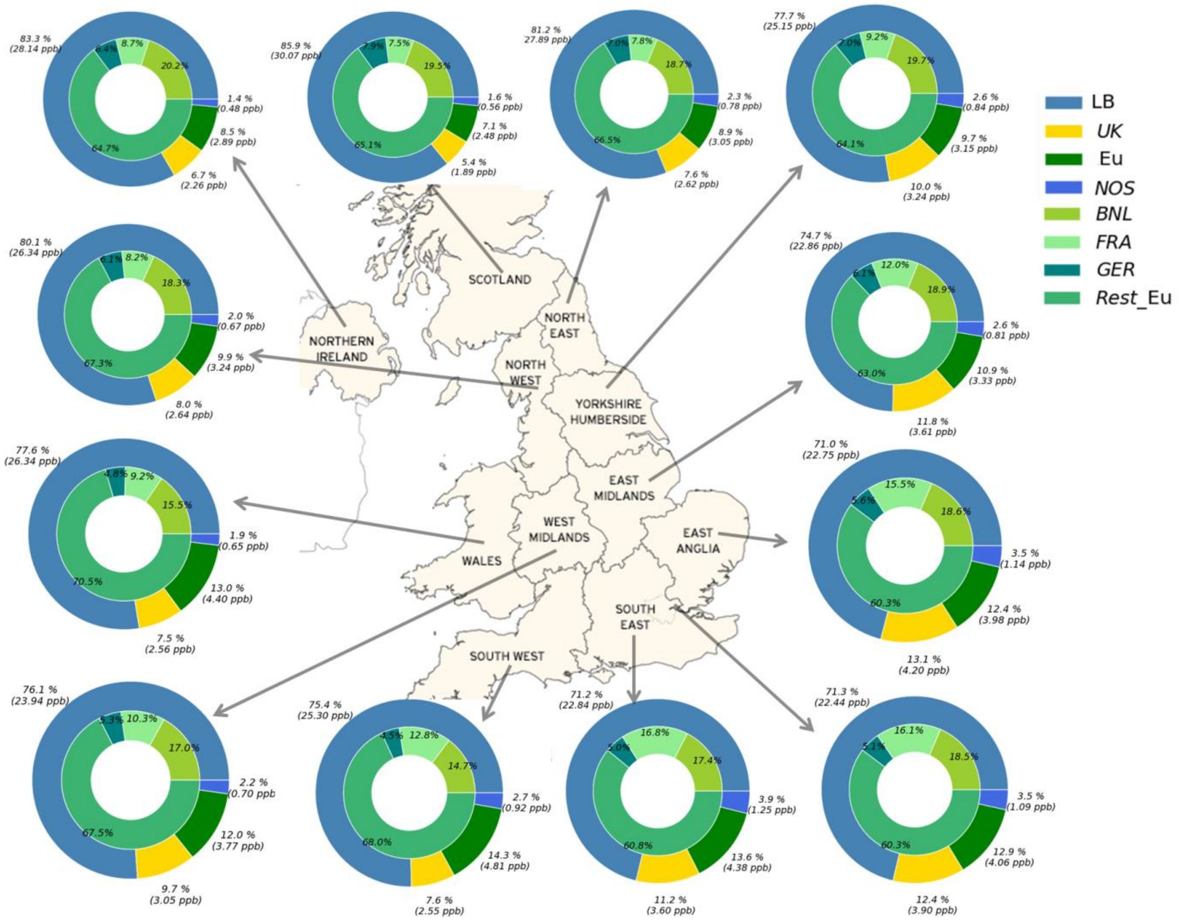

Figure 4.12. Simulated contributions to the mean O_3 mixing ratios in May 2015 over 12 receptors regions in the UK. Outer circle depicts the contributions from LB, UK, Eu super-region, and the NOS. The inner circle breaks up the contribution from the Eu super-region into four sub-regions: the Benelux (BNL), France (FRA), Germany (GER), and the rest of Europe (Rest_EU). Note that the values correspond to the contributions from anthropogenic sources only, with exemption to the LB which includes O_3 from stratospheric origin.

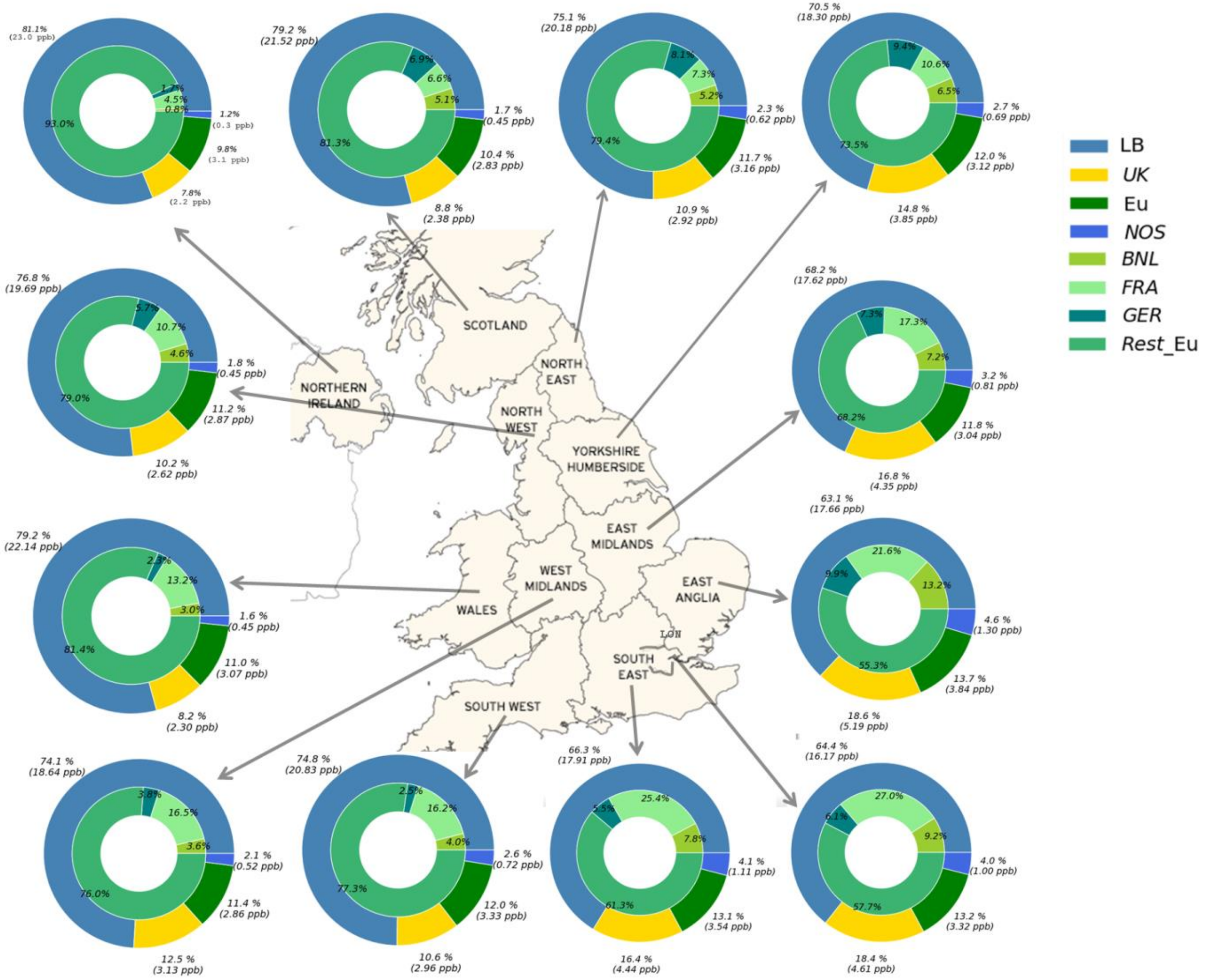

Figure 4.13. As in Fig. 4.12 but for June 2015.

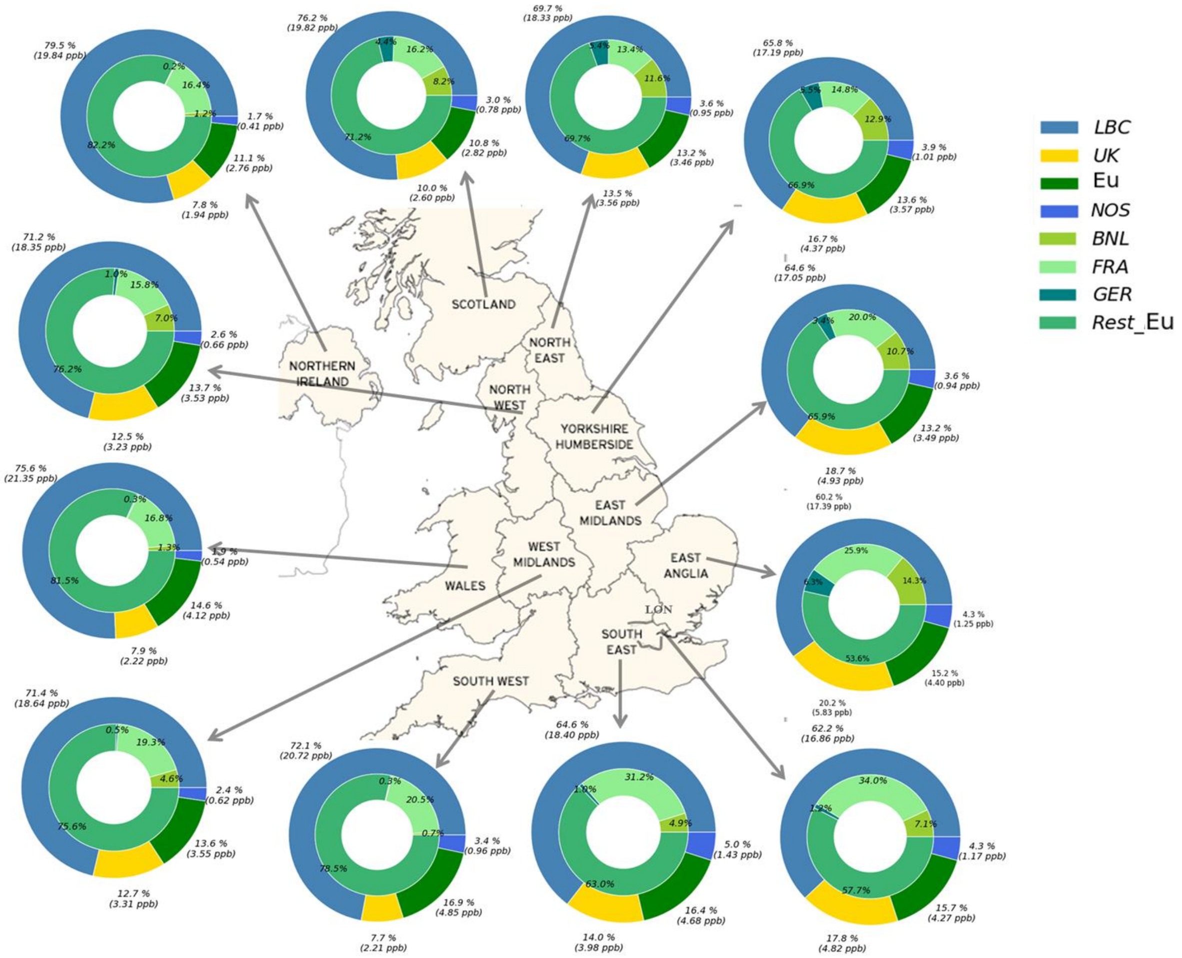

Figure 4.14. As in Fig. 4.12 but for July 2015.

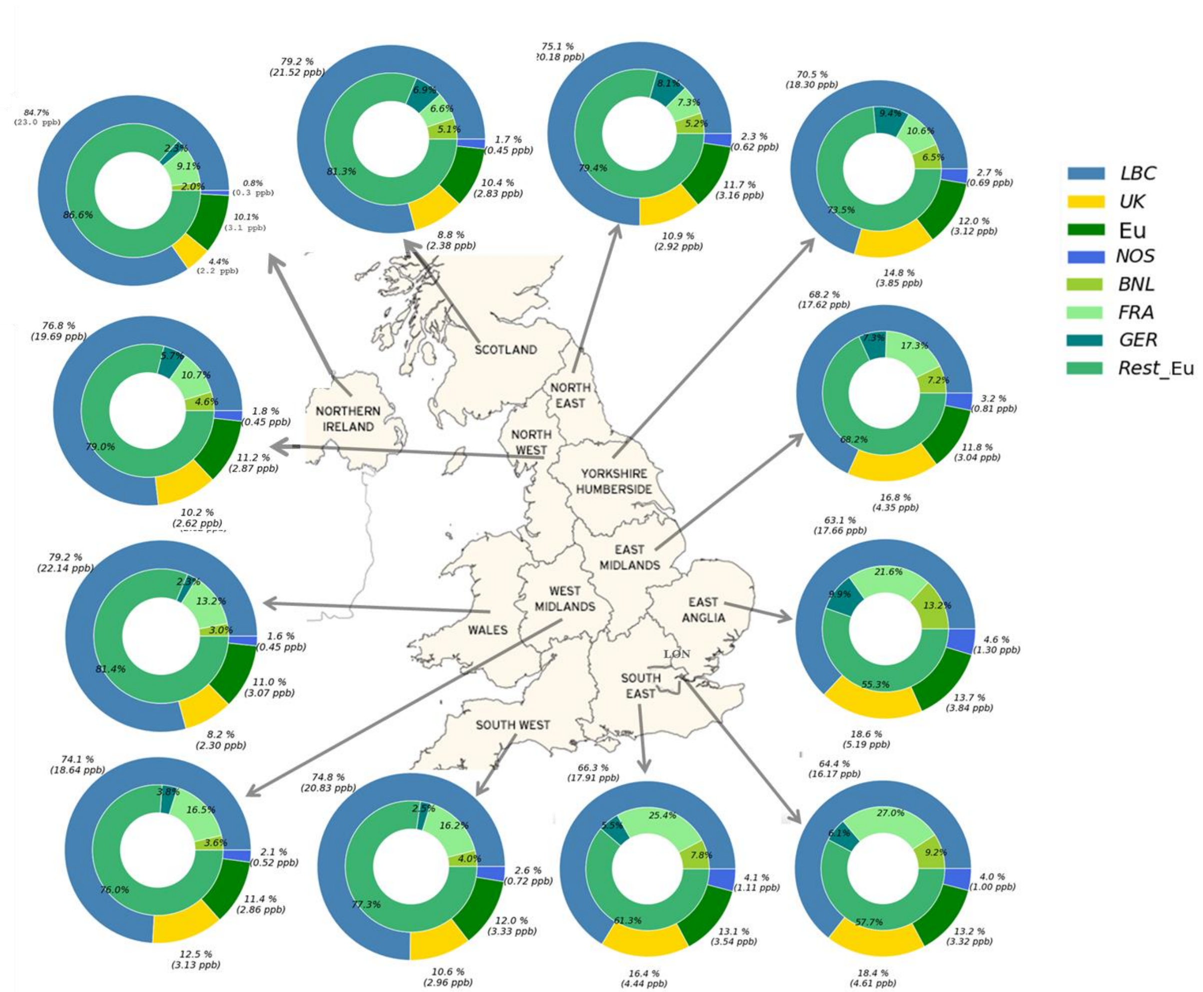

Figure 4.15. As in Fig. 4.12 but for August 2015.

4.4.2 Contributions from domestic source region

The share of the domestic contributions (both the absolute and the relative values) is higher in the south-east, east and the Midlands. The contributions peak in June and July in every receptor area, providing up to 20% of the surface O_3 in East Anglia, 18% in the London area and East Midlands, and 16% in Yorkshire and Humberside and the South East, making the domestic contribution the second biggest source at these locations. However, the differences in the absolute contribution over these receptor areas are very small (less than 1 ppbv except for the East Anglia region) when compared with the contributions from Eu super-region.

4.4.3 Contributions from the Eu super-region

The Eu super-region is the second largest source region in the northern and western UK, with contributions in summertime reaching up to 10% in Scotland and up to 16% in South-West England and 14% in Wales. Nonetheless, the source region still has a large impact on the South-East and East Anglia where the relative contributions increased from 12% in May to up to 16% in July.

4.4.4 Contributions from the North Sea

The contributions from ship emissions on the North Sea and English Channel are significantly lower than those from domestic sources and Eu super-region (3-4% of the total contribution in the South and East Anglia in May and up to 6% of the total surface O_3 during the summer months). The impact is also less important in the west than in the east and south of the UK.

4.4.5 Contributions from the Eu sub-regions

As for the relative contributions from the different Eu sub-regions (inner circle in

Figs. 4.12 to 4.15), these are largely influenced by the geographical situation of the receptors and the predominant wind direction. In every receptor, the principal contributor from the Eu super-region is the Rest_Eu source region, providing between 60-70% of the Eu O_3 in May and up to 90% of the O_3 from Eu during summertime. The relative contributions of the Rest_Eu region are stronger in the northern and western locations, in particular during the summer months. There is also a marked difference in the distribution of the contributions across the UK regions between May and the summer months. In general, the share of the Rest_Eu source region is somewhat smaller throughout the receptor regions in May (Fig. 4.12), ranging from about 60-70%. Therefore, the north-south and east-west differences in the contributions are lower. By contrast, the differences in the contributions are more marked in the summer months due to an increase in the input from France, Germany and the Benelux region, in particular over the receptor regions located in the south and east of the UK (e.g. South East England, East Anglia, the London area and the East Midlands).

The contributions from the Benelux region and Germany are more significant in the east of the UK due to the proximity with the continent (about 14% and 6% of the total contribution in the East Anglia during the summer months comes from these two source regions respectively). Nonetheless, small quantities of O_3 from the Benelux and Germany can be seen in remote regions in the UK such as Northern Ireland, e.g., Figs. 4.12 and 4.14. Depending on the predominance of the wind direction, O_3 from anthropogenic sources within France can impact both the west and the east of the UK. The contribution is greater in the southern UK due to the proximity to the source region (up to 34% of the Eu super-region share in the London area in July, see Fig. 4.14). Yet, O_3 from France is also observed to a lesser extent in the western UK and Northern Ireland.

4.4.6 Summary

In this section, the regional variation in the contributions from the Eu super-region, domestic and NOS anthropogenic NO_X, and LB O_3 to surface O_3 in different receptor regions across the UK was quantitatively estimated (research question II). The shares from four additional sub-regions within the Eu super-region (the Benelux, FRA, GER and the Rest of Eu) were also assessed (research question IV). It has been demonstrated that the LBs are the principal contributor to the simulated monthly mean O_3 at all receptor regions between May and August 2015. Moreover, domestic NO_x emissions are the second largest contributor to surface O_3 in the East Midlands, West Midlands, Yorkshire and the Humberside, East Anglia, South East England and the London. In the northern and most of the western sites, NO_x emissions from the Eu super-region are instead the second most important source of surface O_3. When the Eu super-region contribution is split into sub-regions, it is observed that Germany and the Benelux have a large impact in the south and east of the UK. Nonetheless, small contributions from these source regions are found as far as Northern Ireland. On the other hand, impact from France is remarkably wider, in particular during the summer months, reaching most of the UK in the whole analysed period.

4.5 Implications for policy standards

4.5.1 Ozone contributions when the MDA8 O_3 of 50 ppbv is exceeded

Fig. 4.16 shows the statistical distribution of the absolute contributions from each source region for all hours when the MDA8 O_3 exceeded 50 ppbv at each receptor area from May to August. The ranges between the maximum and minimum contributions highlight the fluctuations in the hourly contributions. However, because the intention of this section is to elucidate the differences in the contributions at each receptor area, the discussion is mainly based on the mean of the contributions hereafter.

The most remarkable feature in Fig. 4.16 is the important contributions coming from source regions that did not show dominance in the monthly contributions. France, for example, becomes a major source in particular in the regions located in the south and east of the UK. The absolute mean contributions at the sites can easily equal and even surpass the input from the LB O_3 (mean value ranging between 10 and 15 ppbv, and maximum reaching up to 35 ppbv in the London area). The impact from domestically produced O_3 varies across the sites, but in general the share increased from the south-east to the north. In the Midlands, the North East, North West, Scotland and Yorkshire and the Humberside, O_3 from domestic sources becomes dominant surpassing the LB mean input in most of the receptor regions. In the rest of the locations the domestic source is the third largest input for surface O_3 after France and the LBs with the exception of the South West where most of the O_3 comes from France (mean ~18 ppbv), the LB (mean ~14 ppbv), NOS (mean ~6 ppbv) and Rest_Eu (mean ~8 ppbv).

The Rest_Eu region has a larger impact in the southern sites, in particular in East Anglia where the share can be greater than the contributions from domestic sources (mean value ~7 ppbv). The impact decreases towards the northern regions showing sporadic large values e.g. the North West which could be apportioned to emission sources in the Irish Sea.

The impact from the shipping component (NOS) also becomes important in all receptor regions with an estimated mean of 4-7 ppbv. Moreover, the source region did not show a greater impact on for eastern or southern locations as in Figs. 4.14 to 4.15. O_3 from Central Eu, Germany, Netherlands, Belgium and Luxembourg, on the other hand, is almost negligible in the west of the UK (mean less than 1 ppbv), however their impact increases towards the east and north with mean values ranging about 1-6 ppbv (e.g. in the East Midlands, North-East, Yorkshire and the Humberside and Scotland) likely reflecting the efficient transport of polluted-loaded air masses under anticyclonic conditions.

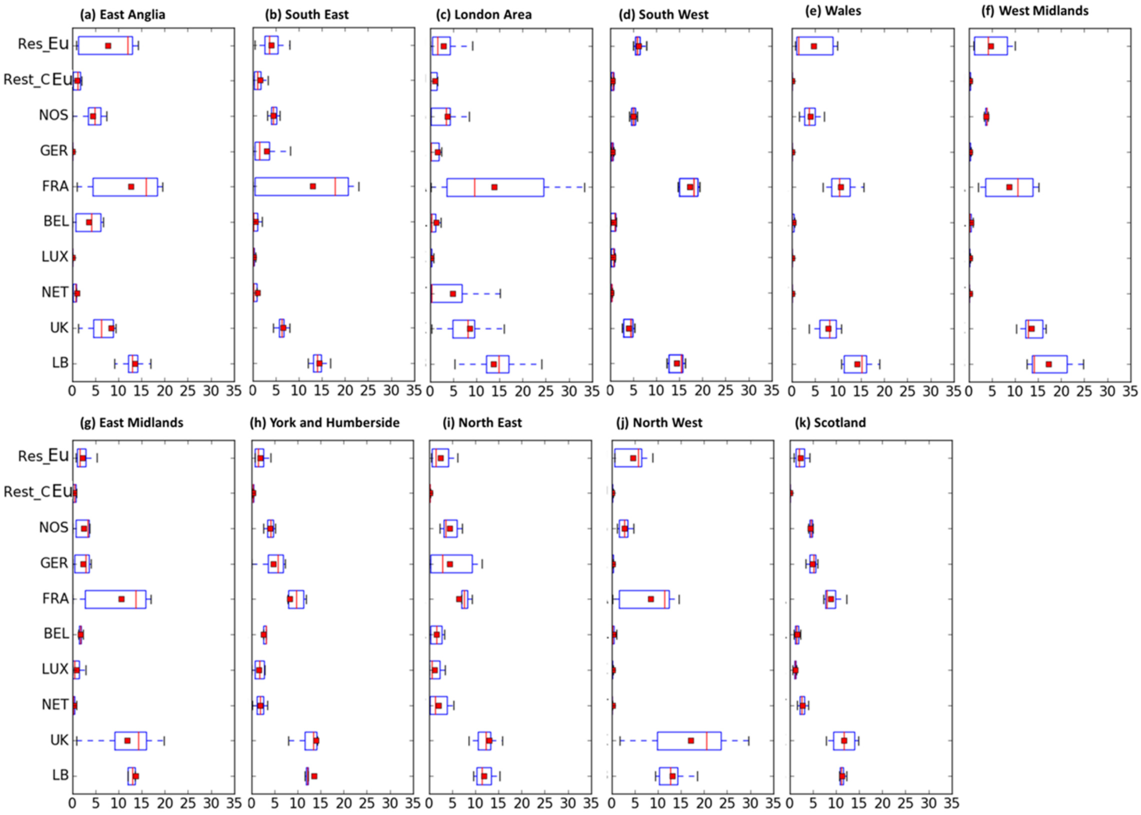

Figure 4.16. Hourly contributions, in ppbv, to surface O_3 at 11 UK receptor regions from 10 sources (domestic (UK), background (LB), the Netherlands, Luxembourg, Belgium, France, Germany, rest of Central Europe, North Sea and English Channel (NOS) and rest of Eu) during days when the MDA8 is above 50 ppbv between May and August. The lower and upper ends of the boxes indicate the 25th and 75th percentiles, the bars the medians, the dots the mean and the whiskers the minima and maxima.

4.5.2 Ozone contributions when the MDA8 O_3 of 60 ppbv is exceeded

Fig. 4.17 illustrates the differences in the contributions at each receptor area to elucidate the differences in the spatial distributions of the statistical distributions of the contributions to hourly surface O_3 when the MDA8 O_3 exceeded the 60 ppbv threshold.

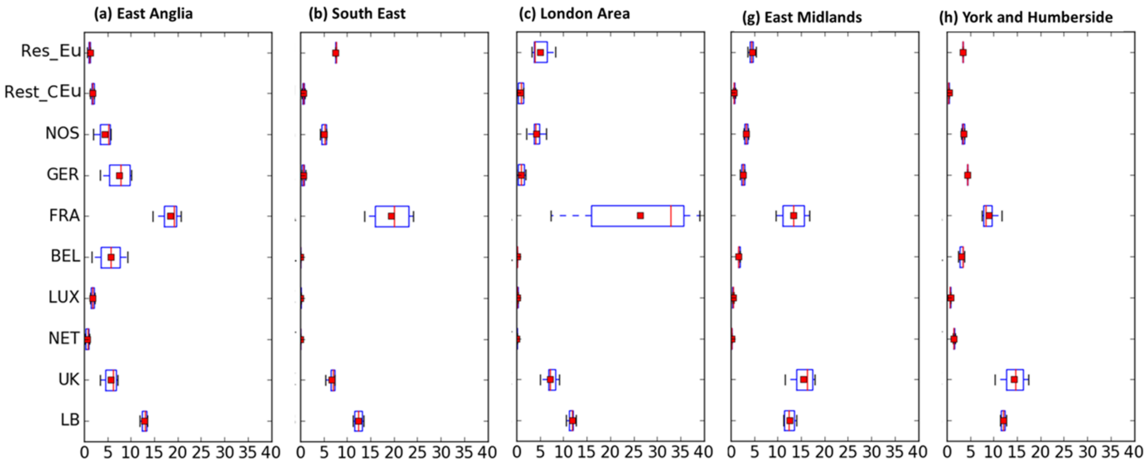

Figure 4.17. Hourly contributions, in ppbv, to surface O_3 at 3 UK receptor regions from 10 sources (domestic (UK), background (LB), the Netherlands, Luxembourg, Belgium, France, Germany, rest of Central Europe, North Sea and English Channel (NOS) and rest of Eu) during days when the MDA8 is above 60 ppbv between May and August. The lower and upper ends of the boxes indicate the 25th and 75th percentiles, the bars the medians, the dots the mean and the whiskers the minima and maxima.

The figures reveal the hourly fluctuations of the contributions during the peak O_3 event recorded on 1st July. France is the most significant contributor to the build-up of O_3 when the mixing ratios exceeded the EU threshold in South East England (mean ~18), East Anglia (mean ~21) and the London area (mean ~26 ppbv). O_3 from domestic sources, on the other hand, has a greater impact on the East Midlands (mean ~16), Yorkshire and Humberside (mean ~15). In the South-East and the London area, the contributions from Rest_Eu equal those from domestic O_3, while the influence is comparable to that from the west and Central Europe in the rest of the regions. As in the contributions to the MDA8 O_3 of 50 discussed in section 4.5.1, the lateral boundary component remained nearly constant in all receptors areas with a mean contribution about 12 ppbv. The impact from the North Sea and English Channel is also important in all receptor regions with a similar estimated mean between 4-7 ppbv.

Results suggest that ship emissions along these routes affect the air quality of the UK, in particular over the East and South-east. However, it is worth noting that the current model configuration does not consider the chemical evolution of the different emitted species (chemical loss and production rates) during the dispersion of the ship plume. In fact, once species are emitted, they are instantaneously mixed in each model grid cells (27 x 27 km). In the case of chemically reactive species such as NOx, this can lead to overestimations of both NOx and O_3 concentrations due to the non-linearity of the chemical processes involving NOx and O_3 evolution during the dispersion of the ship plume (e.g., Kasibhatla et al., 2000; Huszar et al., 2010).

4.5.3 Ozone contributions to the AOT40 index

The average simulated AOT40 for 2015 at the two most relevant arable areas in the UK: East Anglia and the South East is 3674 and 1833 μg m^{-3}hours, respectively (the EU target value is the 18000 μg m^{-3} hours). Fig. 4.19 shows the source contributions to the surface O_3 when the mixing ratio exceeded 40 ppbv during the daytime hours (08:00 and 20:00) Central European Time from May to July in two receptor regions in the UK.

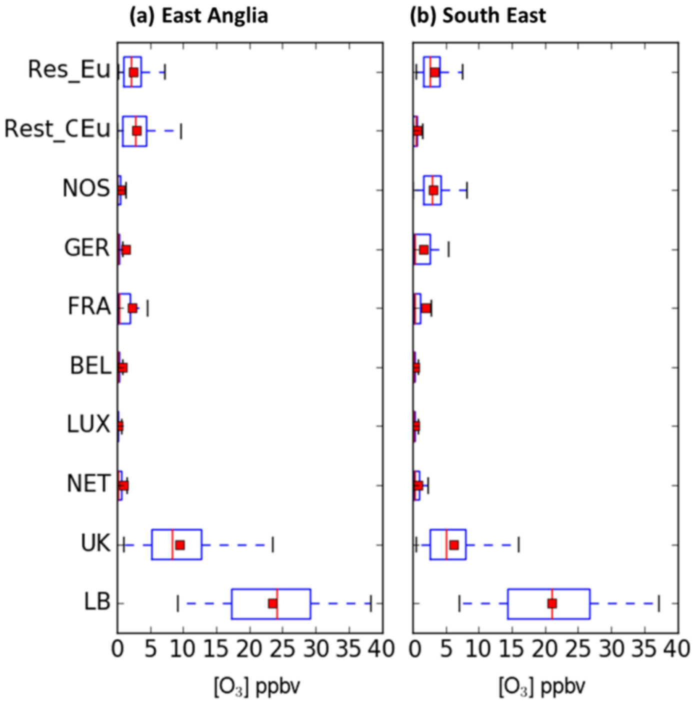

Figure 4.18. Hourly contributions, in ppbv, to surface O_3 at 11 UK receptor regions from 10 sources (domestic (UK), background (LB), the Netherlands, Luxembourg, Belgium, France, Germany, rest of Central Europe, North Sea and English Channel (NOS) and rest of Eu) during days when the MDA8 is above 60 ppbv between May and August. The lower and upper ends of the boxes indicate the 25th and 75th percentiles, the bars the medians, the dots the mean and the whiskers the minima and maxima.

Fig. 4.18 demonstrates that the O_3 contributions behave differently depending on the metric considered. Compared with the contributions to the MDA8 O_3 of 50 and 60 ppbv discussed in sections 4.5.2 and 4.5.4, when the exceedance to the hourly surface O_3 mixing ratios above 40 ppbv are considered, the LB component becomes the dominant source in both receptors regions (estimated mean concentration between 21-24 ppbv) followed by the domestic component. The impact of domestic O_3 is greater in the East Anglia region (estimated mean concentration 10 ppbv) than in the South East (estimated mean concentration 6 ppbv). Moreover, in East Anglia the third, fourth and fifth contributions come from the Rest_Eu and Rest_CEU regions and France, while in the South East the contributions come from the North Sea and English Channel, Rest_Eu and Germany. The contributions from the Netherlands, Belgium and Luxembourg become almost negligible.

It is important to note that plants act as a sink for O_3, through stomatal and non-stomatal processes (Heath et al., 2009). When plants open their stomata to take up CO_2 for photosynthesis other gases, such as O_3, can also enter the plant tissue where they undergo chemical interaction, ultimately oxidizing leaf tissues as in the case of O_3. The AOT40 metric assessed the impacts of O_3 on the vegetation by considering an O_3 threshold (e.g., concentrations above 40 ppbv) during the months when plant growth is most likely to be affected and when daytime O_3 concentrations are at its highest. However, research experiments have shown that the response of plants to O_3 exposure is non-linear due to a mismatch between the peak daytime O_3 concentrations and stomatal opening (Heath et al., 2009). This means that the ambient O_3 concentrations are not always correlated to the effective amount of O_3 up taken by plants. The AOT40 index does not account for the plant's physiological control of stomatal opening, which limits the index to assess the impacts of O_3 on the vegetation accurately. Future work should consider flux-based metrics which have proven to be more suitable for ozone-risk assessment on plants as they take into account the ambient concentration of O_3, the physiological control on stomatal openings, and the efficiency of leaf antioxidant system (Fares et al., 2010).

4.5.4 Summary

In this section the impacts of European and domestic NO_x emissions on ozone-policy relevant standards as well as the importance of the lateral boundary O_3 was estimated (research question III and IV). It was concluded that emission controls would be required in different source regions for compliance of UK and EU O_3 standards, e.g. MDA8 O_3 of 50 and 60 ppbv. As an instance, emissions controls in France are important for the South East, South West and the East Anglia region while domestic emissions controls are more relevant for the Midlands and the north of the UK. Regarding the attainment of lower exposure thresholds such those in the AOT40 O_3 metric, the LB component becomes the dominant source followed by the domestic component. This means that emission controls must be applied over a larger area (e.g. North hemisphere) to mitigate the health-related metric MDA8 O_3 above 50 and 60 ppbv.

4.6 Conclusions

The most important findings from the analysis of the contribution of domestic and EU NO_x emissions and LB O_3 to the monthly surface O_3 in the UK are:

- ✓ Between May and August 2015, 71% of the modelled UK surface O_3 comes from the lateral boundaries, 16 % is produced from anthropogenic NO_x emissions from the Eu super-region and the least 13% comes from domestic UK NO_x emissions. The relative contribution from the LB O_3 peaks in May while the contributions from UK and the Eu super-region increase towards the June and July.
- ✓ The absolute monthly contribution of the LB has a marked dependence on latitude. High mixing ratios are simulated for the north and west while low values are obtained in the south-east of the UK. Moreover, it has been demonstrated that LB O_3 is chemically lost near emissions sources in the Midlands, the London area and shipping lanes in the North Sea, and the

Atlantic Ocean, and over an extended sector in the Atlantic below latitude 50° which might be attributed to the photolysis of O_3 rather than to reaction with NO.

- ✓ The relative monthly contributions from the Eu super-regions decreased towards the northern and inner regions of the UK. Moreover, it has been demonstrated that the contribution from O_3 from Eu NOx is predominantly due to transport of O_3 rather than its NO_Y precursors.
- ✓ The monthly relative contribution from the UK has a marked spatial gradient, with high mixing ratios obtained in the south-east and lower values in the north and west which is mainly caused by larger photochemical activity taking place downwind of emission sources in these areas.
- ✓ Domestic NO_x emissions are the second largest contributor to monthly surface O_3 after the LBs in the East Midlands, West Midlands, Yorkshire and Humberside, East Anglia, South East England and London. While, in the north and most of the western regions NO_x emissions from the Eu super-region are the second most important source. Furthermore, Germany and the Benelux have a large impact in the south and east of the UK. While the impact from France is remarkably wider, in particular during the summer months, reaching most of the UK in the whole analysed period.
- ✓ When the contributions on short-term O_3 mixing ratios such those used in the health-related metrics MDA8 O_3 for 50 and 60 ppbv are assessed, source regions that did not show a previous dominance in the contributions emerge as important sources. France becomes a key source region in in particular over the East Anglia, South-East, South-West and the London. O_3 in the East Midlands, Yorkshire & Humberside, North-East, North-West and Scotland, on the other hand, comes largely from domestic sources. In conclusion, emission controls would be required over Europe, in particular France and the UK, to mitigate the health-related metric MDA8 O_3 above 50 and 60 ppbv in the UK.

- ✓ When looking at lower exposure thresholds, such as those in the AOT40 O_3 metric, the LB component becomes the dominant source follow by the domestic component. Meaning that emission controls would be required over a bigger area (e.g. hemispheric) than those to mitigate the health-related metric MDA8 O_3 above 50 and 60 ppbv.

Chapter 5

THE SOURCE OF OZONE DURING A HIGH CONCENTRATION EPISODE: A CASE STUDY FROM THE ICOZA CAMPAIGN –PART I: PROCESSES CONTRIBUTING TO THE BUILD-UP OF OZONE

5.1 Rationale

In the last 30 years, actions to control the emission of O_3 precursors within Europe have successfully reduced the intensity of regional peak O_3 episodes (Jenkin, 2008; Derwent et al., 2010). However, under certain meteorological conditions, some regions still experience values of O_3 exceeding the European threshold of 60 ppbv 8 hour (h) average (Jenkin et al., 2002; Lee et al., 2006). As a result, exposure to O_3 continues to cause substantial damage to human health in Europe with an estimated 17,000 premature deaths (EEA, 2016).

In summertime 2015, which was the second warmest year in a row in Europe (WHO, 2016), several heatwaves caused elevated O_3 concentrations in Central and Western Europe that exceeded the EU information threshold of 1 h average mixing ratio of 180 $\mu g\ m^{-3}$ (~90 ppbv) (CAMS, 2016; DEFRA, 2017). In the UK the most significant episode occurred between the 30th June and 3rd July. This period coincided with the Integrated Chemistry of Ozone in the Atmosphere (ICOZA) field campaign, which was carried out at Weybourne Atmospheric Observatory (WAO), Norfolk. At WAO, and in several stations in the southeast of the UK, south-easterly winds prevailed from 30th June to 1st July and surface O_3 concentrations reached 100 ppbv in the evening of the 1st July. Modelling studies, such as Jenkin et al. (2002), point to Europe as a major source of O_3 during such south-easterly conditions. Even though increases in O_3 mixing ratios during hot summer days are expected (AQGE, 2009), such O_3 levels are surprisingly high given the reduction in emissions of O_3 precursors in Europe that have occurred over the last decade. It is therefore important to understand the factors that influenced the build-up and evolution of surface O_3 during this episode in order to provide useful information for the formulation of adequate cross-border management strategies.

In this chapter, WRF-Chem is used to characterize the physical and chemical processes influencing the evolution of O_3 during ICOZA with a focus on the origin and build-up of surface O_3 during the pollution episode at WAO and the East Anglia region. Physical processes, including long-range transport from outside the UK, are investigated using inert tracers simulations. The study addresses the following research questions:

i. Which meteorological conditions (e.g. advection, convection, vertical mixing and deposition) are associated with the build-up of O_3 during the pollution episode?
ii. How important are the contributions of the individual meteorological and chemical processes to the build-up of O_3 during the pollution episode?
iii. Where is the O_3 coming from, is it produced in-situ or transported?

The reader is referred to Chapter 2 for details on the general WRF-Chem settings. Description of the pollution episode using observational data from ICOZA and the associated synoptic situation is provided in section 5.2. Section 5.3 briefly describes the model setup as well as the different modelling approaches used to investigate the processes involved in the build-up of O_3. The contributions of different processes to O_3 formation (advection, vertical mixing and net chemical production) are presented and discussed in section 5.4. The probable pathways for pollution inflow to Weybourne (research questions iii) are discussed in section 5.5. Conclusions are given in section 5.6.

5.2 ICOZA observational data

Most of the ICOZA campaign was dominated by westerly and south-westerly winds as shown in the wind-rose in Fig. 5.1. Although mostly moderate with an average of 6 ms^{-1}, strong winds associated with the passing of a low pressure system through southern England (Met Office, 2016) were observed between July 24 and 25 (max 18 ms^{-1}), Fig. 5.2. The temperatures ranged between 9 and 29 °C, with an average temperature of 16 °C, see Fig. 5.2. The highest daytime and night-time temperatures were recorded during the first days of the campaign, i.e. between 30th June and 2nd July, as indicated in Fig. 5.2. Concurrently, record-breaking temperatures were measured in some regions in Southeast England such as London Heathrow, which experienced the highest temperature since August 2003 heatwave (36.7 °C) (WMO, 2016). Heat-health alerts were in force for Southeast England and the East Anglia region and the hot weather may have contributed to a large fire in Thetford Forest (Met Office, 2016). The UK Met Office attributed the elevated temperatures to a humid southerly flow coming from Spain that at the time experienced its longest recorded heatwave, from 27th June to 22nd July (WMO, 2016).

The most interesting period from the point of view of air pollution was observed between 30th June and 3rd July. This would be referred hereafter as the pollution period. Surface O_3 peaked above the information threshold of 1 h average O_3 mixing ratios of 180 μg m^{-3} (90 ppbv) at several stations in southeast UK and Western Europe on 1st July, as shown in the plot of hourly surface O_3 concentrations at the investigated stations in Fig. 5.3. This peak was recorded in the evening when the O_3 photochemical production is expected to decrease as the solar radiation weakens.

Weather conditions and variations of O_3, NO_x, and CO concentrations during this episode are described in detail in the following subsections. Surface pressure charts for 30th June to 3rd July 2015 are presented in Fig. 5.4.

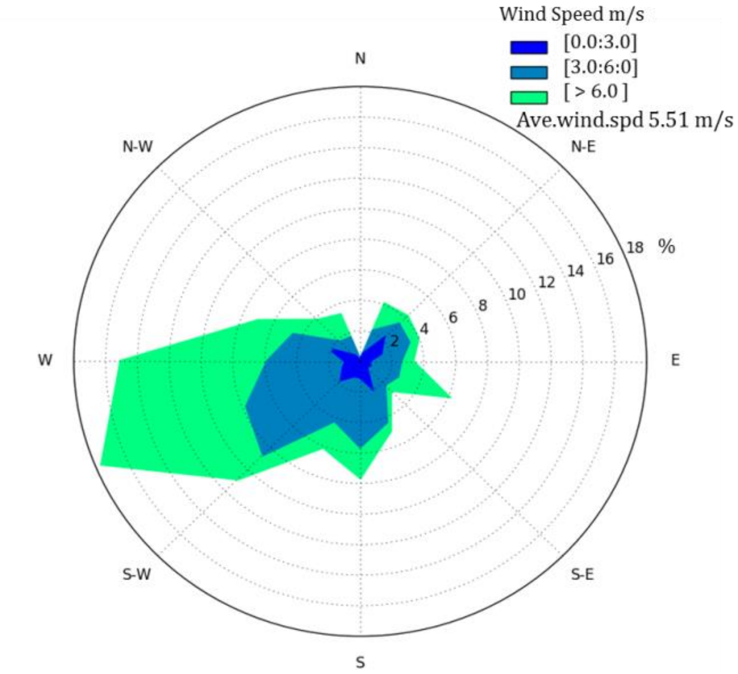

Figure 5.1. Wind-rose showing wind speed and direction measured at WAO between the 29th June and 1st August. The length of the spokes represents the frequency of the wind direction.

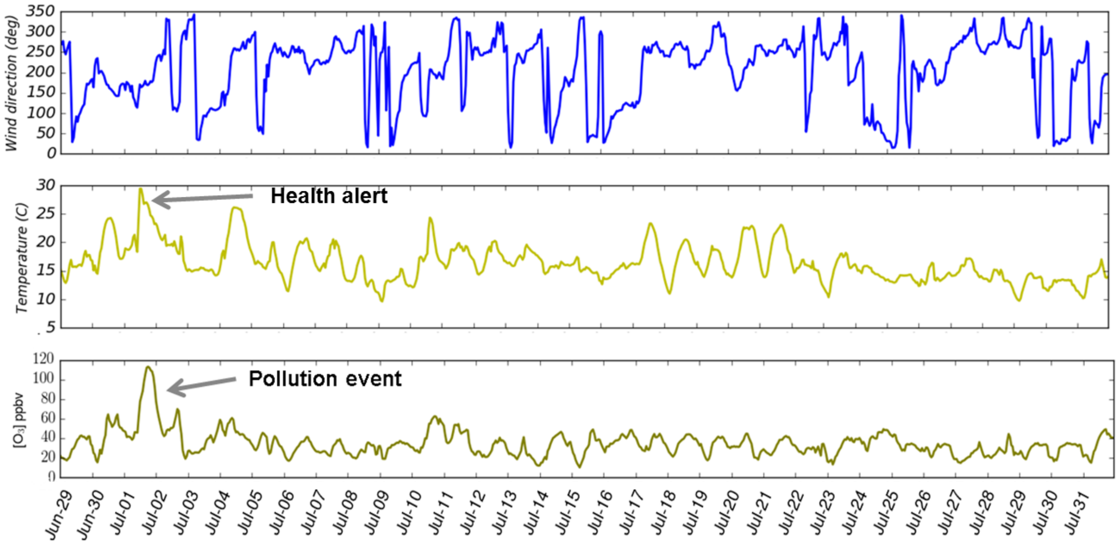

Figure 5.2. Time series of wind direction, temperature and surface O_3 recorded at WAO during the ICOZA field campaign. The heat-alert and the pollution event are labelled.

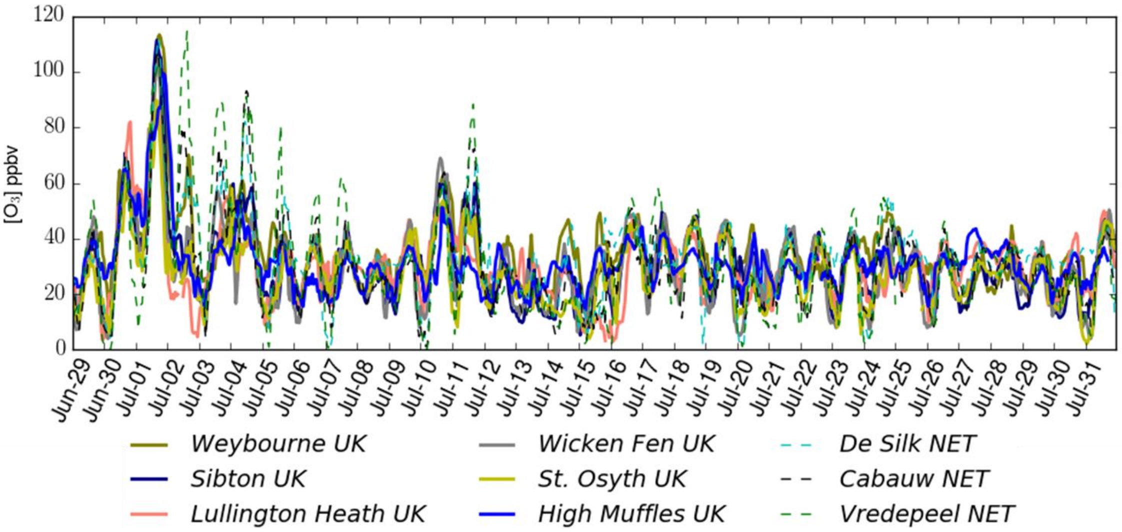

Figure 5.3. Hourly surface O_3 concentrations at stations in the UK and the Netherlands (NET) from 29th June to 31st July.

5.2.1 Overview of the pollution episode

5.2.1.1 30th of June

A wide area of high pressure centred over the Netherlands coast affects most of England on the 30th June (Fig. 5.4). On this day, WAO registered temperatures as high as 24 °C and light winds predominately from south-southeast. An increase in the O_3 mixing ratio of 16.6 ppbv h^{-1} was observed between 10:00 and 11:00 UTC, which coincided with a change in the wind direction from south-southwest to south-southeast, Fig. 5.5. A maximum mixing ratio of 64 ppbv was reached at 19:00 UTC. At night, the temperatures remained over 17 °C, and the O_3 mixing ratios decreased to 40 ppbv remaining almost constant until the next morning. Time series from EMEP monitoring sites across UK show that O_3 started to build-up also at stations located in southeast UK and parts of Western Europe, Fig. 5.3, indicating that accumulation of O_3 was a regional scale phenomenon.

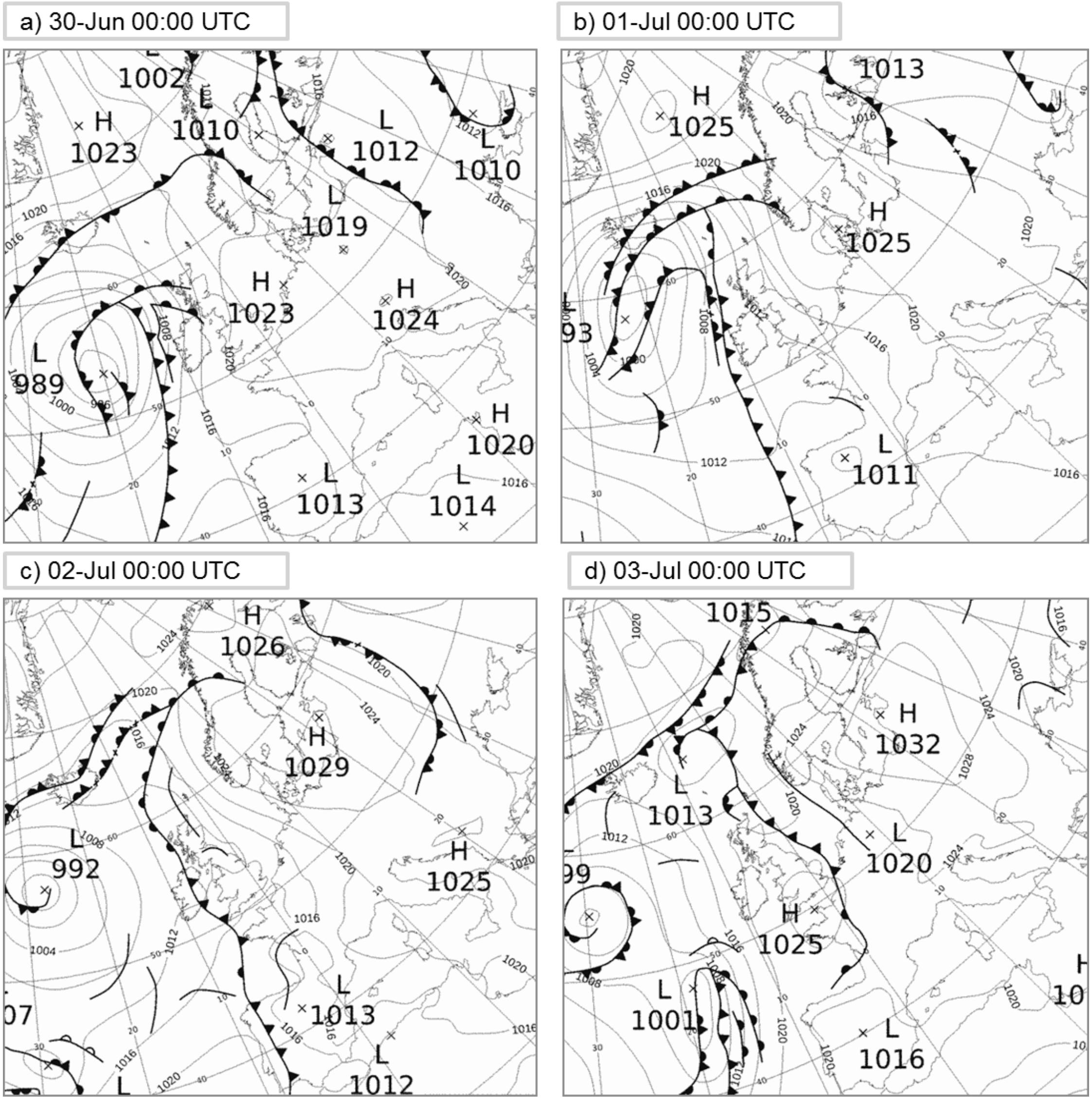
a) 30-Jun 00:00 UTC

b) 01-Jul 00:00 UTC

c) 02-Jul 00:00 UTC

d) 03-Jul 00:00 UTC

Figure 5.4. Surface pressure charts from the UK Met Office at 00:00 UTC for (a) 30-Jun, (b) 01-Jul, (c) 02-Jul, and (d) 03-Jul.

Ten-day integrated atmospheric footprints in Fig. 5.6, which were generated by Dr. Zoe Fleming (National Centre for Atmospheric Science, NCAS UK) using the UK Met Office Numerical Atmospheric Dispersion Modelling Environment (NAME) (Jones et al., 2007), show a change in the air mass origin happening between the 29th and 30th June. The footprints indicate the geographical areas that could have influenced the build-up of O_3 observed at WAO during ICOZA. The NAME model was run in a backward mode with particles released at 10 m altitude every 3 hours using meteorological fields from the Unified Model. Fig. 5.6 illustrates the density of particles below 100 m above the ground over the previous 10 days. This identifies where surface emissions from different geographical regions are likely to have impacted the air mass that arrived at WAO. The reader is referred to Fleming et al. (2012) for details regarding the application of the NAME model to classify air mass types at WAO. The footprints indicate that on the 29th June the origin of the air particles reaching WAO were mainly from the Atlantic and with some influence from Midlands while on the 30th June most of the particles arriving at WAO after midday passed over Belgium and the Netherlands and the North Sea before reaching Weybourne. This agrees with the temperature and CO measurements at WAO presented in Fig. 5.5 showing CO mixing ratios near background levels on the 29th June (daily mean 101 ppbv) as well as colder air (daily mean temperature 16°C) when compared with the 30th June (daily mean CO 113 ppbv and temperature 20°C).

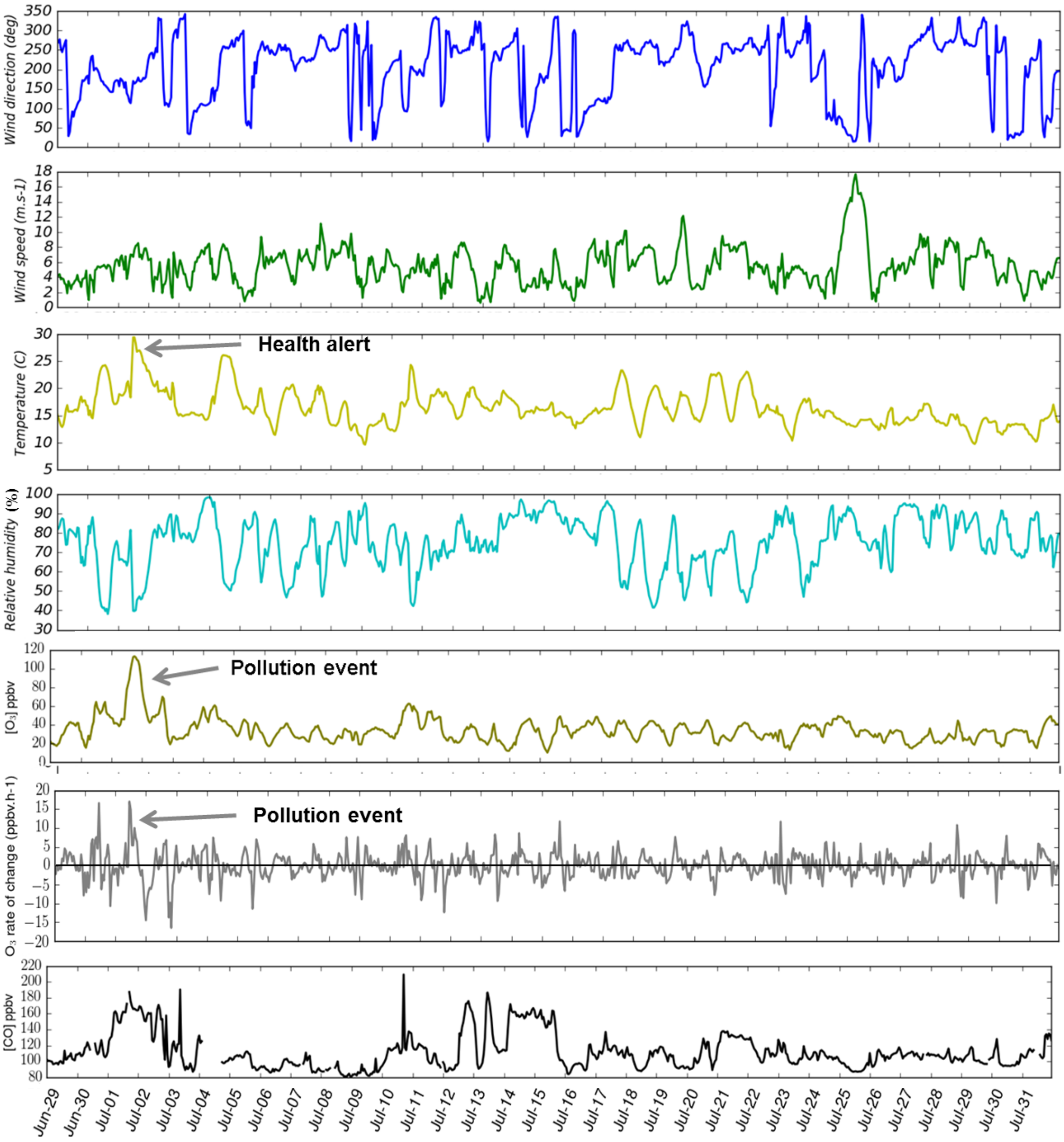

Figure 5.5. Time series of wind direction and speed, temperature, relative humidity surface ozone, rate of change in surface O_3 and CO measured at WAO during the ICOZA field campaign. The pollution event is labelled.

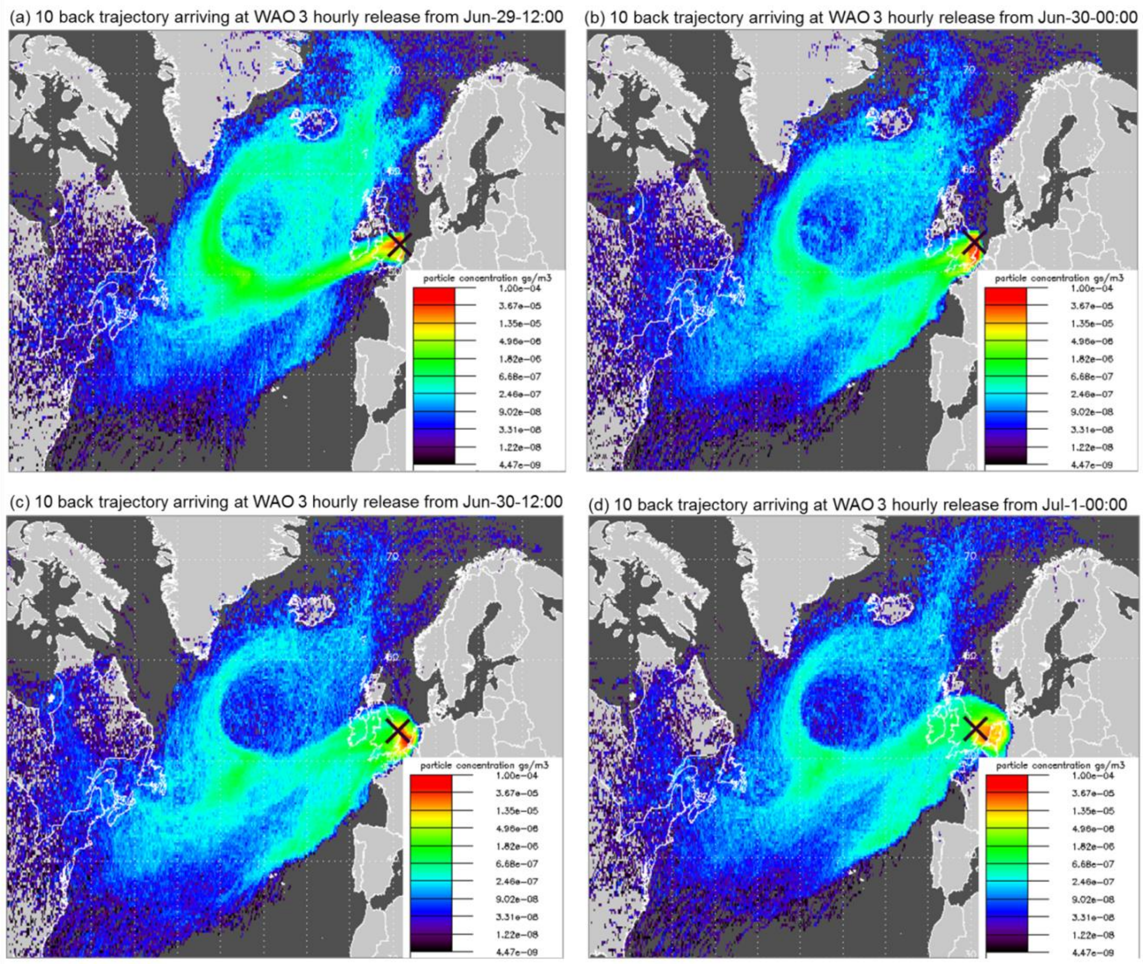
(a) 10 back trajectory arriving at WAO 3 hourly release from Jun-29-12:00

(b) 10 back trajectory arriving at WAO 3 hourly release from Jun-30-00:00

(c) 10 back trajectory arriving at WAO 3 hourly release from Jun-30-12:00

(d) 10 back trajectory arriving at WAO 3 hourly release from Jul-1-00:00

Figure 5.6. WAO 10-day integrated footprints on the (a) 29 June 12:00 UTC, (b) 30 June 00:00 UTC (c) 30 June 12:00 UTC and (d) 1 July 00:00 UTC.

5.2.1.2 1st of July

By the 1st July 00:00 UTC, the high pressure system had moved to Denmark (Fig. 5.4) and WAO was under the influence of moderate winds (average 6 ms^{-1}) fluctuating between the east, southeast and the south direction, see Fig. 5.5. Between 7:00 and 10:00 UTC, O_3 mixing ratios started increasing and by 11:00 WAO recorded an increased in the O_3 concentrations of about 17 ppbv h^{-1}, see Fig. 5.5. The morning increase in the concentrations of O_3 has been also reported in field campaigns studies such as Lee et al. (2006) and is attributed to both the mixing down of ozone-rich masses from the residual layer to the surface level (Entwistle et al., 1997; Lee et al., 2006; Francis et al., 2011) and photochemical production of O_3 throughout the troposphere (Lee et al., 2006). The increase in the morning O_3 mixing ratios was accompanied by a shift in the wind direction from east-southeast (113°) at 10:00 UTC to southeast and south (141 and 170° at 11:00 and 12:00 UTC, respectively), and a rise in the surface temperature of about 6 °C. The relative humidity dropped in the same time interval from 81 % at 10:00 UTC to 58 % and 39 % at 11:00 and 12:00 UTC respectively, suggesting the advection of hot and drier continental air. A maximum mixing ratio of 78 ppbv was reached at 12:00 UTC. Temperatures reached 29 °C at 13:00 UTC and the O_3 concentrations increased steadily throughout the afternoon reaching a 116 ppbv at 18:00 UTC, see Fig. 5.7a.

Rural stations located in the east of the UK (e.g. Wicken Fen, Sibton, St Osyth and High Muffles) and southeast UK (e.g. Lillington Heath) also experienced levels of O_3 exceeding the EU information threshold of the 1-h average of 180 µg m^{-3}. O_3 also reached similar concentrations at sites in the Netherlands (e.g. de Silk, Cabauw Wielsekade and Vredepeel) and in Germany (e.g. Schauinsland). The NAME footprint presented in Fig. 5.8a show that when the particles reaching WAO at 12:00 UTC on 1st July had been close to the surface during the previous 10 days they had done so over Western Europe and the North Sea, suggesting that the pollution event in the UK was most likely caused by transport of O_3 3 from continental Europe. This is supported by enhanced CO mixing ratios also recorded on 1st July, in particular after 13:00 UTC, reaching up to 187 ppbv at 17:00, see Fig. 5.7b.

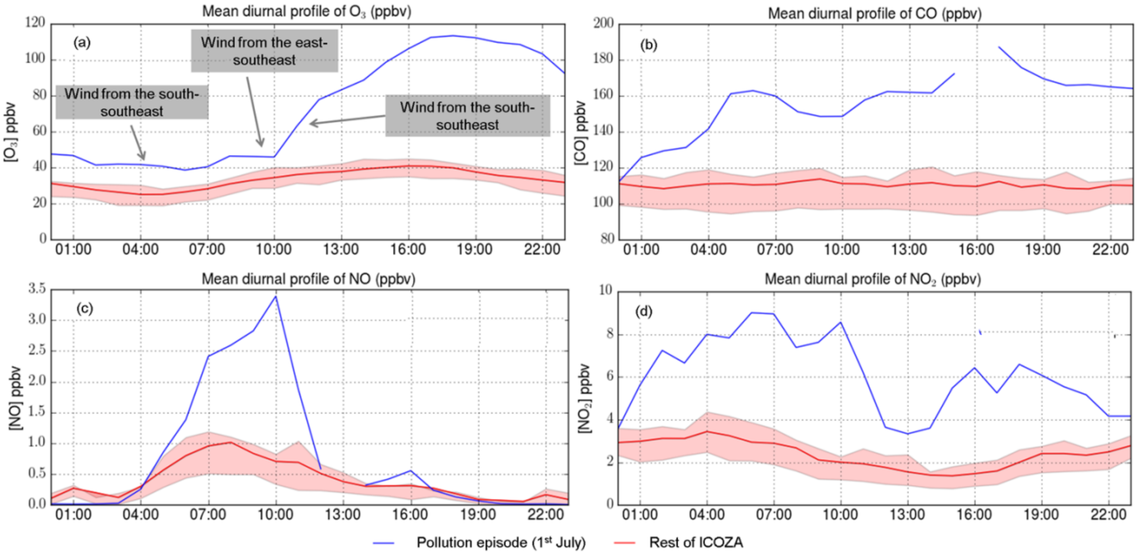

Figure 5.7. Diurnal cycle of (a) O_3, (b) CO, (c) NO and (d) NO_2 during 1st July (blue line) and the average for the rest of the field campaign (red line). The shaded areas represent the variability between days showing the 25th and 75th percentiles.

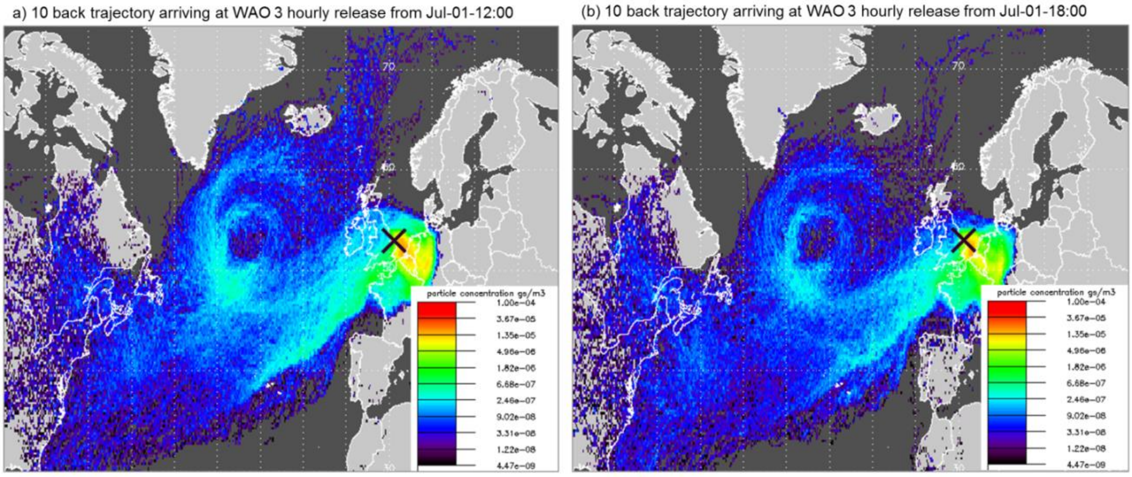

Figure 5.8. WAO 10-day integrated footprints on the (a) 1st July 12:00, (b) 1st July 18:00 UTC.

NO concentrations were also enhanced in the morning of 1st July with a maximum mixing ratio of 3.4 ppbv recorded at 10:00 UTC (almost three times higher than the mean concentration recorded during the rest of the campaign), see Fig. 5.7c. NO_2 concentrations were also high, in particular the morning peak reached 9 ppbv at 10:00 UTC (more than four times higher than the mean concentration recorded during the rest of the campaign), while the secondary peak reached 6.6 ppbv at 18:00 UTC (doubling the concentration recorded during the rest of the campaign), see Fig. 5.7d.

5.2.1.3 2nd and 3rd July

The episode was interrupted following a change in the wind direction from the south (180°) to the southwest (203°) which brought cooler and cleaner air from the Atlantic in the late night of 1st July and early morning of 2nd of July, see Fig. 5.9. O_3 mixing ratios dropped 14 ppbv between 12:00 and 01:00 UTC. Lower concentrations of NO_x compare with the day before (NO maximum mixing ratios lower than 1 ppbv and NO_2 near 2 ppbv) were observed during the morning of 2nd July. In the afternoon, an increase in the concentrations of O_3 (up to 6.7 ppbv h^{-1}) coincided with a change in wind direction from west-southwest to south-southeast. This increase in the O_3 levels was most likely caused by O_3 been transported from the North Sea where O_3 deposition occurs in a slower rate (this is further explored in Chapter 6). Background stations located in the west coast of the Netherlands, such as de Silk and Kollumerwaard, further show that O_3 reached mixing ratios as high as 100 ppbv on that day, see Fig. 5.3. On a regional scale the episode lasted several days and in east and southeast UK O_3 exhibited variability depending on the wind direction.

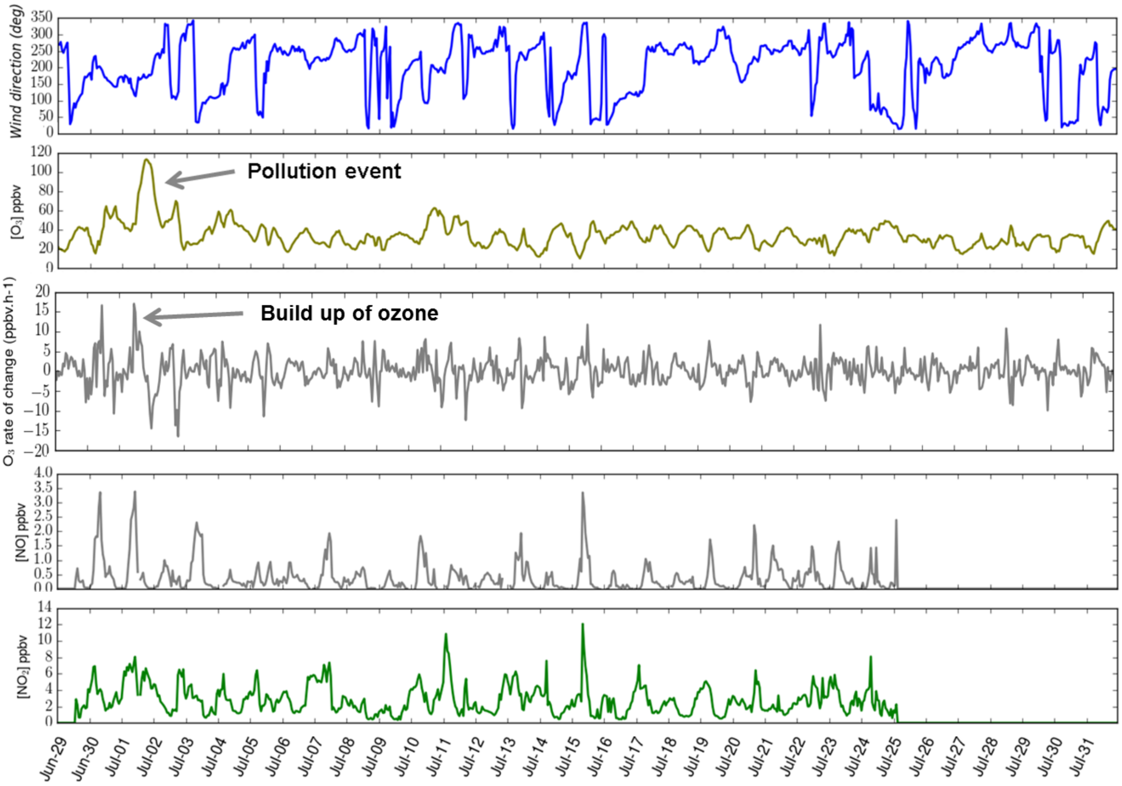

Figure 5.9. Time series of wind direction, temperature, surface ozone, rate of change in surface O_3 and NOx (NO_2 and NO) measured at WAO during the ICOZA field campaign. The pollution event is labelled.

On 3rd July 00:00 UTC, most of the south of UK was under the influence of high pressure see Fig. 5.4. Winds from the north-northwest and northeast dominated the morning of the 3rd July at WAO, while south-southeast winds prevailed after midday (see Fig. 5.2). O_3 started to build up once more after 14:00 UTC. The highest increase in the O_3 mixing ratios, 5.6 ppbv h^{-1}, was recorded at 23:00 UTC, Fig. 5.9, reaching a maximum concentration of 53 ppbv. The temperature also increased during that night. Since this occurred at night when photochemical production of O_3 is suppressed, the most likely explanation is that the easterly flow (from about 107°-112°) draws ozone-loaded air from a warmer southern North Sea, where the loss in O_3 is much low due to low rates of dry deposition.

High O_3 values were observed until 5th July at several stations across Central and Western Europe as a high-pressure dominated the weather. In particular, Schauinsland in Germany reported maximum O_3 values around 120 and 115 ppbv on 2nd and 3rd July, respectively. The weather in East Anglia and

Southeast England on the 5th July, on the other hand, was generally dominated by an area of rain (Met office, 2016).

5.3 Methods

5.3.1 Model set up and input data

The WRF-Chem model was setup with one nested domain using the one-way nesting method. The nested domain (see Fig. 5.10) has a horizontal resolution of 9 km and 35 vertical levels with 12 levels in the first 3 km and 23 levels between 3 and ~20 km (10 hPa). The lowest vertical level corresponds to ~30 m. Simulations were conducted for the period between 28th June and 1st August 2015 with a 45 seconds time step for both the meteorology and the chemistry modules. The first two days were taken as spin-up and therefore discarded. The meteorology was not nudged but re-started every three days following the methodology used in the AQMEII inter-comparison project. This decision was justified by the sensitivity analysis discussed in Chapter 2 having shown that nudging of winds and temperature on the parent domain following Mar et al. (2016) leads to a representation of hourly NO_2 and O_3 mixing ratios that is inconsistent with observations.

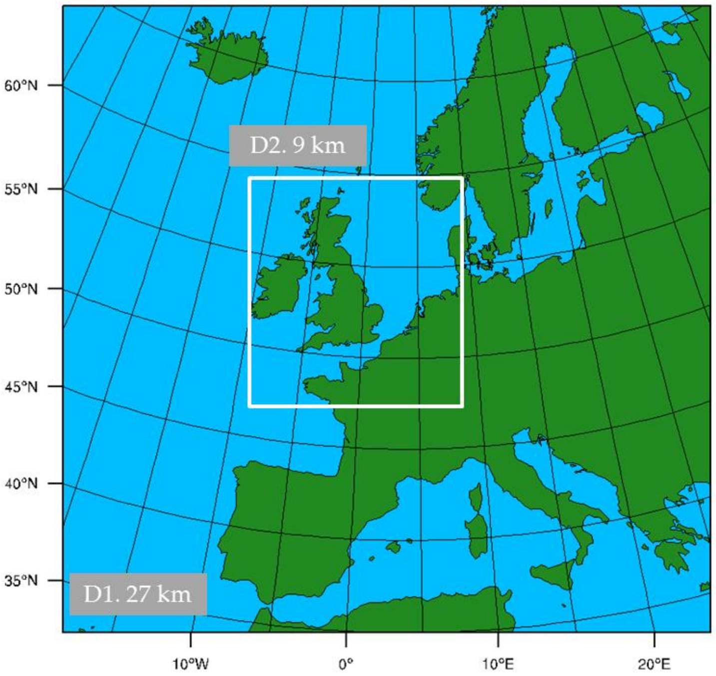

Figure 5.10. Preview of the WRF-Chem domain used in this study.

The gas-phase chemistry is represented by the CRImech chemical mechanism (Watson et al., 2008; Archer-Nicholls et al., 2014), which considers 240 species, including 26 non-methane VOCs, which participate in 609 reactions. This decision was made based on previous sensitivity tests (see Section 3.4.3) showing that CRImech gives better predictions of the MDA8 O_3 than MOZART-4, in particular over east and the southeast UK the Netherlands.

The anthropogenic emissions consist of a hybridization of the latest UK National Atmospheric Emissions Inventory (NAEI) for the year 2014 and the most recent version of TNO emissions inventory for the year. Details regarding the implementation of the inventories are presented in Chapter 2. The NAEI database is used over the UK, while the TNO is used for mainland Europe, the Republic of Ireland, and ship emissions. Both inventories have been previously used in modelling studies in EU and UK (e.g. Archer-Nicholls et al. 2014; Im et al., 2014; Lowe et al., 2015; Kuik et al., 2016; Mar et al., 2016).

5.3.2 Processes analysis

The physical and chemical processes contributing to the build-up of surface O_3

are investigated using the processes analysis scheme available in WRF-Chem (Wong, 2013). The process analysis method has been widely applied to regional photochemical pollution studies (e.g. Francis et al., 2006; Lei et al., 2007; Gao et al., 2016). The approach involves separating the continuity equation for atmospheric trace gases into its component operators: horizontal advection ($v \cdot \nabla$), vertical advection (wdz), convective transport (Δ_{conv}), vertical mixing/dry deposition (Δ_{vmix}), net chemical production/loss (Δ_{chem}), emission (E), and other loss processes such as wet deposition (L) (Wong, 2013). Horizontal advection refers to the transfer of mass in the eastward and northward direction, while vertical advection refers to the transfer of mass in the upward direction. Convection refers to the sub-grid cloud process, e.g. convective clouds transporting pollutants vertically. Vertical mixing on the other hand represents both dry deposition and diffusion. The change in the mixing ratio (C) of a given species between time steps *t* and *t+1* is then:

$$C_{(t+1)} - C_{(t)} = (\Delta_{chem} + \Delta_{conv} + \Delta_{vmix} + \mathbf{v}\,\nabla + wdz)C_{(t)}\,dt + E_{C(t)} + LC_{(t)} \quad (E5.1)$$

The decoupled advective components are extracted from within the WRF dynamic core, while the contributions from convective, vertical mixing, and chemical processes are calculated as the difference in the specie mixing ratio before and after each module is executed. Both meteorology and chemistry are computed simultaneously using the same time-step thus no information is lost during the process. In the case of O_3, the emission term (E) should be zero as O_3 is a secondary pollutant. Moreover, the wet deposition (L) is not accounted for in this study so that the evolution of O_3 mixing ratio reads:

$$C_{O3\,(t+1)} - C_{O3\,(t)} = (\Delta_{chem} + \Delta_{conv} + \Delta_{vmix} + v \cdot \nabla + wdz)C_{O3\,(t)}\,dt \quad (E5.2)$$

In this chapter, the process analysis scheme is used to assess the contribution of the various atmospheric processes to the O_3 build-up at Weybourne and at three additional nearby rural sites (Sibton, St. Osyth, and Wicken Fen, see Fig. 3.3) to better characterise the formation and evolution of the O_3 pollution episode in the East Anglia region. The technique is tested by comparing the modelled rate of change against the sum of the contributions from the five processes during each model output interval. Fig. 5.11 shows that the sum of the five processes broadly equals the modelled hourly change in the O_3 mixing ratios over Weybourne.

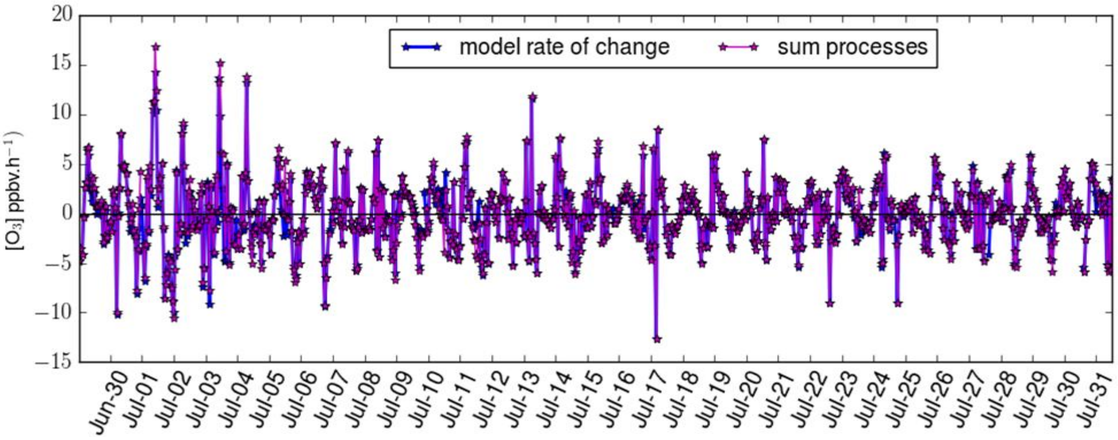

Figure 5.11. Hourly rate of change of O_3 (blue) and the sum of the processes (purple) from June 29th to August 1st 2015 at the model bottom level (~30 m) at the nearest grid cell to Weybourne.

5.3.3 Passive tracers experiment

Seven passive tracers were released in different regions across Western Europe to explore the dispersion and transport of pollutants during the O_3 episode. Each source region consisted of a box of 4 × 4 grid cells (each cell 9 × 9 km) located in Western Europe as shown in Fig. 5.12. The tracers were released at each time step at the lowest two model levels (~30 and 100 m) of each grid box in those source regions. This is equivalent to 2,592 tracer particles released in each source region every time step. The tracers do not interact with the chemistry of the model; instead, they are subject to advection, convection, and vertical mixing.

The source regions have been selected based on the NAME footprints provided in Fig. 5.6 as these give indication of the origin of the air masses sample at WAO on the 30th June and 1st July.

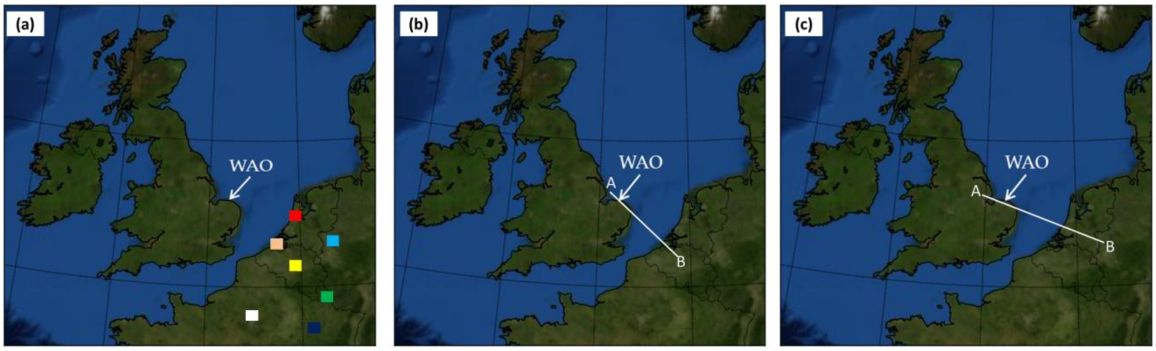

Figure 5.12. (a) Map with the locations of source regions of the tracers: the red square locates the tracer released in the Netherland coast within the Rotterdam port; salmon the coast on the border between Belgium and the Netherlands; yellow east Belgium; turquoise the west of Germany; green Luxembourg; white northwest of Paris (outside Paris); and blue the northeast France. (b) Cross-sectional orientation through tracer released in east Belgium from A [latitude 53.20, longitude 0.50] to B [latitude 50.94, longitude 4.07]. (c) Cross-sectional orientation through tracer released in the west of Germany from A [latitude 53.012, longitude 0.36] to B [latitude 51.23, longitude 6.98]

5.4 Results

5.4.1 Overview of the evolution of surface ozone

Fig. 5.13 and Fig. 5.14 show that the model captures the morning growth in O_3 observed on the 1st July, ~15 ppbv h^{-1} (see Fig. 5.13 grey arrow), as well as the geographical extent and evolution of the pollution episode.

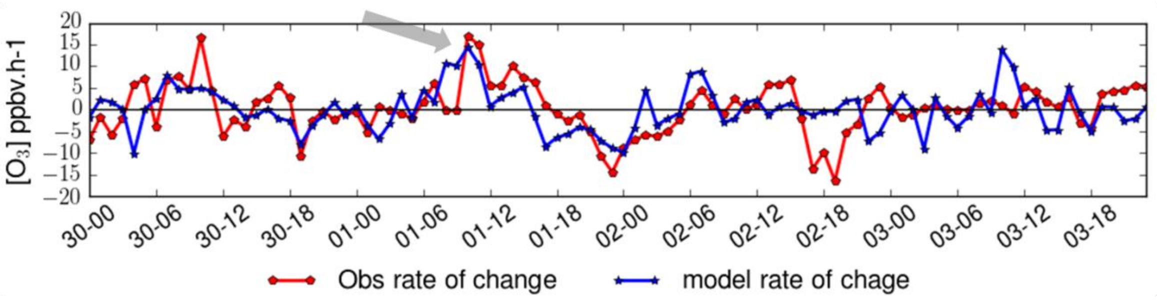

Figure 5.13. Modelled and observed rate of change of O_3 from June 30th to July 3rd 2015. The grey arrow denotes the morning increase in the rate of change on 1st July.

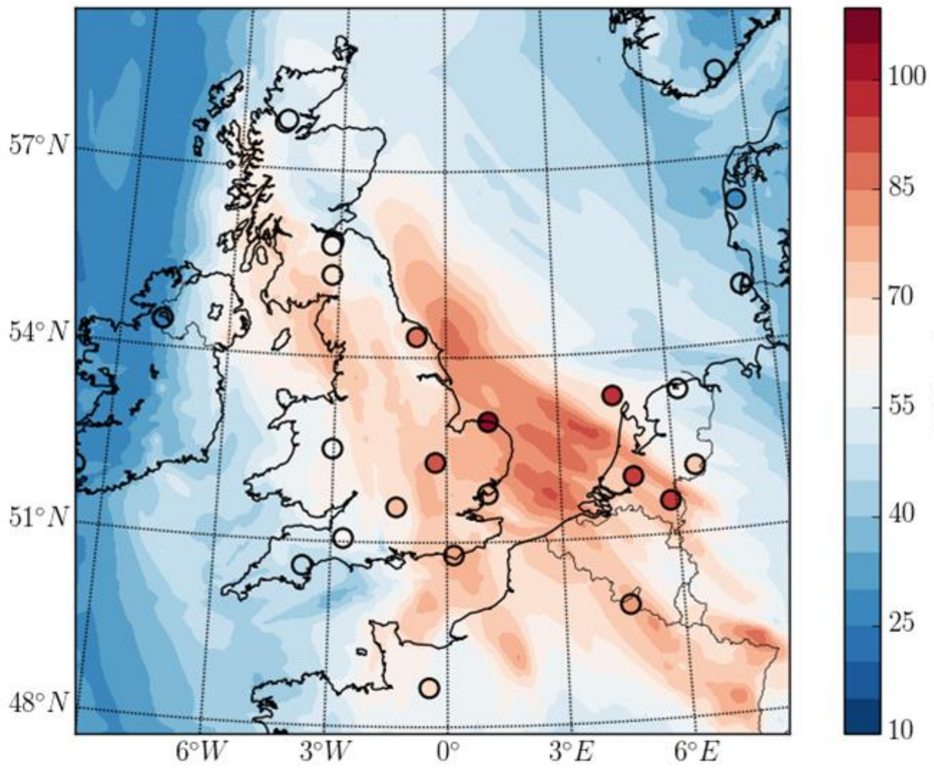

Figure 5.14. Surface MDA8 O_3 on July 1st, 2015. Shaded contours are model output while filled dots represent measurements at EMEP stations with altitude < 400 m.

Fig. 5.15 shows one hour modelled O_3 mixing ratios, surface level pressure (SLP), and 10 m wind vectors for the period between 30th June and 3th July. During the 30th June, O_3 reached about 60 ppbv in the southeast and east of the UK as the regions were influenced by easterly and south-easterly winds (Fig. 5.15a and 5.15b). O_3 mixing ratios above 60 ppbv are visible also in Western Europe (the north of France, Belgium and Netherlands) and along the southern North Sea coast and English Channel. This section of the North Sea is well-known for dense traffic of the largest cargo-ships that head for the biggest ports in Europe, such as Rotterdam, Antwerp, and Hamburg (Aulinger et al., 2016).

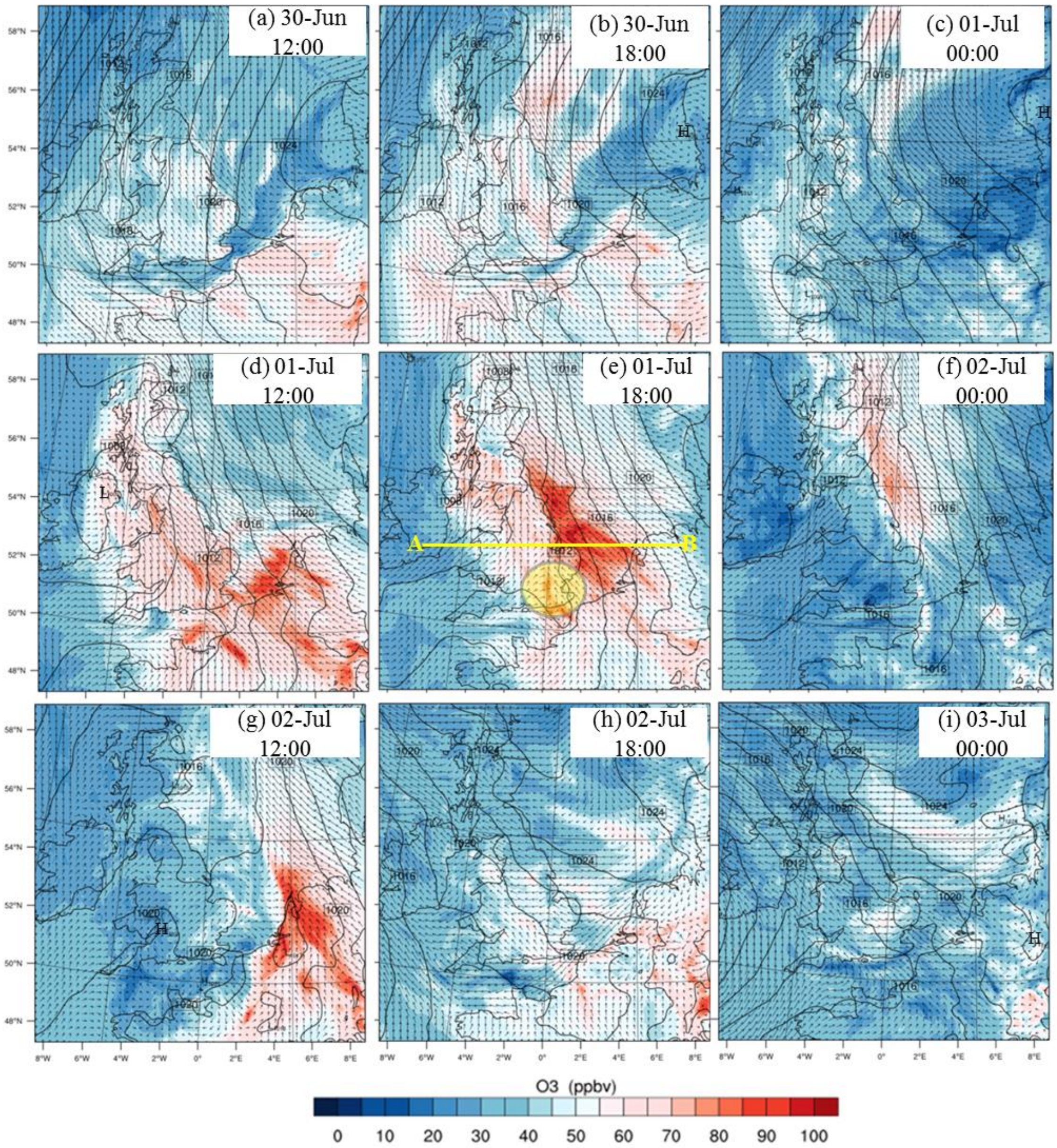

Figure 5.15. Modelled surface O_3 mixing ratio (coloured shading), 10 m wind vectors (black arrows), and surface level pressure (black contours) for the period 30th June – 3rd July at 12:00, 18:00 and 00:00 UTC. The thick black line in e indicates the vertical cross section shown in Fig.5.16 from A [latitude 52.30, longitude -6.76] to B [latitude 52.74, longitude 6.26] through Weybourne. The yellow oval in **e** highlights a key feature referred to in the text.

The model captured the evolution of the pollution episode exhibiting maximum concentrations at WAO of ~90 ppbv on 1st July. On that day, the southeast of UK experienced south-easterly and south-south-easterly winds during most of day see Figs. 5.15d and 5.165e, suggesting that the build-up of O_3 was probably associated with transport of O_3 from mainland Europe (this is explored in more detail in section 5.5). Moreover, a convergence zone of westerly and easterly winds developed on the eastern side of the UK (see Fig. 5.15e yellow circle) which facilitated the accumulation of O_3 in southeast England, as shown in Figs. 5.16b-c. The resulting convergence led to an increase in the O_3 concentration that lasted until the westerly flow was strong enough to push the polluted air eastwards, and away from the surface in the evening (Figs. 5.16d-f). Similar results were also found in the modelling study in Francis et al. (2011), in which the convergence of easterly and westerly flow combined with stagnant conditions was shown to contribute to the high surface O_3 concentrations on the August 2003 heatwave.

On 2nd July, O_3 mixing ratios increased again after midday, in particular in the Netherlands, Germany and the eastern North Sea, where concentrations reached ~90 ppbv. At Weybourne, however, maximum concentration of O_3 of about 50 ppbv, i.e. below the EU 8 hour threshold of 60 ppbv, were predicted, see Figs. 5.15g and 5.15h.

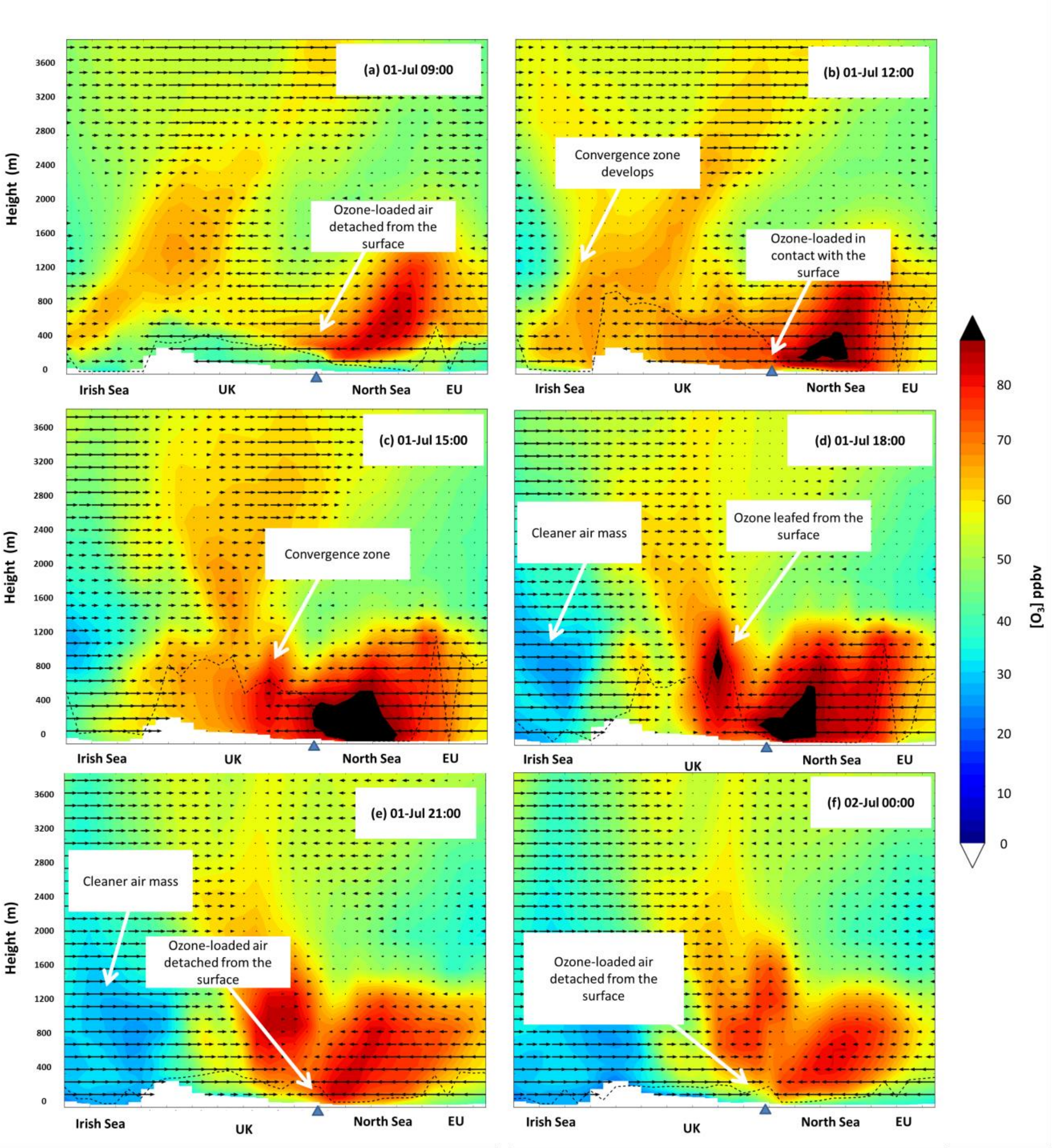

Figure 5.16. Simulated vertical cross-section (A–B) (Fig. 5.15) of O_3 mixing ratios (coloured shading) and zonal wind vectors (black arrows) every three hours from July 1st 09:00 to July 2nd 00:00 UTC. The triangle denotes the location of WAO. The black dashed line denotes the simulated PBL height.

5.4.2 Process analysis of O_3 build-up

The O_3 mixing ratios at a given location are the result of the interaction of in-situ chemistry (chemical production/destruction), transport and deposition processes (Monks et al., 2015). In this section the process analysis scheme is used to estimate the contributions of the chemical (production/destruction) and physical processes (horizontal advection, vertical advection, convective transport, vertical mixing/dry deposition) to the evolution of O_3 during a pollution event. Both the horizontal and vertical advection components often showed similar magnitudes but with opposite signs, for this reasons in this chapter the advective components are combined into one advection-related term and referred to as ***adv*** thereafter. Moreover, the contribution of convective transport (conv) was less than 1 ppbv h^{-1} during the four days, thus it is not discussed further.

5.4.2.1 Weybourne

The average diurnal cycle of surface O_3 and of the process tendencies (adv, vmix and chem) from 30th June 00:00 to 4th July 00:00 UTC at WAO presented in Fig. 5.17. Fig. 5.17a shows a typically mid-afternoon peak in the O_3 mixing ratios and a night-time and early morning minimum. Fig. 5.17b shows that vertical mixing (vmix) is an important source of O_3 from around sunrise until shortly before midday when it switches to a sink in the afternoon. Chemistry (chem) is an important source from around sunrise to later afternoon. At night, removal of O_3 occurred through gas-phase chemical reactions and dry deposition (vmix). Advection (adv) is mostly a sink before midday and mostly a source in the afternoon. Therefore, the initial rise on O_3 in the early morning is largely due to vertical mixing and some chemistry. Chemistry and advection sustained such growth into the afternoon. In late afternoon, the dry deposition term started to dominate.

The simulation is in line with the current general knowledge regarding the diurnal variation of surface O_3 within the atmospheric boundary layer over land. After the sun rises, turbulent mixing within the PBL induced by solar heating of the ground (free convection) and wind shear (forced convection) cause the mixing-down of O_3 and other pollutants from the residual layer and the free troposphere (Stull, 1989; Wallace and Hobbs, 2006). In the presence of NO_x and VOCs, solar radiation might trigger photochemical production of O_3. As the surface cools during the night and early morning, the lower levels of the boundary layer are transformed into a stable layer (the nocturnal boundary layer) detached from the rest of the troposphere and characterized by statically stable air. The stable air within the nocturnal boundary tends to reduce turbulence and therefore O_3 entrainment from the residual layer (Stull, 1989), thus the nocturnal boundary layer experiences additional O_3 depletion because the losses due to dry deposition and chemical loss (e.g. titration by NO_x emissions and ozonolysis) cannot be replenished.

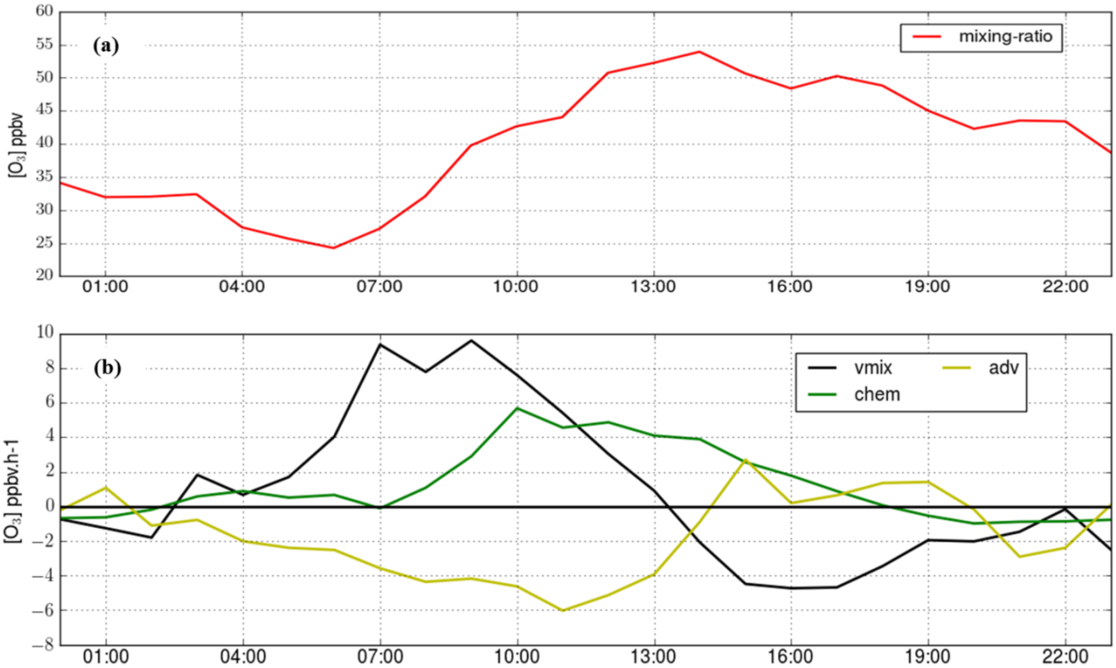

Figure 5.17. Average diurnal cycle O_3 (a) and average diurnal profile of the process tendencies and rate of change of O_3 at the model bottom level (~30 m) at Weybourne from 30th 00:00 UTC to 3rd July 00:00 UTC.

Figs. 5.18 and Fig. 5.19 show the evolution of the O_3 mixing ratios and the contributions of the different processes, sequentially, in different vertical layers and at the model bottom level (~30 m) during the time interval of interest (30th June to 3rd July) at WAO. Each arrow has an associated number, from 1 to 14, which is used as an index in the discussion. The way to read Fig. 5.18 is to start scanning from left to right at a specific altitude and see how O_3 in panel (a) changes. O_3 mixing ratios increases from blue to red and for O_3 to increases there must have been a positive tendency at that altitude at the same time as the O_3 increases. An example of this is on 30th June around 18 hours, as the PBL collapses the colour at 400 m altitude goes from a pale red to a stronger red. When looking at the advection term at the time of this transition, there is positive change in O_3 (red), this is quite clear because the other tendencies are quite weak.

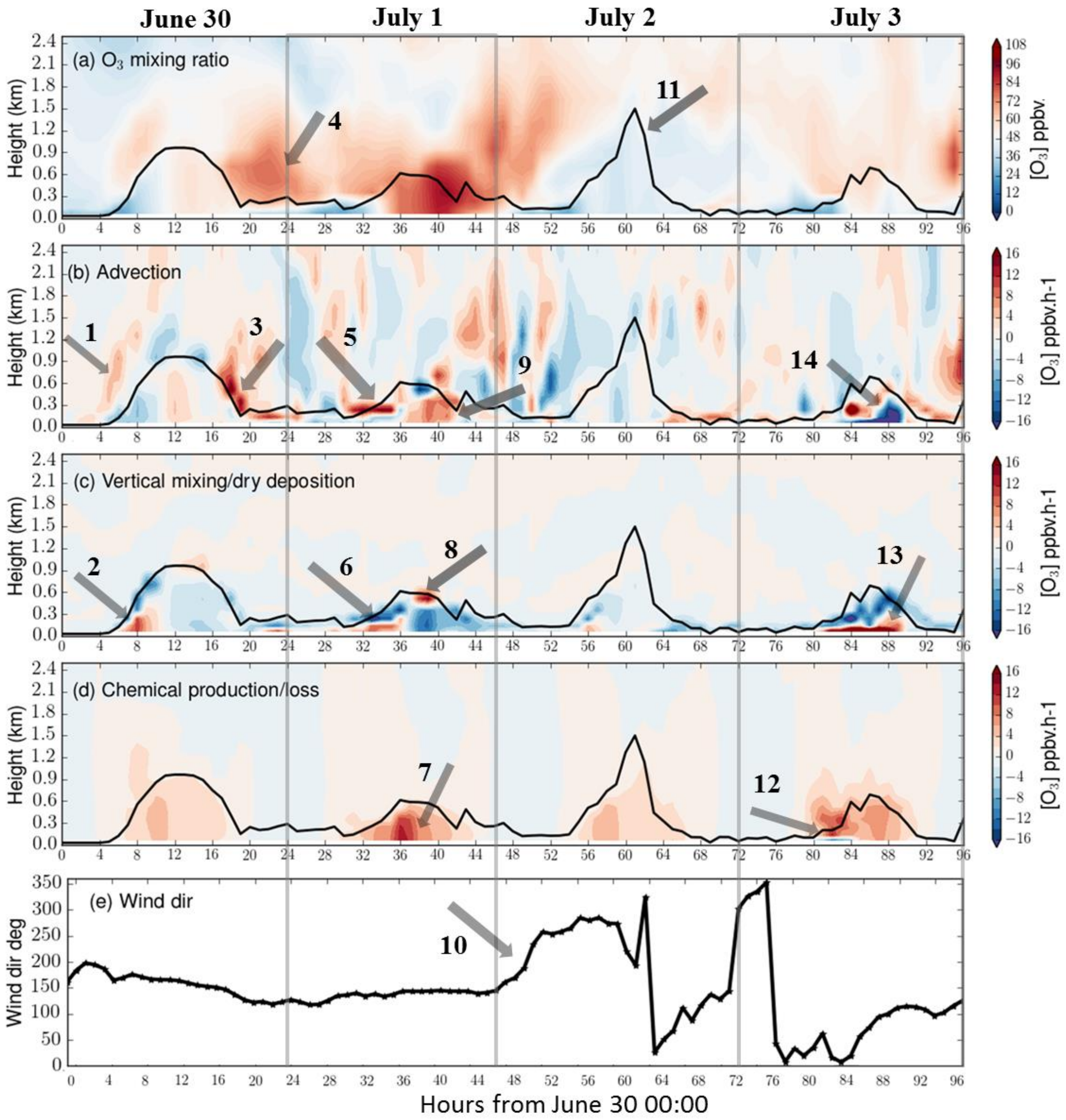

Figure 5.18. Time–height section of O_3 mixing ratios (ppbv) and the process tendencies (ppbv h^{-1}) from June 30th to July 3rd 2015, at Weybourne. (a) O_3 mixing ratio, (b) adv, (c) vmix, (d) chem. Wind direction is also shown in (e). The black line in a-d shows the evolution of the planetary boundary layer height. Grey arrows indicate key features referred to in the text.

1 → Transport of O_3 in layers between 300 and 1200 meters (m) height above the PBL is observable in the early morning of 30th June (see Fig. 5.19b arrow 1).

2 → From 06:00 to 10:00 UTC negative values in the vmix component between 200 and 800 m height at the top of the PBL and positive values at ground levels indicate that O_3 was transported to the ground level by vertical mixing (see Fig. 5.18c arrow 2). Thus, the positive values in the rate of change of O_3 observed in the morning (Fig. 5.19a) were mainly driven by mixing-down of O_3-loaded air masses from the residual layer followed by enhanced chemical production within the PBL (see Fig. 5.18d). Surface O_3 reached ~60 ppbv around midday. The role of downward entrainment of O_3-rich air from the residual layer in promoting the rise of morning O_3 mixing ratios during O_3 pollution days has been also reported in both campaign and modelling studies, e.g. Lee et al. (2006) and Francis et al. (2011). Fig. 5.19a also shows that the vmix component was the most significant source of surface O_3 in the early morning while chemical production was the biggest source in the late morning. Around midday, the adv term becomes an important source of surface O_3 (Fig. 5.19a), at this point the PBL was well mixed with a maximum height of approximately 1 km.

3 → In the evening and throughout the night, advection of O_3 was visible above the planetary boundary layer (Fig. 5.18b arrow 3).

4 → O_3 accumulates above the PBL at altitudes between 200 –1000 m (Fig. 5.18a arrow 4).

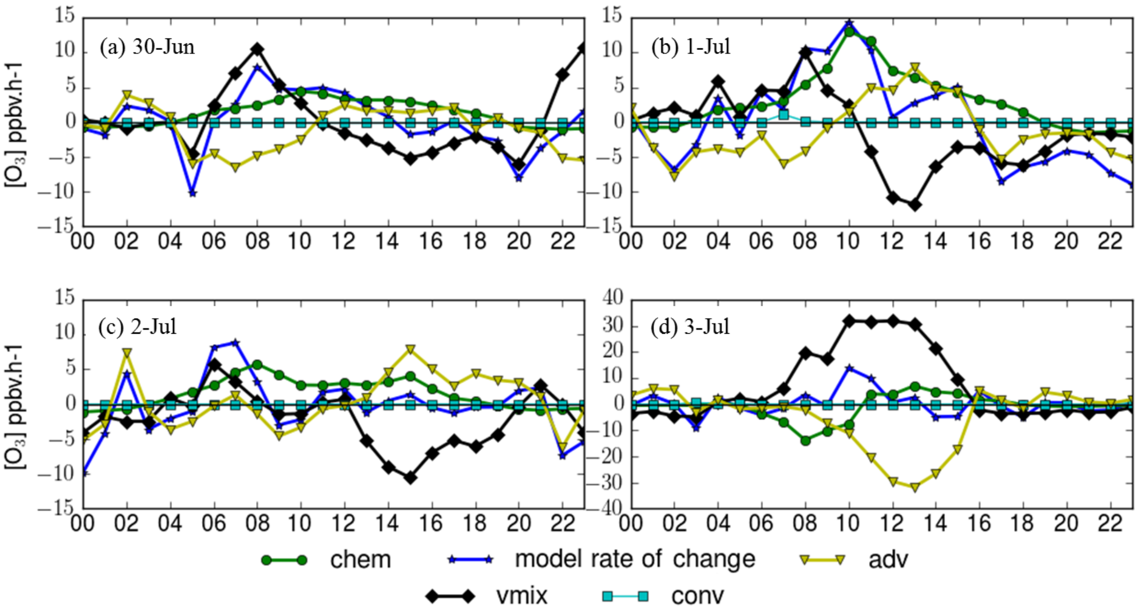

Figure 5.19. Process tendencies at the model bottom level (~30 m) at Weybourne on: (a) 30th June, (b) 1st July, (c) 2nd July, and (d) 3rd July 2015. Note different scale of y-axes in panel *d*.

Fig. 5.18a shows that there was an apparent reservoir of O_3 above the PBL available for downward mixing in the morning of 1st July. An apparent reservoir of peroxyacetyl nitrate (PAN) above the PBL available for downward mixing was also identified in the early morning (see Fig. 5.20 grey arrow). This indicates the likely transport of chemically processed air masses to WAO. PAN is an important reservoir species for NOx, once it is lifted from the ground, it can undergo long-range transport in the free troposphere due to its longer lifetime in colder temperatures (HTAP, 2007). When the air mass eventually descends to the surface, the thermal decomposition of PAN leads to the formation of NO_2, a key species for photochemical O_3 production.

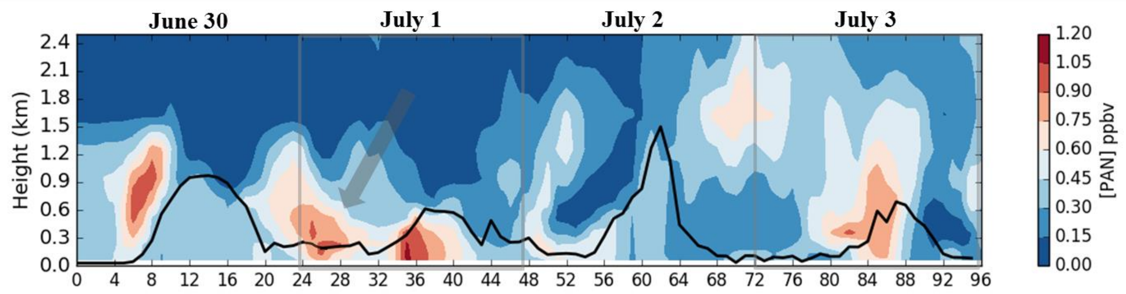

Figure 5.20. Time–height section of PAN mixing ratios (ppbv) from June 30th to July 3rd 2015, at Weybourne. The black line indicates the evolution of the planetary boundary layer height. Grey arrow indicates key features.

5 → High values in the adv tendency from 06:00 to 10:00 UTC in layers between 200-300 m (Fig. 5.18b arrow 5) indicate that O_3 was advected at WAO at these heights.

6 → The positive values in the vmix tendency at the surface and the negative values between the 200 and 300 m height (Fig.5.18c grey 6) suggest that in the early morning O_3 mixing ratios increased mostly by vertical mixing (up to 10 ppbv h^{-1}).

7 → Between 10:00 and 12:00 surface O_3 build-up was mainly driven by enhanced chemical production (Fig. 5.18c arrow 7, and Fig. 5.19b), up to 12 ppbv h^{-1} increased between 09:00 and 10:00 UTC. The input of surface O_3 due photochemistry was larger than the input from downward mixing, with 7.2 and 3.6 ppbv h^{-1} morning average input respectively. A maximum O_3 mixing ratio of 76 ppbv was at 12:00 UTC. In most reported high-ozone events, such as those described in Lee et al. (2006) and Francis et al. (2011), transport of O_3 played a decisive role. This study, however, showed that photochemistry was found to be crucial in increasing the O_3 concentrations during the O_3 episode.

8-9 → After 12:00 and until 15:00 UTC the increase in O_3 mixing ratio was steadier (up to 4 ppbv h^{-1}), see Fig. 5.19b, reaching a maximum of 87 ppbv at 17:00 UTC. Negative values in the vmix component at the surface level indicate that O_3 was largely lost at the surface by mixing within the PBL (up to 11 ppbv h^{-1}), see Figs. 5.18c arrow 8. Nevertheless, the loss was compensated by chemical production and advection of ozone-rich air from the southeast (~150°) (Figs.

5.19d and 5.18b arrow 9). Thus, the continued increased in the surface O_3 mixing ratios after midday was due to chemical production in the first place and advection of O_3 at the surface level in the second place. In the evening, removal of O_3 at the surface was mainly driven by dry deposition and advection (Fig. 5.19b). Loss due to chemical processes became important after 22:00 UTC.

Interestingly, on 1st July the model simulated a shallower planetary boundary layer (in the range 0 - 600 m) compared to that obtained in 30th June. It is suspected that this shallow boundary layer combined with enhanced photochemical production and advection of ozone-rich air mases led to the strong modelled surface O_3 at Weybourne.

10-11 → The episode is interrupted following a change in the wind direction from south-east to the west after midnight 2nd July (Fig. 5.18e arrow 10). Low ozone-air was transported from the west to Weybourne (see Fig. 5.18b). Chemical production within the planetary boundary layer occurred throughout the day (see Fig. 5.18d) in particular around midday; however, a deeper planetary boundary layer (maximum height ~1.4 km) facilitated the vertical mixing of O_3 (see Figs. 5.18a arrow 11 and 5.19c).

12-15 → Despite chemical production in the afternoon (Fig. 5.18.d arrow 12), high mixing-down of ozone-rich air from aloft (Figs. 5.18.c arrow 13 and 5.19d), and the shallow modelled planetary boundary layer, O_3 was largely lost on 3rd June by advection (Figs. 5.18.b arrow 14 and 5.19d) of low-ozone air from the east (Fig. 5.18e).

5.4.2.2 Wicken Fen

The build-up and evolution of surface O_3 during the pollution episode at Wicken Fen was comparable to that observed at Weybourne. Modelling results show that in general the wind direction fluctuated between southeast and east-southeast direction during the 30th June and 1st July. Similar to Weybourne, O_3 started building up after midday on 30th June (see Fig. 5.21a). In the early morning surface O_3 increased due to advection of ozone-rich air in layers between 200-400 m above the PBL (see Fig. 5.21b, grey arrow) followed by the downward mixing of O_3 to the surface (see Fig. 5.21c, grey arrow). The photochemistry contribution to O_3 build-up at the surface became relevant between 10:00 and 18:00 UTC (see Fig. 5.22a). Advection at the surface level also played an important role in the build-up of surface O_3, in particular around 12:00 UTC.

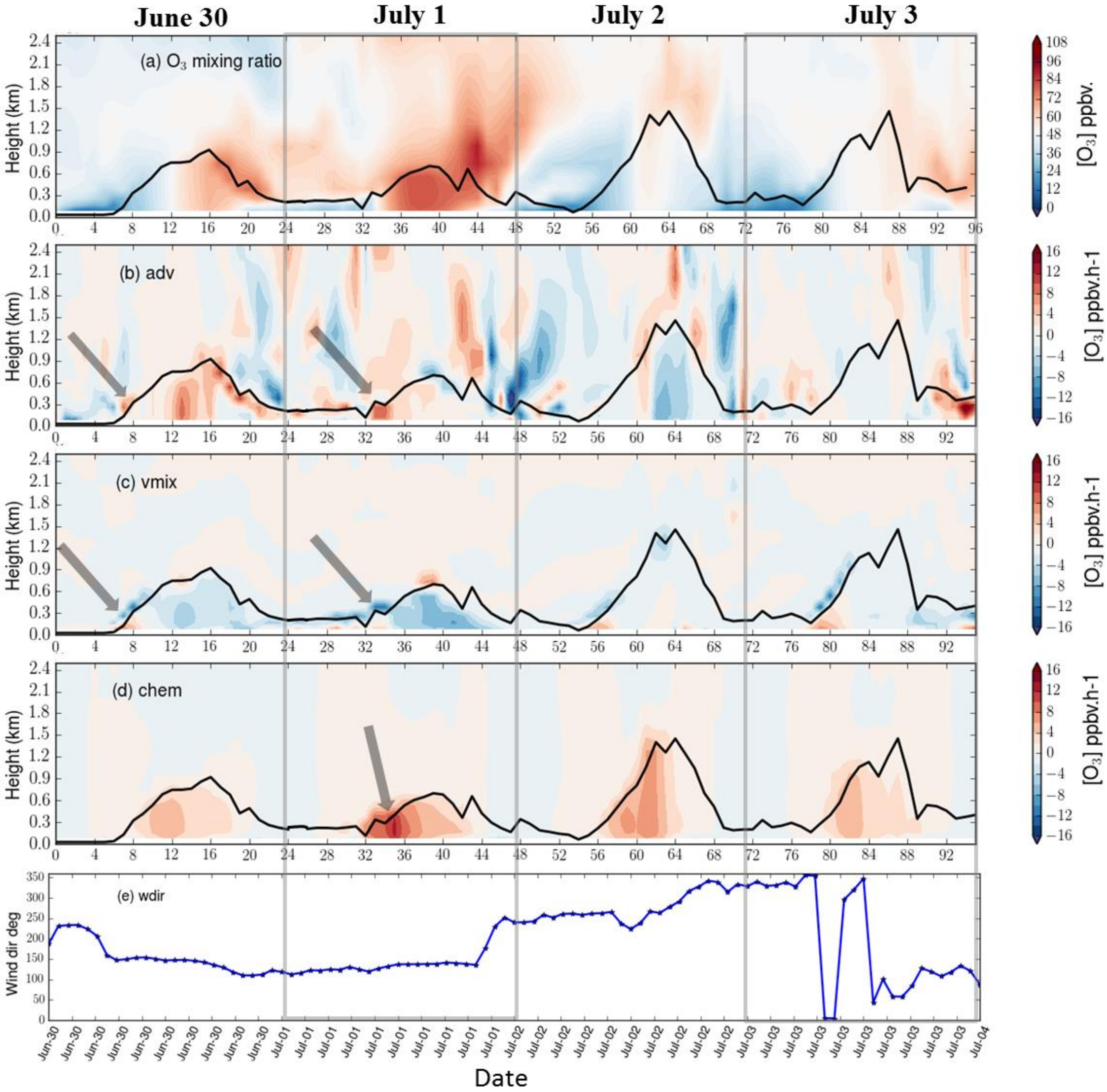

Figure 5.21. Time–height section of O_3 mixing ratios (ppbv) and the process tendencies from June 30th to July 3rd 2015, at Wicken Fen. (a) O_3 mixing ratio, (b) adv, (c) vmix, (d) chem. Wind direction is also showed (e). The black line in a-d shows the evolution of the planetary boundary layer height. Grey arrows indicate key features referred to in the text.

On 1st July, O_3 was advected at ~ 300 m height close to the top of the PBL in the early morning (Figs. 5.22). Negative values in the vmix component between 200 and 400 m height just above the top of the PBL and positive values below indicate that O_3 was transported towards the ground by vertical mixing process (see Figs. 5.21c and 5.22b). Advection of ozone-rich air at the surface was also observable in the morning, from 08:00 to 10:00 UTC (see Fig. 5.21b), followed by photochemical production that extended until 18:00 UTC (see Figs. 5.21d and 5.23b). Like Weybourne, the maximum rate of change in surface O_3 concentrations was observed in the morning from 08:00 to 09:00 UTC (~15 ppbv h^{-1}). Chemical production was the major contributor to the build-up of surface O_3 (up to 14 ppbv increased at 11:00 UTC) followed by advection (about 5 ppbv increased at same time). The maximum modelled surface O_3 concentration was 75.7 ppbv occurring around 16:00 UTC. Surface O_3 was lost in the morning by advection and by dry deposition in the afternoon. Chemical loss on the other hand became important after 19:00 UTC (see Fig. 5.22b). The episode breaks after a change in the wind direction from east-southeast to west-southwest between 19:00 and midnight bringing ozone-depleted air to the site.

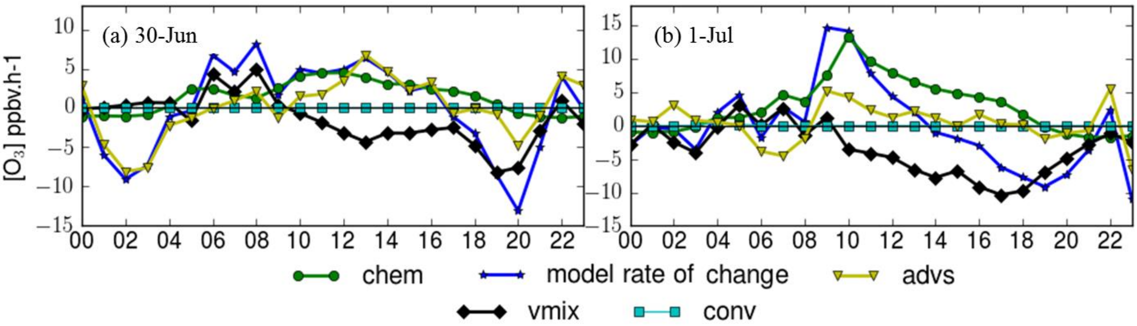

Figure 5.22. Process tendencies at the model bottom level (~30 m) at Wicken Fen on: (a) 30th June, and (b) 1st July.

5.4.2.3 *Sibton*

Figs. 5.23 and 5.24 show the evolution of the O_3 mixing ratios and the contributions of the different processes at the model bottom level (~30 m) and in different vertical layers during the 30th June and 3rd July at Sibton. As shown in

Fig. 5.23, for most of the day vmix was the major process controlling surface O_3 mixing ratios on 30th June at Sibton (up to 40 ppbv h^{-1} increase at 17:00 UTC), followed by chemical production in the morning hours. However, at the same time O_3 is largely lost by advection processes (up to 50 ppbv h^{-1} decrease in surface O_3 at 17:00 UTC). Fig. 5.24b (grey arrow) further shows high O_3 input by adv occurring at 100–300m height alongside the PLB between 08:00 and 20:00 UTC and high chemical production about 100 m height in the morning hours (Fig. 5.24d grey arrow). Moreover, high O_3 input by vmix was observable at the surface level (Fig. 5.24 grey arrow) throughout the same time window. These suggest that the large downward mixing of O_3 at ground level was likely initiated in the morning hours by transport of O_3 and chemical production at heights above the PBL follow by entrainment of O_3 to the surface levels. This results in a positive morning average rate of change in O_3 of 5 ppbv h^{-1}. In the afternoon, surface O_3 increased by adv of O_3 from the south-southeast above the PBL and subsequent mixing down. Interestingly, the model simulated a very shallow PBL (in the range 0 - 300 m) which was nonetheless quite turbulent so that the loss of surface O_3 by advection was compensated by mixing down of ozone-rich air (see Figs. 5.23a and 5.24c).

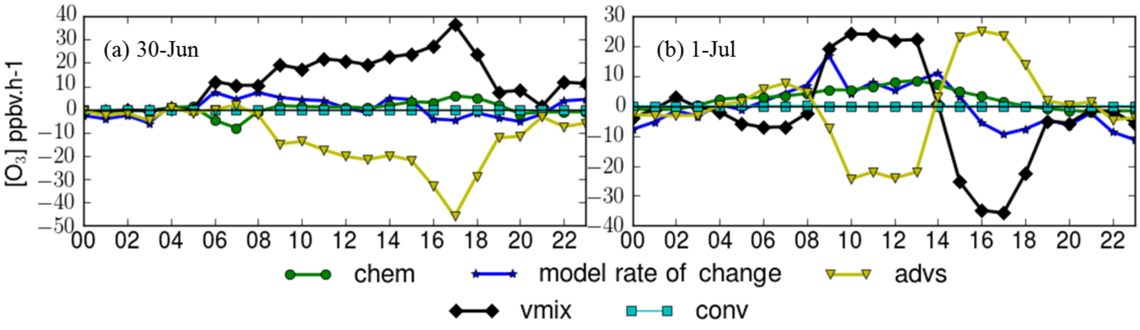

Figure 5.23. Process tendencies at the model bottom level (~30 m) at Sibton on: (a) 30th June, and (b) 1st July.

On 1st July, the increase in surface O_3 concentrations are mostly controlled by vertical mixing and chemical production in the morning, followed by advection and chemical production in the afternoon (See Figs. 5.23b). Similar to Weybourne, the highest increased in the O_3 concentration was observed in the morning hours. O_3 increased about 20 ppbv h^{-1} by 09:00 UTC and kept increasing gradually (at about 6 ppbv h^{-1}) until 13:00 UTC. In the afternoon, surface O_3 increased largely due to advection of ozone-rich air (up to 28 ppbv input of O_3 from the adv term at 17:00 UTC). However, at the same time surface O_3 was largely lost by dry deposition (up to 38 ppbv h^{-1} loss). Resulting in a net loss of up to 10 ppbv h^{-1} at 17:00 UTC. Fig. 5.24b (grey arrow) further shows that the boundary layer was also very shallow on 1st July (in the range 0 - 200 m). In the morning, accumulation by both advection and photochemistry was more pronounced above the PBL (at 100– 300m height) than in the surface layer (Figs. 5.24b, 5.24d, respectively). This led to a strong downward mixing of O_3 from the upper levels to the surface layer (Fig. 5.24c. In the afternoon, surface O_3 increased through advection of O_3 rich air from southeast and was mainly lost by dry deposition (Figs. 5.24b and 5.24c, respectively). Again, the episode breaks following a change in the wind direction from south-southeast to the west-northwest (Fig. 5.24e). Notice that a shallow planetary boundary layer was obtained when the wind direction fluctuated between the east (100°) and southeast (150°), whereas a deeper boundary layer was observed when the wind originates from the west-southwest (300°) and south-southwest (200°), Figs. 5.24 d and 5.24e. Sibton is located about 60 km inland from the Suffolk coast to the southeast of Norwich. Hence, lower planetary boundary layers are obtained when the air came from the southern North Sea while deeper PBL are associated with air arriving from inside the UK. This behaviour was also observed at St. Osyth located about 5 km from the southern North Sea coast as discussed in the next section, see Figs. 5.25d and 5.26e.

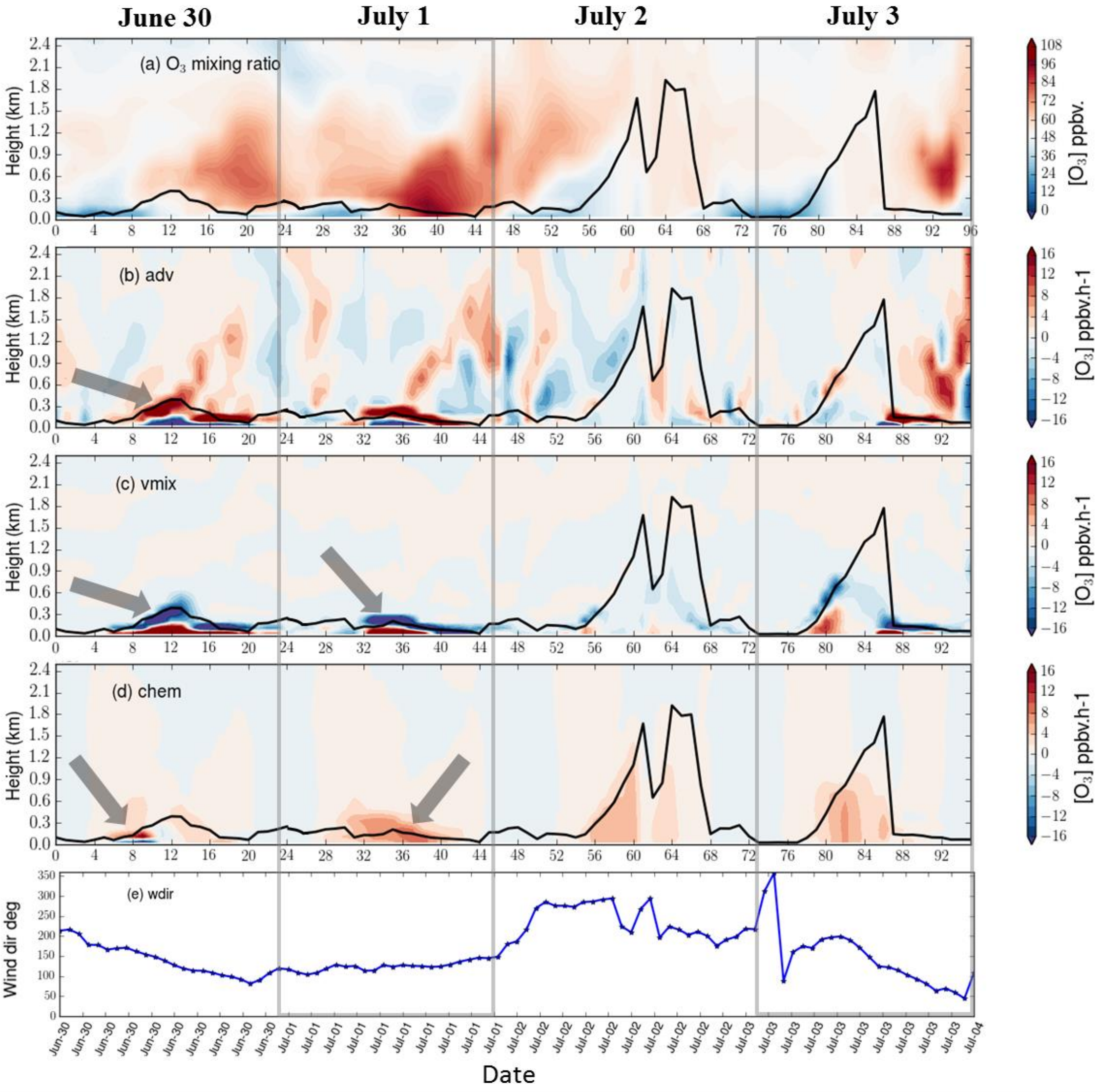

Figure **5.24**. Time–height section of O_3 mixing ratios (ppbv) and the process tendencies from June 30th to July 4th 2015, at Sibton. (a) O_3 mixing ratio, (b) adv, (c) vmix, (d) chem. Wind direction is also showed (e). The black line in a-d shows the evolution of the planetary boundary layer height. Grey arrows indicate key features referred to in the text.

5.4.2.4 St. Osyth

The vertical distribution of O_3 and the process tendencies show in Fig. 5.25 reveals that in the morning of 30th June (between 08:00-12:00 UTC) large O_3 chemical production was obtained at layers between 100 – 200 m alongside the PBL (Fig. 5.25d, grey arrow) whereas at the surface, gas-phase chemistry played an important role in the consumption of O_3 (up to 25 ppbv h^{-1} loss near the surface between 08:00 and 09:00 UTC). The observed chemical loss in the morning hours was compensated by downward transport of O_3 from upper levels to the surface layer (Fig. 5.25c). Surface O_3 reached ~60 ppbv after midday (Fig. 5.25a). The mixed down of O_3-rich air from aloft to the surface was maintained from midday until midnight probably sustained by advection of ozone-rich air at 100– 300m height (Fig. 5.25c grey arrow). Nevertheless, advection at the surface greatly removes O_3 from the site at about ~22 ppbv h^{-1} on average.

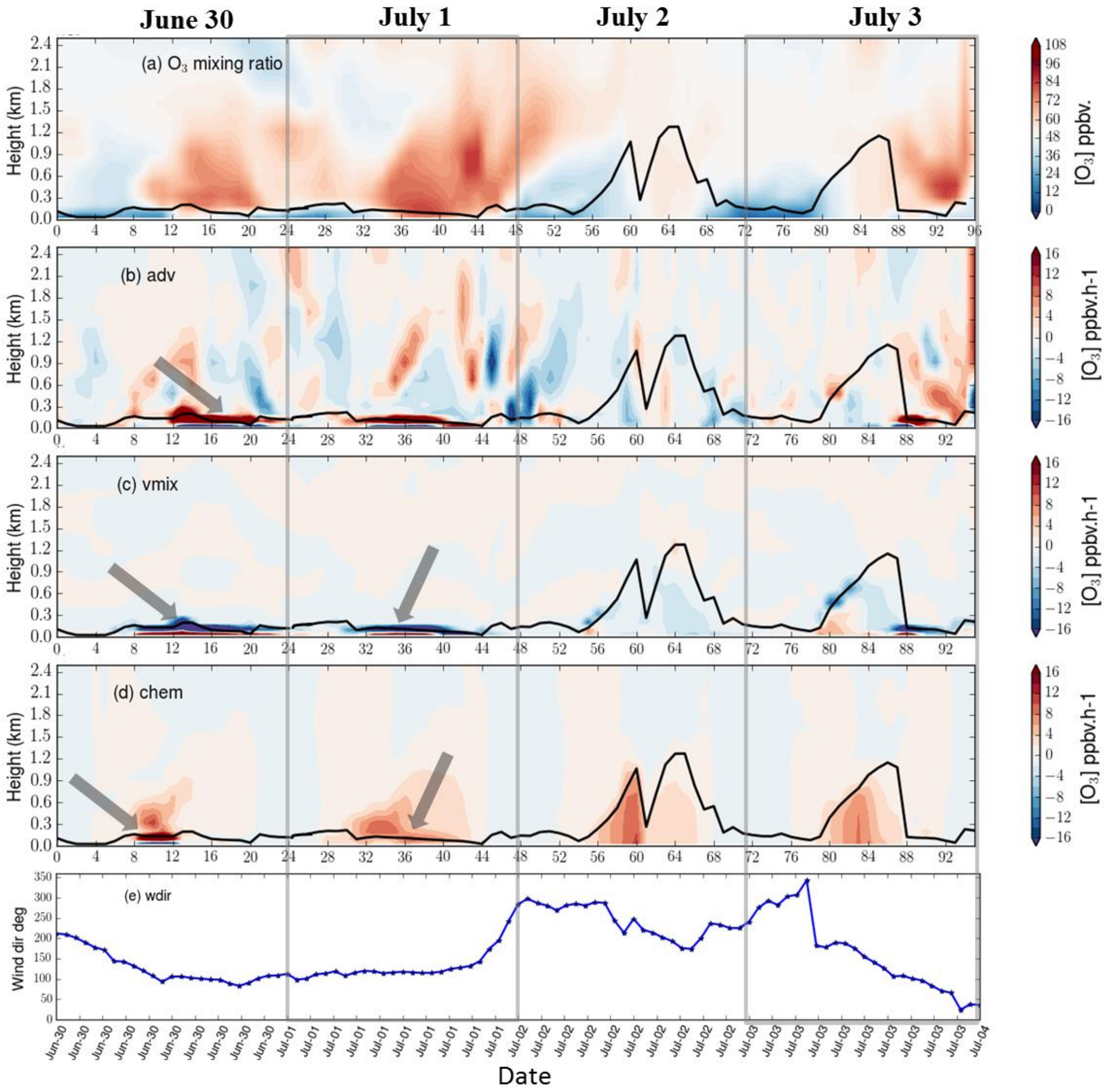

Figure 5.25. Time–height section of O_3 mixing ratios (ppbv) and the process tendencies from June 30th to July 4th 2015, at St. Osyth. (a) O_3 mixing ratio, (b) adv, (c) vmix, (d) chem. Wind direction is also showed (e). The black line in a-d shows the evolution of the planetary boundary layer height. Grey arrows indicate key features referred to in the text.

A similar picture was observed on 1st July. In the morning surface O_3 was lost by advection of low-O_3 air at the surface, however, the loss of O_3 was compensated by downward mixing (vmix term), see Fig. 5.26b. The largest positive rate of change in O_3 was observed at 09:00 UTC (about 10 ppbv h^{-1}), and the increased in O_3 was maintained until 16:00 UTC. In the afternoon O_3 was largely lost by dry deposition, see Fig. 5.26b. Fig. 5.25b further shows that similar to Sibton, in the morning and afternoon advection of O_3 in St. Osyth was greater at layers between 100–200 m above the PBL than at the surface level. Large downward mixing of O_3 from upper levels to the surface layer was obtained at the same time interval. O_3 chemical production was also seen during morning above the PBL and after about 11:00 UTC at the surface. Surface O_3 reaches ~70 ppbv after midday (Fig. 5.25a). Thus, it can be concluded that the increased in the surface O_3 mixing ratios in the morning was mainly due to transport of O_3 and precursors loaded air above the PBL at heights between 100–200 m (see Fig. 5.26) and subsequent downward mixing of O_3 and chemical production. After midday O_3 was mainly advected from the south-southwest at the surface levels. In the evening O_3 was advected at the surface, but lost by dry deposition.

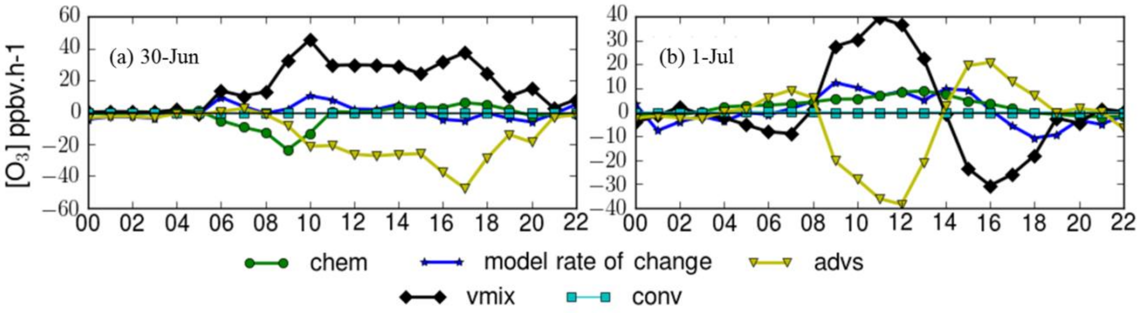

Figure 5.26. Process tendencies at the model bottom level (~30 m) at St. Osyth on: (a) 30th June, and (b) 1st July. Note different scale of y-axes.

5.4.3 Summary

A high ozone concentration episode accompanied by record-high temperatures was observed at WAO and nearby sites in the East Anglia region during the first days of the ICOZA field campaign on summertime 2015 (June 30 – July 1). WRF-

Chem simulations showed a strong association between wind direction and the O_3 concentrations at the assessed sites, suggesting that the transport of O_3 and precursors from south-easterly sources were the likely causes of the episode.

Process analysis indicated that during the build-up period (between June 30 and the morning of July 1) O_3 started accumulating above the PBL after the advection of O_3-loaded air masses to the sites. This was followed by vertical transportation of O_3 from upper levels to the surface layer in the late morning and afternoon. Photochemical production was found to be the largest contributor to the surface O_3 enhancement over Wicken Fen and WAO during the peak event, while at the most eastern sites (Sibton and St Osyth) the increased in O_3 was principally driven by downward mixing of O_3 from upper vertical levels. Dry deposition and advection of O_3 out of the domain were the main sinks for O_3 in the lowest model levels.

It was found that the PBL growth played an important role in the evolution of the O_3 episode. During the peak day, a shallower planetary boundary layer (in the range 0 - 600 m) than that obtained on June 30 was observed in all sites. It is suspected that this shallow boundary layer combined with advection of ozone-rich air masses and enhanced photochemical production resulted in high surface O_3 concentrations. The onset of the event (July 2), on the other hand, was characterised by a changed in the wind direction from south-easts to the wests. A deeper PBL accompanied by losses of O_3 mostly driven by vertical mixing and advection were also observed in the sites. Even though it was not possible to compare the vertical simulation results with measurements, due to the lack of vertical O_3 distribution measurements in the region, these results provide scientific evidence of the transport of ozone-loaded air masses and precursors from south-easterly sources to the East Anglia region.

5.5 Transport pathways for pollution inflow from continental Europe at WAO

Fig. 5.27 shows a vertical cross section of the evolution of the tracers at Weybourne during the two days with the highest modelled surface O_3 mixing ratios: June 30th (onset of the episode) and July 1st.

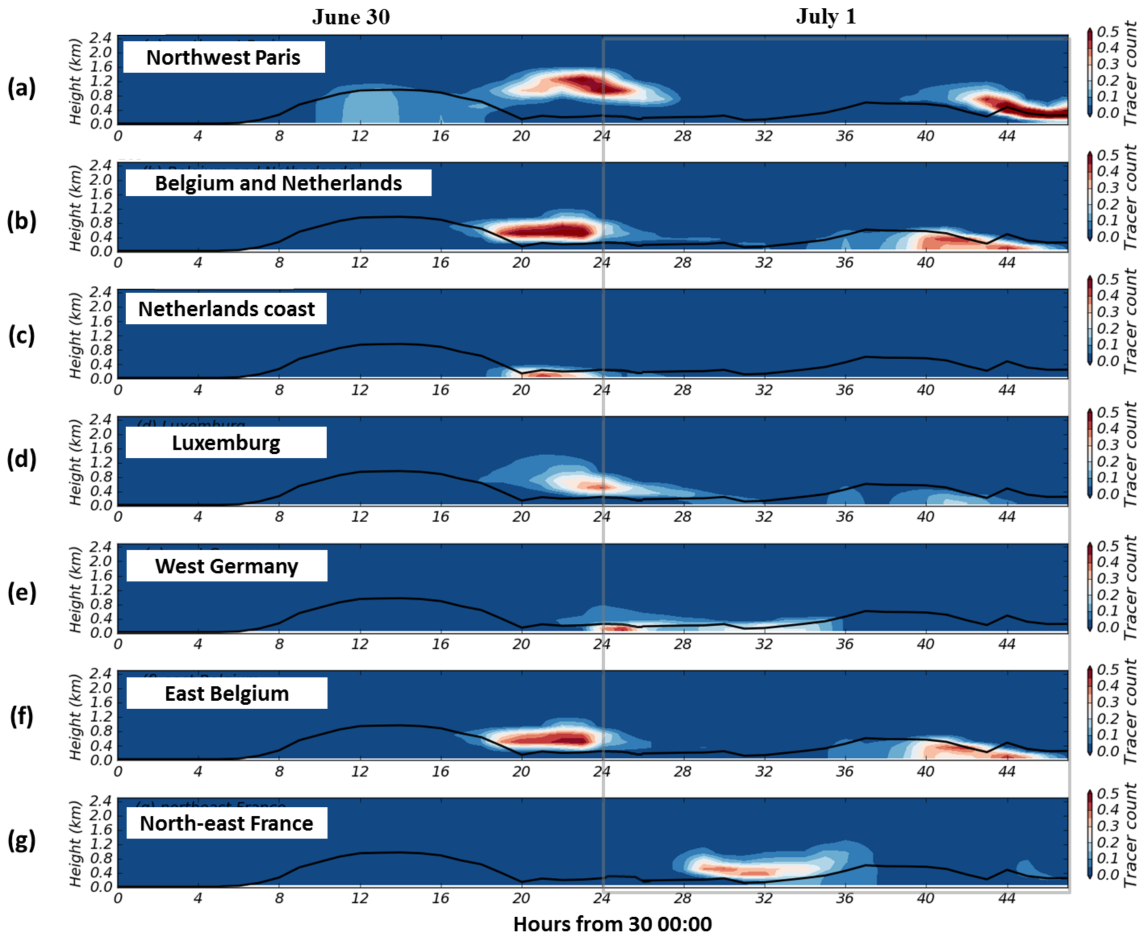

Figure 5.27. Time–height section of tracer counts for June 30th to July 1st at Weybourne. (a) Tracers released at northwest of Paris; (b) coast on the border between Belgium and the Netherlands; (c) Netherland coast within the Rotterdam port; (d) Luxemburg; (e) west Germany; (f) east Belgium; and (g) northeast France.

Fig. 5.27a shows that the tracer released at the northwest of Paris reached the surface of Weybourne on June 30th between 10:00 and 18:00 UTC. The tracer is well mixed within the depth of the boundary layer and is more concentrated around 12:00 UTC. Interestingly, the timing of the arrival of the tracer corresponds to the advection of O_3 at the surface shown in Fig. 5.18b section *5.4.2.1, i*ndicating that pollutant-loaded air from France can easily reach WAO under the meteorological conditions experienced on the 30th June. Similarly, the build-up of the Belgium-Netherlands tracer at levels between 300-900 m height shown in Fig. 5.27b coincides with the accumulation of O_3 at similar heights showed in Fig. 5.18b section *5.4.2.1*. Ultimately, the arrival time of the tracer released close to the port of Rotterdam on the coast of the Netherlands (Fig. 5.27c) reached the surface at Weybourne between 20:00 and 24:00 UTC and corresponds to the O_3 advected at the same heights shown in Fig. 5.18b.

Fig. 5.28a further shows that the tracer released at the coast on the border between Belgium and the Netherlands was mixed up to the top of the boundary layer on June 30th, between 09:00 and 13:00 UTC. By 17:00 UTC, Fig. 5.28a, the tracer was transported in layers above the marine boundary layer (MBL) between 300 and 1200 m high over the North Sea. During the daily hours, a warmer land surface resulted in a higher PBL over land than over the sea (National Research Council, 1992). With horizontal advection from the land to the sea dominating, the differential heating between the land and the sea, as well as the change in the surface roughness, can lead to the formation of an internal boundary layer (IBL) the intersects the land surface at the edge of the temperature and roughness contrast. This IBL could serve as a 'bridge' connecting the continent with stable layers (layers in which the potential temperature increases with height) above the MBL (Dacre et al., 2007), as shown in Fig. 5.28a. Because dry deposition and vertical mixing are limited under such conditions, trace gases can be transported over long distances. This phenomenon of decoupling of pollution from the land surface via the formation of an IBL is referred as 'coastal outflow' (Dacre et al., 2007). Turbulent mixing over land can transport polluted air away from the surface where it is then advected horizontally above the marine boundary layer and across the sea. The mechanism can also be triggered by the convergence of the sea breeze and the prevailing wind. This results in polluted air being ventilated out of the Earth's surface and then advected horizontally across the coast due to the return flow of the sea breeze circulation (Dacre et al., 2007). Fig. 5.28a demonstrates that the tracer is then effectively transported horizontally in these vertical layers across the North Sea reaching Weybourne at 300 – 900 m high after 21:00 UTC. Turbulent mixing after sunrise might mix down the tracer into the surface layer. The study of Dacre et al. (2007) investigated the processes responsible for the ventilation of the atmospheric boundary layer during anticyclonic conditions in the UK using passive tracers within the UK Met Office Unified Model. The study shows that coastal outflow, sea breeze circulation, turbulent mixing, large-scale ascent and shallow convection can efficiently raise tracers away from the surface and distributing them throughout the boundary layer, and even above the boundary layer top to up 2 km height where large-scale flows can eventually transport them.

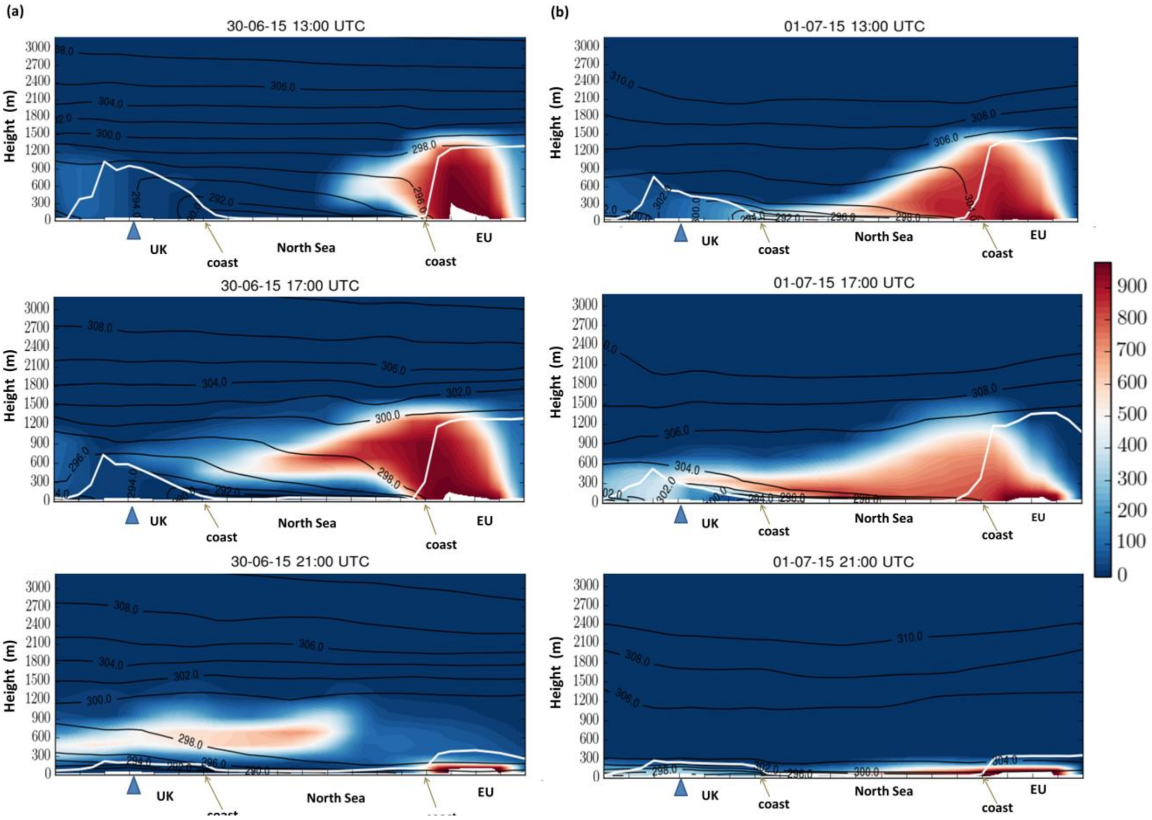

Figure 5.28. Vertical cross sections of tracer counts released at the coast on the border between Belgium and the Netherlands, (A–B) (Fig. 5.12b), overlaid with potential temperature (black contours) on 30th June (column a) and 1st July (column b). The white line shows the evolution of the PBL height, the blue triangle denotes WAO.

On July 1st, the tracers released in Luxembourg, West Germany, and northeast France (Figs. 5.27d, 5.27e, and 5.27g, respectively) arrive at Weybourne in the early morning at layers between 300–900 m height above the PBL. The West

Germany tracer in particular also reached Weybourne at the surface level and remained mostly confined within the PBL. The timing of these plumes corresponds to the increase in O_3 due to advection and subsequent downward mixing of O_3 loaded air shown in Figs. 5.18b and 5.18c section *5.4.2.1*, respectively. This suggests that pollution outflow from these regions can easily affect WAO under the meteorological conditions seen on the 1st July. The evolution of the tracer in the early morning presented in the cross sections in Fig. 5.29b further demonstrates that at about 10:00 UTC the tracer released in West Germany has remained mostly restricted within the marine boundary layer. Thus, it is likely that a proportion of the transport of the tracer from this source region occurred at the surface level. Because O_3 is deposited more slowly to water surfaces than to land surfaces (Wesely et al., 2000), it is likely that the polluted air over the ocean retained most of its chemical characteristics. Emissions outflow from Europe are known to remain in the lower troposphere as convection is less strong over Europe than over the US and continental Asia (Stohl et al., 2002). Thus a substantial proportion of transport of pollutants tends to occur close to the surface below 2 km (Wild et al., 2004).

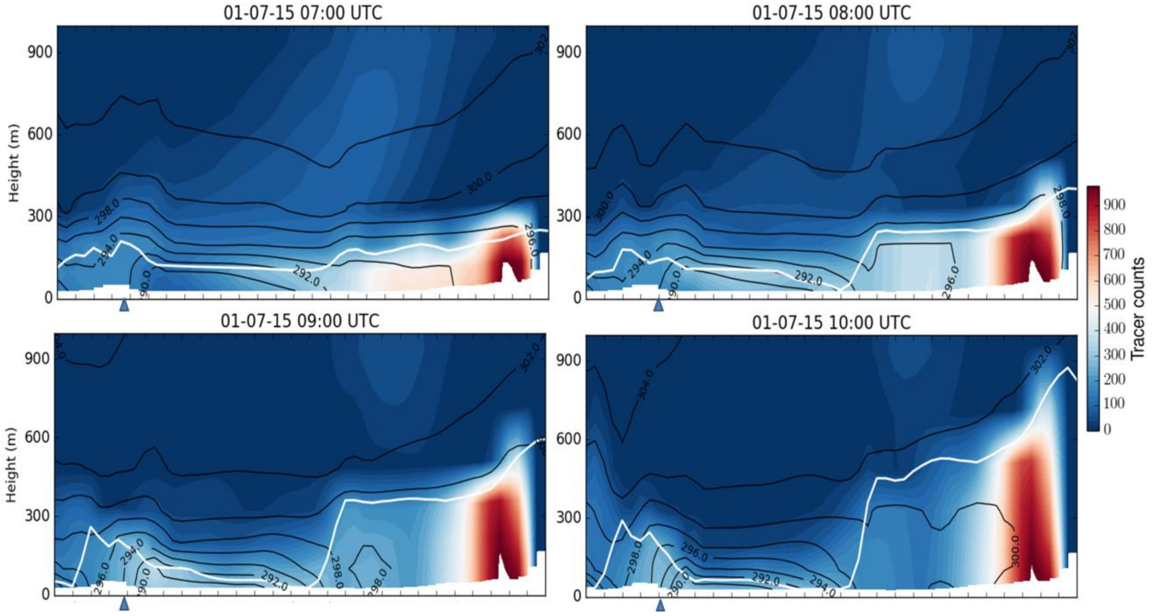

Figure 5.29. Vertical cross sections of tracer counts from West Germany, (A–B) (Fig. 5.12c), overlaid with potential temperature (black contours) on 1st July 10:00 UTC. The white line shows the evolution of the PBLH and the blue triangle denotes WAO.

In the afternoon, plumes from east Belgium and the coast of Belgium and the Netherlands (Figs. 5.27g and 5.27b) reached Weybourne at the surface. The timing concurred with the growth in O_3 caused by advection, in Fig. 5.18b section *5.4.2.1*. Fig. 5.28b further shows that in the afternoon, the transport of the tracer emitted on the coast of Belgium and the Netherlands across the North Sea occurs in a layer between 100 – 800 m height above a very shallow marine boundary layer. The model study of Angevine et al., (2004) shows polluted plumes from the Boston, Massachusetts US, arriving at coastal New Hampshire and coastal southwest Maine via trajectories over coastal waters in stable layers at the surface. These layers retained most of their chemical characteristics due to the lack of deposition or deep vertical mixing on the overwater trajectories allowing pollutant concentrations to remain strong. To the author knowledge, no similar experiment has been conducted so far to illustrate the transport of pollutants from continental Europe to the UK.

5.5.1 Summary

Passive tracers released at seven regions within continental Europe highlight the likely transport pathways and source regions contributing to the build-up of surface O_3 at Weybourne. The arrival time of the seven tracers at Weybourne was compared with the timing in the process analysis discussed in section *5.4.2.1*. To the author knowledge this is the first time a process analysis scheme within an online model has been employed together with inert tracer simulations. It has been shown that the timing in the build-up of O_3 on 30th June agreed with tracers transported from the northwest of Paris, and from Belgium and the Netherlands. In particular, it was shown that the tracer released at the coast of Belgium and the Netherlands was mixed vertically through the boundary layer depth and horizontally transported above the marine boundary layer before reaching the surface of Weybourne. On July 1st, the arrival time of the tracers released in Luxembourg, northeast France, east Belgium and West Germany coincided with the increase in surface O_3 due to advection and subsequent downward mixing of O_3 loaded air at Weybourne as discussed in section *5.4.2.1*. Moreover, it is likely that some of the particles released at southwest Germany and reaching Weybourne at the surface levels in the morning were transported across the North Sea within the marine boundary layer. Ultimately, the growth in O_3 caused by advection in the afternoon of July 1st agrees with the timing in the arrival of the tracers released in east Belgium and the coast of Belgium and the Netherlands. This tracer was likely transported above the marine boundary layer before reaching the surface of Weybourne.

5.6 Conclusions

In this chapter, the evolution of surface O_3 and the factors leading to its build-up during a summertime pollution episode recorded in the first few days of the ICOZA field campaign at WAO were characterized. Three additional sites within the East Anglia region were also investigated. The main results can be summarized as follow:

- ✓ High O_3 concentrations, peaking above the information threshold of 1 h average O_3 mixing ratios of 180 µg m^{-3} (90 ppbv), observed over Western Europe, and Southeast England demonstrates that the pollution episode was a regional scale phenomenon. In the UK the episode was interrupted after midnight on 1st July following a change in the wind direction from the southeast to the southwest which brought cooler and cleaner air from the Atlantic.
- ✓ A strong association between wind direction and the evolution of surface O_3 concentrations during the pollution episode at Weybourne was seen. Accumulation of surface O_3 was associated with southeast and south south-easterly winds while westerly winds (south south-westerly) were linked to surface O_3 concentrations below the EU 8 hour threshold of 60 ppbv.
- ✓ The convergence of westerly and easterly winds approaching from the western side of the UK was found to be key facilitating the accumulation of O_3 in the southeast UK.

- ✓ The mixing down of O_3 from the residual layer and sustained chemical production at the surface level were found a fundamental process increasing the O_3 concentrations during the early morning of the event. In particular, the input of surface O_3 due photochemistry was larger than the input from downward mixing indicating that photochemistry was a crucial process increasing the O_3 concentrations during the episode. Similarly, the sustained increased in the surface O_3 mixing ratios in the afternoon was due to chemical production in the first place and advection of O_3 within the PBL likely from Continental Europe in the second place.
- ✓ Process analysis revealed a reservoir of O_3 and PAN above the PBL on the night of the 30th June and the early morning on the 1st July available for downward mixing. This suggests that the potential for both entrainment of O_3 loaded-air and precursors existed on the day of the episode. It is also likely that the enhanced O_3 chemical production on the day of the event was influenced not only by UK emissions but also by short-range transport of O_3 precursors from continental EU. This is further explored in Chapter 6.
- ✓ Assessment of two additional sites in the Suffolk reveals that on 30th June and 1st July O_3 and precursors entered the Suffolk coast from the North Sea in a layer not in contact with the surface but at altitudes between 100-300 m height. O_3 was eventually mixed down to the surface by vertical mixing process through the day. By contrast, assessment of WAO and an inland site (Wicken Fen) suggests that inside the East Anglia region O_3 and precursors were transported within the PBL.
- ✓ Passive tracers released within the model simulation shows that under south-easterly winds, the particles released from individual sources in France, Belgium, Luxemburg, Netherlands and Germany could reach WAO above the PBL at altitudes about 300–100m and at the surface level. Moreover tracers emitted at the Netherlands and Belgium coast illustrate how precursors and O_3 within the PBL can be lifted to the top of the boundary layer and efficiently transported horizontally in stable layers above the MBL and across the North Sea by coastal outflow before reaching Weybourne. Similarly, tracers released in West Germany illustrated the transport of pollutants towards the UK near

the surface level. These tracers are transported horizontally to Weybourne confined near the surface by the stable MBL.

This chapter furthers the current understanding of the role of long-range transport in the evolution of surface O_3 mixing ratios during high concentrations episodes in the UK. It also highlights the value of passive tracers to distinguish the different transport pathways and source regions contributing to inflow of pollutants to the UK under high O_3 concentration conditions

Chapter 6

THE SOURCE OF OZONE DURING A HIGH CONCENTRATION EPISODE: A CASE STUDY FROM THE ICOZA CAMPAIGN –PART II: CONTRIBUTIONS FROM SOURCE REGIONS

6.1 Rationale

In Part I of the present study passive tracers were used to identify the possible geographical sources and pathways that brought pollution to Weybourne during an O_3 pollution episode. Here, the ozone-tagging method described in Chapter 2 is used to quantify the contributions to surface O_3 at Weybourne from different geographical source regions within Europe. The processes analysis scheme is then applied to investigate through which mechanism O_3 was transported from each source regions to Weybourne. To the author's knowledge this is the first time that an ozone-tagging method within a regional model has been applied to investigate the origin of O_3 during pollution events in the UK. The study addresses the following research questions:

I. How relevant are the contributions from different geographical regions within continental Europe to surface O_3 in Weybourne during high O_3 concentrations?

II. Was O_3 produced in-situ from domestic NO_x emissions or from European NO_x?

For convenience, the model setup is described in section 6.2. Predictions of contributions from the source regions to O_3 concentrations at Weybourne and the mechanisms associated with the build-up of surface O_3 are presented in section 6.2. Conclusions are given in section 6.3.

6.2 Methods

6.2.1 Model setup

The WRF-Chem model was setup with one domain (see Fig. 6.1) with a horizontal resolution of 27 km and 35 vertical levels with 12 levels in the first 3 km and 23 levels between 3 and ~20 km (10hPa). The lowest vertical level corresponds to ~50 m. Simulations were conducted for the period between the 21st April and 1st August 2015 with a 150 seconds time step for both the meteorology and the chemistry module. The first ten days were taken as spin-up and therefore discarded. This chapter focuses only on the period between 30th June and 3rd July, as this coincides with the pollution episode observed during the ICOZA campaign.

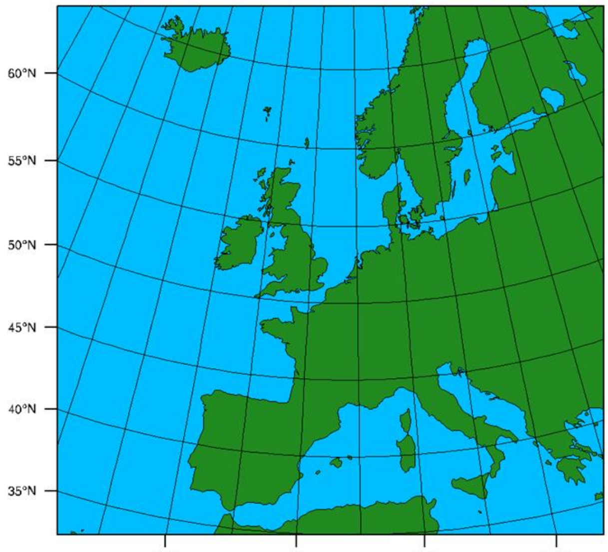

Figure 6.1. Preview of the WRF-Chem domain.

As in Chapter 5, the meteorology was not nudged but re-started every three days. The chemical mechanism however is different and for this chapter an ozone-tagging mechanism which uses the chemistry of the Model for Ozone and Related chemical Tracers (MOZART-4) gas-phase mechanism was used. MOZART-4 was discussed in detail in Chapter 2. The anthropogenic emissions consist of a hybridization of the latest UK National Atmospheric Emissions Inventory (NAEI) for the year 2014 (resolution of 1 km) and the most recent version of TNO emissions inventory (TNO-MACC III) (Kuenen al., 2014) for the year 2011 (resolution 0.125° longitude × 0.0652° latitude). See Section *2.2.2.3* for details regarding the implementation of the anthropogenic emission inventories.

6.2.2 Ozone source apportionment

The contribution of European anthropogenic emissions to tropospheric O_3 in the UK is studied using the ozone tagging mechanism discussed in Chapter 2 in which O_3 molecules are labelled with the identity of their geographic source enabling the direct attribution of O_3 concentrations in the receptor area to a specific source region (Butler et al., 2018). The reader is referred to section 2.3 for details regarding the description and implementation of the ozone-tagging method.

The contribution is calculated by dividing the domain shown in Fig. 6.1 into three regions: 1) the UK, including England, Wales, Northern Ireland and Scotland; 2) Europe; and 3) the lateral boundaries. Europe is further divided into eight sub-regions. Most of the O_3 from precursors originating from this sub-region is tracked as an independent variable. These regions were chosen as shown in Fig. 6.2: 1) France (FRA); 2) Belgium (BEL); 3) The Netherlands (NET); 4) Luxemburg (LUX); 5) Germany (GER); 6) The North Sea and English Channel (NOS); 7) the rest of Central Europe (Rest_CEu), containing Austria, Switzerland, the Czech Republic, Hungary, Poland, Slovakia, Slovenia and Romania; and 8) Rest of Eu (Rest_Eu), containing the remaining areas in the model domain including the Iberian peninsula, Southern Europe, South-eastern Europe, Eastern Europe, Northern Europe, Ireland, and ship emissions from the Atlantic, Baltic

Sea and the Mediterranean. Such setting of source regions enables untangling the derived contributions from western and central Europe and from the busiest shipping route in Europe.

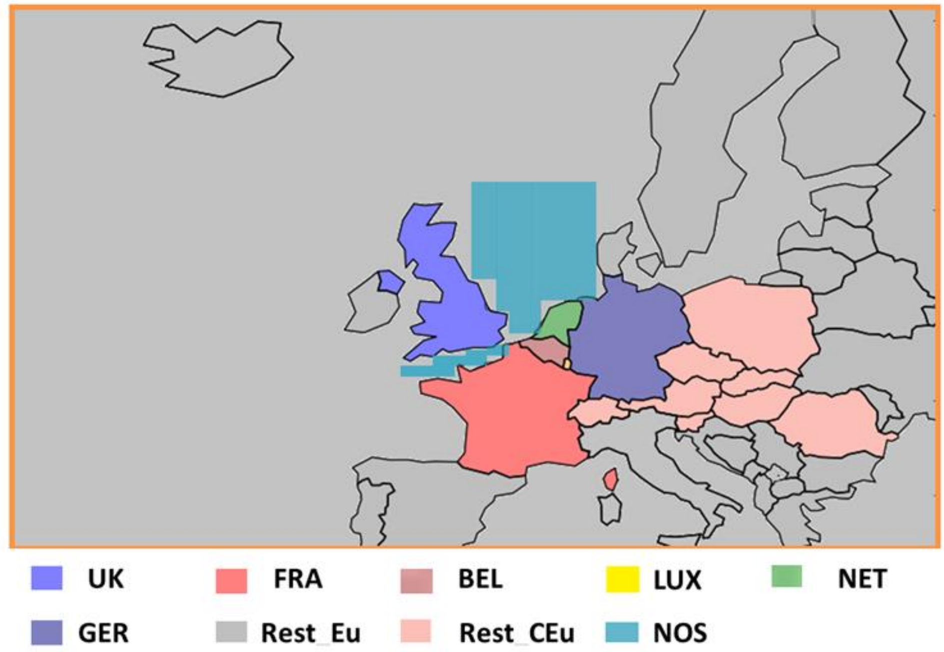

Figure 6.2. Source regions settings: Note that Rest_Eu tagged also includes ship emissions from the Atlantic, Mediterranean and Baltic Sea whilst emissions from shipping routes in the North Sea and the English Channel are tagged as NOS. The orange line surrounding the domain indicates lateral boundary source tag (LB).

6.2.3 Process analysis

The process analysis tool discussed in Chapter 5 was added to the source apportion scheme to explore the O_3 transport mechanism to Weybourne from the different source regions across continental Europe. The process analysis scheme calculates the hourly contribution of net chemical contribution (chem), convective transport (conv), horizontal and vertical advection (adv), and vertical mixing/dry deposition (vmix) at each grid cell.

6.3 Results: contributions to surface ozone from different geographical source regions within Europe

Fig. 6.3 shows the absolute contributions of O_3 from the lateral boundaries, domestic (UK) and European super region to surface O_3 at Weybourne during the ICOZA campaign. Large contributions from the European super region are observed during several time periods, in particular between the 30th June and 3rd July (the time interval of the pollution episode). During this time period, about 54% of the mean modelled surface O_3 came from the European super region while 18% from domestic sources and the rest (28%) from the lateral boundaries.

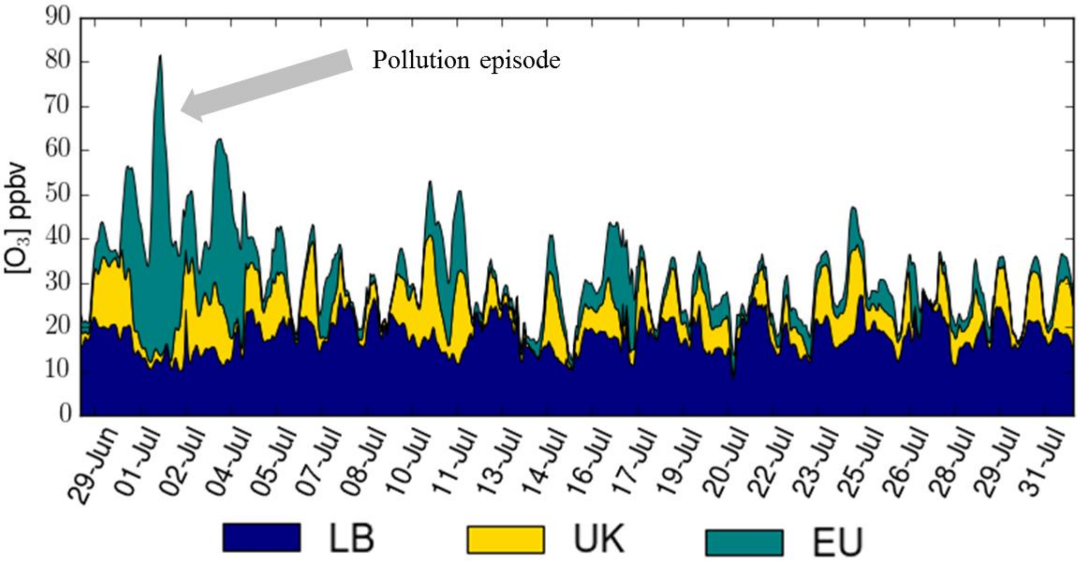

Figure 6.3. Contributions from different sources regions (lateral boundaries (LB, UK and EU) to hourly surface O_3 from June 29th to July 31st 2015 at Weybourne.

Fig. 6.3 also shows that the absolute contribution from domestic O_3 (O_3 formed from UK NO_x emissions) was very small between 30th June and 1st July (~3% of the total surface O_3 predicted on 1st July), i.e. in the time period when the highest O_3 mixing ratios were recorded. This corresponds to the development of a convergence zone of westerly and south-easterly winds near the surface in the west of the UK which pushed domestic O_3 westwards and northwards away from

Weybourne on the 1st July as indicated using white arrows in Fig. 6.4a-b. This convergence reduced the contributions of domestic sources.

The contributions from the lateral boundaries also decreased during the episode, in particular on the 1st July, while those from the European super region increased. This is consistent with the meteorology often observed during high O_3 episodes in the UK, in which a high pressure system establishes over northwest Europe causing easterly and south-easterly flow over the southeast UK (Jenkin et al. 2002). In this situation, air-masses circulate over continental Western Europe before entering the UK (e.g., Jenkin et al. 2002).

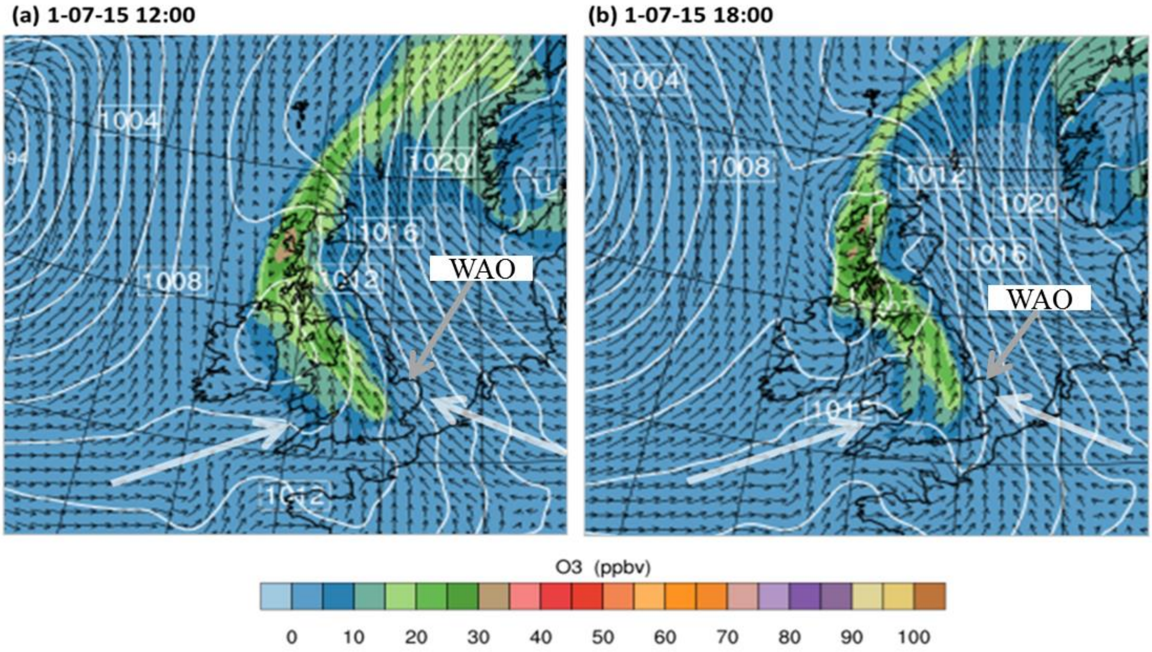
(a) 1-07-15 12:00

(b) 1-07-15 18:00

Figure 6.4. O_3 mixing ratios from the UK source region and the modelled meteorological conditions on July 1st at (a) 12:00 and (b) 18:00. Black arrows depict 10 m winds and white contours the mean sea level pressure (in hPa). The white arrows indicates the convergence of westerly and easterly winds.

6.3.1 Ozone contributions from eight sub-regions within the European domain

Fig. 6.5 shows the contributions from the eight additional sub-regions and Table 6.1 reports their contributions in terms of maximum daytime ozone. The values reported are those obtained when the maximum surface O_3 occurred on each day.

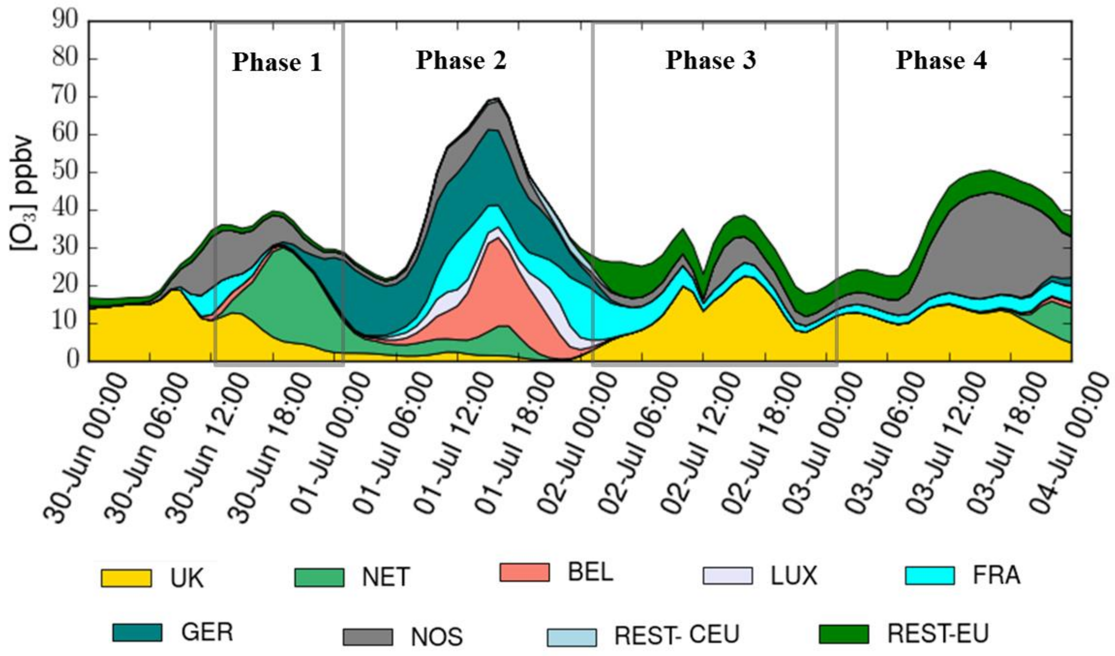

Figure 6.5. Contributions from different source regions across Europe (including UK) to the hourly surface O_3 over Weybourne. Note that the contribution from the lateral boundaries is not included in here. The phases correspond to the different stages of the pollution episode referred in the text.

Table 6.1. Contributions (ppbv and percentage) from nine source regions to the maximum daytime surface O_3 over Weybourne. The reported values correspond to the contributions from anthropogenic sources only.

Source regions	30 June (ppbv)	1 July (ppbv)	2 July (ppbv)	3 July (ppbv)
UK	13.0 (23%)	1.6 (2%)	22.6 (43%)	12.8 (20%)
Netherlands	3.2 (5%)	7.8 (9%)	0.0	0.3
Luxembourg	0.0	2.8 (3%)	0.0	0.0
Belgium	2.2 (4%)	23.4 (27%)	0.0	0.1
France	4.2 (7%)	5.7 (7%)	3.5 (7%)	3.3 (5%)
Germany	0.0	19.7 (23%)	0.0	0.1
Rest of Central Europe	0.0	0.6 (1%)	0.0	0.0
North Sea and British Channel	12.1 (21%)	7.9 (9%)	6.9 (13%)	27.5 (43%)
Rest of Europe	1.5 (3%)	0.2	5.6 (11%)	6.0 (9%)

O_3 source contributions varied during the study time interval, exhibiting different values depending on the specific day. This difference was partly related to the different O_3 build-up mechanisms, as discussed further in the following section. For practicality, the pollution episode can be divided into four segments based on the daily evolution of the O_3 mixing ratios, as indicated Fig. 5.5, and the wind direction. On 30th June when easterly winds prevailed, large contributions from the UK, North Sea and English Channel France, and the Netherlands were obtained. The contributions to the maximum daily surface O_3 at about 12:00 UTC at Weybourne were 23%, 21% 7%, and 5%, respectively. In the afternoon, the Netherlands had the largest impact with about 46% (25.5 ppbv) of the hourly mean surface O_3 at Weybourne coming from the source region. The contribution from Germany became important in the evening of 30th June.

On 1st July, when the receptor regions were under the influence of south easterly winds, Belgium and Germany were the major sources of surface O_3, with 27% (23.4 ppbv) and 23% (19.7 ppbv) of the maximum total O_3 at Weybourne coming from these regions respectively. At this point, the contribution from domestic sources was about 2% (1.6 ppbv) of the total maximum O_3. The shares from the North Sea and English Channel (9%, 7.9 ppbv), the Netherlands (9%, 7.8 ppbv), France (7%, 5.7 ppbv) and Luxembourg (3%, 2.8 ppbv) were also larger than the domestic contribution on this day. This period corresponds to the convergence zone of westerly and easterly flows developed along the western side of the UK.

On 2nd July, when the wind direction changed from southeast to south-southwest, domestic NO_x emissions become a major source of surface O_3, with 43% (22.6 ppbv) of the maximum surface O_3 at Weybourne coming from inside the UK. At this point, the maximum modelled concentration of O_3 over the site was about 58 ppbv, below the EU 8 hour threshold of 60 ppbv. The North Sea, Rest-Eu region and France were also important sources of O_3 on this day accounting for 13%, 11% and 7% of the maximum total O_3 simulated respectively. As the Rest-Eu region includes emissions from the Iberian Peninsula, Southern, South-eastern, Eastern, and Northern Europe, and ship emissions from the Atlantic, Baltic Sea and the Mediterranean, it is difficult to identify with confidence the predominant source of O_3. Nonetheless, as south-westerly winds dominated the morning of 2nd July, O_3 from this source region was likely to be dominated by O_3 from shipping routes in the Atlantic.

On 3rd July, the wind direction was predominately from the east. Surface O_3 at Weybourne was dominated by O_3 produced from NO_X emissions from the North Sea and British Channel and domestic emissions, with 43% (27.5 ppbv) and 20% (12.8 ppbv) of the maximum total O_3 coming from these source regions respectively. The contributions from France were also important during this day, with nearly 9% (6 ppbv) of the maximum surface O_3 coming from the source region. By contrast, the contributions from Western Europe (Netherlands, Luxembourg and Belgium) and Central Europe were practically negligible during most of the day.

6.3.2 Process analysis on the ozone tagging

In this section the processes analysis scheme is used to investigate through which mechanism O_3 was transported from each source region to Weybourne. Fig. 6.6 shows a time-cross section at Weybourne of the process tendencies for O_3 from the Rest-Eu source region.

The key to interpreting Fig. 6.6 is to start scanning from left to right at a specific altitude and see how O_3 in panel (b) changes. O_3 mixing ratios increase from blue to red, and for O_3 to increases, there must have been a positive tendency at that altitude at the same time as the O_3 increases. An example of this is on 2nd July around 48 and 52 hours Fig. 6.6b, as the PBL collapses the colour above 300 m altitude goes from a pale red to a stronger red. When looking at the advection term at the same time interval (Fig. 6.6c), there is a positive change in O_3 (red), this is quite clear because the other tendencies are quite weak. This increase in the O_3 contribution corresponds to high O_3 values in the total O_3 (Fig. 6.6a) at the same time interval and high. The reader needs to keep in mind that these tagged O_3 tendencies are used to explain the change in the total O_3 mixing ratios e.g., Fig. 6.6a

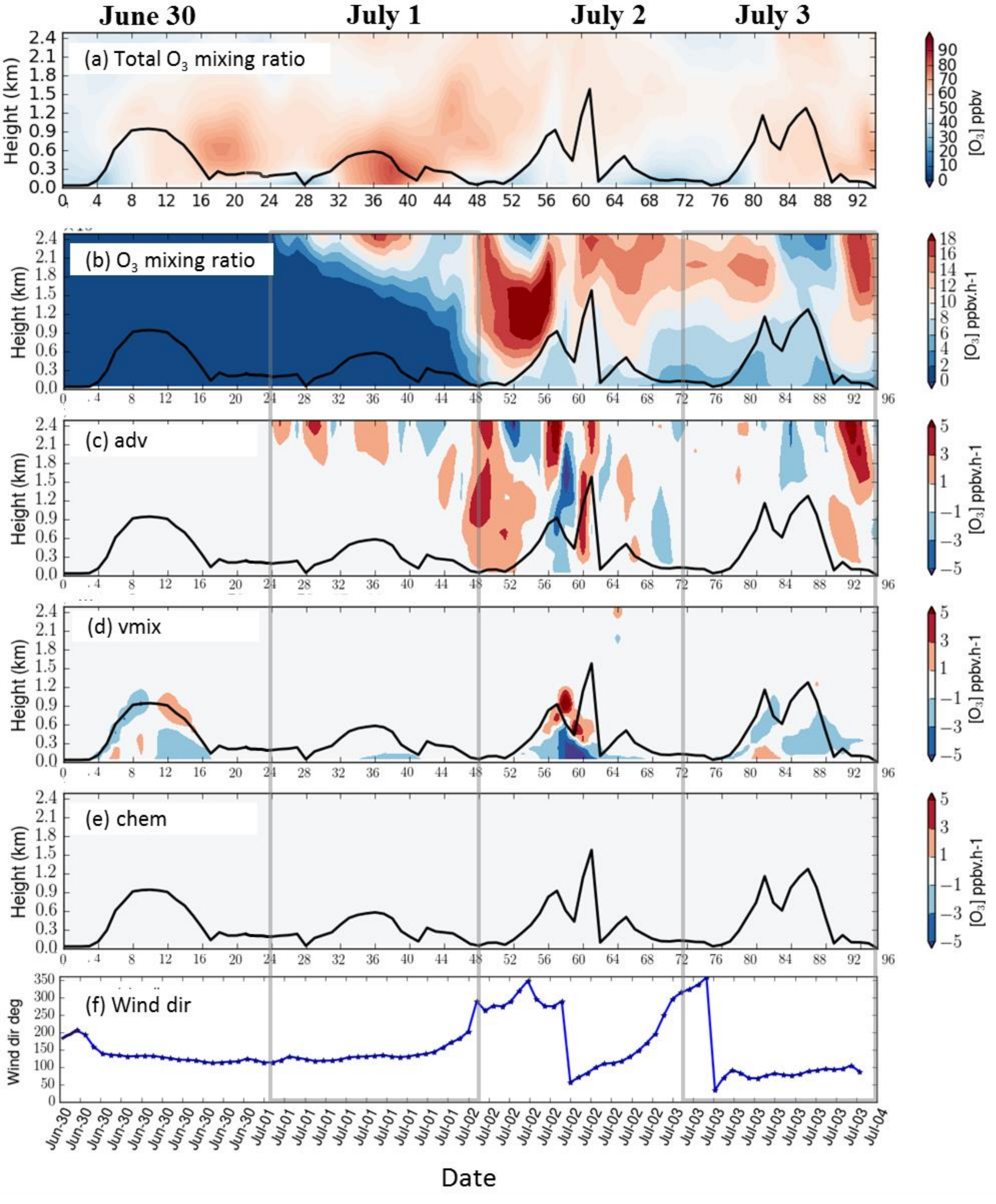

Figure 6.6. Time–height section of O_3 mixing ratios (ppbv) from the Rest-EU region and process tendencies from June 30th to July 3rd 2015 at Weybourne. (a) Total O_3 mixing ratio, (b) contribution of O_3 from the source region in ppbv h^{-1}, (c) contribution from adv, (d) vmix, (e) chem, and (d) wind direction. The black line shows the evolution of the PBL height.

The 30th June started with a change in the wind direction from south-southwest to southeast, see Fig. 6.6d. The rest of the day was mostly under the influence of south south-easterly and south-easterly flow. Positive values at the surface level and the negative values at the top of the planetary boundary layer (PBL) in layers between 300 and 1000 m height (Fig. 6.6c) indicate that vertical mixing process can effectively bring O_3 from layers aloft towards the ground. Thus, boundary layer O_3 at Weybourne started to build-up through downward mixing of O_3 from the Rest-Eu source region in the morning. Advection of O_3 between the surface level and 900 m height from Belgium, NOS and France source regions (Fig. 6.7b, Fig. 6.8b, and Fig. 6.9b, respectively) also made a positive contribution to surface O_3 in the morning. There was also an additional contribution from photochemical production involving NO_x emissions from the NOS source region (Fig. 6.8c) and from the UK (sees Fig. 6.10c). In the afternoon, chemical production involving NO_x emissions from domestic sources was a relevant process within the boundary layer (see Fig. 6.10c), while advection of O_3 at the surface layer from the Netherlands (Fig.6. 11b), the UK and the NOS source regions (see Fig. 6.8b) played also an important role in the build-up of surface O_3 but in a smaller extent. In the evening O_3 was mainly advected to Weybourne at the surface level from Germany (Fig. 6.12b).

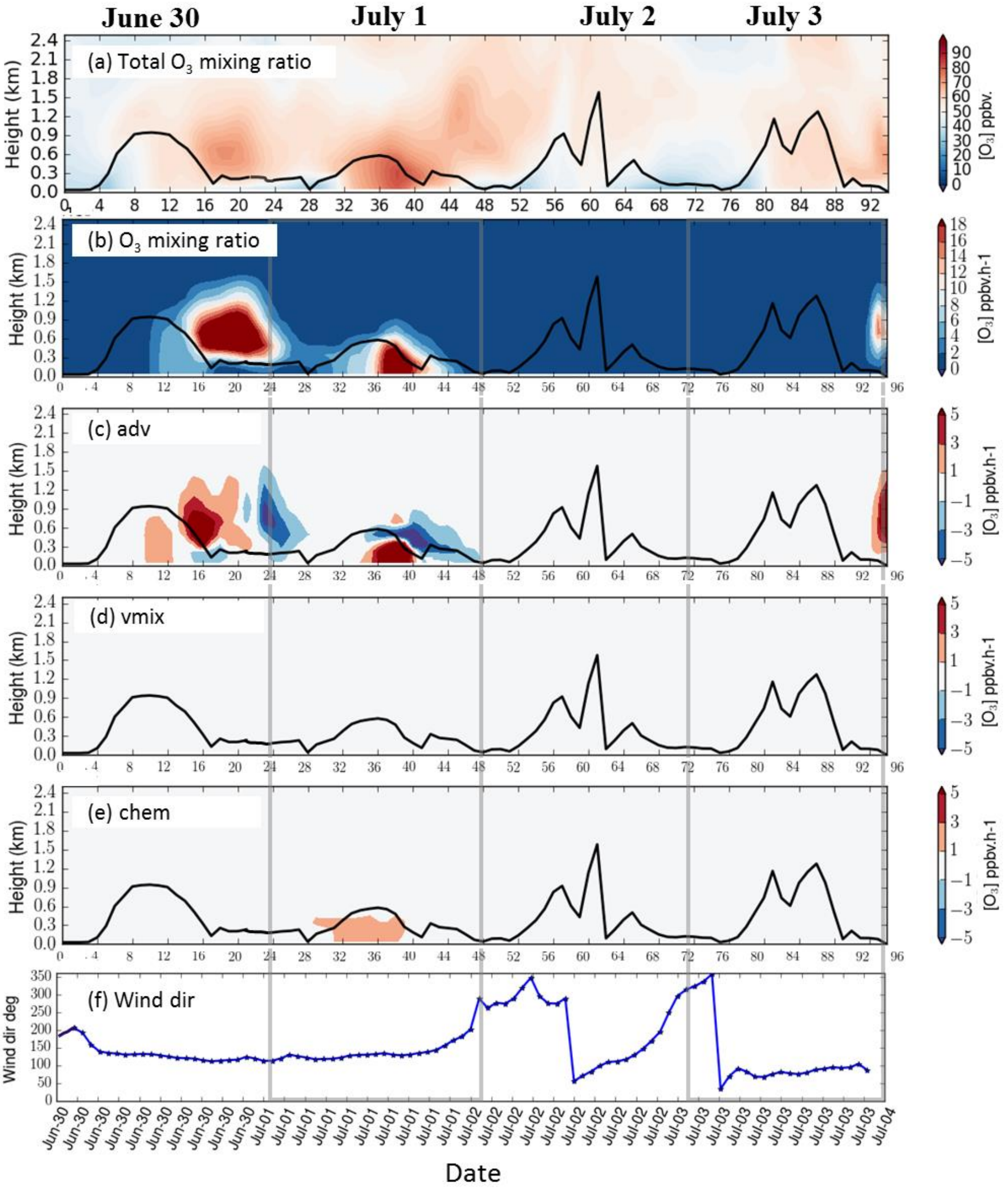

Figure 6.7. Time–height section of O_3 mixing ratios (ppbv) from the Belgium region and process tendencies from June 30th to July 3rd 2015 at Weybourne. (a) Total O_3 mixing ratio, (b) contribution of O_3 from the source region in ppbv h^{-1}, (c) contribution from adv, (d) vmix, (e) chem, and (d) wind direction. The black line shows the evolution of the PBL height.

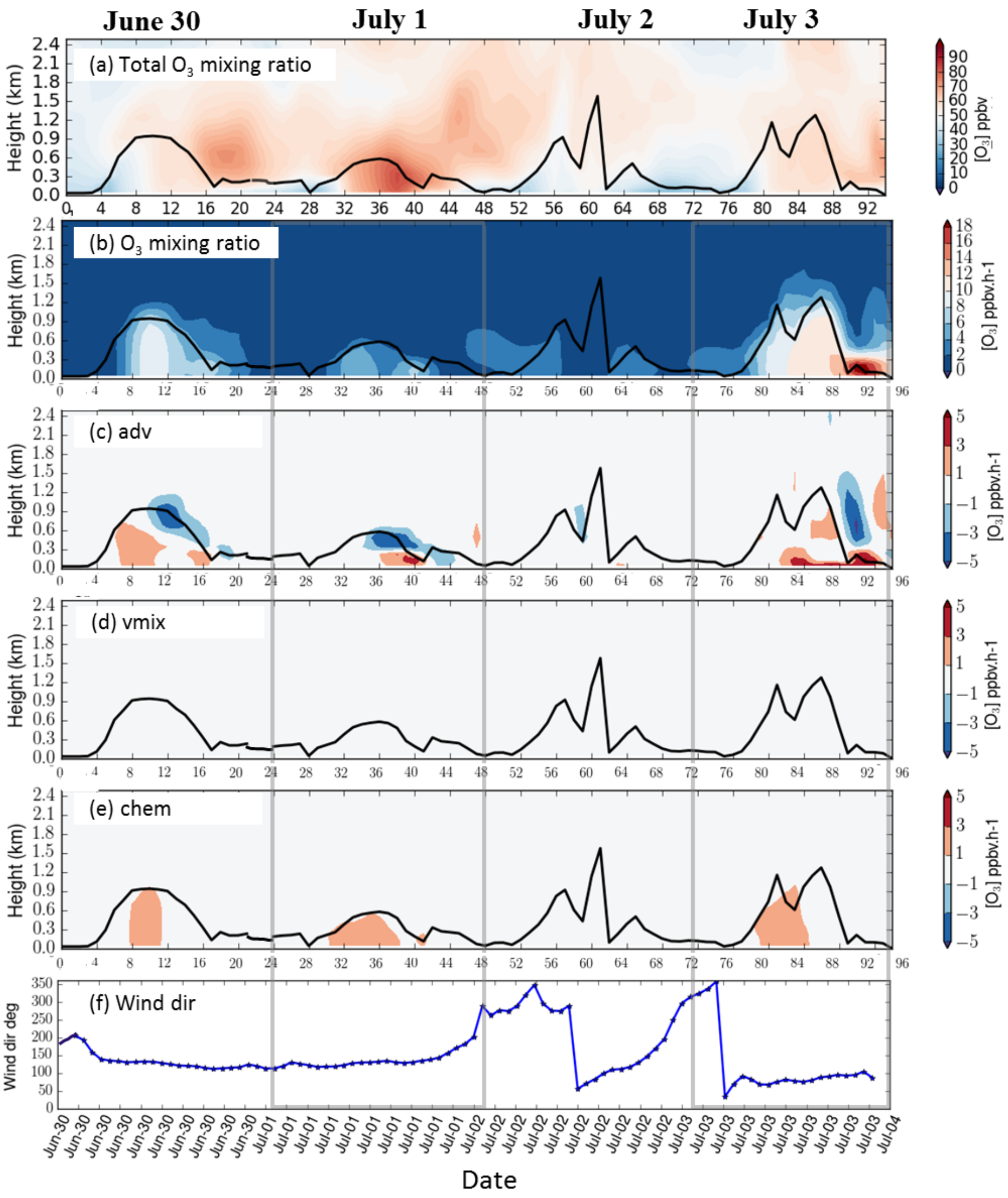

Figure 6.8. Time–height section of O_3 mixing ratios (ppbv) from the North Sea and English channel region and process tendencies from June 30th to July 3rd 2015 at Weybourne. (a) Total O_3 mixing ratio, (b) contribution of O_3 from the source region in ppbv h^{-1}, (c) contribution from adv, (d) vmix, (e) chem, and (d) wind direction. The black line shows the evolution of the PBL height.

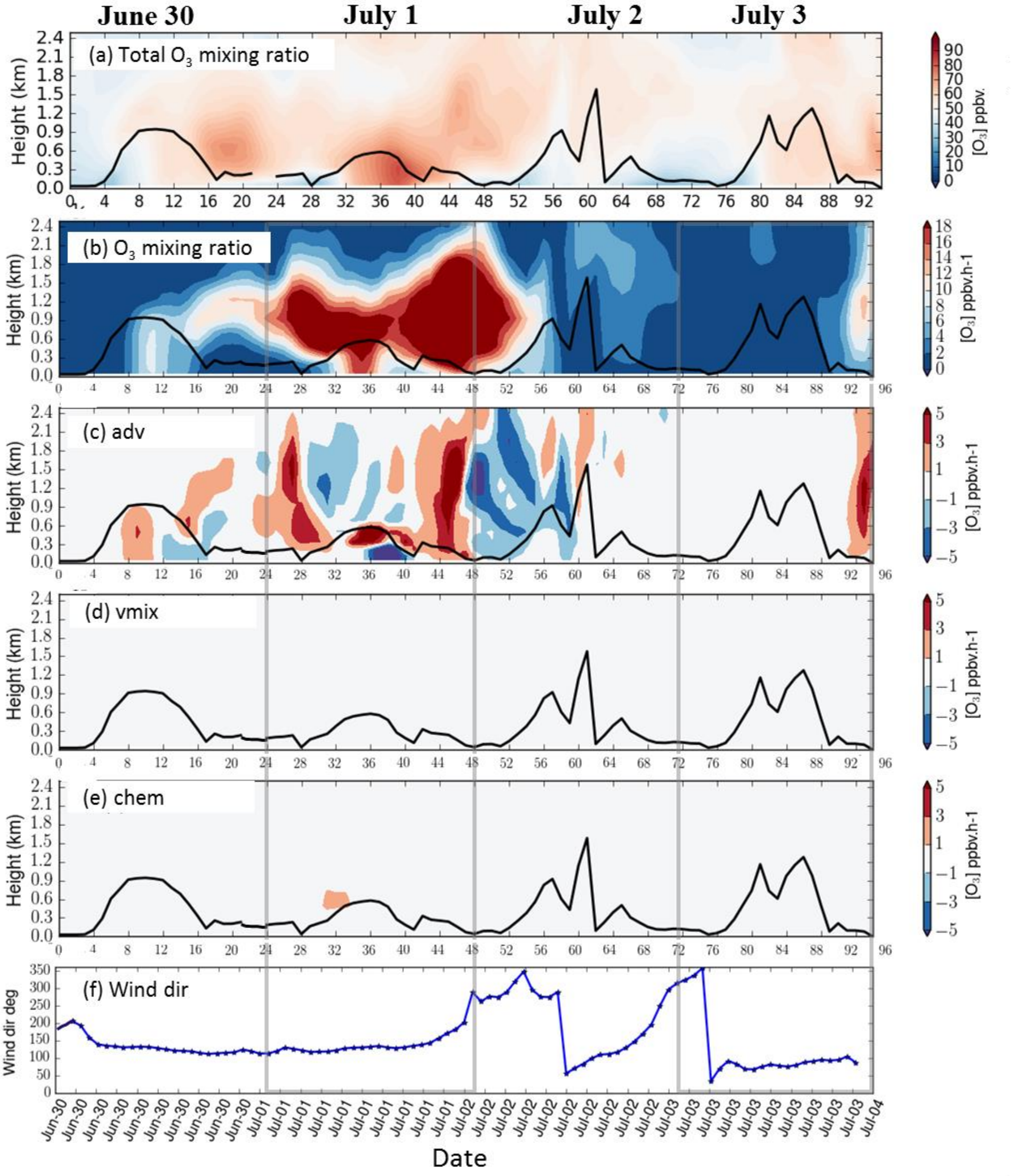

Figure 6.9. Time–height section of O_3 mixing ratios (ppbv) from the France region and process tendencies from June 30th to July 3rd 2015 at Weybourne. (a) Total O_3 mixing ratio, (b) contribution of O_3 from the source region in ppbv h^{-1}, (c) contribution from adv, (d) vmix, (e) chem, and (d) wind direction. The black line shows the evolution of the PBL height.

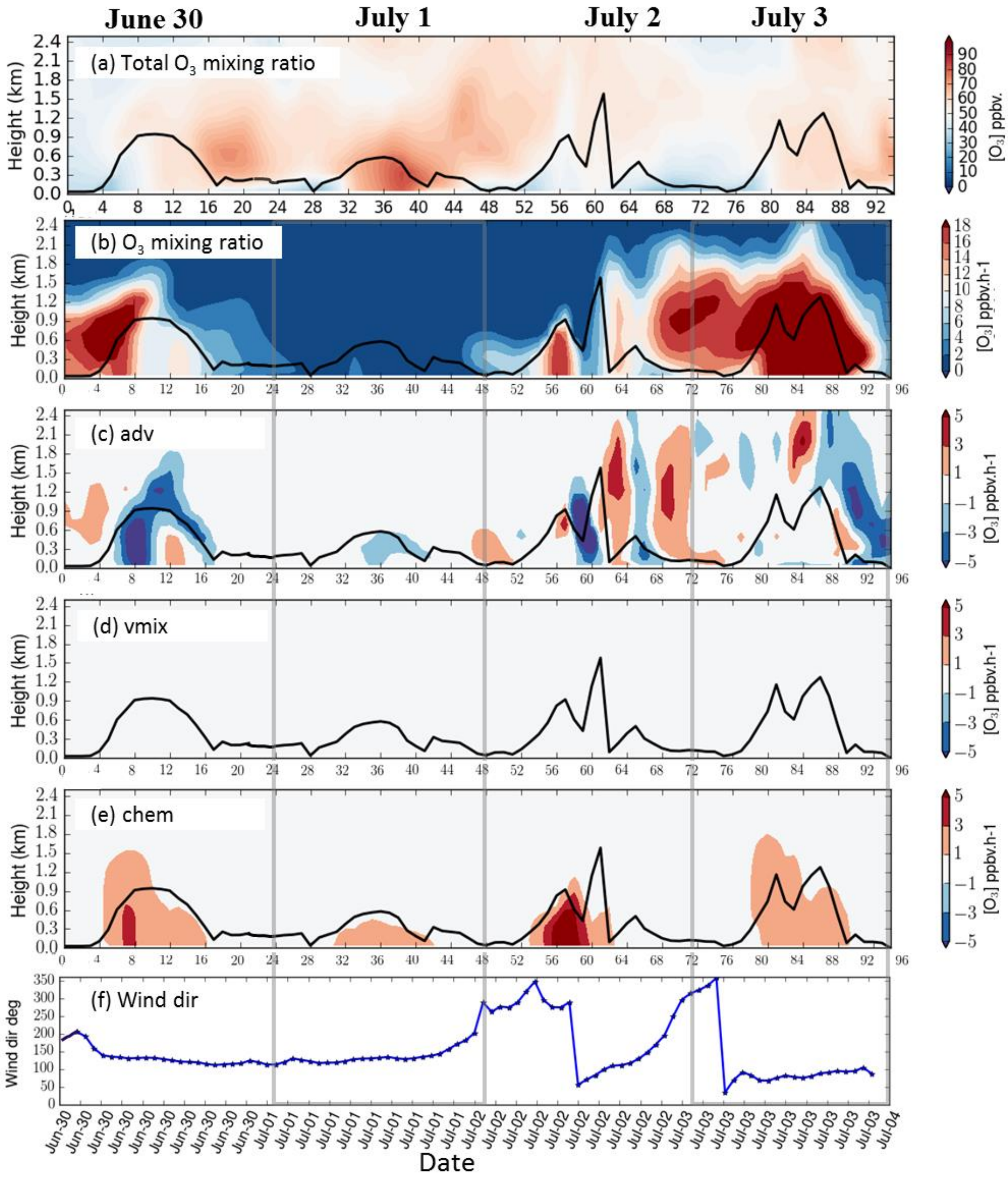

Figure 6.10. Time–height section of O_3 mixing ratios (ppbv) from the UK region and process tendencies from June 30th to July 3rd 2015 at Weybourne. (a) Total O_3 mixing ratio, (b) contribution of O_3 from the source region in ppbv h^{-1}, (c) contribution from adv, (d) vmix, (e) chem, and (d) wind direction. The black line shows the evolution of the PBL height.

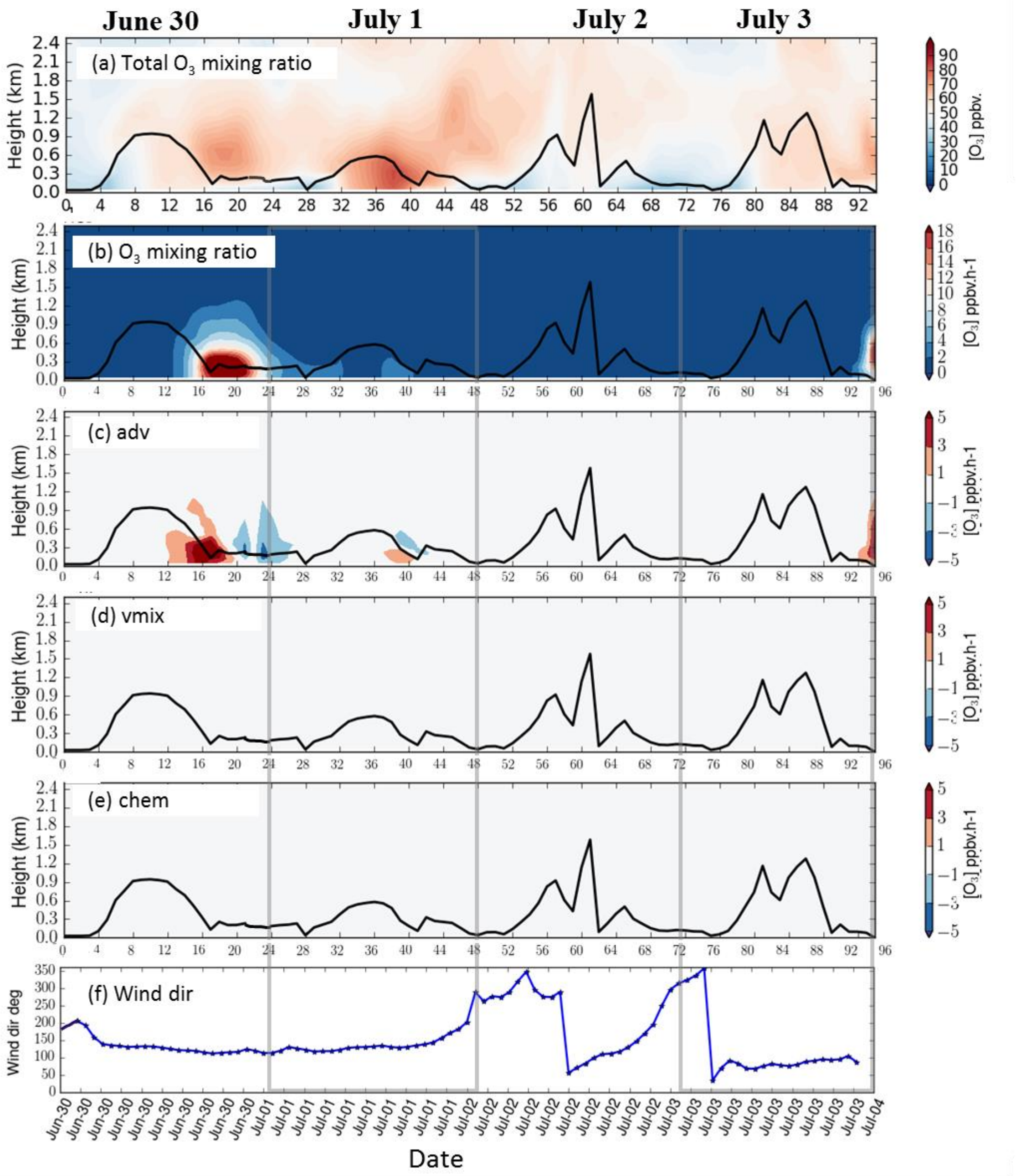

Figure 6.11. Time–height section of O_3 mixing ratios (ppbv) from the Netherlands region and process tendencies from June 30th to July 3rd 2015 at Weybourne. (a) Total O_3 mixing ratio, (b) contribution of O_3 from the source region in ppbv h^{-1}, (c) contribution from adv, (d) vmix, (e) chem, and (d) wind direction. The black line shows the evolution of the PBL height.

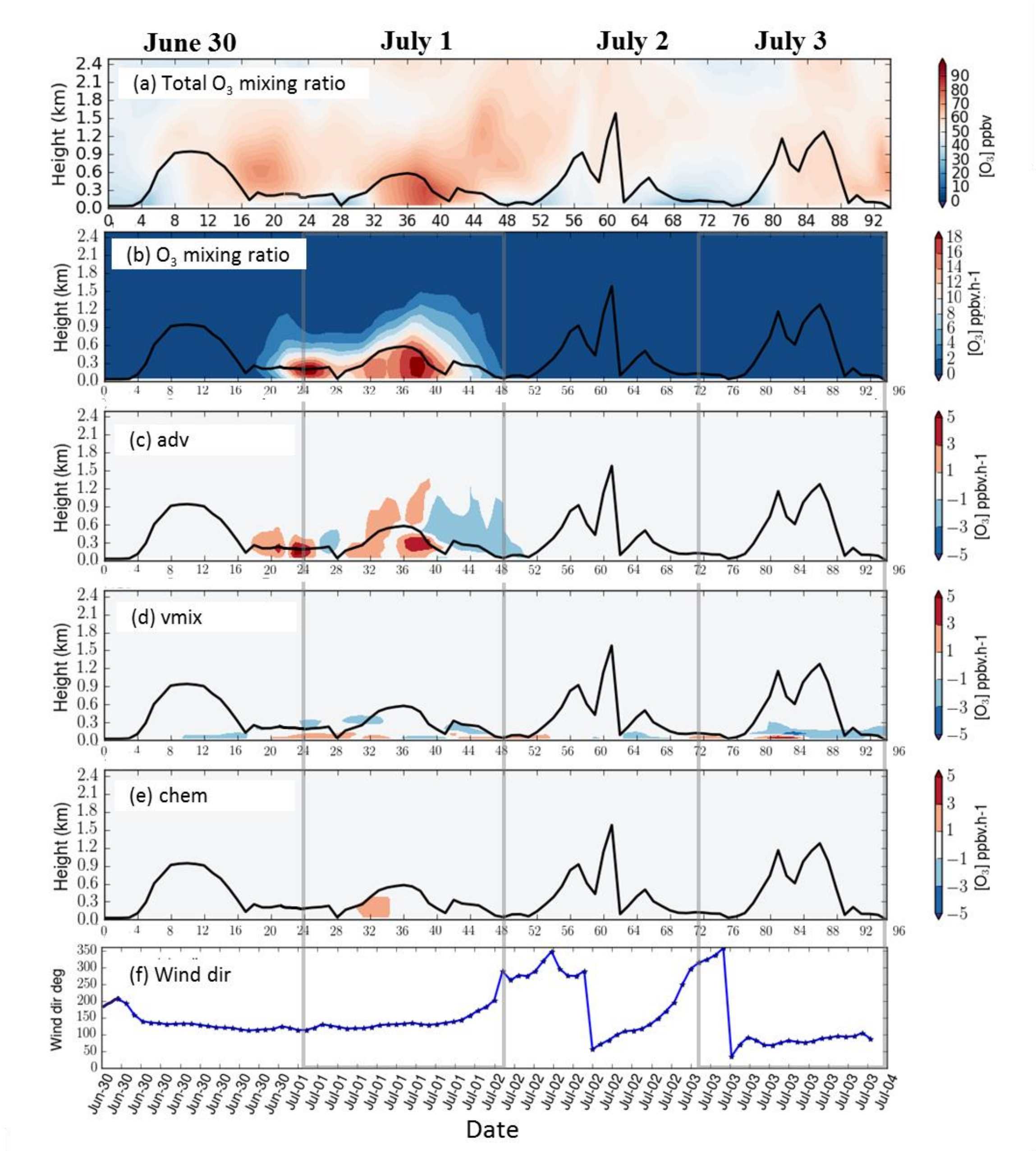

Figure 6.12. Time–height section of O_3 mixing ratios (ppbv) from the Germany region and process tendencies from June 30th to July 3rd 2015 at Weybourne. (a) Total O_3 mixing ratio, (b) contribution of O_3 from the source region in ppbv h^{-1}, (c) contribution from adv, (d) vmix, (e) chem, and (d) wind direction. The black line shows the evolution of the PBL height.

On 1st July, the model predicted winds predominately from the southeast direction (see Fig. 6.12e). In the morning, advection and downward mixing of O_3 from Germany (Fig. 6.12c) had a positive impact in the near-surface O_3 concentrations. Photochemical production involving NO_x emissions from domestic sources (see Fig. 6.10c), NOS (Fig. 6.8c), Germany and Belgium (Fig. 6.7c) also played an important role contributing to the build-up of surface O_3 in the morning hours.

A similar analysis for peroxyacetyl nitrate (PAN) reveals a reservoir of PAN above the PBL available for downward mixing in the early morning suggesting inflow of chemically processed air over WAO. Up to 1.20 ppbv is also seen from around 08:00 UTC until shortly before midday at the surface level (Fig. 613a). Some positive net chemical production of PAN (up to 0.30 ppbv) is also seen at the surface level around midday, Fig. 6.13b, which could have been originated from NOx photochemistry or the thermal decomposition of transported PAN. PAN is a product of NOx photochemistry well-known for its role in the transport of O_3 precursors to less polluted environments (HTAP, 2007). Its stability in cold temperatures allows its long-range transport in the free troposphere. Once it descends to the surface levels, its thermal decomposition can lead to the formation of a peroxy acetyl radical (PA) and NO_2 (Fischer et al., 2014). The PA radical can then undergo reformation PAN when reacting with NO_2, or react with NO to produce NO_2.

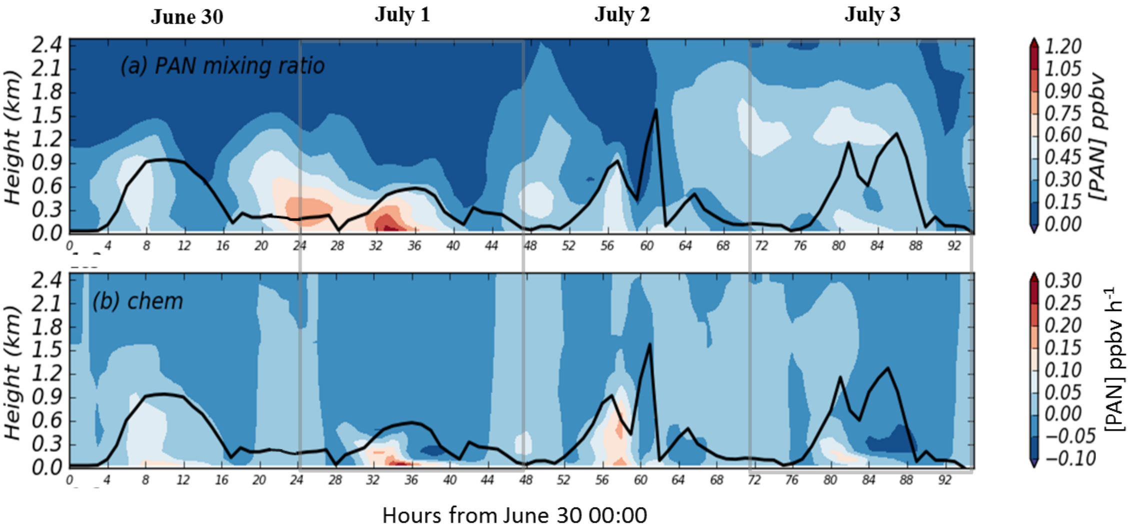

Figure 6.13. Time–height section of PAN mixing ratios (ppbv) (a) and net chemical production (b) from June 30th to July 3rd 2015, at Weybourne. The black line shows the evolution of the PBL height

After midday, O_3 was largely advected from Belgium (Fig. 6.7b) and in a smaller extent from the NOS source region (Fig. 6.8b) and the Netherlands (Fig. 6.11b); while, additional O_3 came from photochemical production involving NO_x emissions from domestic sources and Belgium. Surface O_3 concentrations dropped in the evening, after a change in the wind direction from southeast to the southwest. Fig. 6.9b indicates that advection of O_3 from France at the surface level contributed positively to surface O_3 in the evening, while O_3 from Belgium (Fig. 6.7b) and Luxembourg was advected out of Weybourne. After midnight, surface O_3 from Germany and France was lost by advection, while, O_3 from Rest-Eusource regions was lost by dry deposition and diffusion (see Fig. 6.6c).

Remarkably, photochemical production from domestic NO_x emissions became increasingly dominant on 2nd July (see Fig. 6.10c). On 3rd July, the positive values at ground level and the negative values between 200-600 m height indicate that O_3 from Germany (Fig. 6.12d) and the Rest-Eu source region (Fig. 30c) was mixed down to the surface contributing therefore to surface O_3 concentrations in the morning. Additional surface O_3 came from chemical production at the surface levels involving NO_x emissions from the North Sea and the UK. In the afternoon, O_3 continued to be chemically produced at the surface from domestic NO_x emissions. Surface O_3 was lost in the evening by advection and dry deposition.

6.3.3 Summary

The ozone tagging results showed that, as the wind direction changed from south-southwest to southeast on the 30th June, the impact from domestic NO_x emissions to surface O_3 at Weybourne became less relevant. The onset of the pollution episode, which was dominated by south-easterly and south south-easterly wind conditions, was largely affected by O_3 from the Netherlands, the NOS source region and France. In particular, the Netherlands contributed largely to surface O_3 in the afternoon of 30th June with about 46% of the hourly mean surface O_3 coming from this region at 18:00 UTC. The process analysis further showed that on the 30th June near surface O_3 started to build up in the morning through downward mixing of O_3 from the Rest_Eu source region, advection of O_3 within the PBL from Belgium, NOS and France, and photochemical production involving NOx emissions largely from the UK and the NOS source region in a smaller extent. In the afternoon, advection of O_3 at the surface layer from the Netherlands, the UK and the NOS source regions played an important role in the build-up of surface O_3. While in the evening O_3 was mainly advected within the PBL from Germany.

When the highest O_3 mixing ratio was predicted (1st July), Weybourne was under the influence of south-easterly winds. The site was highly affected by O_3 from Belgium (27% of the maximum total O_3 at Weybourne), Germany (23%), the Netherlands (9%), the NOS (9%), France (7%) and Luxemburg (3%). Domestic NOx emissions was not a key factor during the high O3 episode, as the contribution from domestic O_3 was minimal with 2% (1.6 ppbv) of the maximum total O_3 coming from this within the UK. It was shown that convergence of westerly and south-easterly winds near the surface in the western UK allowed the transport of domestic O_3 westwards and northwards away from Weybourne on the 1st July. Moreover, the contributions from the lateral boundaries decreased during this day.

Process analysis has shown that advection and downward mixing of O_3 from Germany had a positive impact in the surface O_3 concentrations at Weybourne. Photochemical production from domestic sources, the NOS source region, Germany and Belgium also played an important role contributing to surface O_3 concentrations in the morning hours. After midday, O_3 was largely advected from Belgium and in a smaller extent from the NOS and the Netherlands; while additional O_3 came from photochemical production involving NOx emissions from domestic sources and Belgium. The episode was interrupted after surface O_3 from Germany, France and the UK was advected out of Weybourne, and O_3 from Rest-Eu source regions was lost by dry deposition and diffusion.

When the wind direction changed from southeast to south-southwest on 2nd July, the maximum predicted concentration of O_3 over the site was about 58 ppbv, below the EU 8 hour threshold of 60 ppbv. At this point, domestic NO_x emissions were the major source of surface O_3 with 43% (22.6 ppbv) of the maximum surface O_3 at Weybourne coming from the source region. Remarkably, When the site was dominated by easterly winds (3rd July), Weybourne was affected largely by O_3 from the North Sea and the English Channel with 43% (27.5 ppbv) of the maximum total O_3 coming from this source region.

6.4 Conclusions

In this chapter, an ozone-tagging method was used to quantify the contributions from different geographical source regions within Europe to surface O_3 at Weybourne during a high concentrations episode. A process analysis scheme was then applied to distinguish through which mechanism O_3 was transported from each source regions to Weybourne. A strong association between wind direction and the contributions of the source regions were found, the main results can be summarized as follow:

- ✓ As the wind direction changed from south-southwest to southeast, the contribution from domestic NO_x emissions to surface O_3 at Weybourne becomes less relevant. This is because easterly flow can push domestic O_3 westwards away from Weybourne.
- ✓ Convergence of easterly and south-easterly winds can facilitate the accumulation of O_3 during high concentrations episodes.
- ✓ When Weybourne is under south-easterly wind conditions such as those experienced during the first days of the ICOZA campaign, the site can be largely affected by outflow from different geographical source regions within continental Europe, in particular from Belgium, Germany, the Netherlands, the North Sea and English Channel, France and Luxemburg. By contrast, the impact from domestic emissions is found to be minimal under this meteorological condition. Furthermore, the contribution from hemispheric background O_3 are also found to have a reduced impact under south-easterly conditions.

- ✓ O_3 from continental Europe can build up at Weybourne through vertical mixing, in particular in the morning hours, and advection processes. Photochemical processes can also contributed at both surface and high levels, indicating that transport of precursors play an important role in O_3 formation in Weybourne in particular when exceeding the EU guideline maximum 8 h average O_3 concentration of 60 ppbv.
- ✓ Large contributions of O_3 from the North Sea and the English Channel are obtained when Weybourne is dominated by easterly winds, e.g. 3rd July. Moreover, the process analysis of O_3 tags shows that precursors from these sites can be effectively transported to Weybourne where they can eventually form O_3.

Chapter 7

Summary and conclusions

The most relevant findings in this investigation as well as a brief discuss how the work of this investigation could be advanced are summarised on this section.

This thesis has investigated the sources of tropospheric O_3 in the UK using a novel S-R method for O_3 tagging that was implemented into the Regional Weather Forecast and Research Model coupled with chemistry (WRF-Chem). The study aimed to expand the current understanding of the dependence of the UK on domestic and foreign emissions controls to meet the local and European O_3 air quality standards.

Evaluation of the model system has shown that WRF-Chem represents surface meteorological and chemical variable reasonably well, and with biases consistent with previous studies. Nonetheless, wind direction was mostly underrepresented, which could be contributing to the model underrepresenting MDA8 O_3 concentrations above 90 ppbv in the UK.

Overall, the model was able to predict the concentrations of O_3 in the European domain, capturing the spatial distribution in surface O_3 domain-wide. However, the level of hemispheric O_3 entering the western fringe of the UK was underestimated. This has been attributed to lower O_3 concentration in the global model (MOZART-4) used to provide the boundary conditions.

The total number of days with MDA8 O_3 above 50 and 60 ppb was also underestimated, consistent with previous modelling studies using MOZART-4 as a chemical mechanism. Evaluation of the O_3 metric for vegetation exposure

AOT40 further has shown that the model captured most of the spatial distribution of the AOT40 in the UK, with the highest values concentrated on East Anglia. However, the model underestimated the values in the southeast (up to - 3000 μg m^{-3} h). Additional comparison of CRImech vs MOZART-4 has shown that the former gives better predictions of the MDA8 O_3, in particular over the Netherlands, east and the southeast UK indicating that the CRImech mechanism would be better that MOZART for simulating peak O_3 episodes in the southeast UK.

An analysis of the contribution of domestic vs European NO_x emissions and lateral boundary O_3 to the monthly surface O_3 in the UK was also performed. The results have shown that the contribution of different sources to O_3 production varies with season. It was identify that the relative contribution from the lateral boundaries O_3 peaked in May while the contributions from the UK and Europe increased in June and July.

Moreover, it was found that the absolute monthly contribution of the lateral boundary exhibited a marked dependence on latitude. High mixing ratios were predicted in the north and west while low values were obtained in the southeast of the UK. Additionally, it has been demonstrated in Chapter 4 that lateral boundary O_3 is chemically lost by NO_x titration in the Midlands, the southeast and the London area and shipping lanes in the North Sea, and the Atlantic Ocean. An extended area over the Atlantic also exhibited depletion of O_3 that was attributed to the photolysis of O_3 and subsequent production of OH radicals rather than NO_x titration. By contrast, the relative monthly contributions from Europe were shown to decrease towards the northern and inner regions of the UK. Moreover, the contribution from O_3 from European NO_x is predominantly due to transport of O_3 rather than transport of NO_y precursors. Regarding the monthly relative contribution from the UK, it has been shown that it had a marked spatial gradient caused primarily by larger photochemical activity taking place downwind of emission sources in these areas. High mixing ratios were obtained in the southeast and the Midlands and lower values in the north and west.

Following the lateral boundary source region, domestic NOx emissions were the second largest contributor to monthly surface O_3 in the East Midlands, West Midlands, Yorkshire and Humberside, East Anglia, South East England and London. On the other hand, NO_x emissions from Europe were the second most significant source in the north of UK and most of the western areas.

It has been demonstrated that emission controls are required in different source regions for compliance of UK and EU O_3 standards, e.g. MDA8 O_3 of 50 and 60 ppbv. In particular, emissions controls in France would impact the South East, South West and the East Anglia region while domestic emissions controls would be most relevant for the Midlands and the north of the UK.

When looking at lower exposure thresholds such as the AOT40 O_3 metric, it was found that the LB component becomes the dominant source, followed by the domestic component. It was concluded that emission controls would be required over a bigger area (e.g. hemispheric) than those to mitigate the health-related metric MDA8 O_3 above 50 and 60 ppbv. This result improves the current understanding of the effects of long and short-range transport on the spatial distribution of near-surface O_3 in the UK. In particular, it highlights the dependence of the UK on foreign emissions controls to meet the national and EU O_3 standards.

This thesis also assessed the sources and evolution of surface O_3 during a summertime pollution episode and the factors leading to its build-up. Chapter 5 demonstrated a strong association between wind direction and the evolution of surface O_3 concentrations at Weybourne and at three additional sites across the East Anglia region. Accumulation of surface O_3 was associated with south-easterly and south south-easterly winds while westerly winds (south south-westerly) were linked to surface O_3 concentrations below the European 8h threshold of 60 ppbv. Also, consistent with previous studies, the convergence of westerly and easterly winds approaching from the western side of the UK was found to be key facilitating the accumulation of O_3 in the southeast UK.

Process analysis indicated that mixing down of O_3 and precursors from the residual layer and sustained chemical production at the surface level were the dominant processes leading to the increase in the O_3 concentrations during the early morning of the episode. Afternoon advection of O_3 within the PBL, likely from continental Europe, was also found to play a role. In the majority of studies on high-ozone events in the southeast UK, transport of O_3 has been a decisive factor leading to the build-up of PBL O_3 during peak days. This study, however, found that photochemistry was the primary process increasing the O_3 concentrations during the pollution episode. This diversion from previous investigations is attributed to the specific features of the pollution episodes as well as to the differences in the methodology used leading to divergent estimates of the O_3 shares attributable to transport and in-situ production. Passive tracers released within the model simulation further showed that under south-easterly winds, the particles released from individual sources in France, Belgium, Luxemburg, Netherlands and Germany could reach WAO above the PBL at altitudes between 300 and 1000 m and at the surface level. Some of these tracers were lifted to the top of the boundary layer and transported horizontally in stable layers above the MBL across the North Sea by coastal outflow before reaching Weybourne. Similarly, tracers released in West Germany have shown that transport of pollutants towards the UK can also occur near the surface level. These tracers were transported horizontally to Weybourne confined near the surface by the stable MBL.

Application of the ozone-tagging mechanism to the pollution episode at Weybourne has further shown that easterly winds can push domestic O_3 westwards away from Weybourne, causing the contribution from domestic NOx emissions to surface O_3 at Weybourne to become less relevant than the European one. When Weybourne is under south-easterly wind conditions, such as those experienced during the first days of the ICOZA campaign, the site can be largely affected by the outflow from different geographical source regions within continental Europe, in particular from Belgium, Germany, the Netherlands, the North Sea and the English Channel, France and Luxemburg. It was also demonstrated that O_3 from continental Europe can build up at Weybourne through vertical mixing, in particular in the morning hours, and by advection processes. Large contributions of O_3 from the North Sea and the English Channel were obtained when easterly winds dominated Weybourne. Moreover, it has been demonstrated that precursors from these sites can be effectively transported to Weybourne, where they can eventually form O_3.

Detailed quantification of O_3 transport from continental Europe remains a challenging task that requires further model development. In the future, this can be achieved by adding additional source regions to disentangle emissions from source regions and shipping routes, e.g., the Mediterranean, the Irish Sea and the Atlantic Ocean, the Iberia Peninsula and the Mediterranean region. Moreover, more extended simulation periods would allow to identify possible seasonal cycles in the contributions to surface O_3. Longer simulation periods would also allow assessing the representativeness of the reported results on longer time scales, in particular, the likely changes in the meteorological conditions that can alter transport patterns. Such investigations are nonetheless computationally demanding, as long integration times are required.

An important application of air quality models is to investigate the impact of future emission scenarios to assist with the developing of effective O_3 control strategies. Sensitivity simulations may then be carried out by combining the use of a tagging scheme with emissions perturbations, as the synergy of the two methods can provide additional valuable insights into the effects of the mitigation options on the contributions to O_3.

A NOx emission tagging approach was here used to quantify the impact of domestic vs foreign NOx precursors on the build-up of PLB O_3 during a peak episode. Nonetheless, it is known that summer O_3 maxima in most regions are due to photochemistry involving anthropogenic NOx and NMVOCs, particularly biogenic species. Therefore, future calculations could include the tagging of VOCs species to gain a robust understanding of the relationship between precursor emissions for the different sources and O_3 concentrations in the UK. However, the implementation of a VOC's tagging approach into the model would require substantial computational resources. The simulation of meteorology could be also improved, in particular during the O_3 episode, by testing the sensitivity of O_3 to the available boundary layer schemes.

References

Angevine, W. M., Buhr, M. P., Holloway, J. S., Trainer, M., Parrish, D. D., MacPherson, J. I., Kok, G. L., Schillawski, R. D., and Bowlby, D. H. (1996). Local meteorological features affecting chemical measurements at a North Atlantic coastal site. *Jurnal Geophysical Research*, 101(D22), 28935– 28946. Retrieved from doi:10.1029/95JD02890.

Angevine, W. M., Senff, C. J., White, A. B., Williams, E. J., Koermer, J. P., Miller, S. T. K., … Downs, T. (2004). Coastal Boundary Layer Influence on Pollutant Transport in New England. *Journal of Applied Meteorology*, 43, 1425–1437. Retrieved from https://doi.org/10.1175/JAM2148.1

AQEG. (2009). *Ozone in the united kingdom. Food and Chemical Toxicology* (Vol. 33). Retrieved from 10.1016/0278-6915(95)80257-6

Archer-Nicholls, S., Lowe, D., Utembe, S., Allan, J., Zaveri, R. a., Fast, J. D., … McFiggans, G. (2014). Gaseous chemistry and aerosol mechanism developments for version 3.5.1 of the online regional model, WRF-Chem. *Geoscientific Model Development*, 7(6), 2557–2579. Retrieved from https://doi.org/10.5194/gmd-7-2557-2014

Atkinson, R. (2000). Atmospheric chemistry of VOCs and NOx. *Atmospheric Environment*, 34(12–14), 2063–2101. Retrieved from https://doi.org/10.1016/S1352-2310(99)00460-4

Aulinger, A., Matthias, V., Zeretzke, M., Bieser, J., Quante, M., & Backes, A. (2016). The impact of shipping emissions on air pollution in the greater North Sea region - Part 1: Current emissions and concentrations. *Atmospheric Chemistry and Physics*, 16(2), 739–758. Retrieved from https://doi.org/10.5194/acp-16-739-2016

Auvray, M., & Bey, I. (2005). Long-range transport to Europe: Seasonal variations and implications for the European ozone budget. *Journal of Geophysical Research D: Atmospheres*, 110(11), 1–22. Retrieved from https://doi.org/10.1029/2004JD005503

Badia, A., & Jorba, O. Gas-phase evaluation of the online NMMB/BSC-CTM model over Europe for 2010 in the framework of the AQMEII-Phase2 project. *Atmospheric Environment,*(0), 2014. ISSN 1352-2310. doi: http://dx.doi.org/10.1016/j.atmosenv.2014.05.055

Baklanov, A., Schlnzen, K., Suppan, P., Baldasano, J., Brunner, D., Aksoyoglu, S., …

Zhang, Y. (2014). Online coupled regional meteorology chemistry models in Europe: Current status and prospects. *Atmospheric Chemistry and Physics*, 14(1), 317–398. Retrieved from https://doi.org/10.5194/acp-14-317-2014

Beljaars, A. C. M. (1995). The parametrization of surface fluxes in large- scale models under free convection. *Q. J. Royal Meteorological Society*, 121, 255–270. Retrieved from doi:10.1002/qj.49712152203

Bieser, J., Aulinger, a., Matthias, V., Quante, M., & Builtjes, P. (2010). SMOKE for Europe – adaptation, modification and evaluation of a comprehensive emission model for Europe. *Geoscientific Model Development Discussions*, 3(3), 949–1007. Retrieved from https://doi.org/10.5194/gmdd-3-949-2010

Bohnenstengel, S. I., Belcher, S. E., Aiken, A., Allan, J. D., Allen, G., Bacak, A., … Zotter, P. (2015). Meteorology, air quality, and health in London: The ClearfLo project. *Bulletin of the American Meteorological Society*, 96(5), 779–804. Retrieved from https://doi.org/10.1175/BAMS-D-12-00245.1

Brasseur, G., Orlando, J. J., & Tyndall, G. S. (1999). Atmospheric chemistry and global change. New York: Oxford University Press

Brown, S. S. & Stutz, J. Nighttime radical observations and chemistry, Chem. Soc. Rev., 41, 6405–6447, 2012.

Brunner, D., Savage, N., Jorba, O., Eder, B., Giordano, L., Badia, A., … Galmarini, S. (2015). Comparative analysis of meteorological performance of coupled chemistry-meteorology models in the context of AQMEII phase 2. *Atmospheric Environment*, 115, 470–498. Retrieved from https://doi.org/10.1016/j.atmosenv.2014.12.032

Butler, T., Lupascu, A., Coates, J., & Zhu, S. (2018). TOAST 1.0: Tropospheric ozone attribution of sources with tagging for CESM 1.2.2. *Geoscientific Model Development*, 11(7), 2825–2840. Retrieved from https://doi.org/10.5194/gmd-11-2825-2018

CAMS. (2016). Interim Annual Assessment Report for 2015 - European air quality in 2015 Interim Annual Assessment Report, (September). Retrieved from https://doi.org/10.13140/RG.2.2.15127.78249

Carslaw, D. C., & Ropkins, K. (2012). Openair - An r package for air quality data analysis. *Environmental Modelling and Software*, 27–28, 52–61. Retrieved from https://doi.org/10.1016/j.envsoft.2011.09.008

Chen, F. and Dudhia, J. (2001). Coupling and advanced land surface- hydrology model with the Penn State-NCAR MM5 modeling system, Part I: Model implementation and sensitivity. *Monthly Weather Review*, 129, 569–585

Chen, Fei. (2007). The Noah Land Surface Model in WRF. The Institute for Integrative and Multidisciplinary Earth Studies (LSM) NCAR. LSM group meeting. Retrieved from https://www.atmos.illinois.edu/~snesbitt /ATMS597R/notes/noahLSM-tutorial.pdf

Chou, M.-D. and Suarez, M. J. (1994). An efficient thermal infrared radia- tion parametrization for use in general circulation models. *NASA Tech. Memo*., 104606, Greenbelt, MD, USA, 85 pp

Coyle, M., Smith, R. I., Stedman, J. R., Weston, K. J., & Fowler, D. (2002). Quantifying the spatial distribution of surface ozone concentration in the UK. *Atmospheric Environment*, 36(6), 1013–1024. Retrieved from https://doi.org/10.1016/S1352-2310(01)00303-X

Crilley, L.; Kramer, L.; Reed, C.; Lee, J.D.; Massey-Woodward, R.; Whalley, L.; Forster, G.; Bandy, B. (2018): ICOZA: Atmospheric species measurements of OH, HONO, HO2, NO, NO2, NOy, O3, SO2 and CO from Weybourne Atmosphere Observatory July 2015. Centre for Environmental Data Analysis. Retrieved from http://catalogue.ceda.ac.uk/uuid/ddf1032d626b45f78ce1c5e94f289a66

Dacre, H. F., Gray, S. L., & Belcher, S. E. (2007). A case study of boundary layer ventilation by convection and coastal processes, 112, 1–18. Retrieved from https://doi.org/10.1029/2006JD007984

DEFRA. (2015), Air Modelling for DEFRA. Retrieved from https://uk-air.defra.gov.uk/research/air-quality-modelling?view=modelling

DEFRA. (2017). Air Pollution in the UK 2016. *Annual Report 2016 Issue 2*, , 131. Retrieved from https://uk-air.defra.gov.uk/assets/documents/annualreport/ Derwent, D., Fraser, A., Abbott, J., Jenkin, M., Willis, P., & Murrells, T. (2010). *Evaluating the Performance of Air Quality Models*. *Pollution Research*.

Derwent, R. G., Stevenson, D. S., Collins, W. J., & Johnson, C. E. (2004). Intercontinental transport and the origins of the ozone observed at surface sites in Europe. *Atmospheric Environment*, 38(13), 1891–1901. Retrieved from https://doi.org/10.1016/j.atmosenv.2004.01.008

Derwent, R. G., Stevenson, D. S., Doherty, R. M., Collins, W. J., & Sanderson, M. G. (2008). How is surface ozone in Europe linked to Asian and North American NOxemissions? *Atmospheric Environment*, 42(32), 7412–7422. Retrieved from https://doi.org/10.1016/j.atmosenv.2008.06.037

Derwent, R, Witham, C., Utembe, S., Jenkin, M., & Passant, N. (2010). Ozone in Central England: the impact of 20 years of precursor emission controls in Europe.

Environmental Science and Policy, 13(3), 195–204. Retrieved from https://doi.org/10.1016/j.envsci.2010.02.001

Derwent, Richard, Beevers, S., Chemel, C., Cooke, S., Francis, X., Fraser, A., … Vieno, M. (2014). Analysis of UK and European NOx and VOC emission scenarios in the Defra model intercomparison exercise. *Atmospheric Environment*, 94(x), 249–257. Retrieved from https://doi.org/10.1016/j.atmosenv.2014.05.036

Derwent, Richard G., Utembe, S. R., Jenkin, M. E., & Shallcross, D. E. (2015). Tropospheric ozone production regions and the intercontinental origins of surface ozone over Europe. *Atmospheric Environment*, 112, 216–224. Retrieved from https://doi.org/10.1016/j.atmosenv.2015.04.049

Derwent, Richard G, Manning, A. J., Simmonds, P. G., Spain, T. G., & O'Doherty, S. (2013). Analysis and interpretation of 25 years of ozone observations at the Mace Head Atmospheric Research Station on the Atlantic Ocean coast of Ireland from 1987 to 2012. *Atmospheric Environment*, 80, 361–368. Retrieved from https://doi.org/10.1016/j.atmosenv.2013.08.003

Directive, E. U. A. Q., Mechanism, M. C., Climate, P., Model, M., & Data, K.-A. I. R. M. (2008). Defra ' s Modelled Air Quality Datasets, 2020(2).

EEA. (2015). *Air quality in Europe-2015 report*. Retrieved from https://doi.org/10.2800/62459

EEA. (2017). *Air quality in Europe — 2016 report*. Retrieved from http://www.eea.europa.eu/publications/air-quality-in-europe-2016/at_download/file%0Apapers3://publication/doi/10.2800/80982

Ehlers, C., Klemp, D., Rohrer, F., Mihelcic, D., Wegener, R., Kiendler-Scharr, A., and Wahner, A. (2016). Twenty years of ambient observations of nitrogen oxides and specified hydrocarbons in air masses dominated by traffic emissions in Germany. *Faraday Discuss*. Retrieved from doi:10.1039/C5FD00180C

Emmons, L. K., Hess, P. G., Lamarque, J. F., & Pfister, G. G. (2012). Tagged ozone mechanism for MOZART-4, CAM-chem and other chemical transport models. *Geoscientific Model Development*, 5(6), 1531–1542. Retrieved from https://doi.org/10.5194/gmd-5-1531-2012

Emmons, L. K., Walters, S., Hess, P. G., Lamarque, J. F., Pfister, G. G., Fillmore, D., … Kloster, S. (2010). Description and evaluation of the Model for Ozone and Related chemical Tracers, version 4 (MOZART-4). *Geoscientific Model Development*, 3(1), 43–67. Retrieved from https://doi.org/10.5194/gmd-3-43-2010

Entwistle, J., Weston, K., Singles, R., & Burgess, R. (1997). The magnitude and extent of elevated ozone concentrations around the coasts of the British Isles. *Atmospheric Environment*, 31(13), 1925–1932. Retrieved from https://doi.org/10.1016/S1352-2310(97)00022-8

Fares, S., Goldstein, A., & Loreto, F. (2010). Determinants of Ozone Fluxes and Metrics for Ozone Risk Assessment in Plants. Journal of Experimental Botany 61 (3): 629–33. doi:10.1093/jxb/erp336

Fischer, E. V, Jacob, D. J., Yantosca, R. M., Sulprizio, M. P., Millet, D. B., Mao, J., … Pandey Deolal, S. (2014). Atmospheric peroxyacetyl nitrate (PAN): A global budget and source attribution. *Atmospheric Chemistry and Physics*, 14(5), 2679–2698. Retrieved from https://doi.org/10.5194/acp-14-2679-2014

Fleming, Z. L., Monks, P. S., & Manning, A. J. (2012). Review: Untangling the influence of air-mass history in interpreting observed atmospheric composition. *Atmospheric Research*, 104–105, 1–39. Retrieved from https://doi.org/10.1016/j.atmosres.2011.09.009

Forkel, R., Balzarini, A., Baró, R., Bianconi, R., Curci, G., Jiménez-Guerrero, P., … Žabkar, R. (2015). Analysis of the WRF-Chem contributions to AQMEII phase2 with respect to aerosol radiative feedbacks on meteorology and pollutant distributions. *Atmospheric Environment*, 115, 630–645. Retrieved from https://doi.org/10.1016/j.atmosenv.2014.10.056

Francis, X. V., Chemel, C., Sokhi, R. S., Norton, E. G., Ricketts, H. M. A., & Fisher, B. E. A. (2011). Mechanisms responsible for the build-up of ozone over South East England during the August 2003 heatwave. *Atmospheric Environment*, 45(38), 6880–6890. Retrieved from https://doi.org/10.1016/j.atmosenv.2011.04.035

Fuhrer, J. (2009). Ozone risk for crops and pastures in present and future climates. *Naturwissenschaften*, 96(2), 173–194. Retrieved from https://doi.org/10.1007/s00114-008-0468-7

Gao, J., Zhu, B., Xiao, H., Kang, H., Hou, X., & Shao, P. (2016). A case study of surface ozone source apportionment during a high concentration episode, under frequent shifting wind conditions over the Yangtze River Delta, China. *Science of the Total Environment*, 544, 853–863. Retrieved from https://doi.org/10.1016/j.scitotenv.2015.12.039

Garcia, M., Fita, L., & Yag, C. (2013). Seasonal dependence of WRF model biases and sensitivity to PBL schemes over Europe. *Q. J. R. Meteorological Sociaty*, 139(January), 501–514. Retrieved from https://doi.org/10.1002/qj.1976

Grell, G. A. and Dévényi, D. (2002): A generalized approach to parameterizing convection combining ensemble and data assimilation techniques. *Geophysical Research Letters*, 29, 38-1–38-4. Retrieved from doi:10.1029/2002GL015311

Grell, G. a., Peckham, S. E., Schmitz, R., McKeen, S. a., Frost, G., Skamarock, W. C., & Eder, B. (2005). Fully coupled 'online' chemistry within the WRF model. *Atmospheric Environment*, 39(37), 6957–6975. Retrieved from https://doi.org/10.1016/j.atmosenv.2005.04.027

Grewe, V. (2004). Technical Note: A diagnostic for ozone contributions of various NO_x emissions in multi-decadal chemistry-climate model simulations. *Atmospheric Chemistry and Physics Discussions*, 4(1), 327–342. Retrieved from https://doi.org/10.5194/acpd-4-327-2004

Grünhage, L., Pleijel, H., Mills, G., Bender, J., Danielsson, H., Lehmann, Y., Castell, J. F., and Bethenod, O.: Updated stomatal flux and flux-effect models for wheat for quantifying effects of ozone on grain yield, grain mass and protein yield, *Environmental Pollution*, 165, 147–157. Retrieved from https://doi:10.1016/j.envpol.2012.02.026, 2012

Guenther, A. B., Jiang, X., Heald, C. L., Sakulyanontvittaya, T., Duhl, T., Emmons, L. K., & Wang, X. (2012). The model of emissions of gases and aerosols from nature version 2.1 (MEGAN2.1): An extended and updated framework for modeling biogenic emissions. *Geoscientific Model Development*, 5(6), 1471–1492. Retrieved from https://doi.org/10.5194/gmd-5-1471-2012

Heath, R. L., Lefohn, A. S., & Musselman, R. C. (2009). Temporal Processes That Contribute to Nonlinearity in Vegetation Responses to Ozone Exposure and Dose. Atmospheric Environment 43 (18). doi:10.1016/j.atmosenv.2009.03.011

Hodnebrog, Øivind, Frode Stordal, and Terje K Berntsen. 2011. "Does the Resolution of Megacity Emissions Impact Large Scale Ozone ?" *Atmospheric Environmen,* 45 (38). Retrieved from doi:10.1016/j.atmosenv.2011.01.012

Hong, S.-Y., Noh, Y., and Dudhia, J. (2006). A New Vertical Diffusion Package with an Explicit Treatment of Entrainment Processes. *Monthly Weather Review*, 134, 2318–2341. Retrieved from doi:10.1175/MWR3199.1, 2006

HTAP. (2007). *Hemispheric Transport of Air Pollution 2007*. Retrieved from 10.18356/2c908168-en

Huszar, P., Cariolle, D., Paoli, R., Halenka, T., Belda, M., Schlager, H., Miksovsky, J.,& Pisoft, P. (2010). Modeling the Regional Impact of Emissions on NOx and Ozone Levels over the Eastern Atlantic and Western Europe Using Ship Plume Parameterization. Atmospheric Chemistry and Physics 10 (14): 6645–60. Retrieved from doi:10.5194/acp-10-6645-2010

Iacono, M. J., Delamere, J. S., Mlawer, E. J., Shephard, M. W., Clough, S. A., Collins, W. D. (2008). Radiative forcing by long- lived greenhouse gases: Calculations with the AER radiative transfer models, J. *Geophys. Res.-Atmos.,* 113. Retrieved from doi:10.1029/2008JD009944

Im, U., Bianconi, R., Solazzo, E., Kioutsioukis, I., Badia, A., Balzarini, A., ... Yahya, K. (2014). Evaluation of operational on-line-coupled regional air quality models over Europe and North America in the context of AQMEII phase 2. Part I: Ozone. *Atmospheric Environment*, 115, 404–420. Retrieved from https://doi.org/10.1016/j.atmosenv.2014.09.042

Jenkin, M. E. (2008). Trends in ozone concentration distributions in the UK since 1990: Local, regional and global influences. *Atmospheric Environment*, 42(21), 5434–5445. Retrieved from https://doi.org/10.1016/j.atmosenv.2008.02.036

Jenkin, M. E., Davies, T. J., & Stedman, J. R. (2002). The origin and day of week dependence of photochemical ozone episodes in the UK. *Atmospheric Environment*, 36(6), 999–1012. Retrieved from https://doi.org/10.1016/S1352-2310(01)00360-0

Johnson, C., Collins, W., Stevenson, D., and Derwent, R. (1999). Relative roles of climate and emissions changes on future tropospheric oxidant concentrations. *J. Geophys. Res.-Atmos*, 104, 18631– 18645

Jones A., Thomson D., Hort M., Devenish B. (2007). The U.K. Met Office's Next-Generation Atmospheric Dispersion Model, NAME III. In: Borrego C., Norman AL. (eds) Air Pollution Modeling and Its Application XVII. Springer, Boston, MA

Karamchandani, P., Long, Y., Pirovano, G., Balzarini, A., & Yarwood, G. (2017). Source-sector contributions to European ozone and fine PM in 2010 using AQMEII modeling data. *Atmospheric Chemistry and Physics*, 17(9), 5643–5664. Retrieved from https://doi.org/10.5194/acp-17-5643-2017

Kasibhatla, P., Levy II, H., Moxim, W. J., Pandis, S. N., Corbett, J. J., Peterson, M. C., Honrath, R. E., Frost, G. J., Knapp, K., Par- rish, D. D., and Ryerson, T. B. (2000). Do Emissions from Ships have a Significant Impact on Concentrations of Nitrogen Oxides in the Marine Boundary Layer?. Geophysical Research Letters, 27(15), 2229–2232, 2000

Kley, D., Geiss, H., & Mohnen, V. A. (1994). Tropospheric ozone at elevated sites and precursor emissions in the United States and Europe. *Atmospheric Environment*, 28(1), 149–158. Retrieved from https://doi.org/10.1016/1352-2310(94)90030-2

Knote, C., Tuccella, P., Curci, G., Emmons, L., Orlando, J. J., Madronich, S., ... Zhang, Y.

(2014). Influence of the choice of gas-phase mechanism on predictions of key gaseous pollutants during the AQMEII phase-2 intercomparison. *Atmospheric Environment*, 115, 553–568. Retrieved from https://doi.org/10.1016/j.atmosenv.2014.11.066

Kong, X., Forkel, R., Sokhi, R. S., Suppan, P., Baklanov, A., Gauss, M., … Galmarini, S. (2014). Analysis of meteorology–chemistry interactions during air pollution episodes using online coupled models within AQMEII phase-2. *Atmospheric Environment*, 115. Retrieved from https://doi.org/10.1016/j.atmosenv.2014.09.020

Kuenen, J. J. P., Visschedijk, a. J. H., Jozwicka, M., & Denier van der Gon, H. a. C. (2014). TNO-MACC_II emission inventory: a multi-year (2003–2009) consistent high-resolution European emission inventory for air quality modelling. *Atmospheric Chemistry and Physics*, 14(2013), 10963–10976. Retrieved from https://doi.org/10.5194/acpd-14-5837-2014

Kuik, F., Lauer, A., Churkina, G., Denier van der Gon, H. A. C., Fenner, D., Mar, K. A., & Butler, T. M. (2016). Air quality modelling in the Berlin-Brandenburg region using WRF-Chem v3.7.1: sensitivity to resolution of model grid and input data. *Geoscientific Model Development Discussions*, 0(2), 1–46. Retrieved from https://doi.org/10.5194/gmd-2016-190

Kulkarni, P.S., Bortoli, D., Silva, A.M. Reeves, C.E. (2015). Enhancements in nocturnal surface ozone at urban sites in the UK. *Environ Science Pollution Research,* 22: 20295. Retrieved from https://doi.org/10.1007/s11356-015-5259-z

Lee, J. D., Lewis, A. C., Monks, P. S., Jacob, M., Hamilton, J. F., Hopkins, J. R., … Jenkin, M. E. (2006). Ozone photochemistry and elevated isoprene during the UK heatwave of august 2003. *Atmospheric Environment*, 40(39), 7598–7613. Retrieved from https://doi.org/10.1016/j.atmosenv.2006.06.057

Lelieveld, J. and P. J. Crutzen (1994), Role of deep cloud convection in the ozone budget of the troposphere. *Science,* 264(5166): 1759-1761

Lelieveld, J., Berresheim, H., Borrmann, S., Crutzen, P. J., Dentener, F. J., Fischer, H., … Ziereis, H. (2002). Global air pollution crossroads over the Mediterranean. *Science*, 298(5594), 794–799. Retrieved from https://doi.org/10.1126/science.1075457

Li, Q. (2002). Transatlantic transport of pollution and its effects on surface ozone in Europe and North America. *Journal of Geophysical Research*, 107(D13), 4166. Retrieved from https://doi.org/10.1029/2001JD001422

Li, X., Choi, Y., Czader, B., Roy, A., Kim, H., Lefer, B., & Pan, S. (2016). The impact of observation nudging on simulated meteorology and ozone concentrations during

DISCOVER-AQ 2013 Texas campaign. *Atmospheric Chemistry and Physics*, 16(5), 3127–3144. Retrieved from https://doi.org/10.5194/acp-16-3127-2016

Lowe, D., Morgan, W., Allan, J., Utembe, S., Ouyang, B., Aruffo, E., & Breton, M. Le. (2015). WRF-Chem model predictions of the regional impacts of N2O5 heterogeneous processes on night-time chemistry over north-western Europe. *Atmospheric Chemistry and Physics*, 15, 1385–1409. Retrieved from https://doi.org/10.5194/acp-15-1385-2015

Lin, Y.-L., Farley, R. D., and Orville, H. D. (1983). Bulk Parameterization of the Snow Field in a Cloud Model, J. *America Meteorological Society*., 22, 1065–1092. Retrieved from doi:10.1175/15200450(1983)022<1065:BPOTSF>2.0.CO;2

Mar, K. A., Ojha, N., Pozzer, A., & Butler, T. M. (2016). Ozone air quality simulations with WRF-Chem (v3.5.1) over Europe: Model evaluation and chemical mechanism comparison. *Geoscientific Model Development*, 9(10), 3699–3728. Retrieved from https://doi.org/10.5194/gmd-9-3699-2016

Met Office (2006): MIDAS: UK Hourly Weather Observation Data. NCAS British Atmospheric Data Centre, 2016. Retrieved from http://catalogue.ceda.ac.uk/uuid/916ac4bbc46f7685ae9a5e10451bae7

Misenis, C., & Zhang, Y. (2010). An examination of sensitivity of WRF / Chem predictions to physical parameterizations , horizontal grid spacing , and nesting options. *Atmospheric Research*, 97(3), 315–334. Retrieved from https://doi.org/10.1016/j.atmosres.2010.04.005

Monks, P. S., Archibald, a. T., Colette, a., Cooper, O., Coyle, M., Derwent, R., … Williams, M. L. (2015). Tropospheric ozone and its precursors from the urban to the global scale from air quality to short-lived climate forcer. *Atmospheric Chemistry and Physics*, 15(15), 8889–8973. Retrieved from https://doi.org/10.5194/acp-15-8889-2015

Monks, P S, Granier, C., Fuzzi, S., Stohl, A., Williams, M. L., Akimoto, H., … von Glasow, R. (2009). Atmospheric composition change - global and regional air quality. *Atmospheric Environment*, 43(33), 5268–5350. Retrieved from https://doi.org/10.1016/j.atmosenv.2009.08.021

Monks, Paul S. (2000). A review of the observations and origins of the spring ozone maximum. *Atmospheric Environment*, 34(21), 3545–3561. Retrieved from https://doi.org/10.1016/S1352-2310(00)00129-1

Monks, Paul S. (2005). Gas-phase radical chemistry in the troposphere. *Chemical Society Reviews*, 34(5), 376–395. Retrieved from https://doi.org/10.1039/b307982c

Munir, S., Chen, H., & Ropkins, K. (2013). Quantifying temporal trends in ground level ozone concentration in the UK. *Science of the Total Environment*, 458–460, 217–227. Retrieved from https://doi.org/10.1016/j.scitotenv.2013.04.045

Myhre, G., Shindell, D., Bre´eon, F.-M., Collins, W., Fuglestvedt, J., Huang, J., Koch, D., Lamarque, J.-F., Lee, D., Mendoza, B., Nakajima, T., Robock, A., Stephens, G., Takemura, T., and Zhang, H. (2013). Anthropogenic and Natural Radiative Forcing, pp. 659– 740. Retrieved from doi:10.1017/CBO9781107415324.018

Ordóñez, C., Barriopedro, D., Garciá-Herrera, R., Sousa, P. M., & Schnell, J. L. (2017). Regional responses of surface ozone in Europe to the location of high-latitude blocks and subtropical ridges. *Atmospheric Chemistry and Physics*, 17(4), 3111–3131. Retrieved from https://doi.org/10.5194/acp-17-3111-2017

Parrish, D. D., Law, K. S., Staehelin, J., Derwent, R., Cooper, O. R., Tanimoto, H., ... Chan, E. (2013). Lower tropospheric ozone at northern midlatitudes: Changing seasonal cycle. *Geophysical Research Letters*, 40(8), 1631–1636. Retrieved from https://doi.org/10.1002/grl.50303

Pleim, J.E. (2007). A combined local and nonlocal closure model for the atmospheric boundary layer. Part I. Model description and testing. *J. Appl. Meteorol. Climatol*, 46: 1383–1395.

Pleim, J.E. (2007)a. A combined local and nonlocal closure model for the atmospheric boundary layer. Part II. Application and evaluation in a mesoscale meteorological model. *J. Appl. Meteorol. Climatol,* 46: 1396–1409

Pope, R. J., Butt, E. W., Chipperfield, M. P., Doherty, R. M., Fenech, S., Schmidt, A., ... Savage, N. H. (2016). The impact of synoptic weather on UK surface ozone and implications for premature mortality. *Environmental Research Letters*, 11(12). Retrieved from https://doi.org/10.1088/1748-9326/11/12/124004

Reidmiller, D. R., Fiore, A. M., Jaffe, D. A., Bergmann, D., Cuvelier, C., Dentener, F. J., ... Zuber, A. (2009). The influence of foreign vs. North American emissions on surface ozone in the US. *Atmospheric Chemistry and Physics*, 9(14), 5027–5042. Retrieved from https://doi.org/10.5194/acp-9-5027-2009

Royal Society. (2008). *Ground-level ozone in the 21st century: future trends, impacts and policy implications*. *October*. Retrieved from http://www.royalsociety.org/Ground-level-ozone-in-the-21st-century-future-trends-impacts-and-policy-implications-/

Safieddine, S., Boynard, A., Coheur, P., Hurtmans, D., Pfister, G., Quennehen, B., ... Raut, J. (2014). Summertime tropospheric ozone assessment over the Mediterranean region using the thermal infrared IASI / MetOp sounder and the WRF-Chem model, 10119–10131. Retrieved from https://doi.org/10.5194/acp-14-10119

Saiz-Lopez A, Mahajan AS, Salmon RA, Bauguitte SJ-B, Jones AE, Roscoe HK & Plane JMC (2007). Boundary layer halogens in coastal Antarctica. *Science,* 317, 348–351

Sillman, S. (2002). Chapter 12 The relation between ozone, NOx and hydrocarbons in urban and polluted rural environments. *Developments in Environmental Science*, 1(C), 339–385. Retrieved from https://doi.org/10.1016/S1474-8177(02)80015-8

Skamarock, J. B. Klemp, J. Dudhia, D. Gill, D. M. Barker, M. G. Duda, X. Huang, W. Wang, J. G. (2008). A description of the Advanced Research WRF version 3. NCAR Tech. Technical report, Note NCAR/TN-475+STR

Solberg, S., Hov, Søvde, A., Isaksen, I. S. A., Coddeville, P., De Backer, H., … Uhse, K. (2008). European surface ozone in the extreme summer 2003. *Journal of Geophysical Research Atmospheres*, 113(7), 1–16. Retrieved from https://doi.org/10.1029/2007JD009098

Steele, C. J., Dorling, S. R., von Glasow, R., & Bacon, J. (2014). Modelling sea-breeze climatologies and interactions on coasts in the southern North Sea: Implications for offshore wind energy. *Quarterly Journal of the Royal Meteorological Society,* (July), 1821–1835. Retrieved from https://doi.org/10.1002/qj.2484

Stevenson, D. S., Dentener, F. J., Schultz, M. G., Ellingsen, K., van Noije, T. P. C., Wild, O., … Szopa, S. (2006). Multimodel ensemble simulations of present-day and near-future tropospheric ozone. *Geophysical Research Letters*, 111(8). Retrieved from https://doi.org/10.1029/2005JD006338

Stieb, D. M., Szyszkowicz, M., Rowe, B. H., and Leech, J. A. (2009). Air pollution and emergency department visits for cardiac and respiratory conditions: a multi-city time-series analysis. *Environ. Health*, 8, 25. Retrieved from https://doi.org/10.1186/1476-069X-8-25

Stock, Z. S., Russo, M. R., Butler, T. M., Archibald, A. T., Lawrence, M. G., Telford, P. J., … Pyle, J. A. (2013). Modelling the impact of megacities on local, regional and global tropospheric ozone and the deposition of nitrogen species. *Atmospheric Chemistry and Physics*, 13(24), 12215–12231. Retrieved from https://doi.org/10.5194/acp-13-12215-2013

Stockwell, W. R., Lawson, C. V., Saunders, E., and Goliff, W. S.: A Review of Tropospheric Atmospheric Chemistry and Gas-Phase Chemical Mechanisms for Air Quality Modeling. *Atmosphere*, 3, 1–32. Retrieved from doi:10.3390/atmos3010001

Stohl, A., Eckhardt, S., Forster, C., James, P., & Spichtinger, N. (2002). On the pathways and timescales of intercontinental air pollution transport. *Journal of Geophysical Research: Atmospheres*, 107(D23), 1–17. Retrieved from https://doi.org/10.1029/2001JD001396

Stone, D., Evans, M. J., Walker, H., Ingham, T., Vaughan, S., Ouyang, B., Kennedy, O. J., McLeod, M. W., Jones, R. L., Hopkins, J., Punjabi, S., Lidster, R., Hamilton, J. F., Lee, J. D., Lewis, A. C., Carpenter, L. J., Forster, G., Oram, D. E., Reeves, C. E., Bauguitte, S., Morgan, W., Coe, H., Aruffo, E., Dari-Salisburgo, C., Giammaria, F., Di Carlo, P., and Heard, D. E. Radical chemistry at night: comparisons between observed and modelled HOx, NO3 and N2O5 during the RONOCO project. *Atmospheric Chemistry and Physics*, 14, 1299–1321, https://doi.org/10.5194/acp-14-1299-2014

Strong, J., Whyatt, J. D., Metcalfe, S. E., Derwent, R. G., & Hewitt, C. N. (2013). Investigating the impacts of anthropogenic and biogenic VOC emissions and elevated temperatures during the 2003 ozone episode in the UK. *Atmospheric Environment*, 74(August 2003), 393–401. Retrieved from https://doi.org/10.1016/j.atmosenv.2013.04.006

Stull, R. B. (1988). An introduction to boundary layer meteorology. Dordrecht: Kluwer Academic Publishers.

Sudo, K., & Akimoto, H. (2007). Global source attribution of tropospheric ozone: Long-range transport from various source regions. *Journal of Geophysical Research Atmospheres*, 112(12), 1–21. Retrieved from https://doi.org/10.1029/2006JD007992

Tesche, T. W., McNally, D. E., and Tremback, C. (2002). Operational evaluation of theMM5 meteorological model over the continental United States: protocol for annual and episodic evaluation, Re- port prepared for the Office of Air Quality Panning and Standards, US Environmental Protection Agency, by Alpine Geo- physics

Tørseth, K., Aas, W., Breivik, K., Fjæraa, A. M., Fiebig, M., Hjellbrekke, A. G., Lund Myhre, C., Solberg, S., and Yttri, K. E. (2012). Introduction to the European Monitoring and Evalua- tion Programme (EMEP) and observed atmospheric composition change during 1972–2009. *Atmospheric Chemistry and Physics*, 12, 5447–5481. Retrieved from doi:10.5194/acp-12-5447-2012, 2012

Turner, M. C., Jerrett, M., Pope III, C. A., Krewski, D., Gapstur, S. M., Diver, W. R., Beckerman, B. S., Marshall, J. D., Su, J., Crouse, D. L., and Burnett, R. T. (2016). Long-Term Ozone Exposure and Mortality in a Large Prospective Study, Am. *J.*

Resp. Crit. Care, 193, 1134–1142. Retrieved from https://doi.org/10.1164/rccm.201508-1633OC

Vautard, R., Honore, C., Beekmann, M., & Rouil, L. (2005). Simulation of ozone during the August 2003 heat wave and emission control scenarios. *Atmospheric Environment*, 39(August 2003), 2957–2967. Retrieved from https://doi.org/10.1016/j.atmosenv.2005.01.039

Vieno, M., Dore, A. J., Stevenson, D. S., Doherty, R., Heal, M. R., Reis, S., ... Sutton, M. A. (2010). Modelling surface ozone during the 2003 heat-wave in the UK. *Atmospheric Chemistry and Physics*, 10(16), 7963–7978. Retrieved from https://doi.org/10.5194/acp-10-7963-2010

Wallace, J. M., & Hobbs, P. V. (2006). Atmospheric science: An introductory survey. Amsterdam: Elsevier Academic Press

Wang,W., Bruyère, C., Duda, M., Dudhia, J., Gill, D., Kavulich, M., Keene, K., Lin, H.-C., Michalakes, J., Rizvi, S., and Zhang, X. (2015). ARW Version 3.7 Modelling System User's Guide. UCAR Boulder, CO, USA. Retrived from http://www2.mmm.ucar.edu/wrf/users/docs/user_guide_V3.7/ARWUsersGuideV3.7.pdf

Warner, T.T. (2011). Numerical Weather and Climate Prediction, Cambridge University Press, Cambridge, UK

Watson, L. A., Shallcross, D. E., Utembe, S. R., & Jenkin, M. E. (2008). A common representative intermediates (CRI) mechanism for VOC degradation. Part 2: Gas phase mechanism reduction. *Atmospheric Environment*, 42, 7196. Retrieved from https://doi.org/10.1016/j.atmosenv.2008.07.034

Wesely, M. and Hicks, B. (2000): A review of the current status of knowledge on dry deposition, Atmos. Environ., 34, 2261–2282, Retrieved from doi:http://dx.doi.org/10.1016/S1352-2310(99) 00467-7

Wild, O., Pochanart, P., & Akimoto, H. (2004). Trans-Eurasian transport of ozone and its precursors. *Journal of Geophysical Research D: Atmospheres*, 109(11), 1–16. Retrieved from https://doi.org/10.1029/2003JD004501

WMO. (2016). WMO statement on the status of the global climate in 2015. *World Meteorological Organization*, (1108), WMO-No. 1108. Retrieved from http://www.wmo.int/pages/mediacentre/press_releases/documents/WMO_1108_EN_web_000.pdf

Wong, John, "Upper Tropospheric Ozone Enhancement during the North American Monsoon Evaluated Using the Weather Research and Forecasting Model with

Chemistry (WRF-Chem)" (2013). Atmospheric & Oceanic Sciences Graduate Theses & Dissertations. 37. Retrieved from http://scholar.colorado.edu/atoc_gradetds/37

World Health Organization. (2016). Ambient Air Pollution: A global assessment of exposure and burden of disease. *World Health Organization*. Retrieved from 9789241511353

Zhang, Y., Sartelet, K., Wu, S. Y., & Seigneur, C. (2013). Application of WRF/Chem-MADRID and WRF/Polyphemus in Europe - Part 1: Model description, evaluation of meteorological predictions, and aerosol-meteorology interactions. *Atmospheric Chemistry and Physics*, 13(14), 6807–6843. Retrieved from https://doi.org/10.5194/acp-13-6807-2013

Zhang, Y., Sartelet, K., Zhu, S., Wang, W., Wu, S. Y., Zhang, X., … Wang, X. F. (2013)a. Application of WRF / Chem-MADRID and WRF / Polyphemus in Europe – Part 2 : Evaluation of chemical concentrations and sensitivity simulations. *Atmospheric Chemistry and Physics*, 6845–6875. Retrieved from https://doi.org/10.5194/acp-13-6845-2013